Dissertation zur Erlangung des Doktorgrades
der Fakultät für Chemie und Pharmazie
der Ludwig-Maximilians-Universität München

Kinetics and Intermediates of Palladium-catalyzed Negishi Cross-Coupling Reactions

Katharina Böck

aus

München, Deutschland

2023

Erklärung

Diese Dissertation wurde im Sinne von § 7 der Promotionsordnung vom 28. November 2011 von Herrn Prof. Dr. Konrad Koszinowski betreut.
und von Herrn Prof. Dr. Herbert Mayr von der Fakultät für Chemie und Pharmazie vertreten.

Eidesstattliche Versicherung

Diese Dissertation wurde eigenständig und ohne unerlaubte Hilfe erarbeitet.

München, 02.08.2023

Katharina Böck

.....

Dissertation eingereicht am	12.4.2023
1. Gutachter:	Prof. Dr. Herbert Mayr
2. Gutachter:	Prof. Dr. Konrad Koszinowski
Mündliche Prüfung am	22.5.2023

Acknowledgements

Zwei großartigen Männern möchte ich gleichermaßen für die Möglichkeiten danken, die Sie mir gewährten.

Prof. Dr. Konrad Koszinowski danke ich für das interessante Thema, die fachliche Unterstützung, seine Geduld und das Vertrauen bei der Anfertigung meiner Dissertation. Unsere Unterhaltungen gaben mir immer neue Denkanstöße und führten zu wertvollen wissenschaftlichen Erkenntnissen.

Prof. Dr. Herbert Mayr danke ich für die finanzielle Unterstützung und für den Platz in der Mitte seiner Arbeitsgruppe. Seine fachlichen Anregungen ermöglichten mir neue Blickwinkel und Arbeitsansätze für meine Forschung.

Prof. Dr. Konstantin Karaghiosoff danke ich für die Hilfe bei den NMR-Studien und seine herzliche Motivation.

Ich danke allen, die den freien Wissens- und Informationsaustausch ermöglichen, besonders wenn die zugrunde liegende Forschung aus öffentlichen Mitteln bezahlt wurde.

Weiter möchte ich mich bei meinen ehemaligen Kolleginnen und Kollegen Julia Feil, Christina Müller und Areenan In-Iam, Johannes Ammer, Nathalie Hampel, Elija Wiedemann, Francisco Coral, Angel Puente und Tobias Nigst für die emotionale und fachliche Unterstützung bedanken.

Besonders dankbar bin ich diesen Menschen für die wertvolle Freundschaft, die uns bis heute verbindet.

Am meisten danke ich meiner Familie und Stefan für ihr Verständnis, Unterstützung und Liebe.

Parts of the results of this thesis have been published in:

Anionische Palladium(0)- und Palladium(II)-At-Komplexe

Anionic Palladium(0) and Palladium(II) Ate Complexes

M. Kolter, K. Böck, K. Karaghiosoff, K. Koszinowski, *Angew. Chem.* **2017**, *129*, 13427-13431; *Angew. Chem. Int. Ed.* **2017**, *56*, 13244-13248.

Catalyst Activation, Deactivation, and Degradation in Palladium-Mediated Negishi Cross-Coupling Reactions

K. Böck, J. E. Feil, K. Karaghiosoff, K. Koszinowski, *Chem. Eur. J.* **2015**, *21*, 5548-5560.

0 Abstract

The kinetics and intermediates of Pd-catalyzed Negishi cross-coupling reactions were analyzed by NMR spectroscopy, electrical conductivity measurements, gas chromatography and electrospray ionization (ESI) mass spectrometry. The measurements were carried out using the model reaction of ethyl 4-iodobenzoate and BuZnBr·LiBr catalyzed by $Pd(OAc)_2$/2 S-Phos. The effect of various additives like LiBr and $ZnBr_2$, different precatalysts ($Pd(OAc)_2$/2 S-PHOS, PEPPSI-IPr, PPh_3), different substrates ArX (X = I, Br, OTs), and different organozinc reagents (e.g., BuZnBr, PhZnBr, BnZnBr) were investigated. The kinetic measurements point to a rate-determining oxidative addition. However, it turned out that not only the Pd catalyst and the aryl halide substrate, but also the organozinc reagent is involved in this step.

The measurements of the involved intermediates indicate degradation of the catalyst due to Pd aggregation and C−P bond cleavage of the S-PHOS ligand. This explains the gradual decrease in activity found in the kinetic measurements. The observation of novel heterobimetallic Pd–Zn complexes $[L_2PdZnR]^+$ (L=S-PHOS, PPh_3, R=Bu, Ph, Bn) was particularly revealing. Gas-phase fragmentation experiments suggest that these species feature a direct Pd-Zn bond.

Investigations on the rate of the Negishi cross-coupling reaction of ethyl 4-bromobenzoate and BuZnBr·LiBr catalyzed by $Pd(OAc)_2$/2 S-Phos indicate that the presence of methyl 4-iodobenzoate resulted in higher conversion to the alkylarene cross-coupling product stemming from the aryl bromide substrate. A similar increase in conversion was observed upon addition of phenyl iodide to the model reaction conducted under otherwise identical conditions. The increased conversion may occur in consequence of halogen exchange at the aryl compound.

Different methods were used to investigate the tendency of Pd species to form ate complexes.

Pd^0 is better able to add Br-Anions when ligated by L_F (tris[3,5-bis(trifluoromethyl)-phenyl]phosphine) than ligated by PPh_3 or S-PHOS. The resulting ate complex $[(L_F)_3PdBr]^-$ easily loses one L_F ligand to give a tri-coordinated complex, which supposedly corresponds to the catalytically active intermediate in cross-coupling reactions. Upon the addition of the aryl iodide ArI, the newly formed ions $[(L_F)Pd(Ar)I_2]^-$, $[(L_F)_2Pd(Ar)I_2]^-$, and $[(L_F)_2PdI_3]^-$ were detected by ESI mass spectrometry.

1 Introduction[a]

1.1 History of cross-coupling reactions

"Organic synthesis is considered, to a large extent, to be responsible for some of the most exciting and important discoveries of the twentieth century in chemistry, biology and medicine and continues to fuel the drug discovery and development processes with myriad processes and compounds for new medical breakthroughs and applications." K. C. Nicolaou et al.[1] These words demonstrate the status of synthetic organic chemistry over the last three decades. There is no doubt about the importance and urgency of developing new, more efficient, and environmentally friendly methods of performing chemical transformations.[2]

The development of transition metal-catalyzed cross-coupling reactions has allowed chemists to assemble complex molecular frameworks leading to the total synthesis of biologically and pharmaceutically important molecules. The same advancements facilitated industrial process development. Cross-coupling is a particularly popular method because it allows a high degree of flexibility.

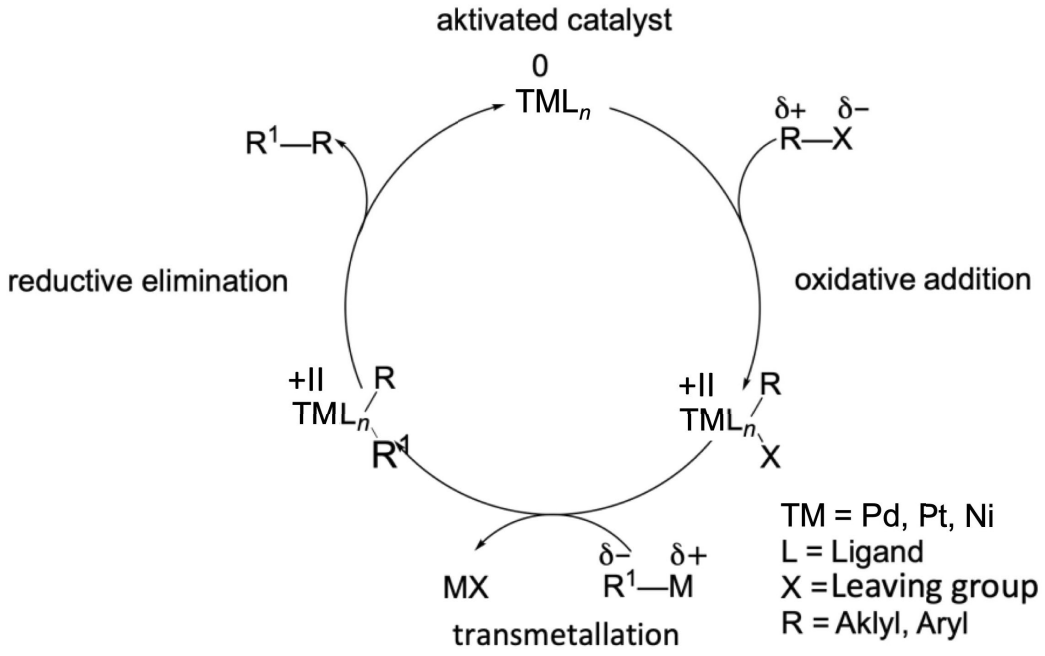

Scheme 1.1 General reaction scheme of cross-coupling reaction.

Different organometallic reagents and a broad range of functional groups can be used.[3]

[a] Some of the schemes and text passages of this chapter have partially been published already in Lit [126] and [156].

Therefore many opportunities arose. However, there is still an ongoing effort to further expand the possibilities of cross-coupling reactions. Among these methods, palladium-catalyzed processes are of outstanding importance in the synthesis of biologically and pharmaceutically important molecules.[4]

Palladium-catalyzed cross-coupling reactions are commonly classified according to the organometallic reagent employed. To this day palladium-catalyzed Heck and cross-coupling reactions are an indispensable part of organic synthesis and are becoming ever more extensive and complex.[5-11]
Negishi first reported the use of orgazinc reagents in these reactions in 1977. Thus, a mild method for the synthesis of biaryls with high chemoselectivity had been developed.[5]

Among the various members of this reaction family, the Negishi cross-coupling reaction[5, 7, 11-12] has recently attracted particular attention.[13]

In this palladium-catalyzed cross-coupling, organozinc halides RZnX are used as coupling reagents for organyl halides R'X. Sometimes the corresponding diorganozinc species R_2Zn is also used.

The popularity of organozinc halides results from their high reactivity combined with an excellent functional-group tolerance and easy accessibility.[14, 15, 16]

$$R'X + RZnX \rightarrow R'R + ZnX_2 \qquad (2.1)$$

It is generally believed that Negishi cross-coupling reactions follow the catalytic cycle common to the whole family of palladium-catalyzed transformations. This catalytic cycle includes the distinct elementary steps of oxidative addition, transmetalation, and reductive elimination.[11, 17] This conceptual framework has proven very useful in understanding and optimizing this catalyzed reaction.

The tremendous importance of this class of reactions was internationally recognized in 2010 by the awarding of the Nobel prize in chemistry to Ei-ichi Negishi[7b] together with Richard Heck[18] and Akira Suzuki[9c] “for palladium-catalyzed cross-couplings in organic synthesis”. Likewise, other researchers such as Kumada,[10] Stille,[19] and Hiyama,[20] have also contributed to this field. Buchwald[21] and Hartwig[22] expanded the method to a range of carbon–heteroatom bond forming reactions.

1.2 Mechanism of palladium catalyzed cross-coupling reactions

Palladium catalysis has become an indispensable part of modern organic synthesis. Often the reactivity can be increased by the presence of salts.[23]

Negishi et al. showed in 2005 that the presence of LiCl affects strongly the reactivity of RZnX reagents.[24] Stimulated by this seminal discovery, the effects of salt additives on the nature and reactivity of RZnX compounds have quickly attracted significant interest. Organozinc halides RZnX are valuable and versatile reagents heavily used in modern organic synthesis.[25]

Generally, the mechanism for palladium catalyzed cross-coupling reactions is described as a catalytic cycle involving three principal steps outlined in Scheme 1.1: The first step in the catalytic cycle of Negishi cross-coupling reactions is the oxidative addition of an aryl halide Ar–X to a low-valent Pd^0 center to afford a [Ar–Pd–X] intermediate followed by transmetalation between [Ar–Pd–X] and an organometallic reagent R–Zn–X to yield a [Ar–Pd–R] complex usually stabilized by bulky ligands. The final step is then the reductive elimination of [Ar–Pd–R] to produce Ar–R and the concomitant regeneration of the active catalyst. The oxidative addition step investigations were mainly based on stoichiometric experiments.[26] Moreover, many related mechanistic studies show that palladium-catalyzed cross-coupling reactions attracted more and more attention.[13i, 27] In many cases the active catalyst is formed at the beginning of the catalytic cycle starting from a precursor called precatalyst.[28]

Unfortunally these active catalysts are extremely air sensitive and very difficult to synthesize and store. Therefore, these catalysts are relatively rarely utilized. Readily accessible compounds such as the relatively poor catalyst $Pd(PPh_3)_4$ [29, 30] or precatalyst as $Pd(dba)_2$/$Pd_2(dba)_3$ (dba: trans,trans-dibenzylideneacetone) with added ligand are used.[31] It is now widely recognized that dba is not completly displaced and in fact impedes the reaction.[32]

Alternatively catalyst solutions are generated by adding a phosphine to a solution of a palladium(II) compound such as $Pd(OAc)_2$ or $PdCl_2$, the assumption made is that the palladium(II) salts are efficiently reduced to the desired palladium(0) catalytic precursors. [11, 33]

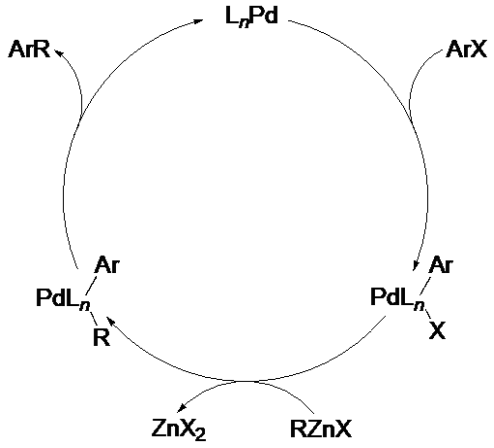

Scheme 1.2 Currently accepted mechanism of Palladium catalyzed Negishi cross-coupling reactions.

To the present day, the mechanistic understanding of the canonical catalytic cycle is very useful to understand the palladium catalyzed Negishi cross-coupling reaction. Still, more recent studies indicate that the currently accepted catalytic cycle depicted in Scheme 1.2 is overly simplistic and does not fully reflect the intermediate steps in Negishi cross-coupling reactions.

1.2.1 Side reactions in Negishi cross-coupling

An additional line of evidence of the higher complexity of actual catalytic cycle was the observation of homo-coupling products.[13h, 27k, 34] These undesired byproducts formed by the combination of two organyl groups from the organyl halide or the organozinc reagent in Scheme 1.3 respectively. The exact mechanism, which leads to the formation of side products such as homo coupling, is not yet completely understood.

$$ArX + RZnX \xrightarrow{[Pd]} 1/2\ Ar_2 \quad (+ \text{further products})$$

$$ArX + RZnX \xrightarrow{[Pd]} 1/2\ R_2 \quad (+ \text{further products})$$

Scheme 1.3 Palladium-catalyzed formation of homo-coupling products.

Various mechanisms have been proposed for such reactions.[27k, 34b-d] Lei and coworkers observed a second transmetalation step that occurs between between an Ar^1-Pd-Ar^2 species and the organozinc reagent.[27k] Analogously, this would result in PdL_nR_2, ArZnX and PdL_nAr_2.

The last two match to the observed dehalogenation (Scheme 1.4) and the homocoupling product (Scheme 1.3).

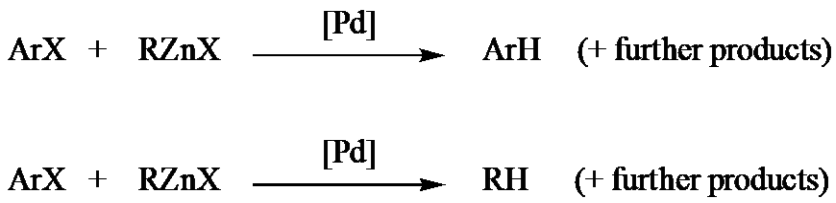

Scheme 1.4 Palladium-catalyzed formation of dehalogenation product.

Further elucidation of the elementary steps in the catalytic cycle should improve our mechanistic understanding, which will then guide optimization of synthetic procedures.
When studying the mechanism of palladium-mediated cross-coupling reactions, a series of variables have to be considered, which will be detailed in the following.

1.2.2 Factors that affect Negishi cross-coupling reactions

Several factors can influence the effectiveness and selectivity with which aryl halides undergo oxidative addition. The choice of ligand can have great impact on this type of reaction. Both steric and electronic properties have an effect.[35]
For many years triaryl phosphines or chelating bis-triarylphosphines were used in cross-coupling reactions. Heck and Ziegler Jr. had already established that the additional steric demand of the bulky ligands indicates that only $(PR_3)_2Pd$ complexes can be formed.[36] Hartwig and coworkers characterised the parent $(PR_3)_2Pd$ complex and further demonstrated that the oxidative addition of ArBr first required further dissociation of one phosphine.[37]
Typically the active catalyst in Negishi cross-coupling reaction is a bis-phosphine palladium(0) compound. [11, 33]
The growing interest in cross-coupling reaction with bulky phosphines was stimulated further by the studies of Fu, utilising P*t*Bu$_3$.[38] Especially, bulky ligands were determined to trigger high reactivities in palladium catalysis. Therefore, it is assumed that the active catalytic species is a monoligated Pd complex.[22, 39] Minor structural variations can make major differences to yield and catalytic reactivity. Important ligands were developed by Buchwald's laboratory. The ability to tune the steric and especially the electronic properties of the R group provides ligands that exhibit broad utility[40] and are hence they are very widely used.[41, 42, 43]

S-PHOS is one of the modern ligands designed by Buchwald and coworkers. Typically, S-PHOS is used in a 1: 2 ratio to the precatalyst $Pd(OAc)_2$[44] and half of the S-PHOS is supposedly consumed in the reduction of the Pd(II) precatalyst to generate the active Pd(0) species.[45] The active Pd(0) species then is coordinated by the remaining ligand. S-PHOS is known to form preferentially 1:1 complexes with Pd(0).[41c, 46, 47]

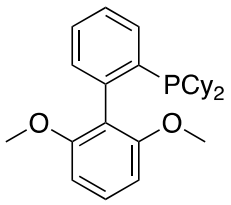

S-Phos [48]

Scheme 1.5 S-PHOS = 2-dicyclohexylphosphino-2',6'-dimethoxy-biphenyl.

Also, the solvents[13g] as well as other additives[35] present in the reaction mixture are particularly important. Depending on these variables different palladium species are formed and control the outcome of a reaction.

In particular the effect of quaternary tetrabutylammonium salts as additives has received remarkable attention in the last years.[23a-f, 23i-q] It seemed that especially the anion, usually a halide, was pivotal, whereas the counter ion played the less important role. As early as 1984 T. Jeffery described that Pd-catalyzed vinylation of organic halides can easily proceed at mild temperature under solid-liquid phase transfer conditions, using tetrabutylammonium as the phase transfer agent.[23a, 23b] Knochel et al observed 1999 the positive effect of tetra-*n*-butylammonium iodide on Pd(0)- and Ni-catalyzed Negishi cross-couplings between aryl or alkenyl triflates and benzyl[49] and / or alkylzinc halides.[50] It was found that with increasing Bu_4NI equivalents also the cross-coupling product increased.
Marder and Lei used $Pd(OAc)_2$ and Bu_4NBr to create Pd(0) nanoparticles.[48] Beside the formation of stabilized Pd(0) nanoparticles also the formation of palladium(0)ate complexes is discussed.[51] The required anions can be added in the form of lithium or magnesium salts.

1.2.3 Preparation of organozinc halides

For a long time, not much attention has been paid to the salts contained in the solution of the organozinc compounds. Salts are not only purposefully admitted to cross-coupling reactions since they are present in the mixture due to the nature of their synthesis.

The role of LiX and MgX_2 in organozinc chemistry has received little attention until Knochel et al. found LiCl to accelerate Zn insertion reactions dramatically (Scheme 1.6).[14b-d] Also many bases employed for zincation reactions contain one or more equivalents of LiCl as well.[16]

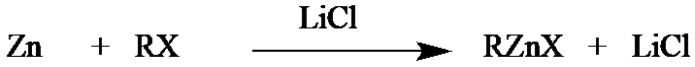

Scheme 1.6 Preparation of organozinc halides by Knochel´s method.

Furthermore, efficient access to these compounds is given by the transmetalation of zinc halides ZnX_2 with organolithium (Scheme 1.7) or Grignard reagents.[25]

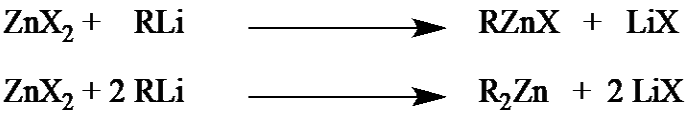

Scheme 1.7 Preparation of organozinc halides by transmetalation.

Alternatively, they can be generated by the insertion of organic halides into activated zinc prepared according to Rieke's method (Scheme 1.8).[52]

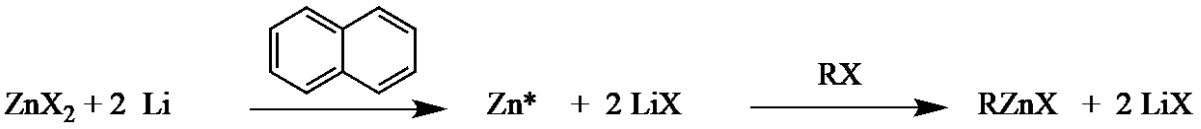

Scheme 1.8 Preparation of organozinc halides by Rieke´s method.

Unless special efforts are taken, the produced solutions of RZnX contain lithium halides LiX or magnesium halides MgX_2 remaining from the transmetalation or the activation step. Earlier studies neglected the presence of these salts, although they can give rise to drastic changes of Negishi cross-coupling and other reactions of organometallics, as is realized today.[27n, 53]

1.2.4 Interaction of the MgX_2 and LiX salts with the organozinc halide

A first set of observations refers to the effect of simple salt additives, such as LiX or MgX_2. These salts are frequently present in reactive mixtures if the RZnX reagent is prepared by different methods.

As Koszinowski[27h, 27i, 27r, 55b] and others [27s, 54, 56, 57] have shown, RZnX species exhibit a high tendency to add X^- anions and form zincate species. For their solutions in tetrahydrofuran, Koszinowski and Böhrer observed organozincate complexes, such as $RZnX_2^-$ or $[LiRZnX_3]^-$ and related polynuclear complexes (X = Cl, Br, and I), by electrospray-ionization mass spectrometry.[27h, 27i, 27q, 27r] Theoretical calculations corroborated the formation of organozincate species from RZnX and LiX.[57]

With respect to $RZnX{\cdot}MgCl_2$, X-ray crystal structures reported by Jin *et al*.[58] as well as by Hevia *et al*.[27n] point to the formation of bimetallic $Mg(\mu\text{-}X)_2Zn(R)X$ species (X = Cl). For a long time no comparably detailed solid-state structural information of RZnX·LiX reagents, was available. 2010 Clyburne and coworkers determined the crystal structure of $[Et(Cl)Zn(\mu\text{-}Cl)_2Zn(Cl)Et]$ and $EtZnBr_3^{2-}$.[56]

Jin *et al*. then used kinetic measurements to demonstrate that $PhZnCl{\cdot}MgCl_2$ is far more reactive in the transmetalation step of a Ni-catalyzed oxidative homocoupling reaction in THF than PhZnCl·LiCl.[58] These results are in line with the earlier findings of Negishi and coworkers, who has compared the cross-coupling reactions of PhZnBr·LiBr and PhZnBr·MgClBr in THF.[24] These authors found that both LiCl/Br and MgX_2 salts led to an acceleration of Pd-catalyzed Negishi cross-coupling reactions but that the effect of the former was more pronounced.[55a]

In parallel, evidence accumulated that the presence of LiX and MgX_2 salts also changes the reactivity of RZnX reagents in their Pd- or Ni-catalyzed reactions with organic halides, *i.e*., Negishi-type cross-couplings, and related transformations.

Several studies reported that LiX salts also change the rates of further transition-metal catalyzed reactions involving RZnX in carboxylations,[59] transmetalations,[60] hydroalklyations,[61] and oxidative homo-coupling[34b, 58] without investigating this phenomenon in detail.[62] The Organ group screened various different salt additives in the palladium-mediated reaction of alkyl halides with BuZnBr and found that LiBr led to the largest rate enhancement.[27p, 27s, 62] In the year 2011 Hevia and Mulvey summarized the effects of simple additives.[53b]

For most of these examples, the observed effects were surmised to result from an interaction

of the salt additive with the RZnX reagent.[58-60] The authors rationalized this effect by the formation of lithium organozincates, whose increased nucleophilicity supposedly accelerates the transmetalation step; the tendency of RZnX to add X^- anions and form zincate species indeed is well-documented.[27h, 27i, 27p, 27r, 27s, 51, 55a, 56, 57, 62, 63]
In marked contrast, lithium halides were reported to have a negative effect in some nickel-catalyzed Negishi cross-coupling reactions.[64]

1.2.5 Interaction of the ZnX_2 salts with the organozinc halide

A second finding pointing to the occurrence of reactions beyond the conventional catalytic cycle relates to the effect of zinc halides ZnX_2, which are formed as stoichiometric byproducts of Negishi cross-coupling, equation 2.1. Thus, their possible interference with the catalytic cycle would be of considerable relevance. Organ and coworkers observed that added $ZnBr_2$ slowed down Pd-catalyzed Negishi cross-coupling reactions of alkylzinc reagents and ascribed this effect to the formation of $ZnBr_3^-$ at the expense of alkylzincates;[27p, 27s, 54, 65] in the corresponding reactions of arylzinc reagents, $ZnBr_2$ did not show a detrimental, but a rate-enhancing effect, however.[66] For a Ni-mediated Negishi cross-coupling, $ZnBr_2$ was shown to abstract a Br^--anion from the catalyst, resulting in a cationic Ni(II) complex.[27b] Given the likely importance of cationic pathways in Pd-catalyzed Negishi cross-coupling reactions,[67] a similar role of $ZnBr_2$ in these transformations cannot be excluded either.

Finally, not only simple inorganic salts, such as LiBr or $ZnBr_2$, may interact with the essential components of Pd-catalyzed Negishi cross-coupling reactions, but also these components themselves may possibly interact with each other in unexpected ways. For instance, quantum-chemical calculations suggest that the transmetalation step not merely corresponds to an exchange of organyl and halide substituents, but rather involves an intimate Pd−Zn interaction.[27c, 68] The recent isolation and characterization of several bimetallic Pd−Zn complexes indeed demonstrates that such metal-metal contacts can form.[69] Even more interestingly, González-Pérez et al. recently postulated that Pd−Zn interactions may also control the oxidative addition.[70] This conclusion drawn from quantum-chemical calculations so far lacks experimental verification, however.

1.2.6 Interaction of the LiX salts with the palladium catalyst

Presumably, the LiX salts could also act upon the palladium catalyst. The role of anionic Pd ate

complexes in cross-coupling reactions is frequently discussed in literature.[23i, 23n, 23q, 71, 72] So far, this theoretical prediction lacks experimental proof or disproof, however. The experimental characterization of these intermediates is far from complete.

Evidence for the existence of Pd^0 ate complexes is rare. [30, 73, 74] This species is generally considered to be relatively unstable and therefore can be difficult to observe.

Amatore and Gossen used quantum-chemical calculations to study the model complexes L_2PdX^- (L = PMe_3, PPh_3; X = Cl, Br, I, OAc). The calculations resulted in Pd-X binding energies of only 40 – 90 kJ mol^{-1}.[75, 76] In addition, Goossen, Thiel and coworkers also applied quantum-chemical methods to study the Pd^{II} ate complexes formed during oxidative addition.[77] Unlike Jutand and Amatore, they suggested the formation of square-planar complexes. In these complexes, the Pd center is coordinated by the halogen atom of the aryl halide.[77] Amatore and Jutand and others proposed that Pd^0 ate complexes are formed by the addition halide and acetate anions added to Pd(0) centers.[27n, 51, 53, 63] Instead of the commonly postulated Pd^0L_2-catalyst as the most important intermediate, anionic complexes are formed as reactive species. Therein palladium(0) is ligated by a halide ($Pd^0L_2X^-$) or by an acetate ion ($Pd^0L_2(OAc)^-$). The type of anion has a strong influence on the reactivity of the formed complex and the rate of oxidative addition. Furthermore, the reaction is accelerated by the cation, but the Pd^0-complex formed is destabilized. Postulated trans-$ArPdI(PPh_3)_2$ complexes are not produced as main intermediates, but instead previously unsuspected pentacoordinated anionic complexes, as $ArPdI(Cl)(PPh_3)_2^-$ and $ArPdI(OAc)(PPh_3)_2^-$ are formed.[51, 63b, 78] The influence of the anion is not limited to oxidative addition kinetics since the structure and reactivity of the arylpalladium(II) formed in the oxidative addition strongly depend on the anion ligated to the reacting palladium(0).

Jutand, Amatore, and coworkers were the first to propose a detailed mechanistic rationalization of the beneficial effect of anionic palladium complexes.[51, 63b, 78] Using electrochemical methods and ^{31}P NMR spectroscopy, these authors were able to detect Pd ate complexes, which result from the addition of the anion X^- to the Pd catalyst.[51, 63b, 78, 79] These anionic and nucleophilic zero-valent Pd complexes[30] supposedly have a high reactivity toward aryl halides and readily undergo oxidative addition. After dissociation of the anion, transmetalation, and reductive elimination, the catalytic cycle is closed.

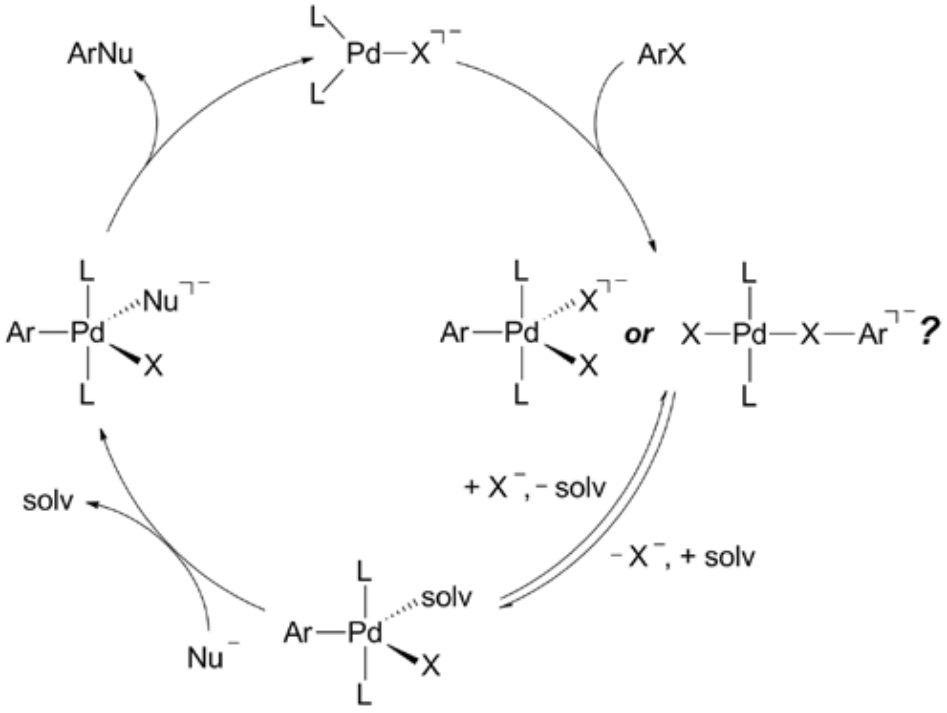

Scheme 1.9 Catalytic cycle of Pd-mediated cross-coupling reactions involving ate complexes (L = phosphine, X = halide). For the intermediate resulting from the reaction of the zero-valent catalyst with the substrate ArX, both a penta- and a square-planar coordination geometry have been suggested.[51, 63b, 77, 78]

In such cases, the salt additive would not influence the transmetalation step, but the oxidative addition. Also note that halide effects[23i] are well-known for Pd-catalyzed Heck[23c, 23d, 72] and Stille[23q, 79b, 80] reactions. This also suggests that during the cross-coupling reaction not only the organozinc species is affected by salts.

1.3 Kinetic investigations on the Negishi cross-coupling reaction

To achieve a better understanding of the catalytic cycle, kinetic measurements are of great interest. Wide ranges of modern techniques were used to study the catalytic cycle, such as GC, HPLC and NMR. The utility of kinetic measurements[81] for the mechanistic analysis of Negishi cross-coupling reactions has been emphasized by Jin and Lei.[27t]

In the first step, the oxidative addition, the active Pd catalyst reacts with the organyl halide. The oxidative addition of transition metal catalyzed coupling reactions was intensively investigated.[23k, 26i, 26k, 51, 82] Various compounds such as the presence of zinc salts influence the oxidative

addition. Jacobi et al. showed that ZnX_2 and thioimidates form an electron deficient complex which promotes oxidative addition with the palladium catalyst.[83] Hartwig and coworkers studied the influence of bulky ligands on the oxidative addition. Kinetic analysis by ^{31}P-NMR showed a lack of inhibition by excess ligand and demonstrated the dependence on the concentration of PhI expected for an associative mechanism.[26k, 26m]

The transmetalation in cross-coupling reactions is the elementary step to split the carbon-metal bond of the organometallic reagent and brings the organyl moiety into the coordination sphere of the transition metal center. This process has received more attention in mechanistic investigations than other elementary steps of the transition metal catalyzed cross-coupling reactions. The organometallic compounds organoboron and organotin, are known to be less reactive than organozinc reagents.[27t] Therefore, most studies focusing on the transmetalation step were done on Stille and Suzuki couplings. The transmetalation step in Negishi couplings has rarely been studied until the more recent efforts by the groups of Lei[27k, 27o] and Espinet.[27d, 67, 68b]

Espinet *et al.* studied the transmetalation step of the Negishi cross-coupling detailed via ^{19}F-NMR. They monitored the reaction of Pd complexes [PdRfCl(PPh_3)$_2$] (Rf = 3,5-dichloro-2,4,6-trifluorophenyl) with the organozinc species $ZnMe_2$ or ZnMeCl.[27d] Their results showed that ZnR_2 and ZnRX reagents act with different kinetic features in the transmetalation step. Lei and coworkers used aryl zinc reagents and reported similar findings.[27k] Based on these results and by DFT calculations, controlling factors that promoted the second transmetalation or the reductive elimination were identified. The DFT calculations showed that a less sterically crowded aryl iodide and an ortho-substituted aryl zinc species yielded less homocoupling and dehalogenation product.

In the reductive elimination step the bond between the two carbon atoms is formed. Usually, the knowledge about reductive elimination is gained from stoichiometric experiments. In these investigations the key intermediates are stabilized by special ligands and substrates.

A large number of kinetic investigations on Negishi cross-coupling was done by the group of Aiwen Lei. They studied for example the accelerating effect of phosphine/electron-deficient olefin ligand on reductive elimination.[27k, 27o, 27t, 84, 85] The organozinc reagents are known as reactive nucleophiles. On this account, the transmetalation step is supposed to be fast and the oxidative addition or the reductive elimination is more likely the rate-limiting step. Consequently, if the oxidative addition is fast, the Negishi coupling reaction could be treated as a proper model to discuss reductive elimination. Stille described in 1980 that electron-deficient ligands promote reductive elimination.[86] The group of Lei revealed quantitative

understanding of reductive elimination using gas chromatography from palladium catalyzed Negishi cross-coupling reactions.[27g, 84, 87] To analyze the kinetic data they used different kinetic models, zero-order kinetics in the case that reductive elimination might be rate determinant, first order kinetics on ArI if oxidative addition might be rate limiting. This approach neglects the possibility of decay of the catalyst in the overall reaction. However, this would make the kinetic behavior more complex.

The simultaneous presence of several components and the possibility of mutual interactions clearly lead to an enormous complexity of Pd-catalyzed Negishi cross-coupling reactions, thereby hampering their mechanistic understanding and rational optimization. The situation is even further complicated by the fact that the rate-limiting step and, correspondingly, the rate-determining states[88] are a priori not known. Depending on the combination of reaction partners, the employed catalyst, and the reaction conditions, either the oxidative addition, the transmetalation, or the reductive elimination may be rate-limiting. As most of the studies reported in the literature probed widely different conditions, a straightforward comparison and evaluation is not possible.

1.4 Intermediates of the Negishi cross-coupling reaction

In addition to kinetics, intermediates have to be determined. The development of modern palladium-catalyzed cross-coupling reactions has been paralleled and assisted by extensive mechanistic studies.[11] Besides aiming at the elucidation of the reaction kinetics, these studies focused on the identification and characterization of the intermediates formed in the catalytic cycle.

In principle, several difficulties arise in the identification of intermediates. The concentrations of the catalyst and the resulting intermediates in a catalytic reaction are very low. Nevertheless, in order to be able to measure the intermediates with the selected methods of measurement, the amounts and ratios of the reactants should be increased. This causes a deviation in intensities and concentrations of the intermediate compared to real catalytic conditions. In addition, the most reactive intermediates are also unstable and thus very short lived. For example, Pd(0), which is believed to be the reactive catalyst in cross-coupling reactions, is readily oxidizable.[89] Often one would like to analyze the intermediates of the one step of the catalytic cycle by mixing the components necessary to this step. For example, Hartwig and coworkers analyzed the catalytic step of oxidative addition in the absence of the organometallic reagent.[26k, 26m] Possibly other intermediates arise than in the presence of the metal organyl solution and key

intermediates are not detected. Ideally, the investigated reactions should be observed under typical reaction conditions for meaningful information to be obtained about the mechanism, because under such conditions salts and anions[51b] are suspected to function as ligands for palladium, which again has complex effects on the reaction efficiency.

To this end, a wide range of different analytical tools has been applied. Among the latter, ^{31}P NMR spectroscopy has proven particularly valuable because it lends itself to the selective detection of phosphine-containing intermediates;[29, 51a, 63b, 74, 90] phosphines are heavily used as ligands in Pd-catalyzed cross-coupling reactions.[11] *Inter alia*, ^{31}P NMR spectroscopy has shown that phosphines reduce Pd(II) precatalysts in situ [90a, 90b]

Further information can be obtained from ^{1}H[90c, 90d, 90k] and ^{13}C[90c, 90d] NMR as well as from IR[91] and UV/Vis[90h, 91-92] spectroscopy. Especially UV/Vis spectroscopy has been used to investigate decomposition reactions of the catalyst.[90h, 92, 93] Apart from spectroscopy in its different variants, electrochemical methods have been instrumental in the identification of reactive intermediates.[51a, 79b, 90a, 90e, 90k]

For instance, Amatore, Jutand and coworkers employed amperometry and cyclic voltammetry to discover the role of anionic Pd ate complexes in cross-coupling reactions.[51, 63b] They proposed that anionic palladium complexes are the effective catalyst in crosscoulping reactions.

Another technique, which selectively detects the ionic components of the sampled solutions, is given by electrospray ionization (ESI) mass spectrometry.[94] ESI-MS has proven to be a very useful tool to study the mechanism of organometallic catalytic reactions. Complex mixtures can be investigated, intermediates of low concentration can be detected and the analysis is very fast. For these reasons, ESI-MS is well suited for the analysis of palladium-catalyzed C-C bond forming cross-coupling reactions.[27q, 89, 95, 96, 97] Most of these studies have focused on the structural identification of short-lived or low-concentration intermediates, but some recent studies have monitored the levels of intermediates or reactants and products over time.[27q, 95f] The unambiguous stoichiometric information afforded by this method can provide valuable insight in the Pd catalyst speciation in solution.[89, 95a-f, 95h-j, 98] Furthermore, gas-phase fragmentation experiments shed light on their stability and unimolecular reactivity.[89, 95d, 95i, 98g, 98l, 100] A drawback of ESI-MS is that only charged substances can be detected.

Two further methods also deserve mentioning although they cannot directly probe intermediates in solution. X-ray crystallography has greatly contributed to the characterization of Pd catalysts by providing accurate structural data for model complexes.[90c-e, 90g, 101] It has been applied to the identification of catalytically active intermediates[101a] and their degradation

products.[92] For example Tomp *et al.* proposed with UV/Vis and X-ray the dimerization and trimerisation of phosphor ligands. Likewise, quantum-chemical calculations can afford additional information by predicting the energetic stabilities of putative intermediates.[77a, 79a, 90d, 90f, 90i, 90k, 102]

An example for successful combination of different methods is the investigation on copper-free Sonogashira cross-coupling by McIndoe et al. using ESI-MS, ^{1}H-NMR and UV/Vis. They observed the intensities of different species during a typical reaction and observed an interesting change in mechanism early in the reaction, whereby the initial fast rate is replaced with a much slower, zero-order process.[98i] Together, the different methods have significantly improved the knowledge on the intermediates of Pd-mediated cross-coupling reactions and supported the generally invoked catalytic cycle with the individual steps of oxidative addition, transmetalation, and reductive elimination.[11] In the specific case of Pd-catalyzed Negishi cross-coupling, however, only relatively few studies have investigated the Pd-containing intermediates formed therein. [13j, 27d, 27k, 27q, 67, 68a, 68b, 70, 103, 104] Thus, the present mechanistic understanding of this tremendously important reaction type is essentially limited to the assumed operation of the conventional catalytic cycle.

1.5 Objectives

The Negishi reaction is a widely used cross coupling reaction which allows access to a broad range of molecules. However, the reaction mechanism is poorly understood, and the effects of different reactive components are hardly quantified. Because of its importance, it is desirable to gain a comprehensive understanding of the Negishi reaction and how various additives and conditions affect the reaction.

To elucidate the mechanism of Pd-catalyzed Negishi cross-coupling reactions under realistic catalytic conditions, the model reaction shall be monitored by taking aliquots and analyzing them by gas chromatography (see Experimental Section for details). Changing the reaction conditions, for example, using different organozinc reagents, different catalysts, and additives such as LiX, influences the kinetics of this reaction. These effects should provide information about the mechanism and conclusions about the rate-determining step of the catalytic cycle.

To complement the macroscopic picture derived from the kinetic experiments with insights at the molecular level, spectroscopic studies shall be performed. ESI mass spectrometry and other techniques such as UV/Vis spectroscopy and ^{31}P NMR spectroscopy are suitable to investigate the intermediates formed during the reaction as part of this work. The synergies of these different methods allow one to gain a deeper insight into parts of the catalytic cycle. Moreover, particular care should be taken to choose reaction conditions identical to or closely resembling those of real catalytic applications. The analysis of such experiments is more cumbersome than that of stoichiometric experiments. However, is the only way to ensure that the effects resulting from the interaction of the various reactive components are taken into account

Interestingly, ethyl 4-bromobenzoate, which reacts relatively slowly under normal cross-coupling conditions, was found to increase its reactivity in the presence of ethyl 4-iodobenzoate. This altered reactivity shall be investigated mechanistically by gas chromatography. A further subproject will focus on the characterization of Pd^0 and Pd^{II} ate complexes. These palladium species are considered reactive intermediates of a variety of cross-coupling reactions, and there is a high level of interest in studying them in more detail. The combination of electrospray ionization (ESI) mass spectrometry, electrical conductivity measurements, and multi-nuclear NMR spectroscopy should provide detailed insight into the existence of Pd ate complexes. Pd^0 compounds with an electron-poor phosphine ligand (L_F = tris[3,5-bis(trifluoromethyl)-phenyl]phosphine should be investigated in this work. Also, aryl halide compounds should be added to the catalyst mixtures to find out more about the oxidative addition step.

The mechanistic insights gained promise to contribute to the systematic and rational optimization Negishi cross-coupling reactions and to make them practically useful.

2 Experimental Section

This chapter presents the experimental methods used in this thesis. First, the two main analytical tools employed, i.e., gas chromatography, ESI mass spectrometry, are described. Moreover, details of the sample preparation for the gas-chromatographic, conductometric, ESI-mass spectrometric, and NMR-spectroscopic measurements are given. Finally, the synthesis of the used starting materials and chemicals is described.

2.1 Electrospray Ionization Mass Spectrometry (ESI-MS)

2.1.1 Theory

A mass spectrometer consists of the following modules: an ionization source producing gas-phase ions, a mass analyzer employing electric and/or magnetic fields, which discriminate between the different ions based on their mass-to-charge ratio and a detector to measure the abundance of the ions. [108]

Electrospray Ionization

2002 the Nobel Prize for Chemistry was given to the scientist Fenn for the development of the ESI Mass Spectrometry. In the 1980s Whitehouse and coworkers coupled an electrospray source to a quadrupole mass analyzer,[109] but already in the 1960s Dole and coworkers developed electrospray as a technique for mass spectrometry.[110] ESI is a soft ionization technique which allows the formation of ions without almost any fragmentation.[111] Due to this fact, ESI-MS is a technique especially for biochemical compounds, as multiply charged proteins.[112] Later the technique was also used for polymers and different small polar molecules. Recently the application of ESI in detection and characterization of various organometallic complexes has been shown.[27r, 113]

A dilute solution of an analyte is pumped through a capillary. A flux rate of 0.1 - 10 µL/min is used and a high potential is applied (3 - 6 kV) to the capillary. (Scheme 2.1) The potential induces an electric field gradient to produce charge separation at the surface of the liquid. From the capillary tip, known also as “Taylor cone” the liquid protrudes. The charge accumulates at

the surface of the liquid until the solution reaches the Rayleigh limit (this is the point at which Coulombic repulsion of the surface charge is equal to the surface tension of the solution). Depending on the electric field the droplets detach from the capillary tip, containing an excess of positive or negative charge. [111, 114]

These droplets are transferred to the entrance of the mass spectrometer and generate gas-phase ions. A coaxial stream of inert gas limits the dispersion of the charged droplets. Due to the evaporation of the solvent the charge density increases and reaches eventually a value when the Coulombic repulsion on the surface of the droplets become large enough for the release of ions into the gas phase.[114]

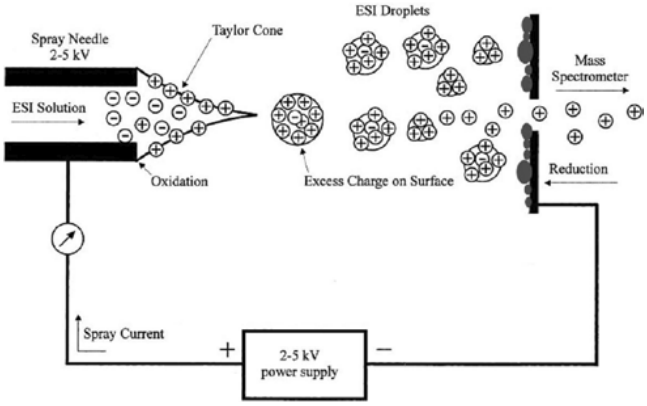

Scheme 2.1 Schematic of the ionization electrospray process (reproduced with permission from Wiley).[111]

Mass Analyzers

The ions generated are separated by mass analyzers according to their mass-to-charge ratio (*m*/*z*) using static or dynamic, magnetic or electric fields. Different mass analyzers like time-of-flight (TOF), quadrupoles analyzers, magnetic sectors and both Fourier transform and quadrupole ion traps are available. Tandem (MS/MS) mass spectrometers can be used for structural and sequencing studies.[108]

2.1.2 Experimental Part

All experiments reported here employed a micrOTO-Q II instrument (Bruker Daltonik), which combines a quadrupole mass filter and a TOF analyzer.[115] Typically, sample solutions were injected into the instrument's ESI source by means of a syringe pump at a flow rate of 8 μL

min^{-1}. The ESI source was operated with a voltage of ±3500 V and N_2 as nebulizer gas (flow rate of 5 L min^{-1}) and drying gas (0.7 bar backing pressure, temperature of 333 K to minimize decomposition of thermo labile species). In simple MS^1 experiments, all generated ions with $50 \leq m/z \leq 2000$ were allowed to pass the quadrupole mass filter and were detected after they had passed the TOF analyzer. Parameters for the ion transfer optics were chosen to ensure reasonably efficient ion transmission for $300 \leq m/z \leq 1500$ [115] while at the same time preventing overly energetic collisions with residual gas in the source region. In MS^2 fragmentation experiments, ions of interest were mass-selected in the quadrupole-mass filter. They were then accelerated to a kinetic energy E_{LAB}, and allowed to collide with N_2 gas. The resulting fragment ions and residual parent ions were then detected after passage through the TOF analyzer. Typically, accuracies of the measured m/z ratios of ±0.02 amu were achieved when the instrument was externally calibrated with a mixture of CF_3COOH and phosphazenes in H_2O/CH_3CN on a daily basis. Presumably, higher accuracies could be attained with a more frequent external or with an internal calibration protocol. For the present purpose, such a procedure involving frequent infusion of aqueous solutions would be impractical, however, because the analysis of intact organometallic species is severely hampered by residual traces of moisture.[27h, 27r, 116] Theoretical exact m/z ratios and isotope patterns were calculated with the DataAnalysis software package (Bruker Daltonik).

2.2 Gas Chromatography

2.2.1 Instrument Overview

Mixtures of compounds that vaporize without decomposition can be separated and analyzed using gas chromatography. For the studies shown here, the gas chromatograph TRACE GC Ultra from Thermo Electron Corporation was applied. The samples were injected using an auto sampler.

To minimize detector drift and for reproducible retention times, the flow of the rate of the carrier gas, nitrogen was carefully controlled.[117] The Merlin Microseal™ High Pressure Valve Septum automatically opens at injection. It acted as a junction through which the injector syringe needle may pass to deliver the sample into the injection port.

After the analyte was injected, it was vaporized in the heated injection port and carried into the column with 0.25 mm diameter, 25 m length and fused silica as stationary phase. The sample was separated into components, depending on the individual interaction with the stationary phase. The column oven permitted a quick heating up and cooling down of the column inside. The sample and the carrier gas passed now through a Flame Ionization Detector (FID). In this detector the compounds were burned in the oxy-hydrogen flame and the resulting ions were detected. Flame Ionization Detector (FID) was characteristic for high sensitivity and robustness. The quantity of the sample was measured by the detector and produced an electrical signal which went to a data system generating a chromatogram.[117]

2.2.2 Experimental Part

For the kinetic measurements, the cross-coupling of butylzinc reagents with ethyl 4-iodo-benzoate catalyzed by $Pd(OAc)_2$/S-Phos was chosen and studied. (Scheme 2.2)

Table 2.1 shows the abbreviations used in this thesis for better understanding. Samples from the reaction mixture were treated with an aqueous solution of NH_4Cl to stop the reaction. The samples were extracted with diethyl ether and analyzed by gas chromatography. Undecane was used as an internal standard (Figure 2.1).

Table 2.1 In this thesis used abbreviations and structure of the aryl compounds.

abbreviation	**structure name**	**chemical structure**
Ar– X	ethyl 4-Xbenzoate	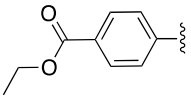
Ar′– X	methyl 4-Xbenzoate	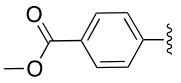
–X = –Br or –I For example ArI means ethyl 4-iodobenzoate		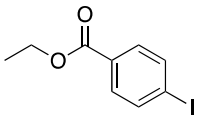

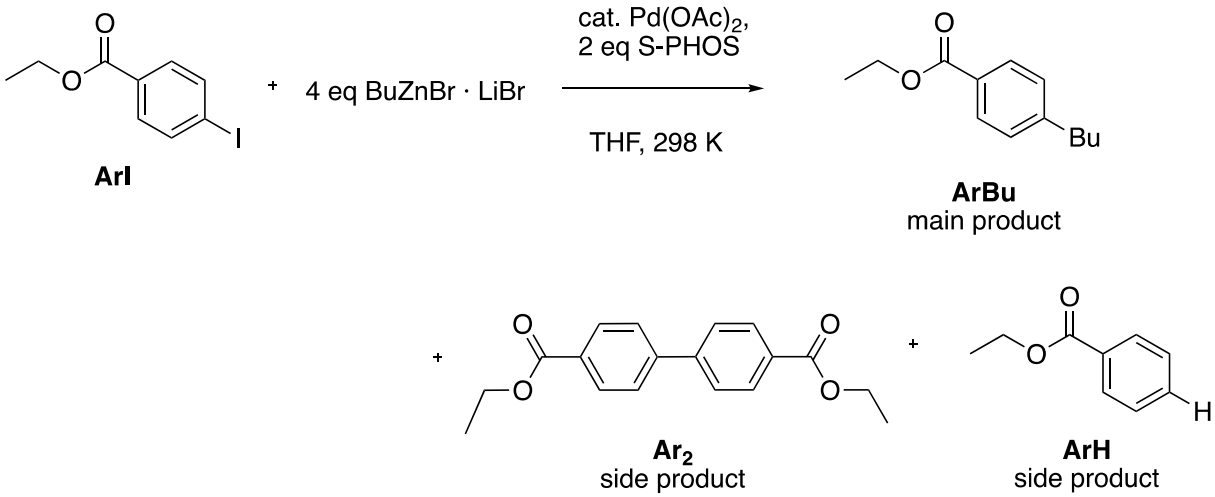

Scheme 2.2 Negishi cross-coupling model reaction.

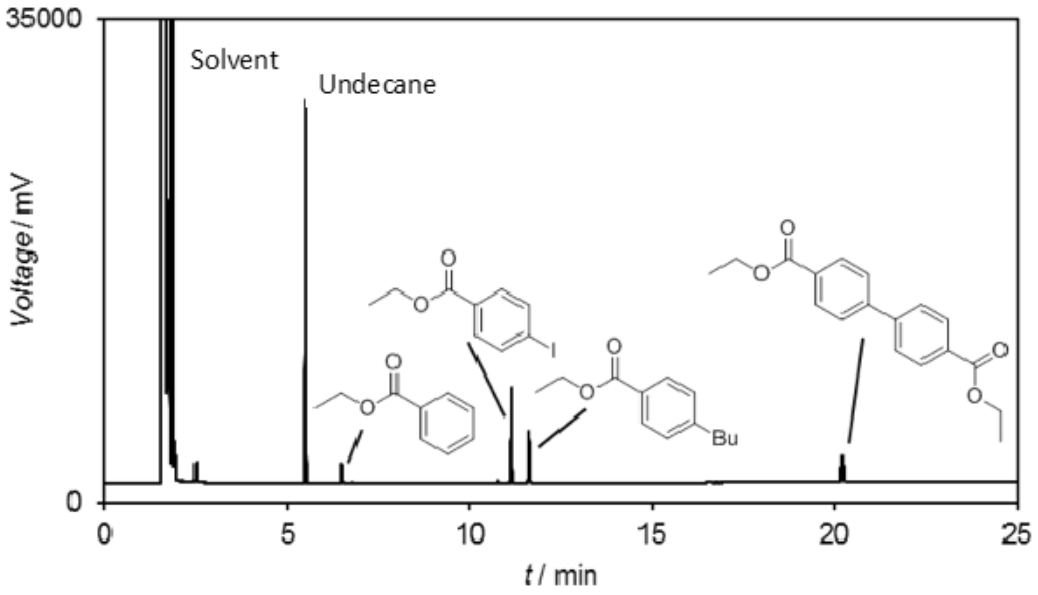

Figure 2.1 Example of a measured chromatogram with the TRACE GC Ultra. It shows the reaction product ArBu, the reactant ArI and the side reaction products Ar_2 and ArH. Undecane is used as internal standard.

To determine the abundances of reactant ethyl 4-iodo-benzoate (ArI), the cross-coupling product ethyl 4-butylbenzoate (ArBu), the homo-coupling product biphenyl-4,4'-dicarboxylic acid diethyl ester (Ar_2) and the dehalogenation product ethyl benzoate (ArH) the integrated measured peak areas were normalized to that of the internal standard and compared to calibration curves for authentic samples of these substances.

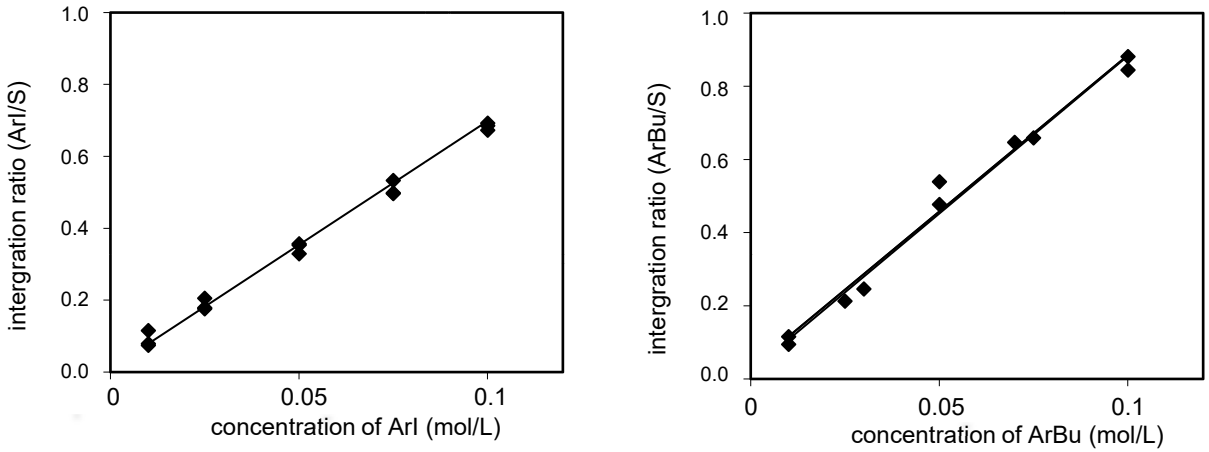

Figure 2.2 Calibration curves of the reactant ethyl 4-iodo-benzoate (ArI, left) and the product ethyl 4-butylbenzoate (ArBu, right) determined by gas chromatograph analysis. The plots show the integration area of the compounds X (X = reagent ArI or ArBu) divided by the integration area of the standard (S) versus the concentration of the respective compound X.

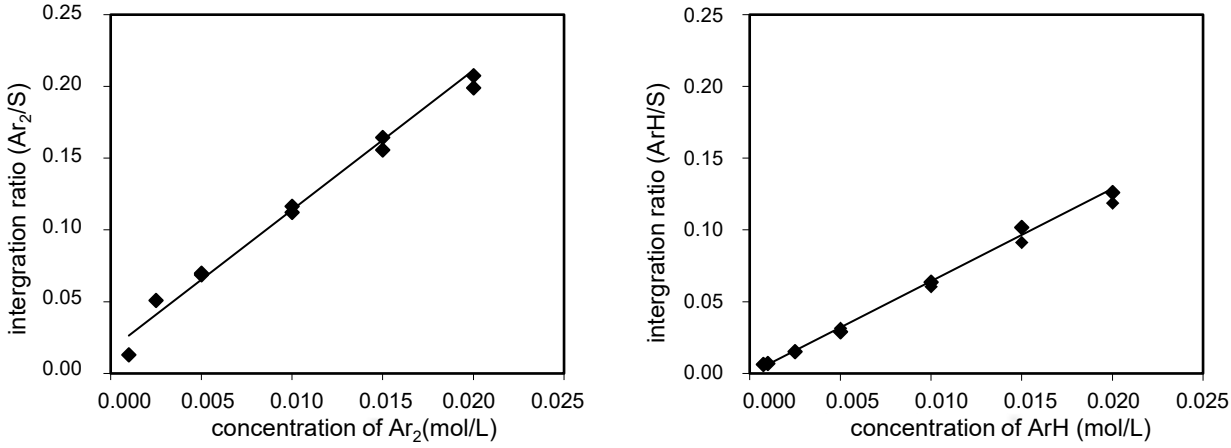

Figure 2.3 Calibration curves of the side products ethyl benzoate (ArH) and biphenyl-4,4'-dicarboxylic acid diethyl ester (Ar_2) determined by gas chromatograph analysis. The plots show the integration area of the compounds X (X = reagent ArH or Ar_2) divided by the integration area of the standard (S) versus the concentration of the respective compound X.

2.3 Synthesis

2.3.1 General considerations

Standard Schlenk techniques were applied in all cases to exclude moisture and oxygen. Gas-tight syringes were used to transfer exact quantities of solutions under the exclusion of moisture and oxygen. LiBr was dried by prolonged heating under vacuum. THF was freshly distilled from sodium benzophenone ketyl under argon.

Solvents

Et_2O (diethylether) was predried over $CaCl_2$ and dried with the solvent purification system SPS-400-2 from INNOVATIVE TECHNOLOGIES INC or was freshly distilled from sodium benzophenone ketyl under argon.

THF (tetrahydrofuran) was freshly distilled from sodium benzophenone ketyl under argon.

THF-d8 (tetrahydrofuran) (euriso-top, 99.50% D) was distilled and stored over molecular sieves (4 Å) under argon at 278 K in the dark.

Analytical data

Infrared Spectroscopy. Infrared spectra were recorded from 4000-400 cm^{-1} on a Perkin 281 IR spectrometer. Samples were measured neat (ATR, Smiths Detection DuraSample IR II Diamond ATR). The absorption bands were reported in wave numbers (cm^{-1}) and labeled as vs = very strong, s = strong, m = medium, and w = weak.

Mass spectrometry. Mass spectra on a Finnigan MAT 95Q or Finnigan MAT 90 instrument for electron ionization (EI), high resolution mass spectra (HRMS) were recorded on FIA/ESI.

Chromatography. Flash column chromatography was performed using SiO_2 60 (0.04 - 0.063 mm, 230 - 400 mesh) from Merck. Thin layer chromatography (TLC) was performed using aluminium plates coated with SiO_2 (Merck 60, F-254). The spots were visualized by UV-light.

Nuclear Magnetic Resonance Spectroscopy. NMR spectra were recorded on Varian Mercury 200, Bruker AC 300, WH 400, or AMX 600 instruments. Chemical shifts are reported as δ values in ppm relative to the solvent signal (in the case of THF-D_8: ^1H δ 1.73 ppm). ^{31}P NMR spectra and ^{19}F NMR were recorded with a Jeol EX 400 Eclipse instrument operating at 161.997

MHz (^{31}P) or 376.548 MHz (^{19}F), respectively. The chemical shifts are given relative to 85% H_3PO_4 or $CFCl_3$, respectively. For the characterization of the observed signal multiplicities the following abbreviations are used: s (singlet), d (doublet), t (triplet), dd (doublet of doublet), dt (doublet of triplet), m (multiplet), q (quartet), quint (quintet), sxt (sextet), as well as br (broad).

Electrical Conductivity Measurements. Electrical conductivity measurements were performed with a SevenMulti Instrument (Mettler Toledo) and a stainless steal electrode (InLab741, Mettler Toledo, Cell constant κ_{Cell} = 0.1 cm^{-1}). The instrument was calibrated against a 0.1 M solution of aqueous KCl.

Reagents

Commercially available reagents were used without further purification unless otherwise stated.

LiX (X = Cl, Br, I) was rigorously dried by prolonged heating under vacuum at 473 K. After cooling to 298 K dry THF (*c* = 0.5 M) was added and the mixture was stirred for 24 h.

ZnX_2 (X = Cl, Br, I) was rigorously dried by prolonged heating under vacuum at 423 K. After cooling to 298 K dry THF (*c* = 0.5 M or 1.0 M) or diethylether (*c* = 0.5 M or 1.0 M) was added and the mixture was stirred for 24 h.

$MgCl_2$ was dried under vacuum at 573 K for several hours, anhydrous THF (*c* = 0.5 M) was added and the mixture was stirred at 323 K for 20 h.

***n*BuLi** was purchased as a solution in hexane from Chemetall Gmbh (Frankfurt, Germany).

PhLi was purchased as a solution in dibutylether from Sigma-Aldrich Chemie Gmbh (Steinheim, Germany).

The concentration of organolithium reagents was determined by titration with dibenzyl tosylhydrazone.[118]

2.3.2 Synthesis

Synthesis of organozinc reagents.[27q]

Particular care was taken to prepare butylzinc reagents of defined composition and free of salts remaining from the synthesis. Bu_2Zn was synthesized from $ZnCl_2$ (1.00 eq) and BuLi (1.00 eq) and purified by distillation. Mixing of Bu_2Zn (1.00 eq) and $ZnBr_2$ (1.00 eq) afforded BuZnBr without LiBr. BuZnBr with LiBr (ratio 1:1) was synthesized from BuLi and $ZnBr_2$ and BnZnBr was synthesized from BnBr (1.00 eq) and Zn (3.00 eq) via zinc insertion. LiBr was added to give BnZnBr with LiBr (ration 1:1). PhZnBr with LiBr (ration 1:1) was synthesized from PhLi (1.00 eq) and $ZnBr_2$ (1.10 eq).

The exact concentration of the active organometallic reagent was determined by iodometric titration (> 90% yield).[14b]

Synthesis of Bu_2Zn.[119]

A flame-dried flask under argon atmosphere was charged with a solution of BuLi in hexane (2.4 M) and the solvent was removed at 273 K under reduced pressure. To the yellow residue was slowly added a solution of $ZnCl_2$ in diethyl ether (1.0 M, 0.5 eq) at 195 K before the reaction mixture was allowed to warm up to room temperature. After stirring for 15 h in the dark, the resulting suspension was subjected to centrifugation (1 h, 2000 rpm). The clear supernatant solution was separated and freed from diethyl ether under reduced pressure. Further purification could be achieved by distillation under high vacuum to give Bu_2Zn as a colorless oil (65% yield).

^{1}H NMR (200 MHz, 296 K, C_6D_6) δ (ppm) 0.35 (t, ^3J(H,H) = 7.7 Hz, 4H, CH_2Zn), 1.08 (t, ^3J(H,H) = 7.2 Hz, 6H, CH_3), 1.45-1.63 (m, 4H, CH_3CH_2), 1.78-1.93 (m, 4H, CH_2CH_2Zn) agreed with those reported in the literature reasonably well.[120] Solutions of Bu_2Zn in THF or THF-d8 (1.3 M, exact determination by iodiometric titration),[121] respectively, were stored under argon in the dark and found stable to degradation for > 2 weeks.

Preparation of ethyl 4-butylbenzoate ArBu

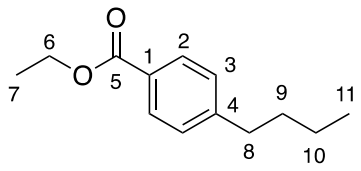

The zinc reagent BuZnBr/LiBr (10.0 mL, 4.9 mmol, 0.49 mM in THF), prepared from BuLi and $ZnBr_2$, was added to a solution of ethyl 4-iodobenzoate (1.16 g, 0.71 mL, 4.2 mmol), $Pd(OAc)_2$ (4.70 mg, 0.021 mmol, 0.50 mol%) and S-PHOS (2-dicycolhexylphosphino-2`,6`-dimethoxybiphenyl, 17.2 mg, 0.042 mmol, 1.0 mol%) in THF (5.50 mL). The reaction mixture was stirred for 12 h at room temperature. A saturated NH_4Cl solution was added and extracted with diethylether (3 × 10 mL). The combined organic layers were washed with an aqueous sodium thiosulfate solution and dried over Na_2SO_4. The solvent was removed under reduced pressure and purification of the crude product by flash chromatography furnished the product as a colorless oil (1.46 g, 3.36 mmol, 80%).

^{1}H NMR (300 MHz, $CDCl_3$) δ (ppm) = 7.95 (d, ^3J(H,H) = 8.2 Hz $C_{Ar}H$, 2 H), 7.23 (d, ^3J(H,H) = 8.1 Hz $C_{Ar}H$, 2 H), 4.35 (q, ^3J(H,H) = 7.1 Hz CH_3CH_2CO, 2 H), 2.66 (t, ^3J(H,H) = 7.7 Hz $C_3H_7CH_2C_{Ar}$, 2 H) 1.66–1.56 (m, $C_2H_5CH_2CH_2C_{Ar}$), 1.36–1.26 (m, CH_3CH_2O, $CH_3CH_2C_2H_4C_{Ar}$, 5 H), 0.93 (t, ^3J(H,H) = 7.4 Hz, 3H).

^{13}C NMR (75 MHz, $CDCl_3$) δ (ppm) = 166.9 (C5), 148.5 (C1), 129.7 (C2), 128.5 (C3), 128.2 (C4), 60.9 (C6), 35.9 (C8), 33.5 (C9), 22.5 (C10), 14.5 (C7), 14.1 (C11).

MS (70 eV, EI): *m/z* (%): 206 (39) [M^+], 161 (100) [$C_{11}H_{13}O^+$], 136 (20) [$C_8H8O_2^+$], 91 (35) [$C_7H_7^+$].

HRMS *m/z*: for $C_{13}H_{18}O_2^+$ calc. 206.1301, found 206.1305.

IR(ATR): $\tilde{\nu}$ (cm^{-1}) = 703 (m), 759 (m), 850 (m), 1021 (m), 1103 (vs), 1176 (s), 1270 (vs), 1610 (m), 1714 (s), 2860 (w), 2872 (w), 2930 (m), 2957 (m).

R_f (Dichloromethane): 0.78.

Preparation of biphenyl-4,4'-dicarboxylic acid diethyl ester (Ar2)[13c, 122]

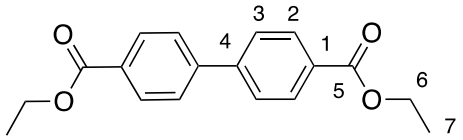

A dry and argon flushed Schlenk flask was charged with palladium acetate $Pd(OAc)_2$ (0.50 mg, 2.0 µmol, 1.0 mol%), S-PHOS (1.70 mg, 4.00 µmol, 2.00 mol%) and 4-(ethoxycarbonyl)phenylzinc iodide (5.0 mL, 2.9 mmol, 0.57 M in THF). After stirring the mixture for 5 min, ethyl 4-iodo-benzoate (614 mg, 0.370 mL, 2.20 mmol) was added dropwise. The reaction mixture was stirred for 2 days under inert gas at room temperature. Then the reaction mixture was quenched with saturated NH_4Cl solution and extracted with ether (4 × 10 mL). The combined organic layers were washed with an aqueous sodium thiosulfate solution and dried over Na_2SO_4. Purification of the crude residue obtained after evaporation of the solvents by flash chromatography (dichloromethane : isohexane 1 : 1, silica) yielded biphenyl-4,4'-dicarboxylic acid diethyl ester (550 mg, 1.85 mmol, 84%) as colorless solid.

^{1}H NMR (300 MHz, $CDCl_3$) δ (ppm) = 8.14 (d, ^3J(H,H) = 8.2 Hz $C_{Ar}H$, 4 H), 7.69 (d, ^3J(H,H) = 8.3 Hz $C_{Ar}H$, 4 H), 4.41 (q, ^3J(H,H) = 7.2 Hz CH_3CH_2CO, 4 H), 1.42 (t, ^3J(H,H) = 7.1 Hz CH_3CH_2CO, 6 H).

^{13}C NMR (75 MHz, $CDCl_3$) δ (ppm) = 166.3 (C5, C5′), 144.3 (C1, C1′), 130.2 (C2, C2′), 130.1 (C4, C4′), 127.2 (C3, C3′), 61.1 (C6, C6′), 14.4 (C7, C7′).

MS (70 eV, EI): *m/z* (%): 298 (56) [M^+], 253 (100) [$C_{18}H_5O_2^+$], 225 (19) [$C_{15}H_{14}O_2^+$], 152 (34) [$C_{12}H_{10}^+$], 151 (10) [$C_7H_3O_4^+$].

HRMS *m/z*: for $C_{18}H_{18}O_2^+$ calc. 298.1200, found 298.1210.

IR(ATR): $\tilde{\nu}$ (cm^{-1}) = 696 (s), 752 (vs), 845 (vs), 1022 (s), 1107 (s), 1265 (vs), 1604 (m), 1702 (s), 2902 (w), 2930 (w), 2960 (w), 2979 (w), 2992 (w).

R_f (Dichloromethane): 0.63.

Preparation of ethyl 4-phenylbenzoate (ArPh)

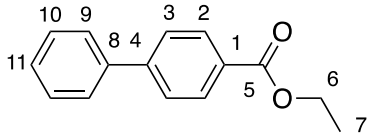

A dry and argon flushed Schlenk flask was charged with palladium acetate $Pd(OAc)_2$ (2.5 mg, 0.010 mmol, 0.80 mol%), S-PHOS (8.5 mg, 0.020 mmol, 1.6 mol%) and phenylzinc bromide (15 mmol, 0.81 M in THF). After stirring the mixture for 5 min, ethyl 4-iodo-benzoate (2.76 mg, 2.20 mL, 13.0 mmol) was added dropwise. The reaction mixture was stirred for 20 h under inert gas at room temperature. Then the reaction mixture was quenched with saturated NH_4Cl solution and extracted with dieethylether (4 × 10 mL). The combined organic layers were washed with an aqueous sodium thiosulfate solution and dried over Na_2SO_4. After evaporation of the solvent, the crude reside was purified by flash chromatography. (isohexane : ethylacetate 30 : 1, silica) yielded biphenyl-4,4'-dicarboxylic acid diethyl ester (0.92 g, 4.1 mmol, 31%) as colorless solid.

^{1}H NMR (300 MHz, $CDCl_3$) δ (ppm) = 8.12 (d, ^3J(H,H) = 8.3 Hz, 2 H), 7.77–7.58 (m, 4 H), 7.49–7.37 (m, 3 H), 4.41 (q, ^3J(H,H) = 7.1 Hz, 2 H), 1.42 (t, ^3J(H,H) = 7.1 Hz, 3 H).

^{13}C NMR (75 MHz, $CDCl_3$) δ (ppm) = 166.9 (C5), 145.9 (C1), 140.4 (C4), 130.4 (C2), 129.6 (C3), 129.3 (C9), 128.4 (C8), 127.6 (C10), 127.3 (C11), 61.3 (C6), 14.7 (C7).

MS (70 eV, EI): *m/z* (%): 226 (59) [$C_{15}H_{14}O_2^+$], 198 (32) [$C_{13}H_9O_2^+$], 181 (100) [$C_{13}H_9O^+$], 152 (54) [$C_{12}H_{10}^+$], 76 (10) [$C_6H_4^+$].

HRMS *m/z*: for $C_{15}H_{15}O_2^+$ calc. 227.1066, found 227.1066.

IR(ATR): $\tilde{\nu}$ (cm^{-1}) = 695 (s), 749 (vs), 865 (w), 1006 (m), 1196 (m), 1276 (s), 1369 (w), 1479 (w), 1606 (m), 1699 (s), 2987 (w).

Preparation of ethyl 4-benzylbenzoate (ArBn)

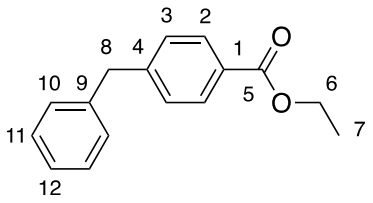

A dry and argon flushed Schlenk flask was charged with palladium acetate $Pd(OAc)_2$ (2.5 mg, 10 µmol, 1.0 mol%), S-PHOS (8.5 mg, 20 µmol, 2.0 mol%) and benzylzinc bromide (11.4 mmol, 0.810 M in THF). After stirring the mixture for 5 min, ethyl 4-iodo-benzoate (2.76 mg, 1.70 mL, 10.0 mmol) was added dropwise. The reaction mixture was stirred for 18 h under inert gas at room temperature. Then the reaction mixture was quenched with saturated NH_4Cl solution and extracted with ether (4 × 10 mL). The combined organic layers were washed with an aqueous sodium thiosulfate solution and dried over Na_2SO_4. After evaporation of the solvents the crude residue was purified by flash chromatography (dichloromethane : ethyl acetate 10 : 1, silica) yielded biphenyl-4,4'-dicarboxylic acid diethyl ester (1.9 g, 7.9 mmol, 80%) as colorless solid.

^{1}H-NMR (300 MHz, $CDCl_3$) δ (ppm) = 8.04 – 7.89 (m, 2 H), 7.35 – 7.13 (m, 7 H), 4.36 (q, J = 7.1, 2 H), 4.03 (s, 2 H), 1.38 (t, J = 7.1, 3 H).

^{13}C-NMR (75 MHz, $CDCl_3$) δ (ppm) = 166.8(C5), 146.7 (C1), 140.5 (C4), 130.1 (C2), 129.2 (C3), 129.2 (C9), 128.9 (C10), 128.8 (C11), 126.6 (C12), 61.1 (C8), 42.2 (C6), 14.6 (C7).

MS (70 eV, EI): *m/z* (%): 240 (20) [M^+], 195 (55) [$C_{14}H_{11}O^+$], 167 (43) [$C_{13}H_{11}^+$], 91 (23) [$C_7H_7^+$].

HRMS *m/z*: calc. for $C_{16}H_{16}O_2^+$ 240.1145, found 240.1152.

IR (ATR): $\tilde{\nu}$ (cm^{-1}) = 695 (s), 749 (vs), 865 (w), 1006 (m), 1196 (m), 1276 (s), 1369 (w), 1479 (w), 1606 (m), 1699 (s), 2987 (w).

2.3.3 Typical procedure kinetic measurements

A flame-dried flask under argon atmosphere was charged with ethyl 4-iodo benzoate (0.15 mmol, 1.0 eq), the butylzinc reagent (0.60 mmol, 4.0 eq), *n*-undecane (0.15 mmol, 1.0 eq) as internal standard and THF as solvent in a volume of 1.5 mL. The resulting solution was stirred and held at 298 K ± 1 K by means of a circulating water/ethanol bath. A solution (0.01 mL) of $Pd(OAc)_2$ (0.005 mol%) and S-PHOS (0.01 mol%) was quickly added at time zero of the kinetic measurement. Samples from the reaction mixture were taken at defined times and immediately treated with an aqueous solution of NH_4Cl. After extraction with diethyl ether and filtration through glass wool, the resulting organic layers were analyzed by gas chromatography (Thermo Electron Corporation, Trace GC Ultra). The abundances of reactant ethyl 4-iodo benzoate (ArI), the cross-coupling product ethyl 4-butyl benzoate (ArBu) were determined by comparing their integrated measured peak areas (normalized to that of the internal standard) to calibration curves for authentic samples of these substances.

3 Kinetic analysis of Negishi cross-coupling reactions[b]

3.1 Introduction

Pd-catalyzed Negishi cross-coupling reactions are difficult to study because of their enormous complexity. The complexity is mainly caused by the presence of several components and the possibility of mutual interactions. This hinders the understanding of their mechanism and their rational optimization. A further complicating factor is that the rate-limiting step and, correspondingly, the rate-determining states[88] are not known. The rate-limiting step can be either oxidative addition, transmetalation or reductive elimination, depending on the combination of reactants, the catalyst used and the reaction conditions. For these reasons, a detailed study of the individual effects of Pd-catalyzed Negishi cross-coupling reactions is necessary.

3.2 Results and Discussion

3.2.1 Model reaction

As model system, the reaction of ethyl 4-iodo-benzoate (ArI) with BuZnBr·LiBr in tetrahydrofuran at room temperature was considered (Scheme 3.1). To start the reaction, a 1:2 mixture of the precatalyst $Pd(OAc)_2$ and the sterically demanding phosphine S-PHOS[13c, 14, 64, 105] as ligand was added. Half of the S-PHOS is supposedly consumed in the reduction of the Pd(II) precatalyst to generate the active Pd(0) species,[44] which then is coordinated by the remaining ligand. Very similar conditions are successfully used in synthetic applications.[27l, 106] The concentration of the organozinc reagent used in excess (4 eq. relative to ArI) could not change by more than 25% during the reaction (in the absence of decomposition reactions). This enables conditions of approximately pseudo-first order conditions to be maintained which facilitates the kinetic analysis. The progress of the reactions was monitored by taking aliquots and analyzing them by gas chromatography (see Experimental Section for details). This method

[b] Some of the schemes and text passages of this chapter have partially been published already in Lit [126].

is rather labor-intensive and does not achieve a high temporal resolution. Nevertheless, its advantage is not to require any label or spectroscopic probe. Thanks to this versatility, gas-chromatographic analysis is widely used for kinetic measurements.[107]

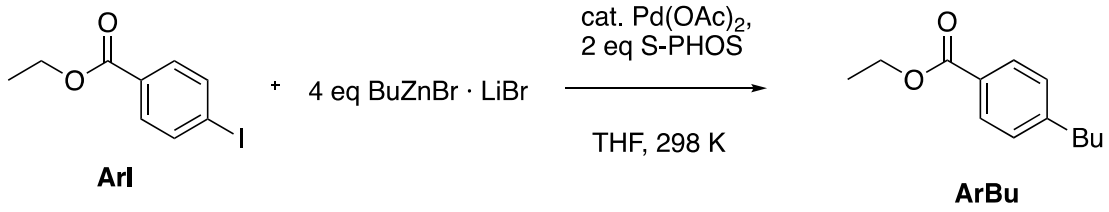

Scheme 3.1 Model reaction investigated.

The catalyst is necessary for the Negishi cross-coupling reaction and without it no reaction takes place. With a catalyst loading of only 0.005 mol%, the reactant ArI is completely consumed in < 2 h. The expected cross-coupling product ArBu is formed with approx. 90% yield (Figure 3.1).

Interestingly, the concentration profiles both of ArI and ArBu showed clearly bimodal features: the reaction proceeds relatively quickly in the initial phase of approx. 60 s, before it slows down significantly. Such a behavior was not just limited to the very experiment shown but was observed consistently. As control experiments did not find any evidence of inefficient mixing being the origin of this behavior, it appears to reflect the genuine kinetics of the model reaction. Obviously, this bimodal nature constitutes a major complication for a quantitative analysis and the extraction of meaningful rate constants.

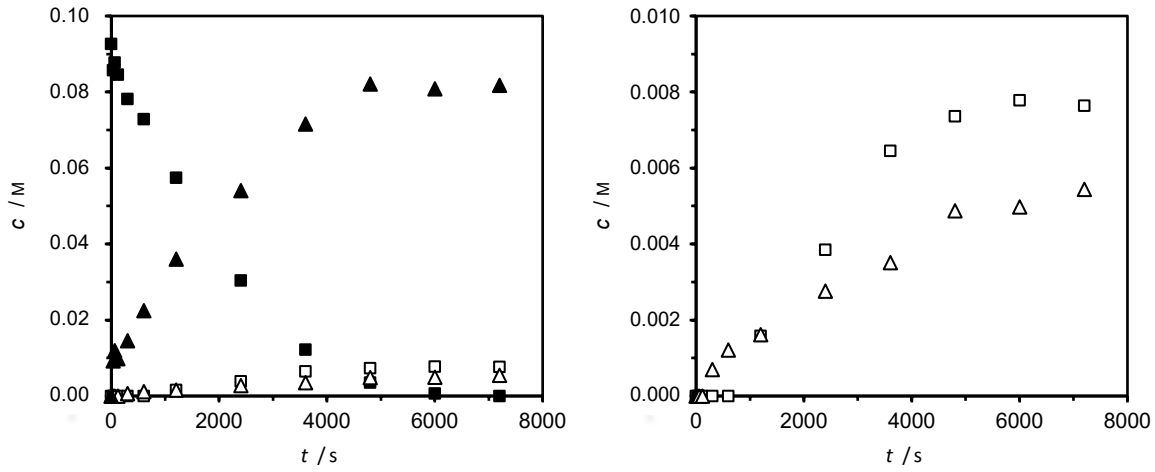

Figure 3.1 Left: Time profiles of the concentrations of reactant ArI (■, c_0 = 0.10 M) and of the products ArBu (cross-coupling product, ▲), ArH (dehalogenation product, △), and Ar_2 (homo-coupling product, □) formed in the reaction with BuZnBr · LiBr (0.40 M) in THF at 298 K (precatalyst: $Pd(OAc)_2$/2 S-PHOS, $5 \cdot 10^{-6}$ M, the concentration refers to Pd, the concentration of S-Phos is twice as high). Right: Time profiles of the concentrations of the byproducts ArH and Ar_2 formed in the same reaction at enlarged scale.

As expected, lowering the temperature resulted in a significant deceleration (Figure 3.2); otherwise, the reaction proceeds in a very similar manner. While most of the further experiments were performed at 298 K, some of them were carried out at 273 K.

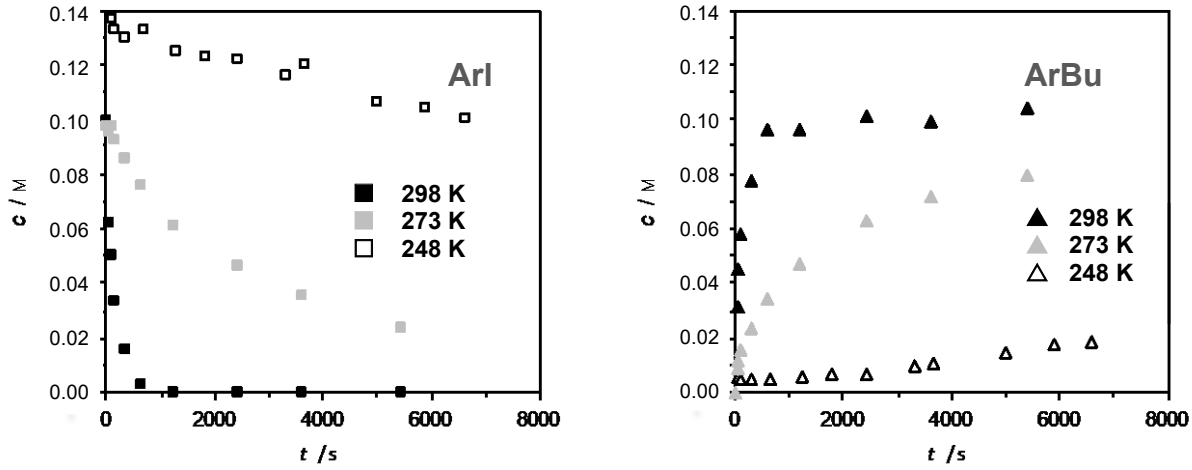

Figure 3.2 Time profiles of the concentrations of reactant ArI (squares) and of the cross-coupling product ArBu (triangle) formed in the reaction with BuZnBr·LiBr (0.40 M) in THF at different temperatures (precatalyst: $Pd(OAc)_2$/2 S-PHOS, $5 \cdot 10^{-5}$ M).

Besides the desired cross-coupling product ArBu, the reaction also affords dehalogenation and homo-coupling products, i.e., ArH and Ar_2, though to only minor extents (approx. 10% in total). Analogous byproducts are well-known from the literature.[27k, 34a-d] The ArZnBr species, which is an intermediate of the formation of ArH and Ar_2, may result from an aryl/alkyl exchange between the conventional transmetalated LPd(Ar)Bu intermediate and BuZnBr (L = S-PHOS, Scheme 3.2, path A with R = Bu). This step is similar to an aryl/aryl exchange reaction suggested by Lei and coworkers.[27k] After this step, the concomitantly generated $LPdBu_2$ undergoes reductive elimination or β-H elimination, but the high volatility of the expected products prohibits their detection in the present experiments (see below, however, for the observation of R_2 products originating from other RZnBr reagents). Alternatively, ArZnBr could result from an aryl/alkyl exchange between LPd(Ar)I and BuZnBr (Scheme 3.2, path B with R = Bu and X = I); analogous reactions haven been postulated by van Asset and Elsevier.[34d] ArZnX can transmetalate LPd(Ar)I to yield $LPd(Ar)_2$, which then releases the homo-coupling product Ar_2 in a reductive elimination and regenerates the catalyst. The measured concentration profiles support the inferred consecutive formation of Ar_2 in that the homo-coupling product starts to build up only after some dehalogenation product has formed. In the following, the focus will be on the cross-coupling reaction channel and not consider the Ar_2 and ArH byproducts unless their combined fraction amounts to significantly more than 10%.

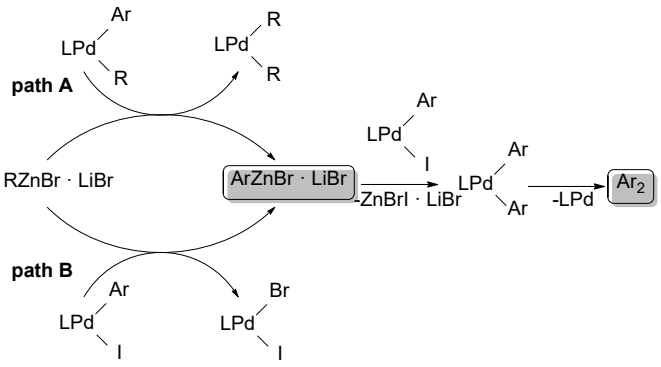

Scheme 3.2 Proposed genesis of the byproducts ArZnBr and Ar_2 (L = S-PHOS).

3.2.2 Effect of LiBr and $ZnBr_2$ additives

The cross-coupling starts at a high rate, but in the absence of LiBr it stops after approx. 120 s. This is shown in Figure 3.3 (right) for the formation of ArBu and in Figure 3.3 (left) for the consumption of ArI. Thus, only a poor conversion (< 20%) is reached. In contrast, addition of 1 or 2 eq. of LiBr (relative to BuZnBr) leads to the complete consumption of reactant ArI and the formation of ArBu in high yields. The concentration profiles measured upon addition of 1 and 2 eq. of LiBr are almost indistinguishable and show similar reaction rates.

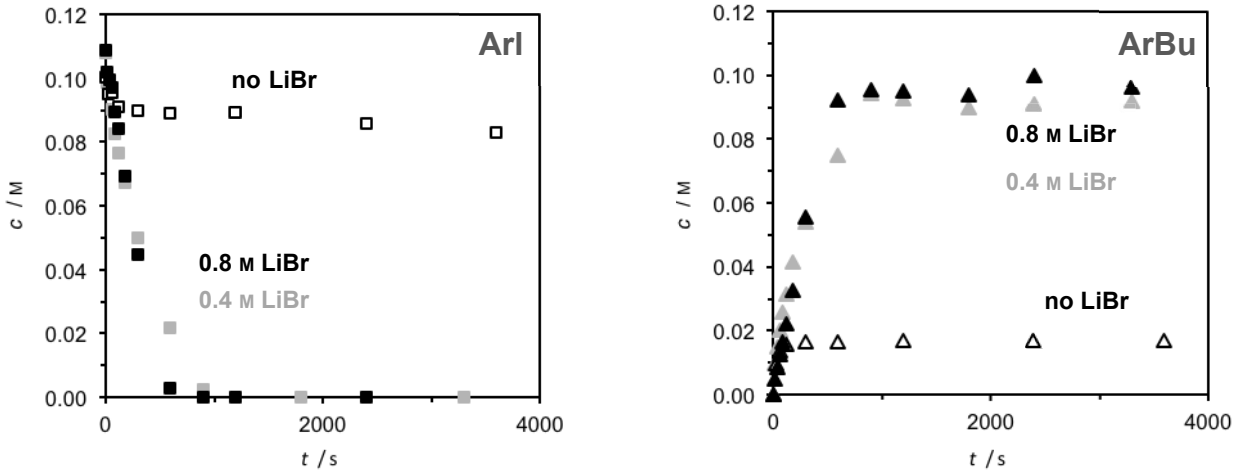

Figure 3.3 Time profiles of the concentration of the cross-coupling product ArBu formed upon reaction of ArI (0.10 M) with BuZnBr (0.40 M) in THF at 298 K (precatalyst: $Pd(OAc)_2$/2 S-PHOS) in the absence (empty triangles, $5 \cdot 10^{-5}$ M precatalyst) or presence of LiBr (black and grey triangles, $2 \cdot 10^{-5}$ M precatalyst).

This finding markedly contrasts the results Organ and coworkers reported for Pd-catalyzed alkyl-alkyl Negishi cross-coupling reaction in a mixture of THF and the polar solvent 1,3-dimethyl-2-imidazolidinone with an *N*-heterocyclic carbene as ligand; in this case, the reaction is inefficient if only 1 eq. of LiBr was added.[27p, 65] The authors rationalized this behavior by the necessity to form so-called higher-order organ zincates $BuZnBr_3^{2-}$ for an efficient transmetalation and overall reaction.[27p, 65] Apparently, such higher-order organozincates do not play a significant role in the present experiments. In line with this assessment, our previous studies did not detect significant amounts of higher-order zincates $RZnX_3^{2-}$ for solutions of RZnX·2 LiX in THF.[27h, 27i, 27q, 27r, 55]

Experiments performed at lower temperatures also found a rate-enhancing effect of LiBr (Figure 3.4).

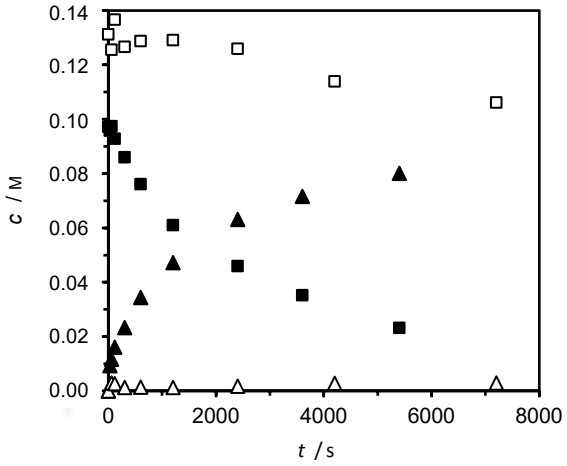

Figure 3.4 Time profiles of the concentrations of reactant ArI (squares) and of the cross-coupling product ArBu (triangles) formed in the reaction with BuZnBr (0.40 M) in THF at 273 K (precatalyst: $Pd(OAc)_2$/2 S-PHOS, $5 \cdot 10^{-5}$ M) in the absence (empty symbols) or presence of LiBr (black symbols).

To exclude that the poor conversion observed in the absence of LiBr resulted from the inadvertent decomposition of the reagents or the catalyst, iodometric titration[121] was first used to check the activity of BuZnBr at later reaction times. This control confirmed the presence of the active organozinc reagent in the expected concentration. Next, 1 eq. of LiBr at later reaction times was added and upon the addition, the cross-coupling reaction sets in again and proceeds to high conversions (Figure 3.5). This observation excludes the (complete) irreversible

decomposition of the reagents or the catalyst. Interestingly, the reaction after the addition of LiBr is significantly slower than that with LiBr present from the very beginning, however, and does not exhibit a pronounced bimodal behavior.

The rate-accelerating effect of LiBr is partly counter-acted by $ZnBr_2$ as shown Figure 3.6 left for the consumption of ArI and in Figure 3.6 right for the formation of ArBu. This finding parallels the observations made by Organ and coworkers for the reaction system mentioned above.[27p, 65] Again, the reaction shows a clearly bimodal behavior. It starts with a relatively fast conversion in the initial phase and a significant slow-down thereafter.

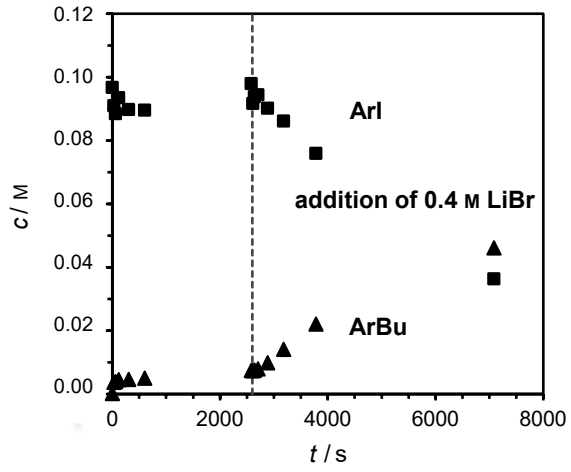

Figure 3.5 Time profiles of the concentrations of reactant ArI (squares) and of the cross-coupling product ArBu (triangles) formed upon reaction with BuZnBr (0.40 M) in THF at 298 K (precatalyst: $Pd(OAc)_2$/2 S-PHOS, $5 \cdot 10^{-5}$ M). The reaction does not proceed to a significant extent before LiBr (0.40 M) is added.

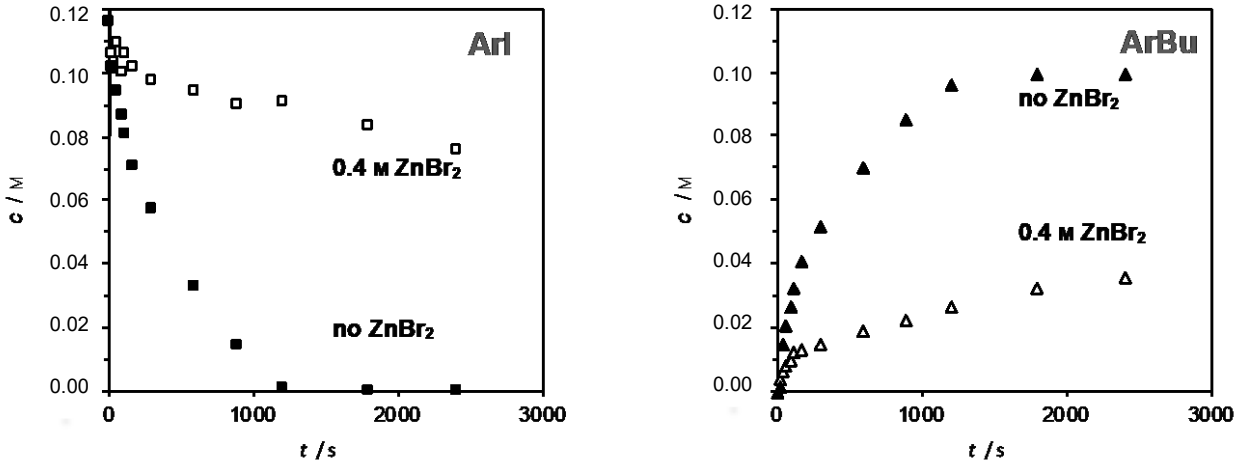

Figure 3.6 Time profile of the concentrations of reactant ArI (left, squares) consumed and the cross-coupling product ArBu (right, triangles) formed in the reaction of ArI (0.10 M) with BuZnBr (0.40 M) in THF at 273 K (precatalyst: $Pd(OAc)_2$/2 S-PHOS, $5 \cdot 10^{-5}$ M) in the absence (black symbols) or presence of $ZnBr_2$ (empty symbols).

3.2.3 Variation of the catalyst

As expected, the rate of the cross-coupling reaction depends on the catalyst loading. The experiments are shown in Figure 3.7. This indicates that the catalyst is involved in the rate-limiting step. To determine the corresponding reaction order, the very first and approximately linear section of each curve, was considered. This simplifies the course of the curve and neglects the bimodal character of the reaction. Plotting the slopes of these sections against the concentration of the precatalyst affords a roughly linear correlation, suggesting a mononuclear Pd complex as catalytically active species (Figure 3.8).

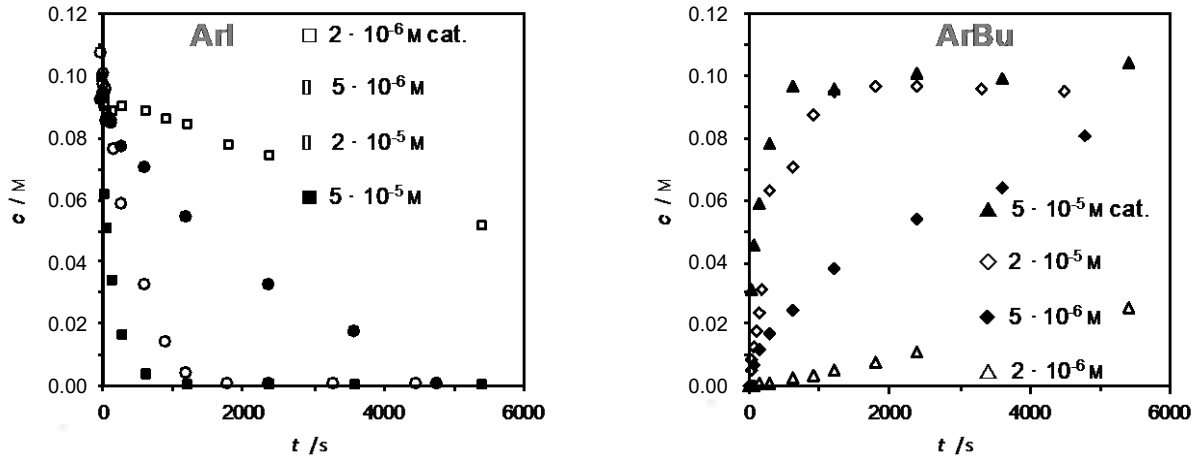

Figure 3.7 Time profile of the concentrations of reactant ArI (left) consumed and the cross-coupling product ArBu (right) formed upon reaction of ArI (0.10 M) with BuZnBr·LiBr (0.40 M) in THF at 298 K in the presence of different amounts of catalyst (precatalyst: $Pd(OAc)_2$/2 S-PHOS, $2 \cdot 10^{-6} - 5 \cdot 10^{-5}$ M).

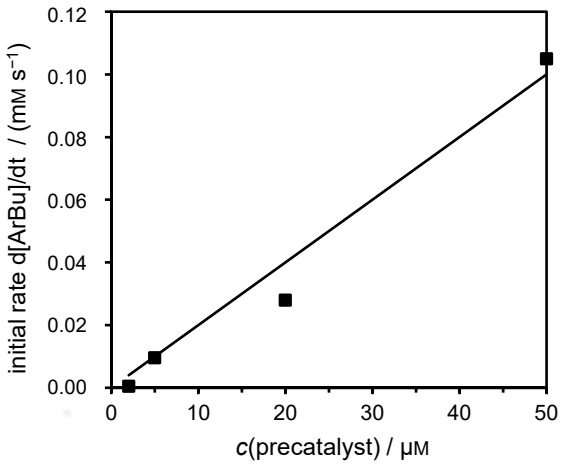

Figure 3.8 Initial rate of the cross-coupling reaction between ArI (0.10 M) and BuZnBr·LiBr (0.40 M) in THF at 298 K as function of the concentration of the precatalyst ($Pd(OAc)_2$/2 S-PHOS) together with a linear fit.

The concentration of the S-PHOS ligand relative to that of $Pd(OAc)_2$ was also varied. Increasing the amount of S-PHOS from 1 to 4 eq. resulted in a rather moderate rate enhancement (Figure 3.9). The slightly slower reaction rate observed in the presence of only 1 eq. of S-PHOS presumably reflects the fact that part of the ligand has been consumed for the reduction of the Pd(II) catalyst precursor (apart from the phosphine, the organozinc reagent can also function as reducing agent). The somewhat faster reaction occurring in the presence of 4 eq. of S-PHOS indicates that this ligand indeed is so large that it does not readily form bis-ligated Pd(0) complexes,[123] which would be reluctant to undergo oxidative addition.

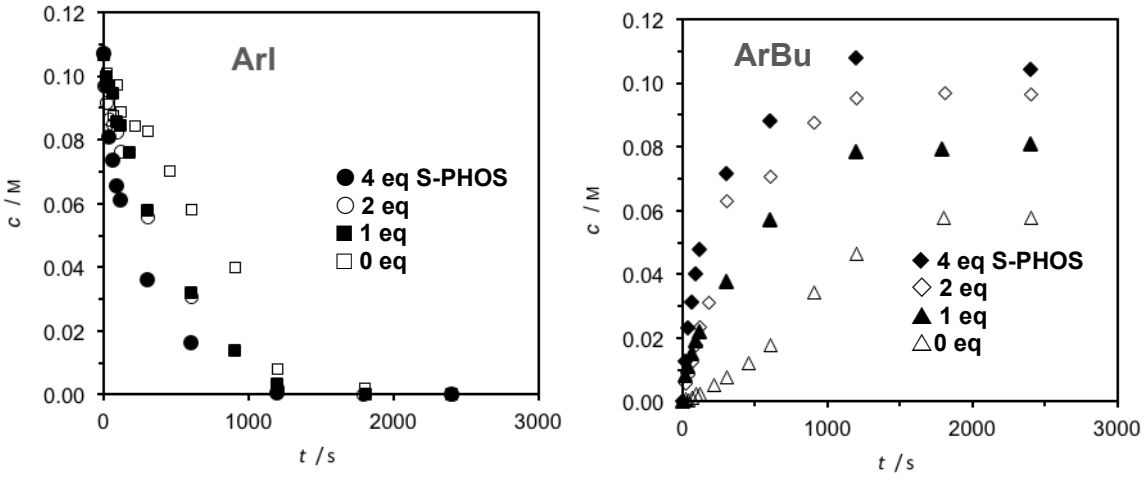

Figure 3.9 Time profile of the concentrations of reactant ArI (left) consumed and the cross-coupling product ArBu (right) formed upon reaction of ArI (0.10 M) with BuZnBr·LiBr (0.40 M) in THF at 298 K in the presence of a fixed amount of $Pd(OAc)_2$ ($2 \cdot 10^{-5}$ M), but variable amounts of S-PHOS (0 – 4 eq relative to $Pd(OAc)_2$).

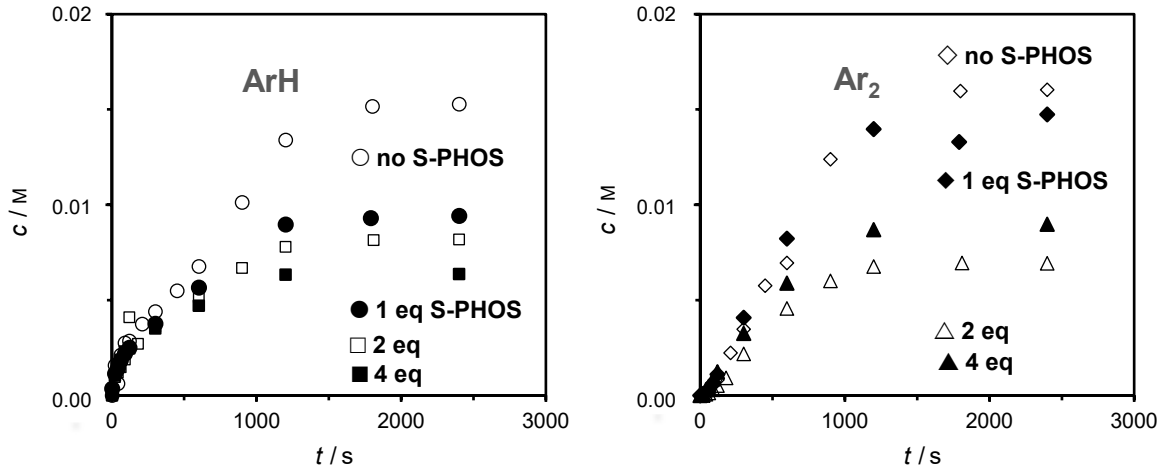

Figure 3.10 Time profiles of the concentration of the byproducts ArH (left) and Ar_2 (right) formed upon reaction of ArI (0.10 M) with BuZnBr·LiBr (0.40 M) in THF at 298 K in the presence of a fixed amount of $Pd(OAc)_2$ ($2 \cdot 10^{-5}$ M), but variable amounts of S-PHOS (0 – 4 eq relative to $Pd(OAc)_2$).

Interestingly, the cross-coupling also proceeded in the absence of S-PHOS (Figure 3.9). This observation echoes recent findings of Lei and coworkers. They investigated the reaction of ArI with *p*-CH_3-C_6H_4-ZnCl in the presence of $Pd(OAc)_2$.[85] At the very low Pd concentrations sampled in that work as well as in the present study, the in-situ formed Pd(0) species apparently does not spontaneously aggregate to metallic Pd. It maintained its catalytic activity for > 0.5 h. At the same time, an increased amount of byproducts was formed in the absence of the phosphine (Figure 3.10); in particular, the dehalogenation reaction was enhanced.

According to the inferred mechanism (Scheme 3.2, path A with R = Bu), the formation of ArZnBr directly competes with the reductive elimination of the cross-coupling product ArBu from LPd(Ar)(Bu). If an analogous mechanism also in the absence of S-PHOS is assumed, the increased formation of ArZnBr indicates a lowered tendency toward reductive elimination. This lowered tendency presumably arises from the decreased steric congestion of the phosphine-free

complex. In turn, the coordinatively highly unsaturated phosphine-free Pd(0) complexes should undergo oxidative addition very efficiently. Lei and coworkers identified the transmetalation as rate-determining step for their model reaction.[85] The question of the rate-determining step for the present catalytic system will be discussed later.

Unlike the concentration profiles measured with added S-PHOS, that of the phosphine-free reaction shows a slope that becomes slightly steeper at medium reaction times ($t \geq 500$ s). Presumably, this behavior reflects the ongoing reduction of the Pd(II) catalyst in the initial phase of the reaction. The experiments with added S-PHOS lack such an induction period because $Pd(OAc)_2$ and S-PHOS were mixed for an incubation time of approx. 5 – 10 min before their addition to the reaction solution at $t = 0$. The effect of this incubation time in additional experiments (with $Pd(OAc)_2$ and 2 eq. of S-PHOS) was investigated. Extending the incubation time from 5 to 60 min resulted in a modest deceleration of the cross-coupling reaction (Figure 3.11). This finding implies that the reduction of the Pd(II) precatalyst occurs fast in the presence of S-PHOS, but that catalyst deactivation reactions set in at longer times.

The performance of $Pd(OAc)_2$/2 S-PHOS was also compared with that of two other popular precatalysts, namely $Pd(PPh_3)_4$ and PEPPSI-IPr,[62] which contains an N-heterocyclic carbene as ligand was also compared.

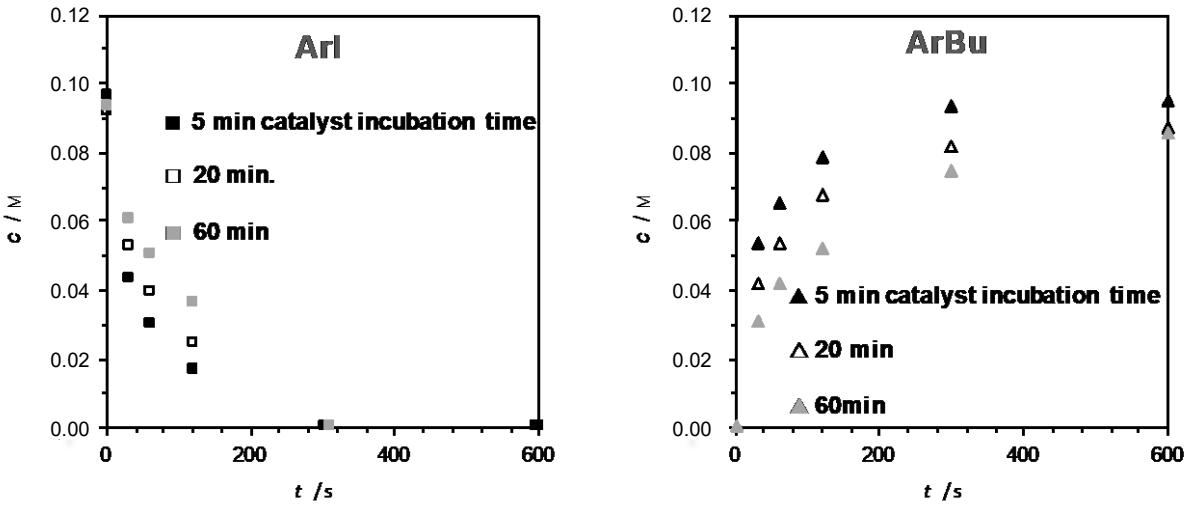

Figure 3.11 Time profiles of the concentration of reactant ArI (left) and the cross-coupling product ArBu (right) upon reaction with BuZnBr·LiBr (0.40 M) in THF at 298 K for different incubation times of the (precatalyst ($Pd(OAc)_2$/2 S-PHOS, $5 \cdot 10^{-5}$ M).

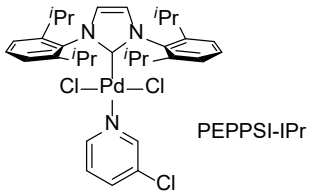

PEPPSI-IPr

Under standard conditions, the reaction in the presence of PEPPSI-IPr is fastest, although the observed rates do not differ very much (Figure 3.12). More importantly, however, the $Pd(PPh_3)_4$-catalyzed reaction falls behind with respect to the yield of the cross-coupling product. This decreased yield does not result from an incomplete consumption of reactant ArI, but rather from the increased formation of the homo-coupling product Ar_2 (Figure 3.12). Given that the amount of the dehalogenation product ArH and, thus, the concentration of the ArZnBr intermediate is not anomalously high for the $Pd(PPh_3)_4$-catalyzed reaction, the relative rates of the transmetalation step presumably make the difference. Apparently, the PPh_3-ligated complex favors transmetalation with ArZnBr·LiBr (Scheme 3.2 with R = Bu) over that with BuZnBr·LiBr more strongly than do the S-PHOS- and the N-heterocyclic carbene-ligated complexes.

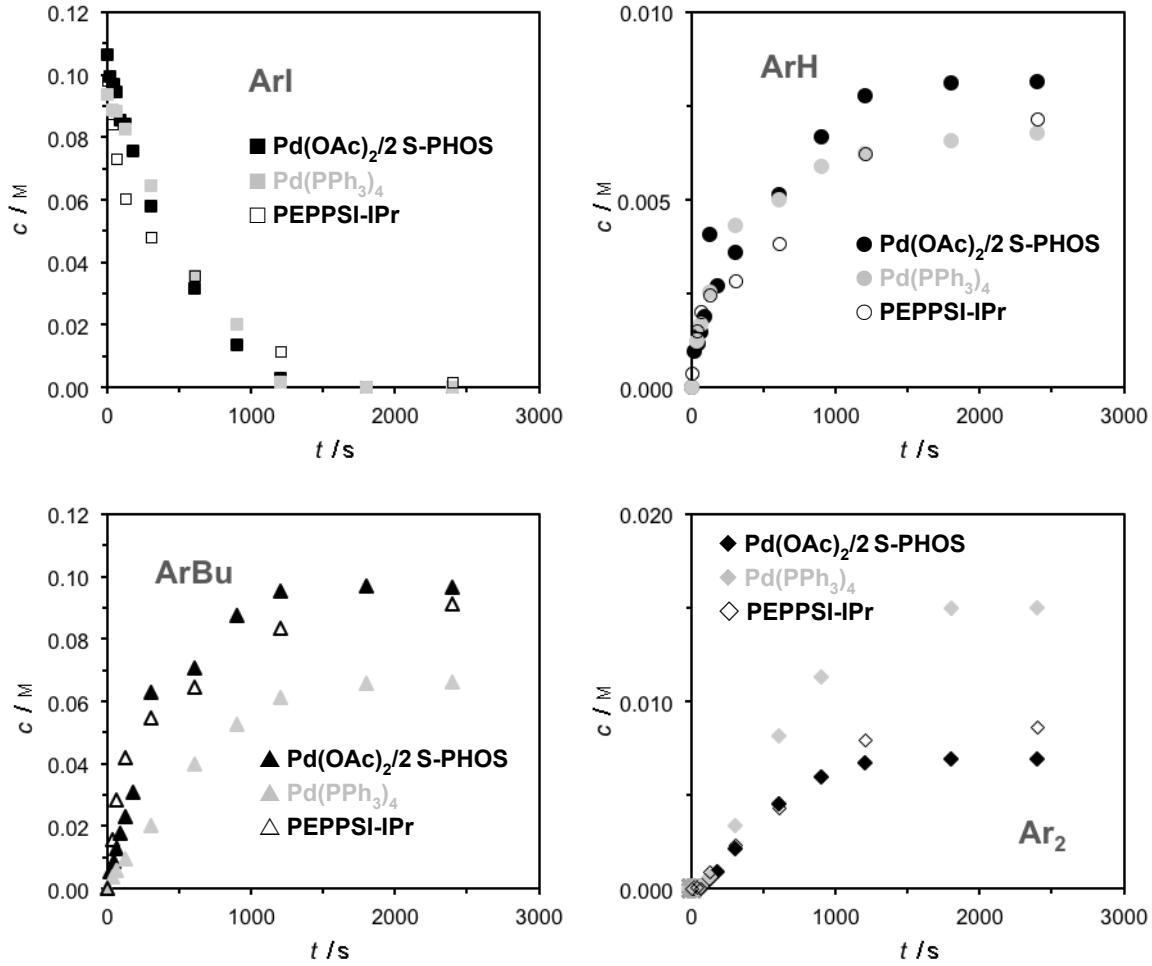

Figure 3.12 Time profiles of the concentration of reactant ArI (top left) and the byproducts ArH (top right) and Ar_2 (bottom right) and of the cross-coupling product ArBu (bottom left) formed upon reaction of ArI (0.10 M) with BuZnBr·LiBr (0.40 M) in THF at 298 K in the presence of different Pd catalysts ($2 \cdot 10^{-5}$ M). Time profiles of the concentration formed upon reaction of ArI (0.10 M) with BuZnBr·LiBr (0.40 M) in THF at 298 K with different catalytic systems ($2 \cdot 10^{-5}$ M)

In the absence of stoichiometric amounts of LiBr, the $Pd(PPh_3)_4$- and PEPPSI-IPr-catalyzed reactions were slowed down (Figure 3.13 and Figure 3.14). This effect was particularly pronounced in the latter case.

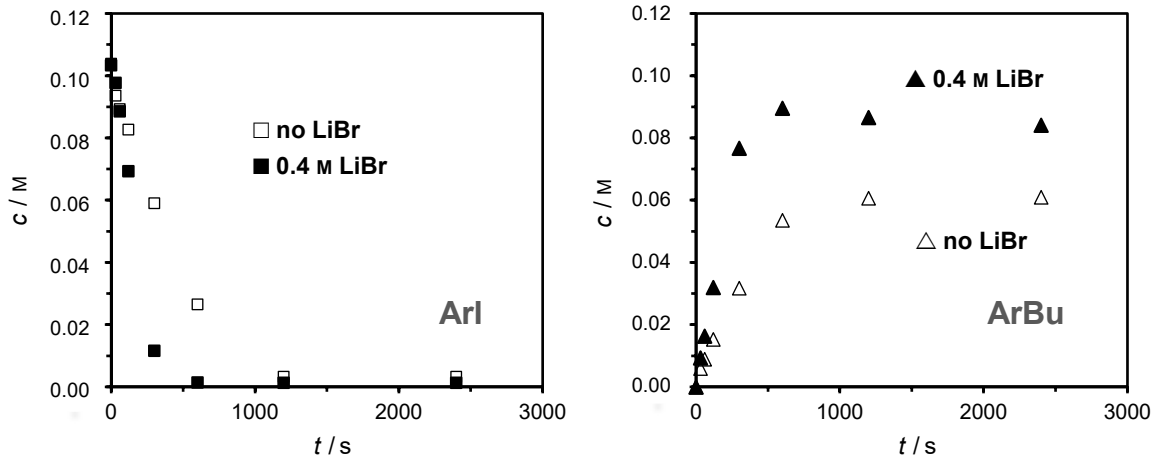

Figure 3.13 Time profiles of the concentrations of reactant ArI (left) and of the cross-coupling product ArBu (right) formed in the reaction with BuZnBr (0.40 M) in THF at 298 K (precatalyst: $Pd(PPh_3)_4$, $1 \cdot 10^{-3}$ M) in the absence (empty symbols) or presence of LiBr (black symbols).

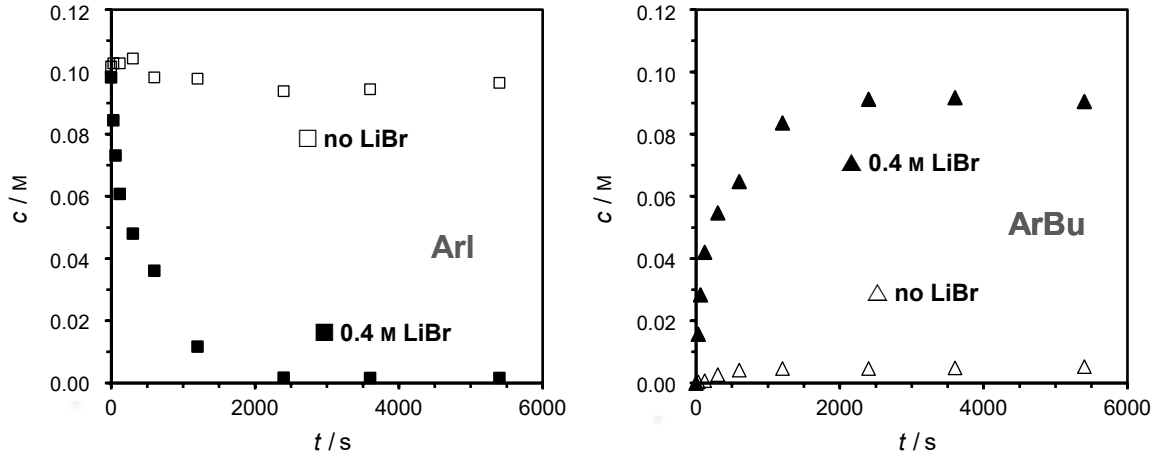

Figure 3.14 Time profiles of the concentrations of reactant ArI (left) and of the cross-coupling product ArBu (right) formed in the reaction with BuZnBr (0.40 M) in THF at 298 K (precatalyst: PEPPSI-IPr, $2 \cdot 10^{-5}$ M) in the absence (empty symbols) or presence of LiBr (black symbols).

3.2.4 Variation of the aryl halide substrate

As the concentration of BuZnBr·LiBr, was present in threefold excess, and of the catalyst were held approximately constant during the course of the experiment, the main change in the reaction conditions was brought about by the decline of reacting ArI substrate (if a possible

effect of newly formed ZnX_2 was neglected, see below). This decline then apparently caused the reaction rate to decrease, as evidenced by the bent shapes of the ArI and ArBu concentration profiles.

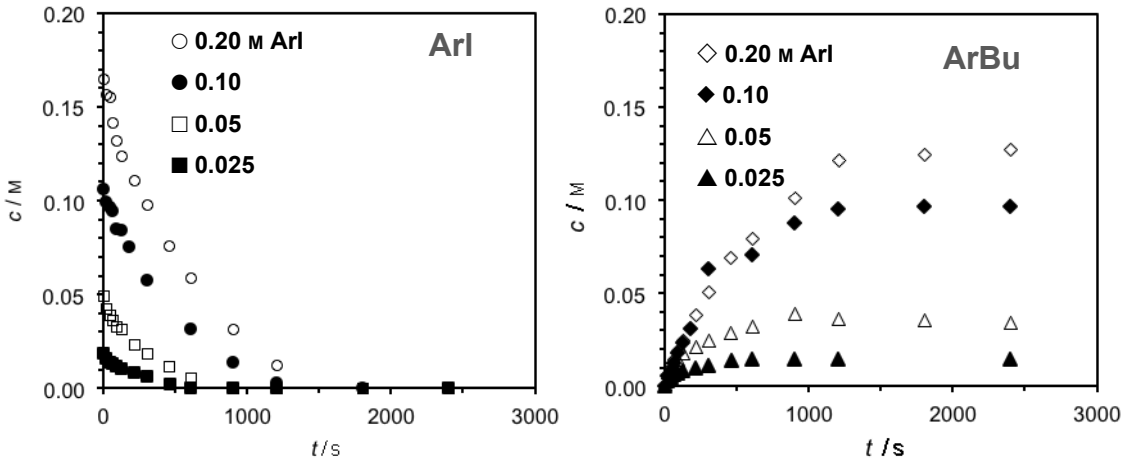

Figure 3.15 Time profiles of the concentration of the reactant ArI (left) and the cross-coupling product ArBu (right) formed upon reaction of ArI (starting concentrations: 0.025 – 0.20 M) with BuZnBr·LiBr (0.40 M) in THF at 298 K (precatalyst: $Pd(OAc)_2$/2 S-PHOS, $2 \cdot 10^{-5}$ M).

To probe this dependence more directly, experiments with different starting concentrations of ArI (Figure 3.15) were also performed. Plotting the initial rates (0 – 5% to 0 – 10% conversion) against c_0(ArI) showed a positive dependence, but no apparent linear correlation (Figure 3.16); in this case, the scattering inherent in the data points at low conversion levels made a rigorous quantitative treatment difficult, however.

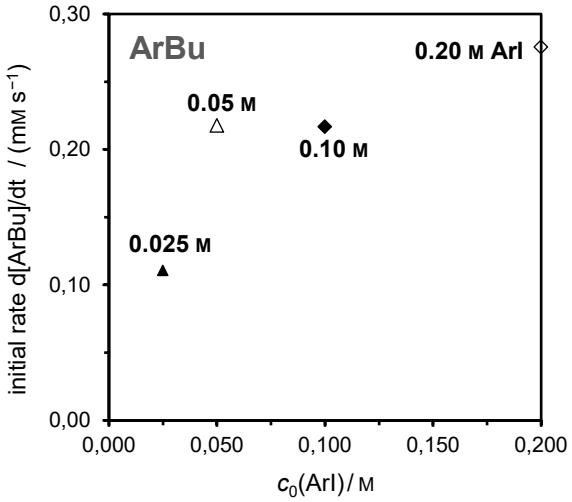

Figure 3.16 Initial rate of the cross-coupling reaction between ArI (starting concentration c_0 = 0.025 – 0.20 M) and BuZnBr·LiBr (0.40 M) in THF at 298 K (precatalyst: $Pd(OAc)_2$/2 S-PHOS, $2 \cdot 10^{-5}$ M).

Next, the substrate ArI was exchanged for ArBr and ArOTs. ArOTs did not react under the chosen reaction conditions (even not with a precatalyst loading of $1 \cdot 10^{-3}$ M) and therefore was not considered any further. ArBr does undergo cross-coupling with BuZnBr·LiBr, but significantly more slowly.

Under the employed conditions the reaction between ArBr and BuZnBr·LiBr was complete within the sampled time window of t = 5400 s. The expected cross-coupling product ethyl 4-butylbenzoate ArBu was obtained in 45% yield. For comparison, the yield of the cross-coupling product in the model reaction using ethyl 4-iodobenzoate as reactant was almost 95%. (Figure 3.1) Thus, the use of the bromo-electrophile is less effective. With a precatalyst concentration $Pd(OAc)_2$/2 S-Phos of $1 \cdot 10^{-3}$ M, ethyl 4-butylbenzoate, but also a high amounts of the homocoupling product Ar_2 and the dehalogenated product ArH were observed.

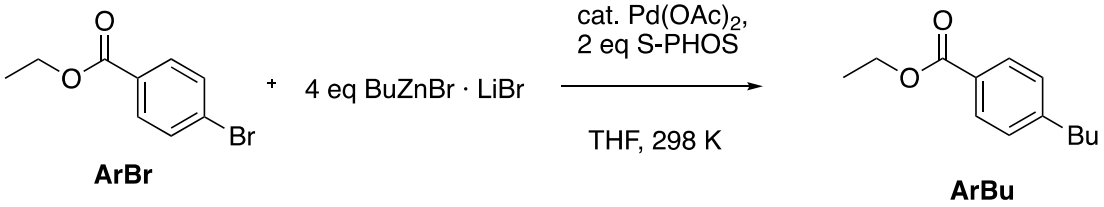

Scheme 3.3 Reaction of ArBr with BuZnBr·LiBr.

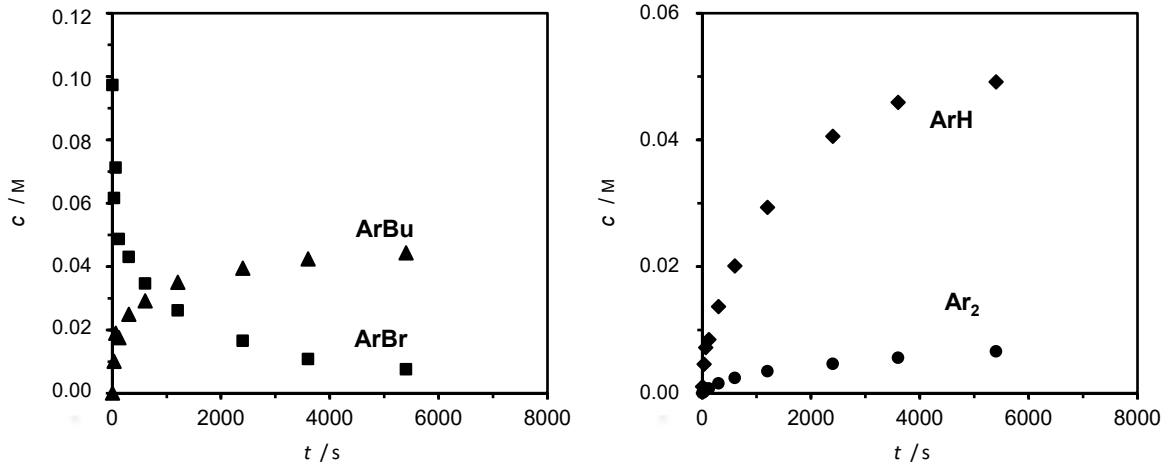

Figure 3.17 Left: Time profiles of the concentrations of reactant ethyl 4-bromobenzoate ArBr and the cross-coupling product ethyl 4-butylbenzoate ArBu, which is formed upon reaction with BuZnBr·LiBr (0.40 M) in THF at 298 K (precatalyst: $Pd(OAc)_2$/2 S-PHOS, $1 \cdot 10^{-3}$ M). Right: Time profiles of the concentrations of dehalogenated product ethylbenzoate ArH (◆) and the homocoupling product Ar_2 (●) (the reaction equation is shown Scheme 3.3 Reaction of ArBr with BuZnBr·LiBr).

Compared to the reaction of ArI with BuZnBr·LiBr (Scheme 3.1), the reaction ArBr with BuZnBr·LiBr led to a deceleration of the reaction (Figure 3.17) and also to a lower yield of the cross-coupling product ArBu. For the present system with ArBr, the homo-coupling and dehalogenation side products were formed in higher yields compared to the model system (Figure 3.1). The dehalogenated product ArH is generated by a side reaction of the sensitive intermediate formed in the oxidative addition. The high formation of ArH of almost 50% reveals that half of the intermediate was not able to transmetalate with the BuZnBr·LiBr. The rate of the side reaction and the final concentration of ArH were much higher when ArBr was used, than in the reaction of ArI with BuZnBr·LiBr. However, the amount of the homocoupling compound with 5% is comparably low.

In order to enable a direct comparison, competition experiments with equal amounts of ArBr and Ar′I were performed (Scheme 3.4 and Figure 3.18). It is assumed here that the effect of exchanging the ethyl for the methyl ester is negligible. Considering only the very first data

points at relatively low levels of conversion, the reaction of Ar′I is found to be ≥ 30 faster than that of ArBr.

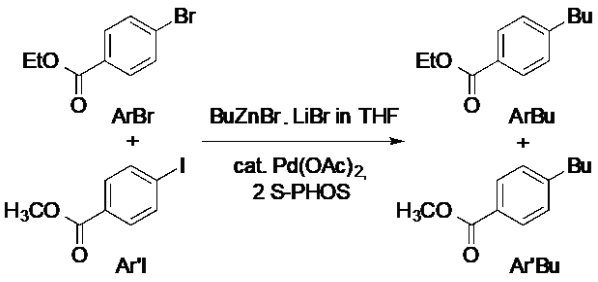

Scheme 3.4 Competition experiment for comparing the reactivity of ArBr and Ar′I.

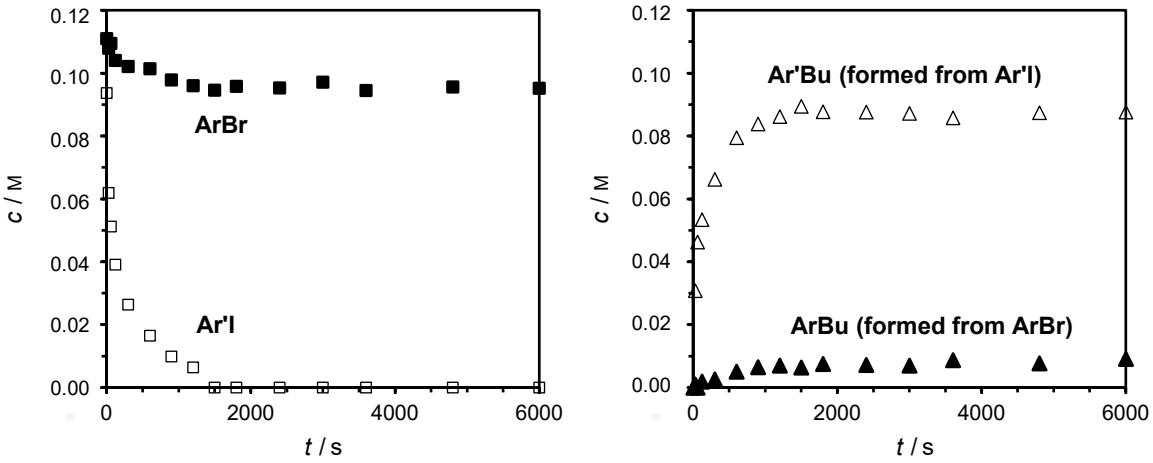

Figure 3.18 Time profiles of the concentration of ethyl 4-bromobenzoate ArBr (black squares, 0.10 M) and methyl 4-iodobenzoate Ar′I (empty squares, 0.10 M) (left) and of the concentration of ethyl 4-butylbenzoate ArBu (black triangles) and methyl 4-butylbenzoate Ar′Bu (empty triangles) (right) formed upon reaction of a 1:1 mixture of ArBr and Ar′I (0.10 M of each component) with BuZnBr·LiBr (0.40 M) in THF at 298 K (precatalyst: $Pd(OAc)_2$/2 S-PHOS, $5 \cdot 10^{-5}$ M).

Moreover, the effect of LiBr addition on the reaction of ArBr was studied. PEPPSI-IPr is a very effective precatalyst and is used in this reaction. Like in the case of ArI, LiBr greatly accelerates the cross-coupling reaction, which again shows a bimodal behavior with a faster initial

conversion (Figure 3.19). However, LiBr has an even stronger effect on the dehalogenation channel, which now becomes the main product (Figure 3.19).

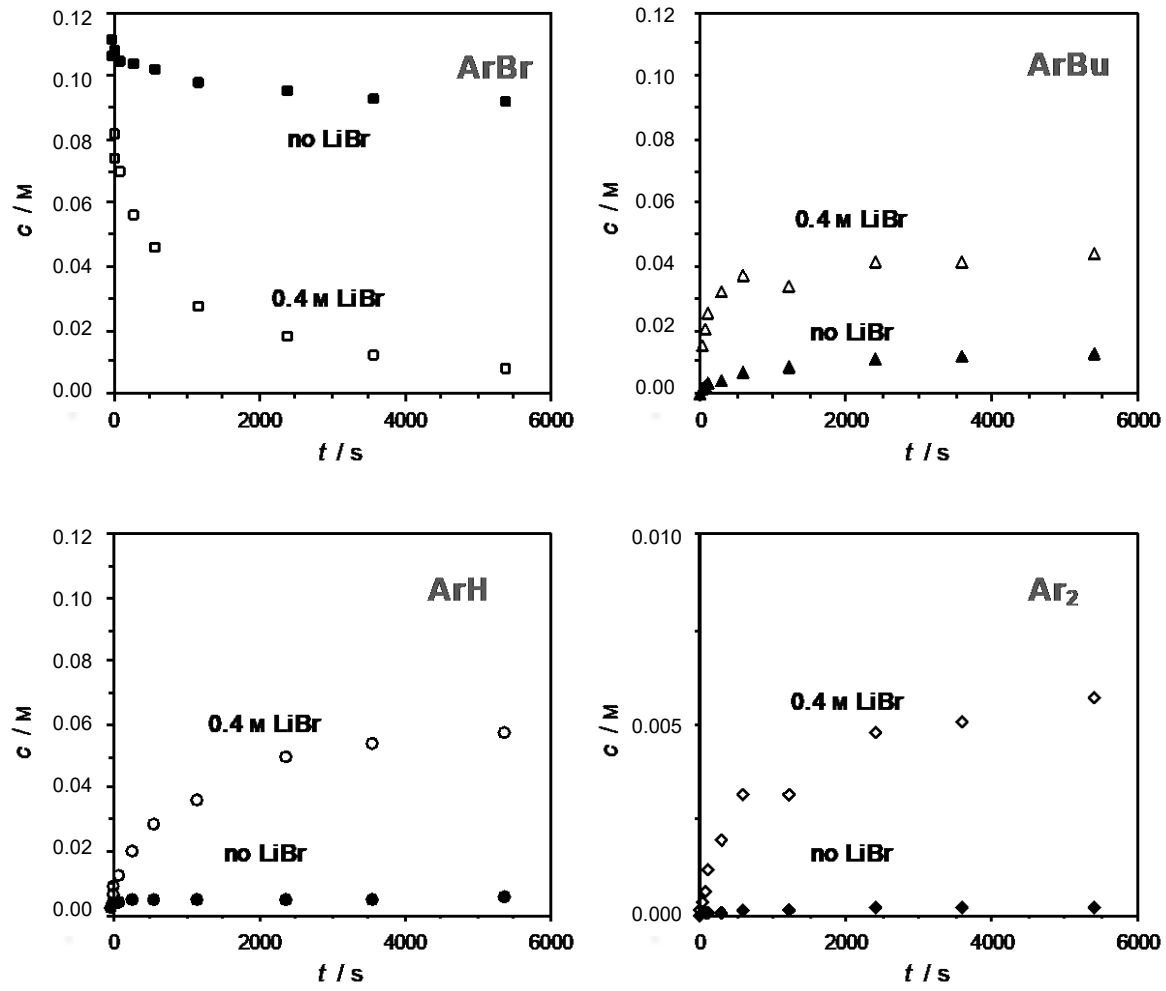

Figure 3.19 Time profiles of the concentrations of reactant ArBr (top left), of the cross-coupling product ArBu (top right), the dehalogenation byproduct ArH (bottom left), and the homo-coupling product Ar_2 (bottom right) formed in the reaction with BuZnBr (0.40 M) in THF at 298 K (precatalyst: PEPPSI-IPr, $1 \cdot 10^{-3}$ M) in the absence (black symbols) or presence of LiBr (empty symbols).

From the two mechanisms considered for the formation of ArZnBr (Scheme 3.2 with R = Bu and X = I) only path B involves the halide stemming from reactant ArX. It therefore seems likely that this mechanism operates at least partially in the reactions with ArBr as substrate.

3.2.5 Variation of the organozinc reagent

Experiments with different concentrations of BuZnBr · LiBr showed that it has no significant influence on the cross-coupling reaction (Figure 3.20). Considering the initial slopes (0 – 12% conversion) confirmed that the reaction was insensitive to the concentration of the organozinc reagent; if any, a small negative dependence was discerned (Figure 3.21).

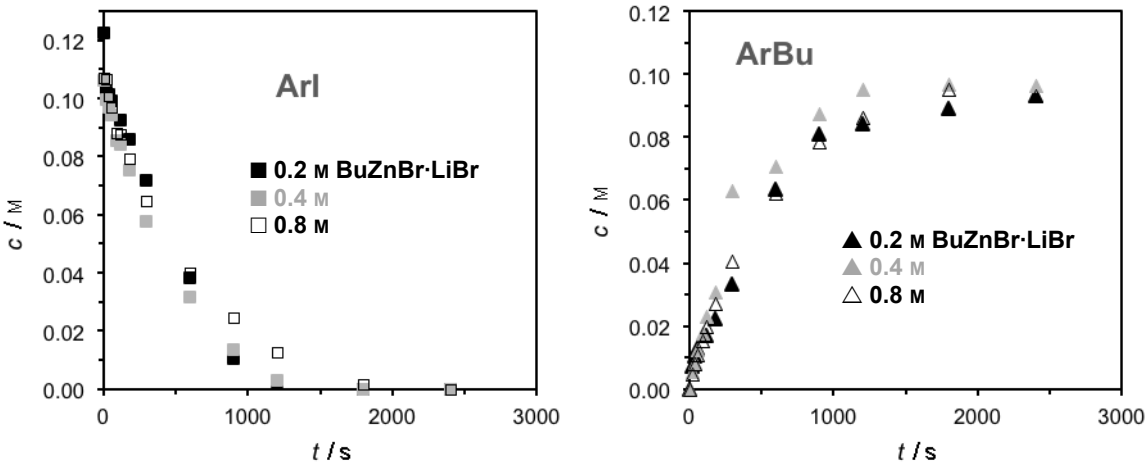

Figure 3.20 Time profiles of the concentration of reactant ArI (left) and of the cross-coupling product ArBu (right) formed in the reaction of ArI with BuZnBr·LiBr (0.20 – 0.80 M) in THF at 298 K (precatalyst: $Pd(OAc)_2$/2 S-PHOS, $2 \cdot 10^{-5}$ M).

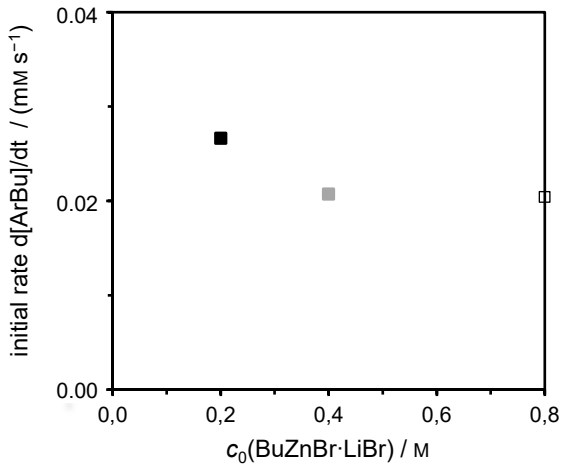

Figure 3.21 Initial rate of the cross-coupling reaction between ArI (starting concentration c_0 = 0.10 M) and BuZnBr·LiBr (c_0 = 0.20 – 0.80 M) in THF at 298 K (precatalyst: $Pd(OAc)_2$/2 S-PHOS, $2 \cdot 10^{-5}$ M).

In addition to BuZnBr·LiBr, the analogous PhZnBr·LiBr and BnZnBr·LiBr reagents and their reactivity were also probed. Both of them undergo cross-coupling with ArI and furnish ArPh and ArBn, respectively, in high yields (Figure 3.22 and Figure 3.23).

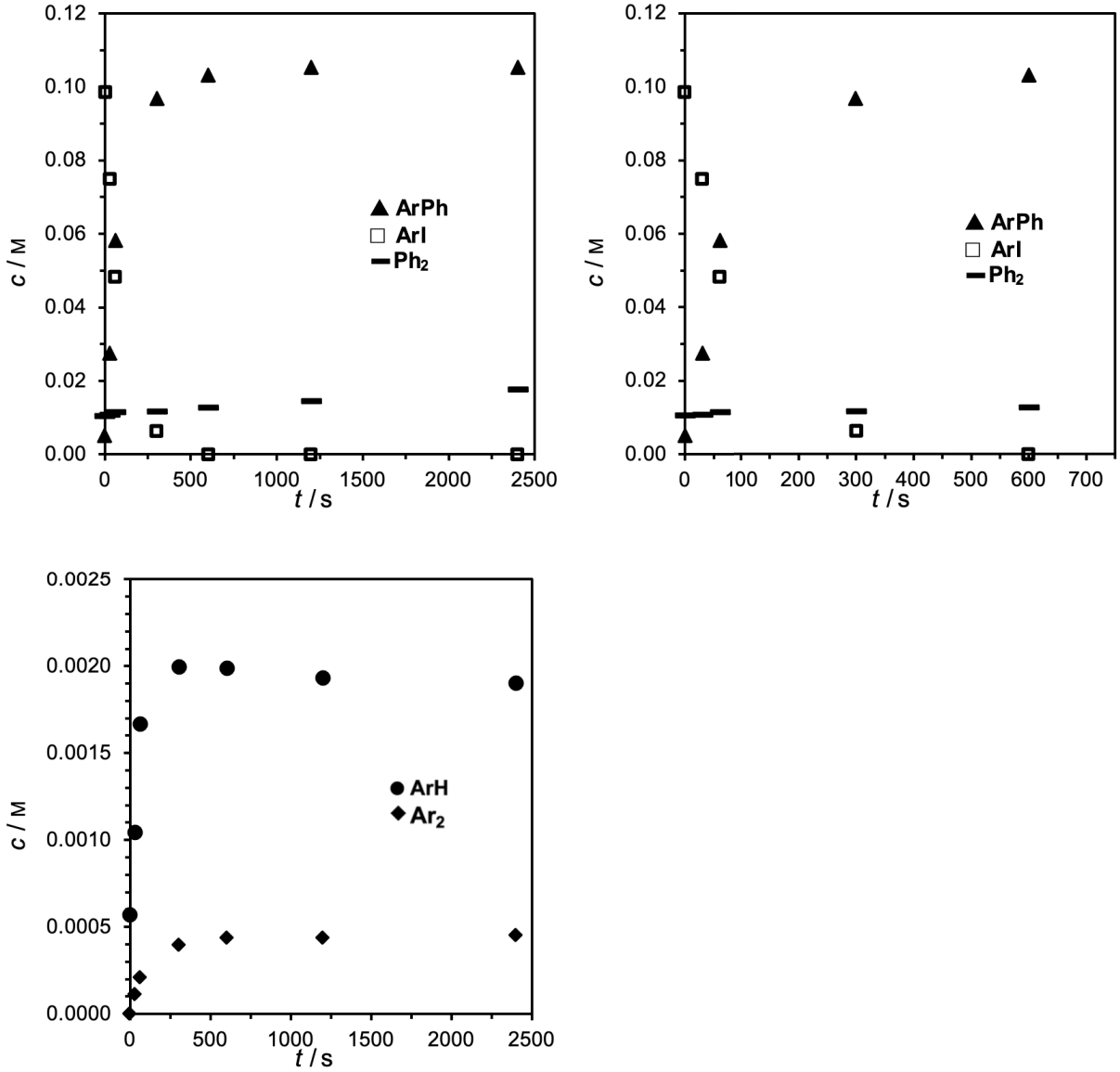

Figure 3.22 Left top: Time profiles of the concentrations of reactant ArI (squares, c_0 = 0.10 M) and of the products ArPh (cross-coupling product, triangles), Ph_2 (homo-coupling product derived from the organozinc reagent, rectangles), formed in the reaction with PhZnBr·LiBr (0.40 M) in THF at 298 K (precatalyst: $Pd(OAc)_2$/2 S-PHOS, $1 \cdot 10^{-5}$ M). Right: Enlargement of Figure 3.22 Left top in the range up to 750 s. Bottom: Time profiles of the concentrations of the byproducts ArH (dehalogenation product, circles) and Ar_2 (homo-coupling product derived from the aryl halide substrate, diamonds) formed in the same reaction at enlarged scale.

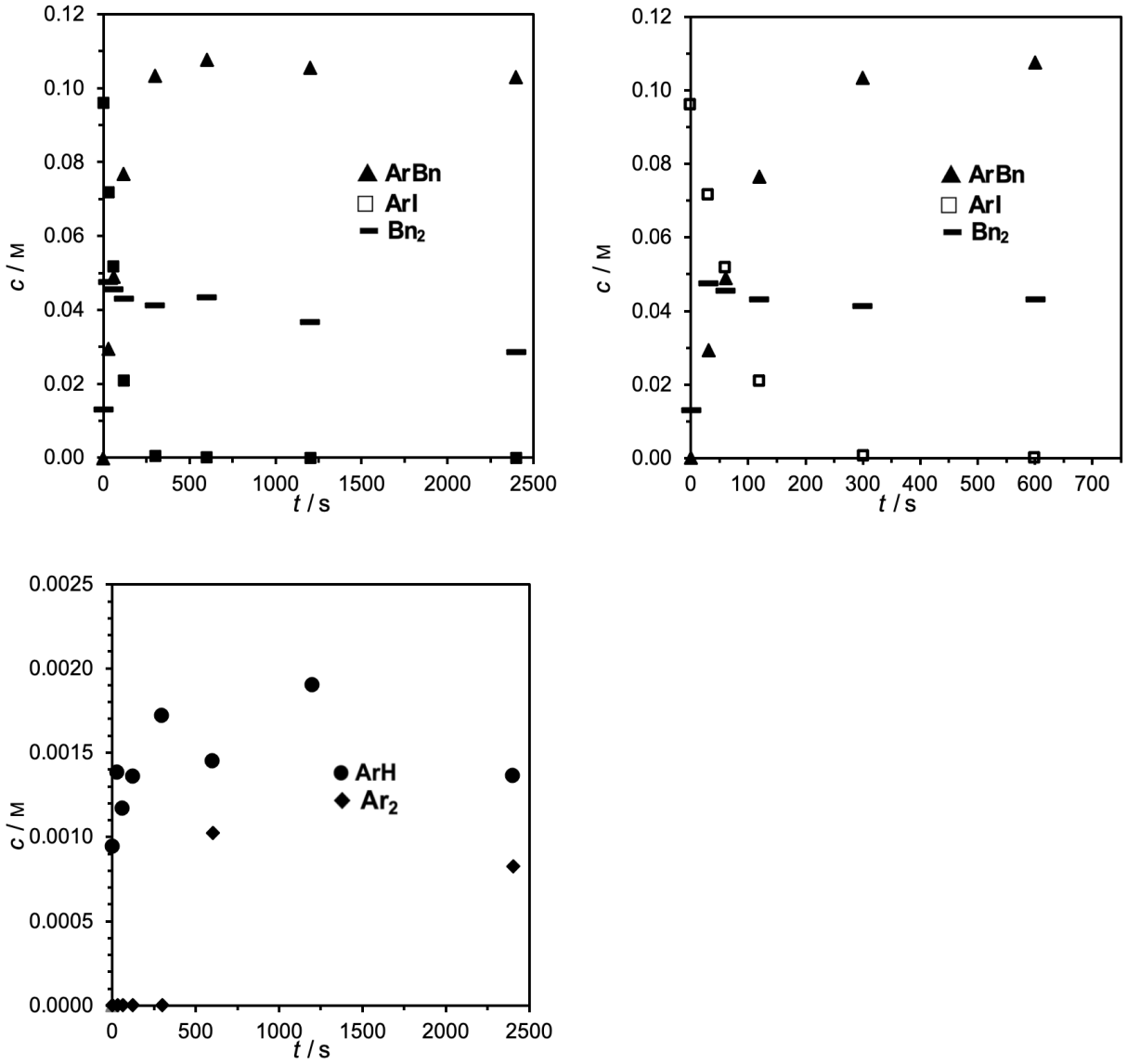

Figure 3.23 Left top: Time profiles of the concentrations of reactant ArI (squares, c_0 = 0.10 M) and of the products ArBn (cross-coupling product, triangles), Bn_2 (homo-coupling product derived from the organozinc reagent, rectangles), formed in the reaction with BnZnBr·LiBr (0.40 M) in THF at 298 K (precatalyst: $Pd(OAc)_2$/2 S-PHOS, $2 \cdot 10^{-4}$ M). Right: Enlargement of Figure 3.23 Left top in the range up to 750 s. Bottom: Time profiles of the concentrations of the byproducts ArH (dehalogenation product, circles), and Ar_2 (homo-coupling product derived from the aryl halide substrate, diamonds) formed in the same reaction at enlarged scale.

Interestingly, in these reactions ArH and Ar_2 byproducts were not only detected, but also Ph_2 and Bn_2, respectively. These compounds were homo-coupling products derived from the organozinc reagent. Although significant amounts of the R_2 homo-coupling products were already observed at $t = 0$ and, thus, apparently resulted from the synthesis of the organozinc reagents (see Experimental Section), the concentrations of R_2 considerably increased upon addition of the precatalyst. This finding suggests that the Pd catalyst can mediate the formation of R_2, presumably via reductive elimination from $LPd(R)_2$ intermediates and, thus, provides strong evidence for the operation of path A in Scheme 3.2.

Variation of the organozinc reagent has a significant effect on the overall reactivity. To make the experiments with different organozinc species comparable, the catalyst loading was varied (Figure 3.22 and Figure 3.23). It was found that PhZnBr · LiBr reacts much faster than BnZnBr · LiBr.

For a direct comparison, again competition experiments employing pairwise equimolar mixtures (Scheme 3.5) were performed. PhZnBr·LiBr was found to be more reactive than BuZnBr·LiBr by a factor of ≥ 25 (Figure 3.24).[124] BuZnBr·LiBr in turn reacted faster than BnZnBr·LiBr by a factor of 2.5 ± 0.5 (Figure 3.25).

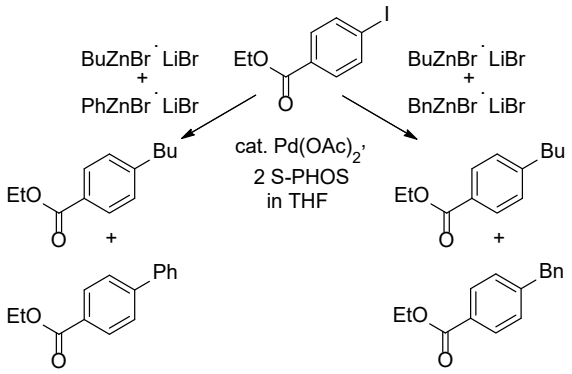

Scheme 3.5 Competition experiments for comparing the reactivity of RZnBr·LiBr reagents.

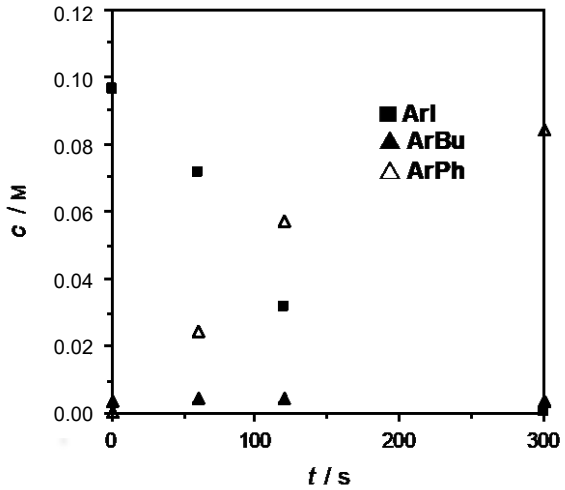

Figure 3.24 Time profiles of the concentrations of reactant ArI (black squares, 0.10 M) and the products ArBu (black triangles) and ArPh (empty triangles) formed in competing reactions with a 1:1 mixture of BuZnBr·LiBr and PhZnBr·LiBr (0.20 M for both components) in THF at 273 K (precatalyst: $Pd(OAc)_2$/2 S-PHOS, $5 \cdot 10^{-6}$ M).

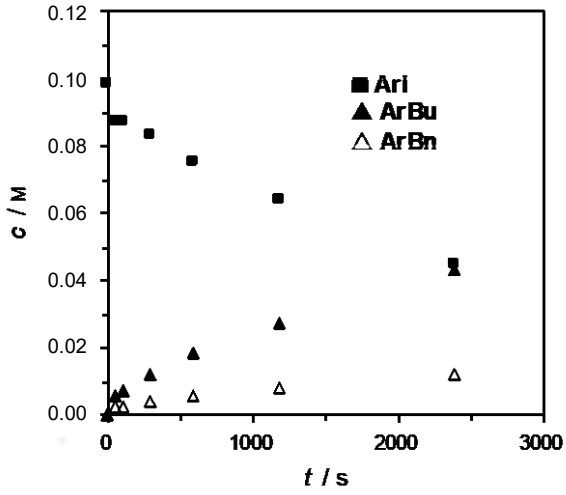

Figure 3.25 Time profiles of the concentrations of reactant ArI (black squares, 0.10 M) and the products ArBu (black triangles) and ArBn (empty triangles) formed in competing reactions with a 1:1 mixture of BuZnBr·LiBr and BnZnBr·LiBr (0.20 M for both components) in THF at 273 K (precatalyst: $Pd(OAc)_2$/2 S-PHOS, $5 \cdot 10^{-5}$ M).

Again, the presence of LiBr is essential for efficient cross-coupling. This is shown on the basis of experiments with and without this additive (Figure 3.26 and Figure 3.27).

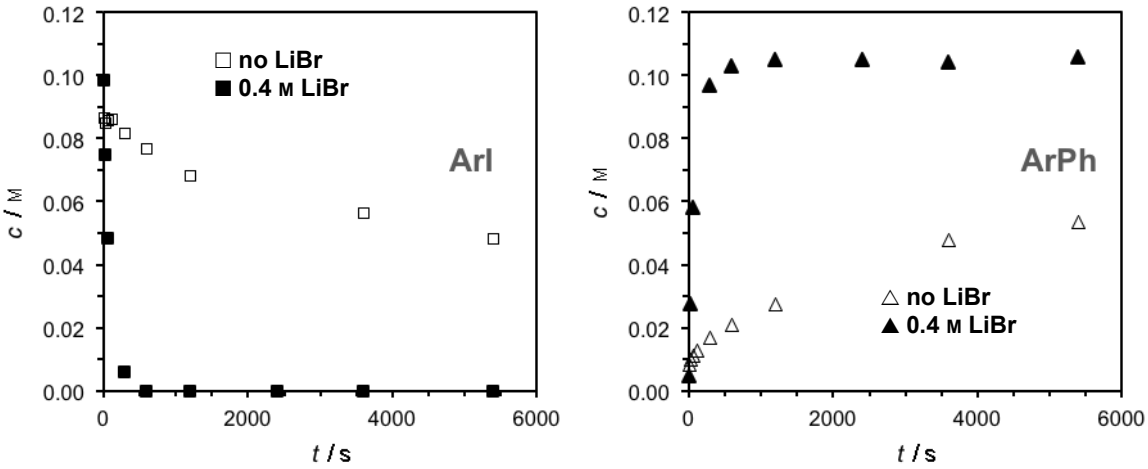

Figure 3.26 Time profiles of the concentrations of reactant ArI (left) and of the cross-coupling product ArPh (right) formed in the reaction with PhZnBr (0.40 M) in THF at 298 K (precatalyst: $Pd(OAc)_2$/2 S-PHOS, $1 \cdot 10^{-5}$ M) in the absence (empty symbols) or presence of LiBr (black symbols).

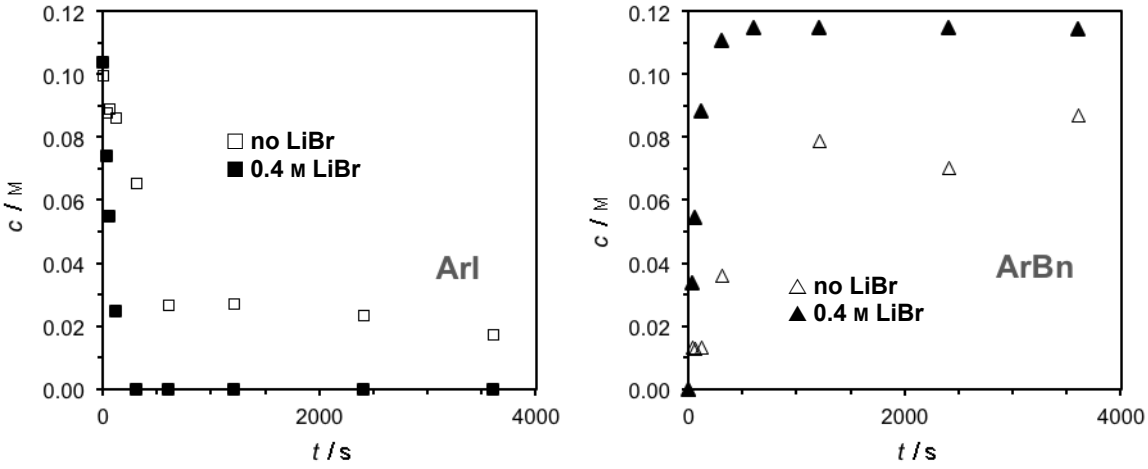

Figure 3.27 Time profiles of the concentrations of reactant ArI (left) and of the cross-coupling product ArBn (right) formed in the reaction with BnZnBr (0.40 M) in THF at 298 K (precatalyst: $Pd(OAc)_2$/2 S-PHOS, $2 \cdot 10^{-4}$ M) in the absence (empty symbols) or presence of LiBr (black symbols).

3.2.6 Rate-limiting step

Information on the nature of the rate-limiting step can be derived from the reaction order. The results indicate that both *c*(Pd) and *c*(ArI) enter the rate law for the model reaction, the former in a linear and the latter apparently in a more complex fashion. In contrast, the rate does not depend on *c*(BuZnBr·LiBr) to a significant extent. Within the framework of the conventional catalytic cycle, these findings are consistent with the oxidative addition, but not with the transmetalation or the reductive elimination being the rate-limiting step. Given that most of the present experiments were performed under roughly pseudo-first order conditions, the predominantly observed bent shapes of the concentration profiles also provide evidence against the transmetalation or the reductive elimination as rate-limiting step (in these cases, approximately linear profiles would be expected).

The effects observed upon variation of the substrate ArX afford further information. The reactivity sharply drops in the series ArI > ArBr ≫ ArOTs, which indeed suggests cleavage of the Ar–X bond in the rate-limiting step[17] and, thus, again points to the oxidative addition. In contrast, the given reactivity order does not appear reconcilable with the transmetalation as rate-limiting step. Previous studies have found that the transmetalation rates of $L_nPd(Ar)Br$ complexes exceed those of their $L_nPd(Ar)I$ counterparts.[125] The observed reactivity pattern is also not compatible with the reductive elimination as rate-limiting step because this step does not involve the leaving group X at all.

The mechanistic picture becomes less clear, however, if the effects resulting from the variation of the RZnX′ reagent are included in the analysis. The organyl group R strongly influence the overall rate of the cross-coupling although they are not involved in the oxidative addition according to the conventional catalytic cycle. This finding indicates severe shortcomings and inconsistencies in our current mechanistic understanding.

3.2.7 Bimodal kinetic behavior

Most of the measured concentration profiles do not follow a simple exponential decay, which would be expected for the oxidative addition as rate-limiting step under approximately pseudo-first order conditions. Instead, a faster reaction in the initial phase and a slower conversion thereafter was found. This bimodality once more points to a mechanistic complexity beyond that of the conventional catalytic cycle. Several explanations for the observed behavior are conceivable. First, the slow-down of the reaction could reflect the increased formation of the ZnX_2 byproduct; the rate-decreasing effect of the latter in independent experiments has been established. Second, the deceleration could result from the partial deactivation/decomposition of the catalyst. The catalytic activity of solutions of $Pd(OAc)_2$/2 S-PHOS slowly decreases with time and, thus, points to the occurrence of such processes. Their time-scale appears too long to account for the bimodal shapes of the concentration profiles, though. Alternatively, the catalyst may become deactivated in the presence of some of the other reaction partners. Theoretical calculations indicate that the organozinc reagent can interact with the Pd(0) species and thereby decrease its catalytic activity.[70] Without any direct experimental data on the processes occurring at the molecular level, an unambiguous mechanistic assignment is difficult, however.

3.2.8 Comparison of different additives

In the reactions investigated, the addition of LiBr (used in combination with RZnBr) leads to a higher reaction rate. Unlike the situation in more polar solvent mixtures,[27p, 65] this increase in reactivity is brought about by just 1 eq. of LiBr. The addition of further LiBr has no significant effect and therefore excludes the involvement of so-called higher-order organozincates, such as $RZnBr_3^{2-}$. The adverse effect of $ZnBr_2$ does not contradict this result because this Lewis-acidic species does not easily release halide anions, but rather scavenges them.[27b, 27p, 27s, 54, 65]

The tendency of RZnX reagents and LiX to combine to organozincates is well-established by now.[27h, 27i, 27q-s, 54-57] As discussed above, the rate-limiting step of the catalytic cycle apparently corresponds to the oxidative addition, for which the involvement of the organozinc reagent is not obvious. Therefore, the possibility that the LiX additives may help to protect the Pd catalyst against deactivation/decomposition, potentially via the formation of Pd ate complexes is also considered.[51, 63] Our experiments indicate that such putative deactivation processes are reversible because the delayed addition of LiBr largely restores the catalytic activity. Again,

more definite and detailed assessments require further insight into the molecular speciation of the different components present in the reaction mixtures.

3.2.9 Practical implications

Aside from mechanistic considerations, the present results also bear practical relevance. The model reaction between ArI and BuZnBr·LiBr in THF and $Pd(OAc)_2$/2 S-PHOS as precatalyst proceeds with high efficiency. The cross-coupling product ArBu is formed with high chemoselectivity. Even a low concentration of the precatalyst of $5 \cdot 10^{-6}$ M (0.005 mol%) still achieves a yield of almost 90% in 2 h at room temperature. With increased catalyst loading, the reaction also proceeds fast at reduced temperatures, which can be advantageous for the transformation of sensitive substrates. An equal or even slightly enhanced catalytic activity is observed for PEPPSI-IPr as precatalyst, whereas that of $Pd(PPh_3)_4$ is somewhat lower and also gives rise to higher amounts of the Ar_2 byproduct. Interestingly, the reaction also proceeds relatively efficiently with plain $Pd(OAc)_2$ and in the absence of any added ligand, thus echoing recent findings of Lei and coworkers.[85] In this case, however, again more byproducts are formed. The versatility of the applied reaction protocol is further demonstrated by the successful exchange of ArI for ArBr and of BuZnBr·LiBr for PhZnBr·LiBr and BnZnBr·LiBr. [13c, 14, 27l, 64, 106]

4 Intermediates of Negishi cross-coupling reactions[c]

4.1 Introduction

On the basis of the currently accepted catalytic cycle, some of the key findings obtained from kinetic measurements on a model reaction Scheme 1.2 and its variants could not be rationalized.[126] Further information on this reaction should be obtained by identifying the intermediates involved. To this end, reaction conditions very similar to those of the kinetic measurements (apart from adjustment of the concentrations of the various reaction partners as required by the analytical methods) are used. To cope with the significant complexity of the reaction, a stepwise approach is pursued. In this way, one component at a time is added before the complete system is finally probed. As analytical methods, ^{31}P NMR and UV/Vis spectroscopy as well as ESI mass spectrometry are considered. The latter proves to be particularly instructive and therefore we predominantly rely on this technique.

4.2 Results and Discussion

4.2.1 ^{31}P NMR spectroscopy [d]

Solutions of $Pd(OAc)_2$ and S-PHOS (molar ratio 1:2) in tetrahydrofuran (THF) were mixed at ambient temperature and immediately investigated by ^{31}P NMR spectroscopy in a temperature range between 198 K and 298 K. The resulting ^{31}P NMR spectra (Figure 4.1, Figure 4.2 and Figure 4.3) reveal the presence of three main products with ^{31}P NMR chemical shifts at 298 K (198 K) of 47.5 (46.7), 39.9 (39.1), and 39.7 (37.9) ppm. At least the latter two values appear to be characteristic of S-PHOS coordinated to Pd(0), as the comparison with (S PHOS)Pd(CH_2=$CHSiMe_2$)$_2$O (δ^{31}P = 35.8 ppm) suggests;[127] in contrast, Pd(I) and Pd(II) complexes of S-PHOS typically resonate at lower fields (δ^{31}P = 85.7 and 53.7 ppm for [(S PHOS)Pd]$_2$(BF_4)$_2$ and (S-PHOS)$_2$$PdCl_2$, respectively).[128] A more definite assignment of the observed main products is not straightforward, however; other cases have been reported, in which ^{31}P NMR spectroscopy alone did not achieve unambiguous assignment of Pd phosphine complexes formed in situ either.[90b, 90c, 90f, 129] Nonetheless, the apparent complexity of the

[c] Some of the schemes and text passages of this chapter have partially been published already in Lit [126]. Prof. Koszinowski carried out the shown ESI mass spectrometry experiments.
[d] Prof. Dr. Karaghiosoff carried out the shown NMR experiments.

present sample is surprising, given the strong tendency of S-PHOS to form only mono-ligated Pd(0) complexes.[101d, 105] Different conformers[26l] and/or different aggregation states may be involved. As Tromp et al. have pointed out, the NMR-spectroscopic distinction of Pd species in different aggregation states is notoriously difficult.[92]

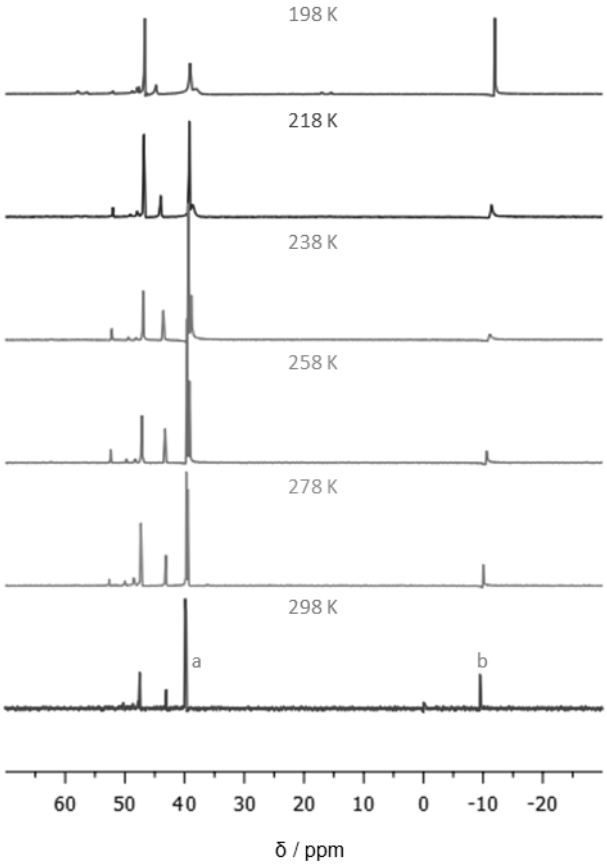

Figure 4.1 ^{31}P NMR spectra of a solution of $Pd(OAc)_2$ (1 mM) and S-PHOS (L, 2 mM) in THF measured at different temperatures (starting at 198 K and warming up the sample to 298 K in the course of 6 h). The signals labeled a and b are assigned to the phosphine oxide and free S-PHOS, respectively.

In addition, the spectra show the presence of remaining free S-PHOS and of the phosphine oxide derived thereof with ^{31}P chemical shifts at −9.5 (−11.9) and 43.1 (44.8) ppm, respectively. These assignments were confirmed by control experiments, in which the ^{31}P NMR spectrum of a solution of S-PHOS in THF was recorded before and after its exposure to air. The phosphine oxide presumably results from the reduction of $Pd(OAc)_2$, see above.[90a, 90b] Apparently, this reaction does not reach completion, though, as both the presence of remaining free S-PHOS and the relatively low abundance of corresponding phosphine oxide indicate. Moreover, it is worth noting the temperature dependence of the ^{31}P NMR signal of S-PHOS, which is sharp at 198 and 298 K, but broad at temperatures in between, reaching a maximum line width at 238 K. A partly similar dependence was observed for the signal at 37.9 ppm, which is broad at 198 K and becomes sharper with increasing temperature. This behavior points to the operation of fast equilibria with the involvement of free S-PHOS. Given the significant complexity of the sample resulting from the combination of just two components and the difficult product assignment, ^{31}P NMR spectroscopy was not applied to the analysis of further systems, but we turned to other analytical methods.

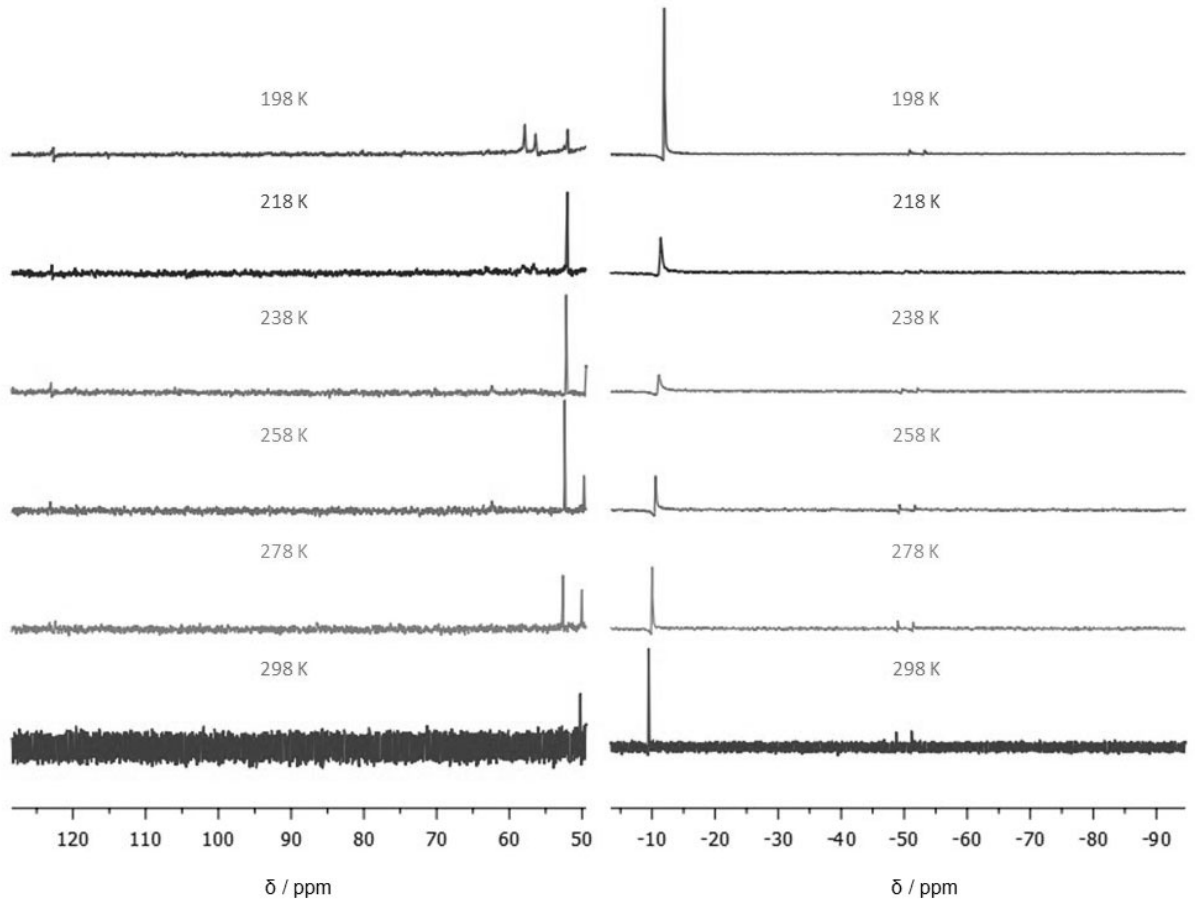

Figure 4.2 Downfield (left) and upfield (right) sections from the ^{31}P NMR spectra of a solution of $Pd(OAc)_2$ (1 mm) and S-PHOS (2 mm) in THF measured at different temperatures (starting at 198 K and warming up to the sample to 298 K in the course of 6 h).

4.2.2 UV/Vis spectroscopy

Solutions of $Pd(OAc)_2$/2 S-PHOS are colored. The color changes with time as well as upon addition of LiBr and BuZnBr. According to UV/Vis spectroscopy, the freshly prepared yellow solutions of $Pd(OAc)_2$/2 S-PHOS show an absorption maximum centered at 390 nm (Figure 4.3, top). With time, the color turnes red and at 495 nm another absorption band evolves, whose flank stretches out beyond 700 nm. The absorption over such an extended range of wavelengths is typical of Pd (and other metal) nanoclusters[130] and, thus, points to the gradual decomposition of the catalyst and Pd aggregation in the current experiments. If LiBr is added to the solution, the $Pd(OAc)_2$/2 S-PHOS solutions change from yellow to orange, but do not turn red as quickly as the solutions without the additive. Apparently, the formation of Pd nanoclusters is slowed down. The absorption band is centered at 430 nm and has a shoulder at 390 nm, which

presumably corresponds to the first maximum observed in the absence of LiBr (Figure 4.3, bottom). A second shoulder around 520 nm evolves almost immediately after combination of the different components, but then vanishes again. This transient absorption is tentatively assigned to $PdBr_4^{2-}$ and related complexes, which can form from residual $Pd(OAc)_2$ and LiBr; $PdBr_4^{2-}$ is known to exhibit an absorption maximum at 508 nm.[90i]

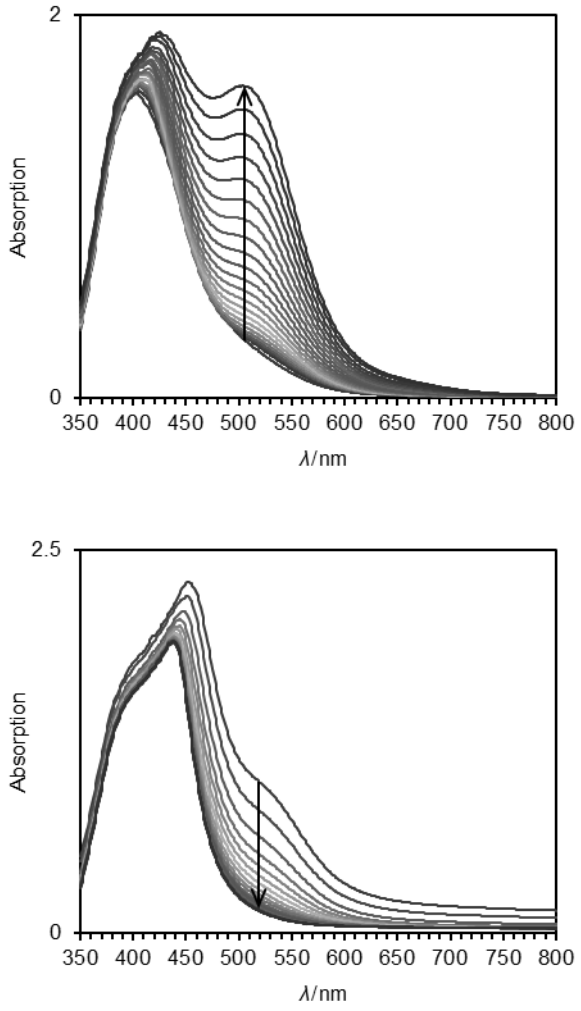

Figure 4.3 UV/Vis spectra of a solution of $Pd(OAc)_2$ (7.5 mM) and S-PHOS (15 mM) in THF in the absence (top) and presence (bottom) of LiBr (0.4 M). Spectra are shown for time intervals of 1 – 45 min (top) and 6 – 46 min (bottom) after combining $Pd(OAc)_2$ and S-PHOS (time steps of 2 min).

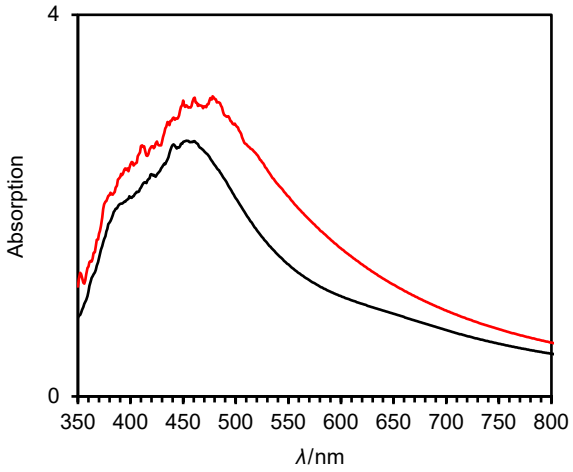

Figure 4.4 UV/Vis spectra of a solution of $Pd(OAc)_2$ (3 mM) and S-PHOS (6 mM) in THF after addition of BuZnBr (15 mM, black curve) or BuZnBr·LiBr (15 mM, red curve), respectively.

As soon as BuZnBr or BuZnBr·LiBr is added, solutions of $Pd(OAc)_2$/2 S-PHOS rapidly darken and show absorption over the entire wavelength range sampled (Figure 4.4).

Apparently, the organozinc reagent reduces residual $Pd(OAc)_2$ and leads to Pd aggregation, eventually resulting in the formation of Pd black. This observation indicates that the amount of ligand employed, although theoretically sufficient, is not enough for stabilizing all of the Pd(0).

4.2.3 ESI mass spectrometry − catalyst in the absence of substrate

Analysis of a solution of the $Pd(OAc)_2$ precatalyst in THF by ESI mass spectrometry affords only rather weak signal intensities. This is to be expected in accordance with its supposedly low tendency toward heterolytic dissociation in this relatively non-polar solvent. This slight tendency to dissociation is also reflected in the high aggregation state of the ions observed, such as $NaPd_3(OAc)_6^+$, $NaPd_6(OAc)_{12}^+$, and $NaPd_3(OAc)_3(OH)_5(HOAc)_n^-$, $n = 0$ and 1 (Figure 8.1, Figure 8.2, Table 8.1 and Table 8.2); the Na^+ incorporated in these species presumably originates from the used glassware. As expected, only Pd(II) species form in the absence of a phosphine ligand.

Upon addition of 2 equiv. of S-PHOS (L) to solutions of $Pd(OAc)_2$ in THF, the ESI mass spectra change significantly. In the positive ion mode, dimeric complexes $L_2Pd_2(OAc)^+$ and $L_2Pd_2(PCy_2)^+$ appear in high abundance (Figure 4.5, Figure 8.3, Figure 8.4, Figure 8.5, Figure 8.6 and Table 8.3).

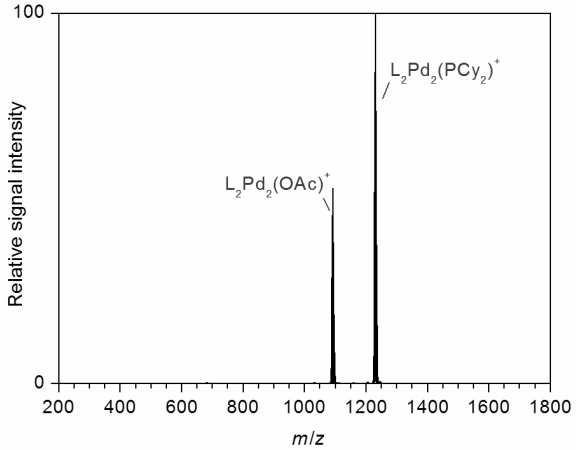

Figure 4.5. Positive-ion mode ESI mass spectrum of a solution of $Pd(OAc)_2$ (3 mM) and S-PHOS (L, 6 mM) in THF directly after mixing.

Related monocationic Pd dimers were not only observed in previous ESI mass-spectrometric studies,[95g, 98h] but were also found in the condensed phase and structurally characterized.[95g] In the case of L = S-PHOS, Barder prepared $L_2Pd_2^{2+}(BF_4^-)_2$ by treatment of L_2PdCl_2 with $AgBF_4$.[128] X-ray crystallography revealed a direct Pd−Pd bond and an end-on coordination of the two phosphine ligands. These phosphine ligands interact with the Pd centers via their aryl groups.[128] A similar geometry may be assumed for the monocations detected in the present study. The additional anionic ligand could adopt an additional bridging mode. Like their well-known neutral counterparts,[131] the cationic Pd dimers are commonly thought to be composed of two Pd(I) centers, which are covalently bound to each other (Scheme 4.1, left).[95g, 128] [131a]

It would also be possible that the Pd dimers arise from a combination of a Pd (0) and a Pd (II) unit. [95g] A dative complex would be formed between the Lewis basic Pd (0) and the Lewis acidic Pd (II) (Scheme 4.1, right).[98h]

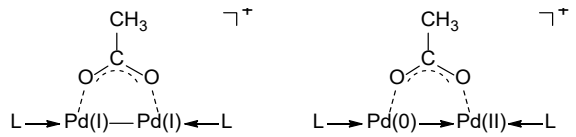

Scheme 4.1. Possible descriptions of the Pd−Pd interaction in $L_2Pd_2(OAc)^+$ as a covalent or dative bond.

Apart from the Pd dimer motif itself, the PCy_2 group as coordinating ligand in $L_2Pd_2(PCy_2)^+$ is also of interest in the present context. Clearly, this entity results from Pd insertion into the Ar−PCy_2 bond of the S-PHOS ligand and its cleavage. Degradation of the S-PHOS ligand at room temperature apparently proceeds continuously, as can be seen from the further increased relative signal intensity of $L_2Pd_2(PCy_2)^+$ at later times (Figure 8.7).

In addition to $L_2Pd_2(PCy_2)^+$, sample solutions exposed to air also afford a Pd cation binding to the aryl fragment of the ligand, thus providing additional evidence for the proposed degradation of the latter.

Further information is given by the negative-ion mode ESI mass spectra. Besides residual $Pd(OAc)_2$ cluster ions and species presumably resulting from the oxidation of S-PHOS and/or a contamination, the trinuclear complex $(LO)Pd_3(PCy_2)(OAc)_2^-$ is observed, with LO denoting the phosphine oxide derived from S-PHOS (Figure 8.11, Figure 8.12 and Table 8.4).

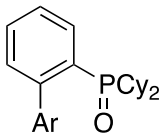

LO, Ar = 2,6-dimethoxyphenyl

The identity of this complex is substantiated by gas-phase fragmentation experiments, which result in the loss of (LO)Pd (or of separate LO and Pd), eq. (1) (Figure 8.13).

$$(LO)Pd_3(PCy_2)(OAc)_2^- \rightarrow Pd_2(PCy_2)(OAc)_2^- + (LO)Pd \quad (1)$$

The trinuclear complex can be viewed as an aggregate consisting of a Pd(I) dimer and a Pd(0) moiety. At the same time, the coordination of a PCy_2 entity corroborates the operation of C−P bond activation processes of the S-PHOS ligand and its partial degradation. Upon exposure of the sample solution to air, the Pd trimer vanishes and only simple $Pd(OAc)_2$ cluster ions remain (Figure 8.14). The addition of LiBr to solutions of $Pd(OAc)_2$ and S-PHOS results in considerable changes of the ESI mass spectra. In the positive-ion mode, the formation of $L_2Pd_2Br^+$ at the expense of $L_2Pd_2(OAc)^+$ points to ligand exchange processes (Figure 8.15, Figure 8.16, Figure 8.17 and Table 8.5).

The greatly decreased signal intensity of $L_2Pd_2(PCy_2)^+$ suggests that the presence of LiBr slows down the degradation of the S-PHOS ligand. In the negative-ion mode, the major species correspond to $Pd(OAc)_2$ cluster anions, some of which show incorporation of Li^+ (Figure 8.18 and Table 8.6).

4.2.4 ESI mass spectrometry – catalyst in the presence of organozinc reagents

ESI mass-spectrometric analysis of a solution of $Pd(OAc)_2$, S-PHOS, and BuZnBr in THF finds $LZnBu^+$ as base peak in the positive-ion mode (Figure 8.19, Figure 8.20, Figure 8.21, Figure 8.22, Figure 8.23, Figure 8.24, Figure 8.25, Figure 8.26 and Table 8.7). This complex resembles other ligated organozinc cations of the type (ligand)ZnR^+, which have been extensively studied previously.[55a, 132] In small quantities the related dimer $L_2Zn_2BuBr_2^+$ is also detected.
Even more interesting, however, is the presence of the heterobimetallic $L_2PdZnBu^+$ ion (Figure 4.6). For this species, three different types of structure are conceivable: (i) The $L_2PdZnBu^+$ ion could feature a direct interaction between the Pd and the Zn center (structure A, Scheme 4.2). (ii) If the Pd and Zn centers are not interacting with each other directly, they could be held together by bridging S-PHOS ligands (structure B). (iii) The cationic ZnBu unit could be attached to one of the OCH_3 groups of an S-PHOS ligand (structure C).

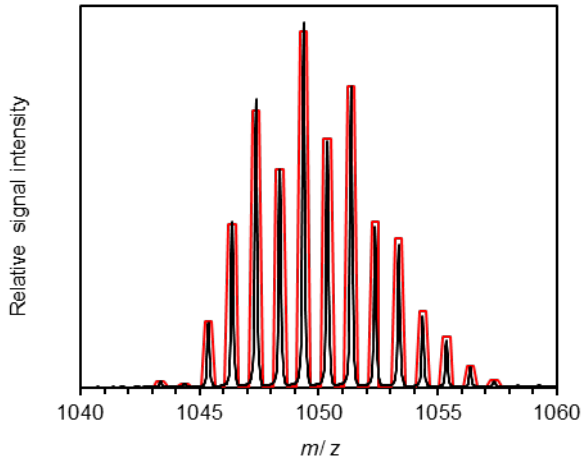

Figure 4.6 Measured (black) and simulated (red) isotope pattern of $L_2PdZnBu^+$ (L = S-PHOS).

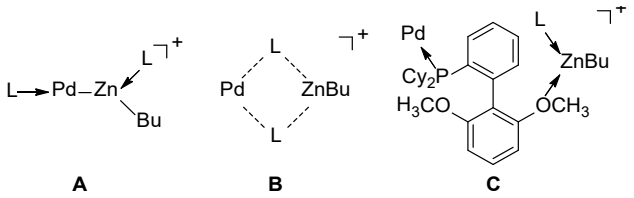

Scheme 4.2. Possible structures of $L_2PdZnBu^+$ (L = S-PHOS).

Compounds with direct Pd-Zn bonds as in **A** have recently been described and structurally characterized.[69] However, the assignment of the oxidation states to the metal centers is never uncomplicated.[69d] **A** can be considered to result from the combination of an LPd(0) and an $LZn(II)Bu^+$ moiety. González-Pérez et al. predicted the formation of $(PMe_3)_2Pd{-}Zn(Me)(Cl)(THF)$ on the model system $Pd(PMe_3)_2$/MeZnCl in THF by quantum-chemical calculations. These calculations of a very similar structure support structure **A**.[70] In contrast, structure **B** seems less likely because such bridging binding modes are uncommon for tertiary phosphines.[133] Structure **C** was also excluded; if it had formed, one would expect other ethers, such as the abundantly present THF, to coordinate to the $ZnBu^+$ moiety as well. The absence of $BuZnL(THF)^+$ or related complexes suggests, however, that such species are not sufficiently stable under the chosen experimental conditions.

Further insight is obtained from the gas-phase fragmentation of $L_2PdZnBu^+$, which leads to losses of a phosphine ligand, a neutral PdL unit, and a Zn atom together with butene and the phosphine, eq. 4.2a – 4.2c with L = S-PHOS, respectively (Figure 8.24).

$$L_2PdZnBu^+ \rightarrow LPdZnBu^+ + L \quad (4.2a)$$

$$\rightarrow LZnBu^+ + PdL \quad (4.2b)$$

$$\rightarrow LPdH^+ + [Zn, C_4H_8, L] \quad (4.2c)$$

The expulsion of an S-PHOS ligand under conservation of the Pd-Zn core, eq. 4.2a, points to an appreciable stability of the latter, in line with the proposed structure **A** and its Pd−Zn bond. The second fragmentation channel, eq. 4.2b, corresponds to the heterolytic dissociation of the parent ion into its two subunits, which is the back reaction of the putative formation of $L_2PdZnBu^+$. Moreover, the partitioning of the S-PHOS ligands between the two fragments is of interest. The fact that only a Zn-containing fragment with exactly one S-PHOS ligand is observed strongly suggests that already in the parent ion one of the two S-PHOS ligands is bound to the Pd and the other to the Zn center. As already mentioned above, Pd(0) indeed is generally believed to accommodate only a single S-PHOS ligand due to the high steric demands of the latter. [101d, 105] A similar situation can also be expected for the Zn(II) center. The interpretation of the third fragmentation channel, eq. 4.2c, is less straightforward. This reaction could either correspond to a proton transfer reaction affording a protonated PdL complex together with a Zn carbene species and an S-PHOS ligand or it could result in a Pd hydride complex $LPd(II)H^+$ together with neutral Zn, butene, and S-PHOS (Scheme 8.1). The first possibility seems somewhat less likely as none of the previously studied ligated $ZnBu^+$ complexes underwent proton transfer reactions upon fragmentation. The related $ZnCH_3^+$, however, was shown to react with NH_3 under formation of $CH_3NH_3^+$.[134] In analogy, energized $L_2PdZnBu^+$ might also transfer the Bu substituent to the Pd center, followed by rapid β-hydrogen elimination to yield $LPd(II)H^+$. This point will be discussed later.

Negative-ion mode ESI mass spectrometry of solutions of $Pd(OAc)_2$, S-PHOS, and BuZnBr in THF does not detect any Pd-containing species, but only zincate anions, such as $ZnBr_3^-$ and $Zn_2Br_5^-$ (Figure 8.27 and Table 8.8).

These zincates as well as their butyl-containing analogues are already known from BuZnBr solutions and have previously been studied in detail.[27h, 27r] The absence or reduced abundance of organozincates observed in the present work presumably originates from an imperfect insulation of the ESI source from the atmosphere and the occurrence of hydrolysis reactions of theses sensitive species.

In the presence of LiBr, solutions of $Pd(OAc)_2$, S-PHOS, and BuZnBr in THF again show $LZnBu^+$ and $L_2PdZnBu^+$ upon analysis by positive-ion mode ESI mass spectrometry (Figure 4.7, Figure 4.8, Figure 8.28 and Table 8.9). In addition, the Li^+ complexes of S-PHOS and the corresponding phosphine oxide as well as the heterobimetallic dimer L_2PdLi^+ are observed as new peaks. As discussed above, the phosphine oxide presumably stems from the activation of the catalyst.[90a, 90b] The high oxophilicity of Li^+ explains why it readily forms complexes with the phosphine oxide, which are efficiently detected by ESI mass spectrometry. In the negative-ion mode, the anions, $ZnBr_3^-$, $BuZn_2Br_4^-$, and $Zn_2Br_5^-$ are observed (Figure 8.29 and Table 8.10).

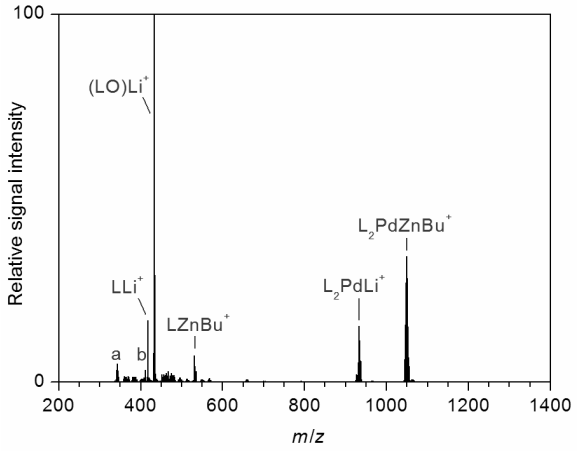

Figure 4.7. Positive-ion mode ESI mass spectrum of a solution of $Pd(OAc)_2$ (3 mM), S-PHOS (L, 6 mM), and BuZnBr·LiBr (15 mM) in THF (a = $Li_3ZnBr(OAc)_3^+$, b = LH^+).

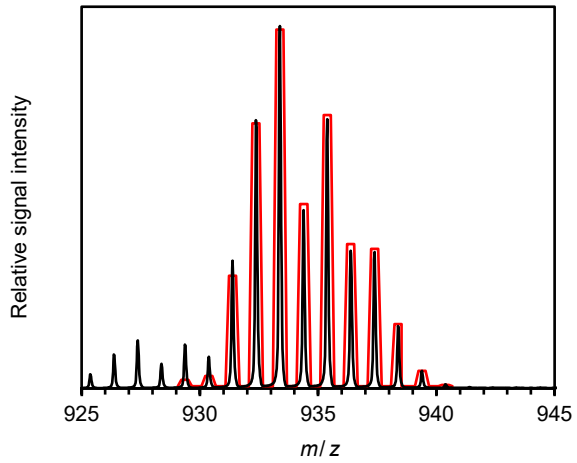

Figure 4.8 Measured (black) and simulated (red) isotope pattern of L_2PdLi^+ (L = S-PHOS).

To test the generality of the present findings, the catalyst is first varied. Positive-ion mode ESI mass-spectrometric analysis of solutions of $Pd(PPh_3)_4$ and BuZnBr·LiBr in THF detects a multitude of cationic species (Figure 4.9, Figure 8.30,Figure 8.31, Figure 8.32, Figure 8.33, Figure 8.34 and Table 8.11). The cations with $m/z < 600$ do not contain any Pd, however, but just Li and/or Zn as metallic component.

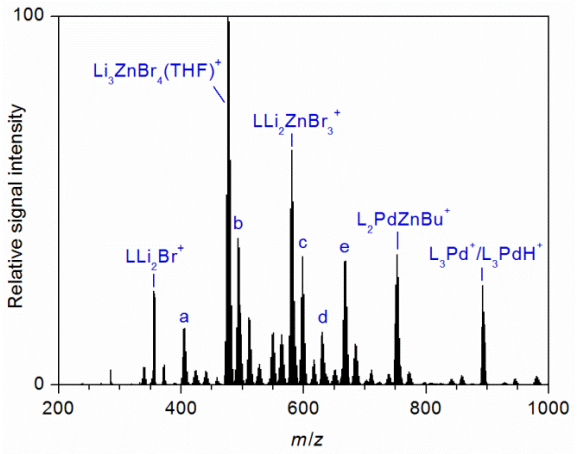

Figure 4.9. Positive-ion mode ESI mass spectrum of a solution of $Pd(PPh_3)_4$ (3 mM) and BuZnBr·LiBr (15 mM) in THF (a = $Li_3ZnBr_4^+$, b = $LLiZnBr_2^+$, c = $LLi_2ZnBr_3(H_2O)^+$, d = L_2Pd^+/L_2PdH^+, e = $LLi_3ZnBr_4^+$, L = PPh_3).

Pd-containing complexes are observed at higher *m*/*z* ratios and include $L_2PdZnBu^+$ (L = PPh_3), for which a structure analogous to **A** (Scheme 4.2) is postulated. This assignment is corroborated by gas-phase fragmentation experiments (Figure 8.33), which demonstrate the facile loss of one phosphine ligand from the parent ion, eq. (4.2a) with L = PPh_3, and a significant stability of the Pd−Zn bond. Further Pd complexes detected correspond to L_2Pd^+ and L_3Pd^+, of which the former has already been observed in previous ESI mass-spectrometric experiments.[95f] These ions are open-shell species and are not expected to form spontaneously. Instead, they probably arise from an anodic oxidation during the ESI process.[95f, 135] A careful inspection of the measured isotope patterns moreover shows that the L_nPd^+ ions are accompanied by L_nPdH^+ complexes (Figure 8.30 and Figure 8.31). The latter could result from the former either by H abstraction from the solvent or by a reaction sequence involving transmetalation and β-H elimination (in analogy to the Scheme 8.1). In the negative-ion mode, only zincate ions are observed, which do not provide additional information (Figure 8.35 and Table 8.12).

The discussion of the $Pd(PPh_3)_4$ catalytic system is concluded by noting the complete absence of phosphine oxide, in marked contrast to the situation encountered for the case of the $Pd(OAc)_2$/2 S-PHOS solutions. This absence reflects the fact that the $Pd(PPh_3)_4$ precatalyst already contains Pd(0) and, thus, does not require initial reduction.
As third precatalyst, PEPPSI-IPr[62] is considered, which contains an N-heterocyclic carbene as ligand.

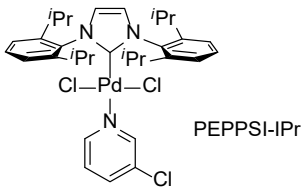

PEPPSI-IPr

Upon positive-ion mode ESI, solutions of PEPPSI-IPr and BuZnBr·LiBr in THF almost exclusively afford the protonated *N*-heterocyclic carbene (Figure 8.36, Figure 8.37 and Table 8.13). Given the extremely high basicity of *N*-heterocyclic carbenes,[136] this observation is not unexpected, although the origin of the proton is not clear.[137] Besides the protonated ligand, small amounts of the protonated Pd complex $(L_2Pd)H^+$ (L = *N*-heterocyclic carbene) are also detected. With respect to the anions observed upon negative-ion mode ESI, again only zincates are found (Figure 8.38 and Table 8.14).

Next, the organozinc reagent is varied. Probing solutions of $Pd(OAc)_2$/2 S-PHOS and PhZnBr·LiBr, a plethora of Pd-free cations (Figure 4.11, Figure 8.44, Figure 8.45, Figure 8.46, Figure 8.47 and Table 8.17) is again found.

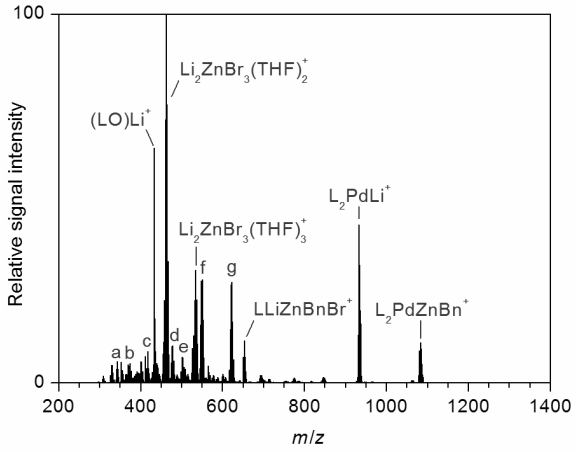

Figure 4.10. Positive-ion mode ESI mass spectrum of a solution of $Pd(OAc)_2$ (3 mM), S-PHOS (L, 6 mM), and BnZnBr·LiBr (15 mM) in THF (a = $Li_3ZnBr(OAc)_3^+$, b = $Li_2ZnBr_2(OAc)(THF)^+$, c = LLi^+, d = $Li_3ZnBr_4(THF)^+$, e = $Li_4ZnBr_2(OAc)_3(THF)^+$, f = $Li_3ZnBr_4(THF)_2^+$, g = $Li_3ZnBr_4(THF)_3^+$).

Of these, two types of species deserve explicit mentioning: (i) $(LO)Li^+$ again points to the oxidation of the phosphine in the course of the precatalyst activation.[90a, 90b] (ii) $LLiZnPhBr^+$ and the related $L_2Zn_2Ph_2Br^+$ once more demonstrate the tendency of organozinc halides toward cationization in the presence of strong ligands.[55a, 132a-f] Besides these Pd-free species, two Pd-containing complexes are also observed: (i) L_2PdLi^+ may be considered as aggregate of an LPd and an LLi^+ moiety, which could be held together by coordination of LLi^+ via one of the ether groups of the second S-PHOS ligand; the presence of a direct Pd−Li interaction cannot be excluded, however. (ii) $L_2PdZnPh^+$ forms the counterpart of $L_2PdZnBu^+$ and supposedly features a structure analogous to **A** (Scheme 4.2). This assumption is fully borne out by fragmentation experiments, which identify three distinct decomposition channels, eq. 4.3a – 4.3c with L = S-PHOS, respectively (Figure 4.12).

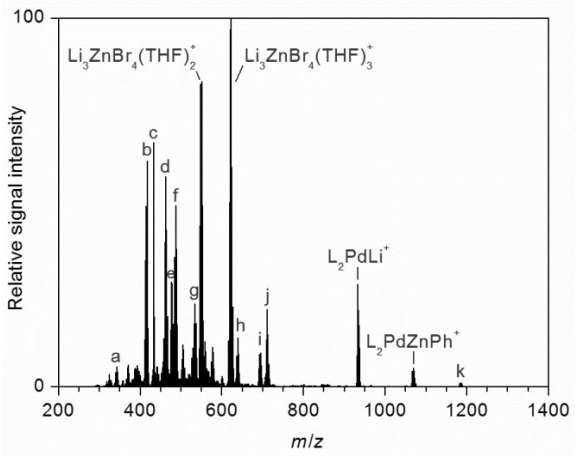

Figure 4.11. Positive-ion mode ESI mass spectrum of a solution of $Pd(OAc)_2$ (3 mM), S-PHOS (L, 6 mM), and PhZnBr·LiBr (15 mM) in THF (a = $Li_3ZnBr_3OH^+$, b = $Li_3H_2Br_4(THF)^+$/LLi^+, c = $(LO)Li^+$, d = $Li_2ZnBr_3(THF)_2^+$, e = $Li_3ZnBr_4(THF)^+$, f = $Li_3H_2Br_4(THF)_2^+$, g = $Li_2ZnBr_3(THF)_3^+$, h = $LLiZnPhBr^+$, i = $Li_3ZnBr_4(THF)_4$, j = $LLiZnPhBr(THF)^+$, k = $L_2Zn_2Ph_2Br^+$).

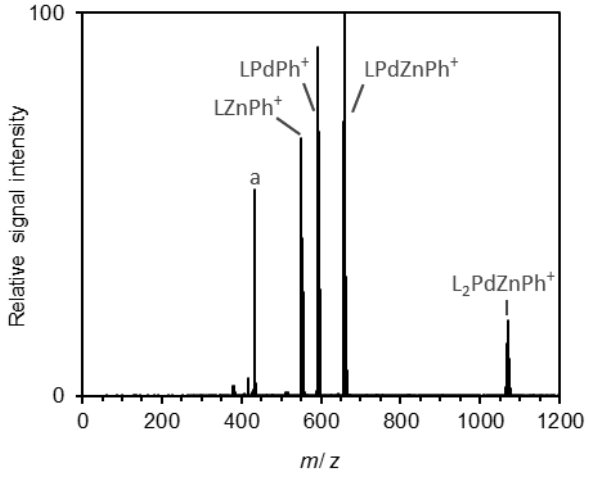

Figure 4.12 Mass spectrum of mass-selected $L_2PdZnPh^+$ and its daughter ions produced upon collision-induced dissociation (E_{LAB} = 30 eV). The peak labeled a corresponds to $(LO)Li^+$, which results from an isobaric contamination of the parent ion.

$L_2PdZnPh^+ \rightarrow LPdZnPh^+ + L$ (4.3a)

$\rightarrow LZnPh^+ + PdL$ (4.3b)

$\rightarrow LPdPh^+ + [Zn, L]$ (4.3c)

Eq. 4.3a and 4.3b directly parallel fragmentation reactions of $L_2PdZnBu^+$, eq. 4.2a and 4.2b, respectively. Eq. 4.3c corresponds to a transmetalation, for $L_2PdZnBu^+$ (Scheme 8.1) which is also inferred. Whereas the transmetalated species derived from $L_2PdZnBu^+$ supposedly undergoes a consecutive β-H elimination, the analogous degradation pathway is not available for $LPdPh^+$, thus explaining its persistence in the present experiments. In the negative-ion mode ESI mass spectrum, only zincate ions are observed (Figure 8.39 and Table 8.15).

The exchange of PhZnBr·LiBr for BnZnBr·LiBr results in the detection of very similar species. Among the cations observed (Figure 4.13, Figure 8.40, Figure 8.41, Figure 8.42, Figure 8.43 and Table 8.16), the heterobimetallic complex $L_2PdZnBn^+$ again is of special interest.

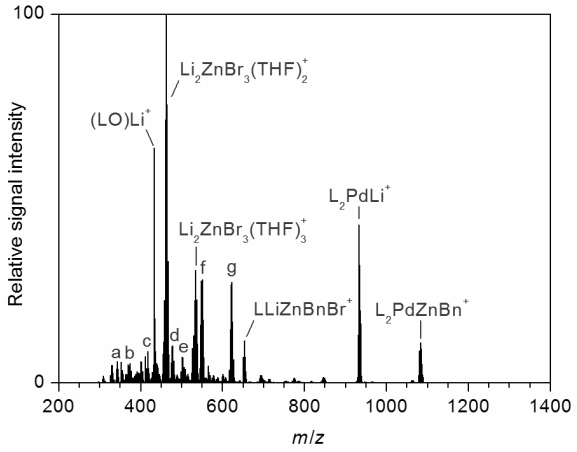

Figure 4.13 Positive-ion mode ESI mass spectrum of a solution of $Pd(OAc)_2$ (3 mM), S-PHOS (L, 6 mM), and BnZnBr·LiBr (15 mM) in THF (a = $Li_3ZnBr(OAc)_3^+$, b = $Li_2ZnBr_2(OAc)(THF)^+$, c = LLi^+, d = $Li_3ZnBr_4(THF)^+$, e = $Li_4ZnBr_2(OAc)_3(THF)^+$, f = $Li_3ZnBr_4(THF)_2^+$, g = $Li_3ZnBr_4(THF)_3^+$).

Fragmentation experiments of this ion find three different decomposition reactions (Figure 8.43), eq. 4.4a – c with L = S-PHOS, which are in line with the parent ion having a structure analogous to **A** (Scheme 4.2).

$L_2PdZnBn^+ \rightarrow LZnBn^+ + PdL$ (4.4a)

$\rightarrow LPdBn^+ + [Zn, L]$ (4.4b)

$\rightarrow LPd^+ + [ZnBn, L]$ (4.4c)

The first two reactions, eq. 4.4a and 4.4b, proceed in analogy to fragmentation reactions occurring for $L_2PdZnPh^+$, eq. 4.3b and 4.3c, respectively. In contrast, eq. 4.4c corresponds to a novel decomposition process. This reaction produces a Pd(I) species, thus pointing to a homolytic cleavage of the Pd−Zn bond. In the negative-ion mode, mainly zincate anions are observed (Figure 8.48 and Table 8.18).

Solutions of $Pd(OAc)_2$/2 S-PHOS and $ZnBr_2$·LiBr are also probed, but no ions of interest are detected in these experiments (Figure 8.49, Figure 8.50, Figure 8.51, Table 8.19 and Table 8.20).

4.2.5 ESI mass spectrometry – catalyst in the presence of aryl iodide substrate

Positive-ion mode ESI of solutions of $Pd(OAc)_2$/2 S-PHOS and ArI (Scheme 3.1) affords two Pd dimers, namely $L_2Pd_2I^+$ and $L_2Pd_2(PCy_2)^+$ (Figure 4.14, Figure 8.52, Figure 8.53 and Table 8.21). As discussed above, the latter is also generated in the absence of ArI. The former, in turn, necessarily involves ArI as iodine source and indicates the occurrence of an Ar−I activation reaction, such as an oxidative addition.

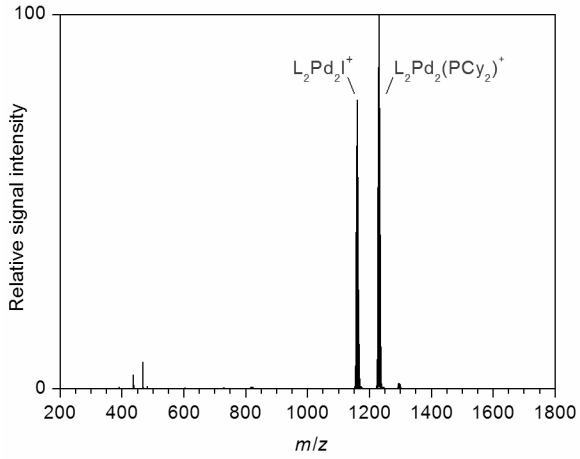

Figure 4.14. Positive-ion mode ESI mass spectrum of a solution of $Pd(OAc)_2$ (3 mM), S-PHOS (L, 6 mM), and ArI (*p*-EtOOC-C_6H_4-I, 15 mM) in THF.

Direct evidence for the occurrence of oxidative additions/Pd insertions under the present reaction conditions is provided by negative-ion mode ESI mass spectrometry. Besides simple palladium acetate/hydroxide cluster ions, these experiments detect the insertion products $ArPdI(OAc)^-$ and $ArPdI_2^-$ (Figure 4.15, Figure 8.56, Figure 8.57, Figure 8.58, Figure 8.59 and Table 8.23); the propensity of Pd(II) insertion products to add anions and form negatively charged complexes is well-known.[51b, 77a, 79a, 102b, 102c] Somewhat unexpectedly, the observed intermediates do not contain any phosphine ligand, however. During fragmentation in the gas phase, $ArPdI(OAc)^-$ and $ArPdI_2^-$ undergo C−H activation reactions and/or lose the Ar substituent (Figure 8.58 and Figure 8.59). In contrast, reductive elimination of ArI is not found, which would correspond to the reverse of the oxidative addition. The absence of this fragmentation channel implies that the oxidative additions occurs virtually irreversibly, in accordance with reports in the literature.[138]

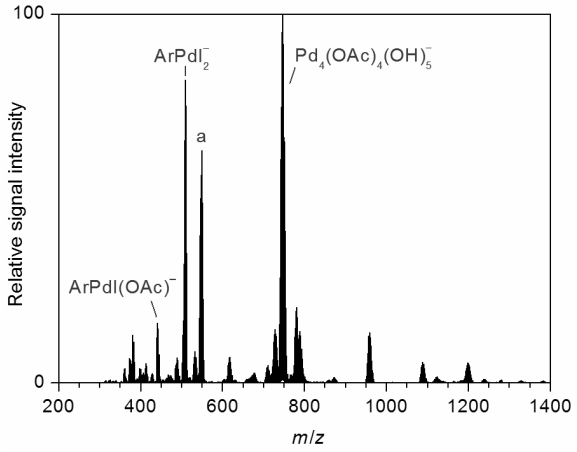

Figure 4.15. Negative-ion mode ESI mass spectrum of a solution of $Pd(OAc)_2$ (3 mM), S-PHOS (L, 6 mM), and ArI (*p*-EtOOC-C_6H_4-I, 3 mM) in THF (a = $NaPd_2(OAc)_5(OH)^-$).

4.2.6 ESI mass spectrometry – catalyst in the simultaneous presence of organozinc reagent and aryl iodide substrate

Finally, solutions of $Pd(OAc)_2$/2 S-PHOS, BuZnBr·LiBr and ArI are analyzed. This mixture contains all components required for the catalytic cycle and therefore should yield the Negishi cross-coupling product. In the positive-ion mode ESI mass spectrum, prominent species include $LZnBu^+$, L_2PdLi^+, and the heterobimetallic dimer $L_2PdZnBu^+$, all of which are already known from the experiments discussed above (Figure 4.16 and Table 8.24). The most abundant ion corresponds to LLi^+. This ion is superimposed by a second species, however. Careful inspection of the isotope pattern (Figure 8.60) as well as gas-phase fragmentation experiments (Figure 8.61) identify this second species as $(ArBu)_2Li^+$. This complex consists of Li^+ and two molecules of the cross-coupling product.

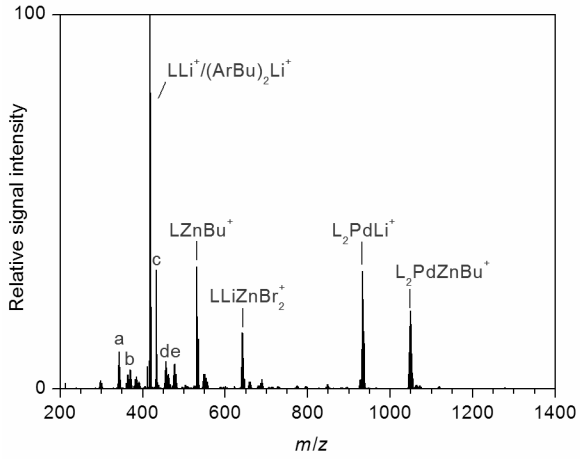

Figure 4.16. Positive-ion mode ESI mass spectrum of a solution of $Pd(OAc)_2$ (3 mM), S-PHOS (L, 6 mM), BuZnBr·LiBr (15 mM), and ArI (*p*-EtOOC-C_6H_4-I, 3 mM) in THF (a = $Li_3ZnBr(OAc)_3^+$, b = $Li_2ZnBr_2(OAc)(THF)^+$, c = $(LO)Li^+$, d = $Li_3ZnBr_3(OAc)(THF)^+$, e = $Li_3ZnBr_4(THF)^+$).

If the catalyst concentration is lowered to the μmolar range, the reaction is slowed down to such an extent that the increase of $(ArBu)_2Li^+$ in time can be monitored (Figure 8.62). As expected, the reaction becomes faster for higher catalyst loadings, but the signal/noise ratio of the obtained data is too poor for a rigorous quantitative analysis; such behavior is typical for ESI mass-spectrometric experiments,[27q] although favorable exceptions are known.[98i, 139] In the negative-ion mode ESI mass spectrum, only zincate ions are detected (Figure 8.63 and Table 8.25).

4.2.7 Mechanistic implications

The present ESI mass-spectrometric experiments reveal an unexpected diversity of Pd species formed in the reaction mixtures and, thus, corroborate the findings both of the ^{31}P NMR-spectroscopic and kinetic measurements.[126] Unlike ^{31}P NMR and UV/Vis spectroscopy, ESI mass spectrometry affords more direct insight into the microscopic speciation. First, the formation of cationic $L_2Pd_2X^+$ complexes (X = Br, I, OAc, PCy_2) is of interest because these Pd(I) dimers (alternatively described as mixed Pd(0)/Pd(II) species, see Figure 4.3) might be considered the onset of aggregation and the formation of nanoclusters, eventually resulting in the precipitation of Pd black.[92] The simultaneous observation of the low-valent

$(LO)Pd_3(PCy_2)(OAc)_2^-$ trimer seems to support this rationale as does the UV/Vis-spectroscopic evidence for the formation of Pd nanoclusters. However, the Pd dimers completely vanish upon addition of the organozinc reagent. This finding indicates that their formation is reversible under real catalytic conditions and that they do not easily undergo further aggregation; Pfaltz and coworkers came to a similar result.[95g]

Moreover, Pd dimers are successfully used as precatalysts.[99-100, 140] Accordingly, the formation of Pd dimers does not appear to be a major pathway of catalyst degradation.

The catalyst deactivation presumably takes place via the decomposition of S-PHOS ligand. The observation of Pd-bound PCy_2 groups proves the occurrence of C−P bond activation processes, which have also been reported in the literature for similar systems.[98g, 141] The increase of the signal intensity of $L_2Pd_2(PCy_2)^+$ in time indicates that the C−P bond cleavage is irreversible. This decomposition reaction could therefore explain the modest decrease in reactivity observed for longer incubation times of $Pd(OAc)_2$/2 S-PHOS solutions.

The addition of LiBr apparently counteracts the degradation of the ligand; the molecular origin of this effect remains unclear, however. Certainly, the protection of the ligand against degradation contributes to the beneficial role of LiBr in Pd-catalyzed Negishi cross-coupling reactions but cannot fully account for it. The kinetic measurements have shown that the later addition of LiBr largely restores the catalytic activity.[126] Such behavior is hardly compatible with the irreversible decomposition of the S-PHOS ligand.

The fact that no Pd dimers are observed upon addition of the organozinc reagent possibly suggests that the former are consumed in a reaction with the latter. The detection of the heterobimetallic dimers L_2PdZnR^+ (R = Bu, Ph, Bn) fully agrees with this hypothesis. Interestingly, these species remarkably resemble their homobimetallic $L_2Pd_2X^+$ counterparts: both complexes can be considered to result from the combination of an electron-rich Pd(0) moiety with a Lewis-acidic M(II) cation. As Zn(II) is more Lewis-acidic than Pd(II),[142] the heterobimetallic complex should be more stable and prevail, in line with the experiment; note that the higher concentration of the organozinc reagent also favors the formation of L_2PdZnR^+. Under real catalytic conditions, the excess of the RZnX reagent will be even higher and so the equilibrium will be further shifted toward L_2PdZnR^+ and the corresponding neutral species, i.e., $L_2PdZn(R)X$. Moreover, the observation of heterobimetallic Pd-Zn complexes for all three sampled RZnBr·LiBr reagents and for both phosphines indicates that their formation is quite a general phenomenon (no analogous species are detected for the PEPPSI-IPr precatalyst, but here the extreme predominance of protonated species in the positive-ion mode ESI mass spectrum may bias the analysis). A notable exception from this rule seems to be the $Pd(OAc)_2$/2

S-PHOS/$ZnBr_2$·LiBr system, for which no $L_2PdZnBr^+$ is observed. We do not see an obvious reason why heterobimetallic Pd-Zn complexes should not form in this case. Possibly because of the increased Lewis acidity of $L_2PdZnBr^+$ a Br^- anion binds to the complex and the resulting neutral species cannot be observed by ESI mass spectrometry.

The apparently ready formation of Pd-Zn complexes most likely also affects the activity of the Pd catalyst and, in particular, the oxidative addition. First, the reactivity of L_2PdZnR^+ as well as that of its neutral counterpart $L_2PdZn(R)Br$ toward aryl halides are expected to depend on the nature of the organyl group. Furthermore, the equilibrium concentrations of these species presumably also differ upon variation of R. The kinetic measurements discussed in Chapter 3 actually found markedly different reaction rates for the cross-coupling of ArI with BnZnBr·LiBr, BuZnBr·LiBr, and PhZnBr·LiBr and, at the same time, identified the oxidative addition as rate-limiting step.[126] These results could not be reconciled within in the concept of the conventional catalytic cycle, but they are rationalized if the involvement of Pd-Zn complexes is taken into account.[143] Quantum-chemical calculations predict that the association of $Pd(PMe_3)_2$ with MeZnCl(THF) significantly slows down the oxidative addition.[70] Possibly an analogous effect could also explain the bimodal behavior observed in the kinetic measurements. In these experiments, the reaction was started by adding a solution of the catalyst to a mixture of ArI and RZnBr·LiBr in THF and found an extremely fast conversion in the initial phase.[126] This extremely fast reaction progress could possibly reflect the exclusive presence of free and more reactive LPd complexes (L = S-PHOS) just after the addition of the catalyst solution. At longer times, the LPd complexes should be largely consumed due to the formation of the Pd-Zn dimers. To test this hypothesis, control experiments were performed, in which the catalyst and BuZnBr·LiBr in THF were premixed and started the reaction by the addition of ArI. Under these conditions, the Pd-Zn complexes should be present from the very beginning on. Indeed, slower reactions are consistently observed although the magnitude of the effect varies to some extent (Figure 4.17, Figure 4.18 and Figure 4.19).[144] Although this finding supports our hypothesis, the control experiments themselves now also exhibit bimodal behavior, with a slower initial and a faster later reaction. The origin of the apparent induction period is unclear. Nonetheless, it remains a striking result that a simple change in the order of addition of the reaction partners strongly influences the reaction rate.

Assuming that $ZnBr_2$ gives rise to (neutral) Pd-Zn dimers as well, the involvement of such complexes also explains the observed rate-decreasing effect of this additive.[27p, 65, 126] In this context, it is also worth considering the role of $ZnBr_2$ generated as byproduct of the reaction; like extra added $ZnBr_2$, it is supposed to slow down the reaction. As the formation of each

$ZnBr_2$ molecule consumes one RZnBr molecule, the concentration of Zn(II) species that can coordinate to LPd does not change in the course of the reaction. Therefore, the overall effect of the newly formed $ZnBr_2$ probably is not overly large.

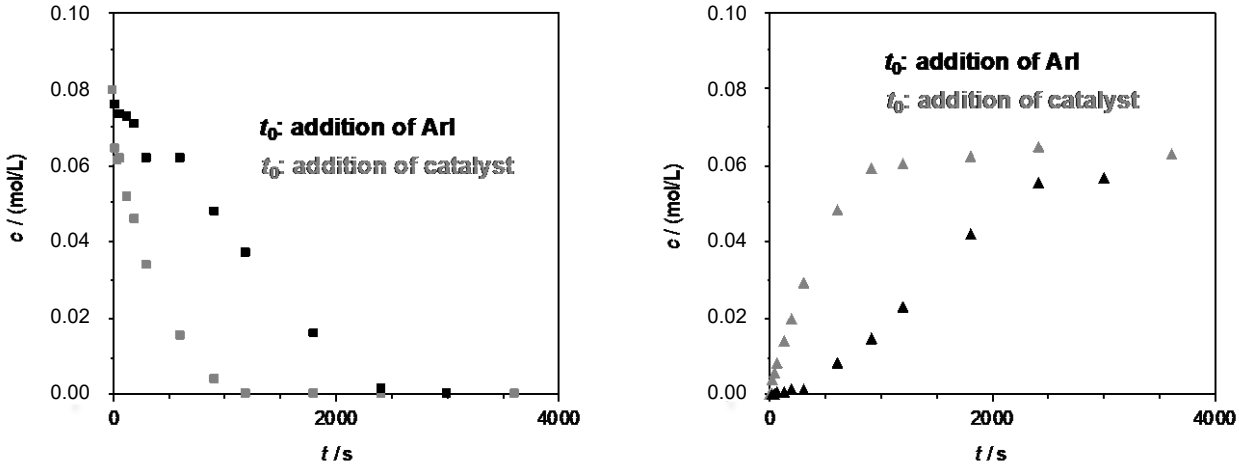

Figure 4.17. Time profiles of the concentration of the cross-coupling product ArBu formed upon reaction of ArI (0.10 M) with BuZnBr·LiBr (0.40 M) in THF at 298 K (precatalyst: $Pd(OAc)_2$/2 S-PHOS, $2 \cdot 10^{-5}$ M) with the reaction partners added in different order.

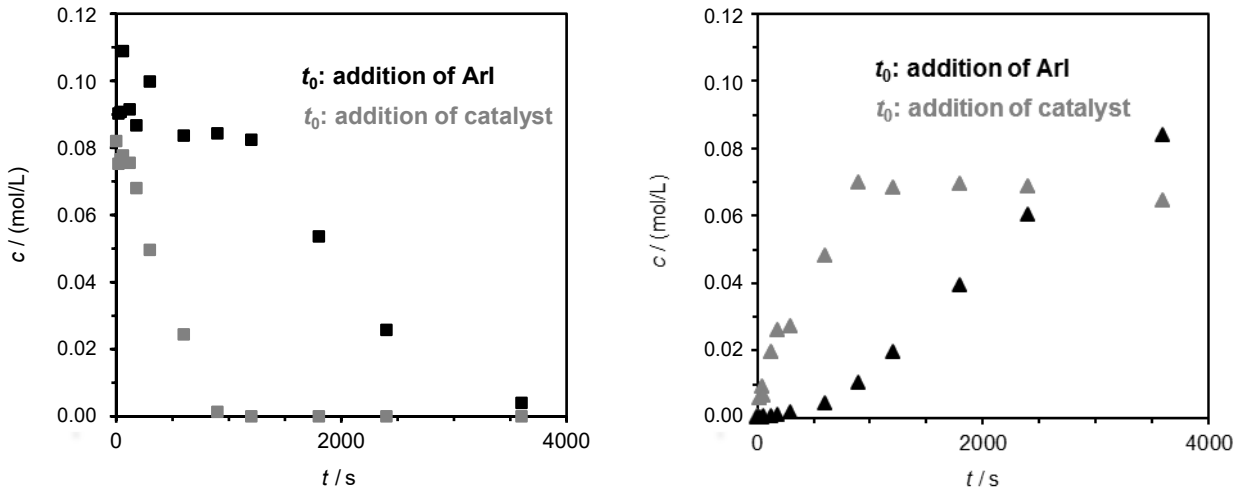

Figure 4.18 Time profiles of the concentration of reactant ArI (left) and of the cross-coupling product ArBu (right) formed upon reaction with BuZnBr·LiBr (0.40 M) in THF at 298 K (precatalyst: $Pd(OAc)_2$/2 S-PHOS, $2 \cdot 10^{-5}$ M) with the reaction partners added in different order (repetition run 1).

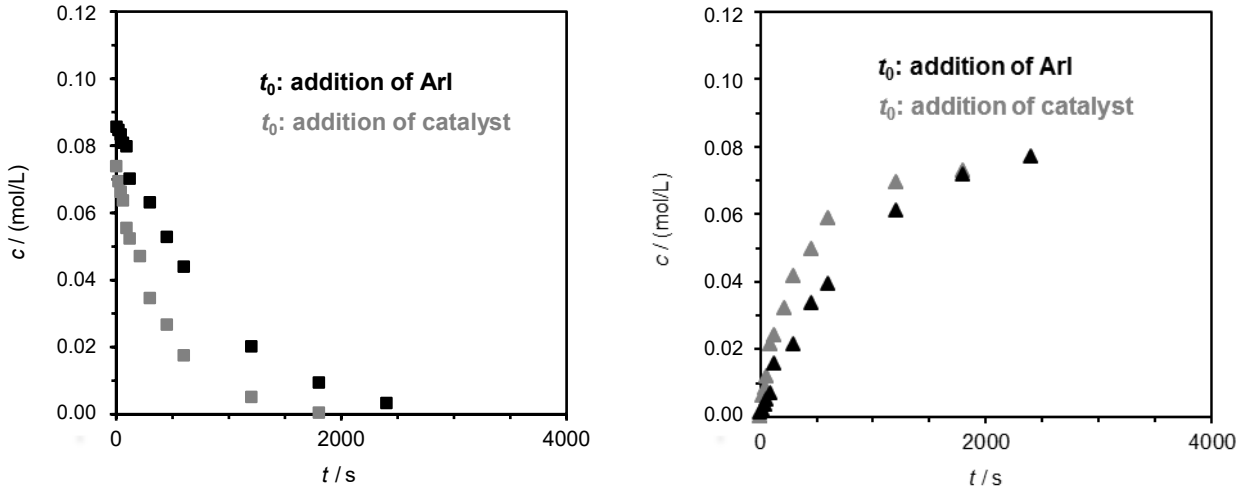

Figure 4.19 Time profiles of the concentration of reactant ArI (left) and of the cross-coupling product ArBu (right) formed upon reaction with BuZnBr·LiBr (0.40 M) in THF at 298 K (precatalyst: $Pd(OAc)_2$/2 S-PHOS, $2 \cdot 10^{-5}$ M) with the reaction partners added in different order (repetition run 2).

In the case of LiBr, the situation is more complex. Apart from its apparent role in protecting the S-PHOS ligand against degradation (see above), the ESI mass-spectrometric experiments do not give any direct clue why it strongly enhances the cross-coupling efficiency.[27p, 27s, 54, 62, 65, 126] It is assumed that LiBr must act upon the oxidative addition, which under the present conditions is the rate-limiting step according to these kinetic measurements.[126]

Koszinowski[27h, 27i, 27r, 55b] and others [27s, 54, 56, 57, 145] have established the tendency of RZnX reagents (and ZnX_2) to add halides anions and form the corresponding zincate anions. The negative-ion mode ESI mass spectra presented also show many zincate anions. Most of these zincate anions, however, are purely inorganic (see above).

Compared to neutral RZnX species, organozincate anions have a drastically reduced Lewis acidity. It is therefore likely that they cannot simply be combined with electron-rich Pd(0) to form heterobimetallic Pd-Zn complexes.

This would explain why more free LPd can be observed in the presence of LiBr. However, it is very difficult to find support for this hypothesis in the experiments. The ESI mass-spectrometric measurements detect $L_2PdZnBu^+$ both in the absence and presence of LiBr and the comparison of absolute or relative signal intensities between different samples is notoriously difficult.

As an alternative rationalization for the effect of LiBr, the involvement of Pd(0) ate complexes in the present experiments was also considered.[51, 63b] The coordination of a Br^- ion to an LPd complex enhances the electron density of the latter, thus possibly also increasing its affinity toward Lewis-acidic RZn^+ or RZnBr species. The concomitant saturation of a vacant coordination site on Pd(0) supposedly lowers its tendency toward further association reactions, however. In the second case, the Pd(0) ate complexes could also counteract the formation of Pd-Zn dimers.

The presence of heterobimetallic Pd-Zn species in Negishi cross-coupling reactions is also very interesting in another respect. These complexes contain both low-valent Pd and an organozinc moiety. Perhaps the elementary steps, the oxidative addition and the transmetalation, do not occur one after the other but in a more concerted manner. It is possible that the order of the elementary steps can be reversed. This alternative route would start with transmetalation and be followed by oxidative addition. Terao and Kambe have suggested mechanisms of this type in a related context.[145] Gas-phase fragmentation experiments demonstrate that the organyl group R of the L_2PdZnR^+ complexes can indeed be transferred to the Pd center, eq. 4.2c, 4.3c, and 4.4b, respectively (also see Scheme 8.1). In the course of this reaction, the Pd adopts an oxidation state of + II and would therefore no longer tend to oxidative addition.

5 Reactivity enhancement of aryl bromides in the presence of aryl iodides

5.1 Introduction

Aryl halides are frequently used in synthesis reactions as substitution targets. In common cross-coupling reactions, aryl iodides and also bromides are used for synthetic applications. The aryl bromides and iodides are particularly common in cross-couplings; they are generally more reactive than the chlorides and fluorides, with the iodides being the most reactive.[138] However, aryl chlorides and bromides are much more readily available and easier to synthesize than the other halogen derivatives,[146] [140a] and therefore, an effective method for the conversion of aryl halide derivatives would be extremely useful. In this way, one could take advantage of the higher reactivity of aryl iodides and the lower cost of aryl bromides and chlorides. Sheppard suggested an alternative for Finkelstein halogen exchange at aromatic compounds, a reaction catalyzed by a transition metal.[138] To date, there have been few reports of aromatic halogen exchange in the literature on transition metal-catalyzed cross-coupling reactions, particularly with palladium. More investigations have been reported on analogous reactions that use copper or nickel catalysis.[138, 147] Currently, research is focused on the development of ligands and reaction conditions of the palladium cross-coupling reactions. In this way, reactions with less reactive aryl chlorides should also be possible. [138, 148]

Schoenebeck et al. studied the replacement of the halogen in a bromide-containing palladium(I) dimer with aryl iodide by experimental and theoretical studies. “9-Iodoanthracene was found to be the most reactive, with 92% conversion to 9-bromoanthracene after 3 hours, with concomitant formation of the palladium(I) iodide dimer.” (Scheme 5.1) [99]

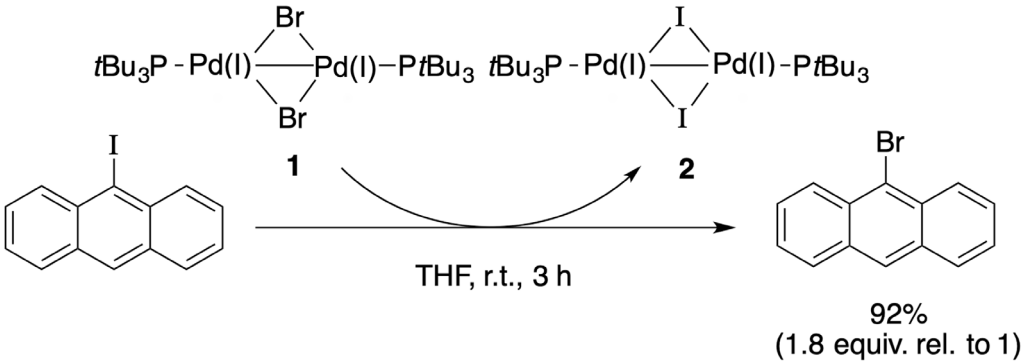

Scheme 5.1 Halogen exchange at 9-iodoanthracene to 9-bromoanthracene in presence of Pd(I)-Br-dimer

They excluded the involvement of Pd(0)/Pd(II) and monomeric Pd(I) radical in this mechanism experimentally and conclude that the reaction takes place at palladium(I) dimer. Until this time, oxidative addition to palladium dimers had not been studied computationally. The data obtained strongly suggests that the aromatic halogen exchange process occurs by direct oxidative addition at the intact palladium(I) dimer.

5.2 Results and Discussion

To compare the reactivity of the electrophiles in the model reaction, ethyl 4-iodobenzoate (ArI) with BuZnBr·LiBr in THF (Scheme 3.1) with other electrophiles, the reaction of ethyl 4-bromobenzoate (ArBr) and BuZnBr·LiBr under analogous condition was studied (Scheme 5.2). This has already been discussed in chapter 3 (Figure 3.17). The experiment indicated that at standard concentration (precatalyst $5 \cdot 10^{-5}$ M), only a small conversion is observed and the concentration of the precatalyst has to be increased. ArBr was found to be less reactive in the oxidative addition, which was determined to be the rate-limiting step. (see chapter 3)

To start the reaction, a 1:2 mixture of the precatalyst $Pd(OAc)_2$[90a] ($1 \cdot 10^{-3}$ M) and the sterically demanding phosphine S-PHOS[105] as ligand were added. The organozinc reagent was employed in four-time excess relative to the ArBr.

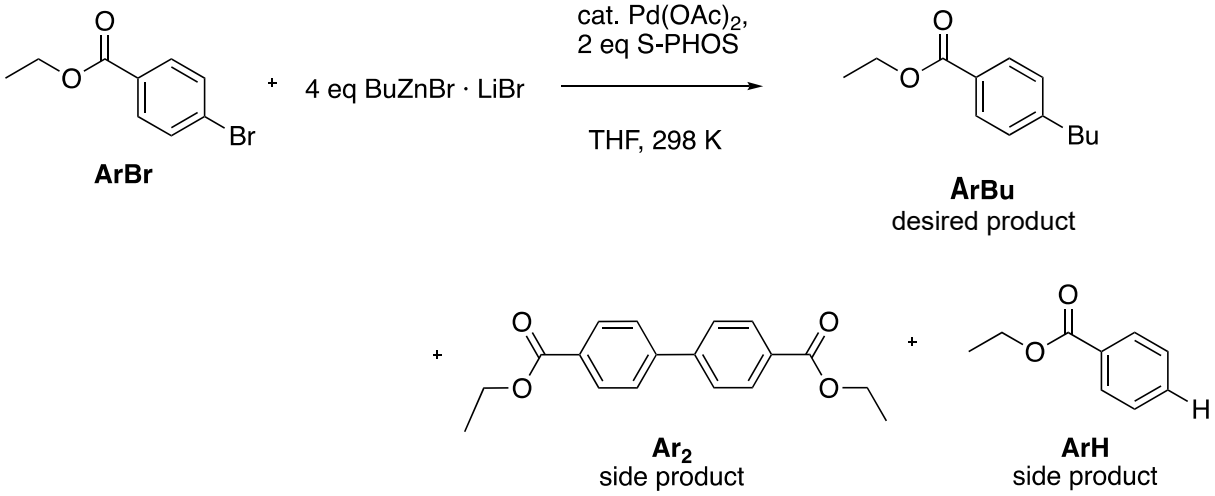

Scheme 5.2 Reaction of ethyl 4-bromobenzoate (ArBr) with BuZnBr·LiBr in THF at room temperature gives the desired cross-coupling product ethyl 4-butylbenzoate (ArBu) and the side products ethyl benzoate (ArH) and biphenyl-4,4'-dicarboxylic acid diethyl ester (Ar_2).

The reaction of ArBr with BuZnBr·LiBr in presence of the $Pd(OAc)_2$/2 S-Phos results in negligible conversion of ArBr to ArBu. (precatalyst $5 \cdot 10^{-5}$ M data not shown) However, if Ar´I is added to the above reaction under otherwise identical conditions (Scheme 5.3), a significant enhancement of the rate of production of ArBr is observed. (Figure 3.18)

The halogen exchange phenomenon is demonstrated by the experiment shown in Scheme 5.3.

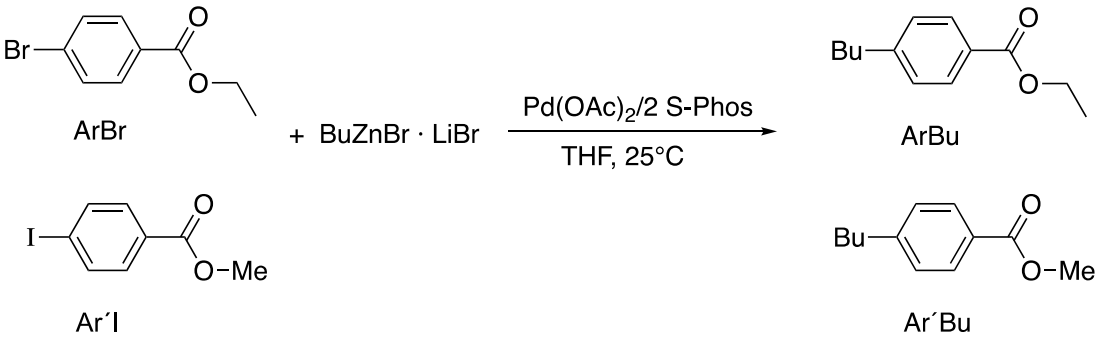

Scheme 5.3 Reaction of ethyl 4-bromobenzoate (0.1 M, ArBr) and methyl 4-iodobenzoate (0.1 M, Ar´I) with BuZnBr·LiBr (0.4 M) and the precatalyst $Pd(OAc)_2$/2 S-Phos ($5 \cdot 10^{-5}$ M) to cross-coupling products ethyl 4-butylbenzoate (ArBu) and methyl 4-butylbenzoate (Ar´Bu).

Methyl 4-iodobenzoate (Ar´I) is used for investigations on the influence of iodide compounds on the rate of the cross-coupling reactions. Structurally, methyl 4-iodobenzoate and ethyl 4-bromobenzoate differ only by the halogen and by the ester group. The latter is necessary to differentiate between the products methyl 4-butylbenzoate and ethyl 4-butylbenzoate.

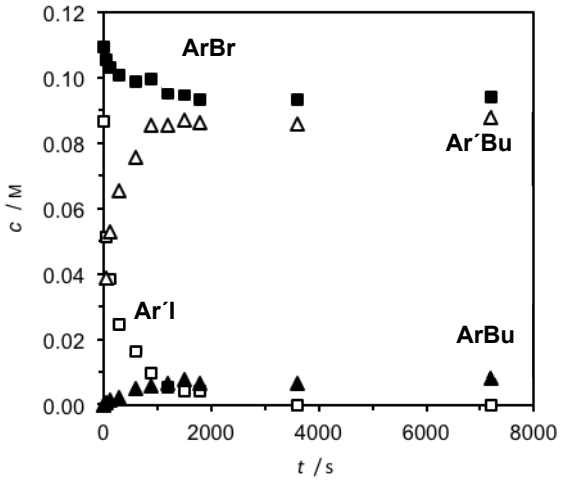

Figure 5.1 Time profiles of the concentrations of reactant ethyl 4-bromobenzoate ArBr (■, 0.1 M) and methyl 4-iodobenzoate Ar´I (□, 0.1 M) reacting to the cross-coupling product ethyl 4-butylbenzoate ArBu (▲) and methyl 4-butylbenzoate Ar´Bu (△) formed upon reaction with BuZnBr·LiBr (0.40 M) in THF at 298 K (precatalyst: $Pd(OAc)_2$/2 S-PHOS, $5 \cdot 10^{-5}$ M).

Further experiments shows that in presence of the methyl 4-iodobenzoate (Ar´I), the conversion of ethyl 4-bromobenzoate (ArBr) with BuZnBr·LiBr is enhanced. (Figure 5.1)

The activating effect becomes more obvious when Ar´I is added with a delay relative to the start of the reaction by adding the catalyst mixture. Using the standard precatalyst loading ($5 \cdot 10^{-5}$ M) only low conversion of ethyl 4-bromobenzoate is observed. Due to the addition of methyl 4-iodobenzoate the conversion of ethyl 4-bromobenzoate is accelerated.

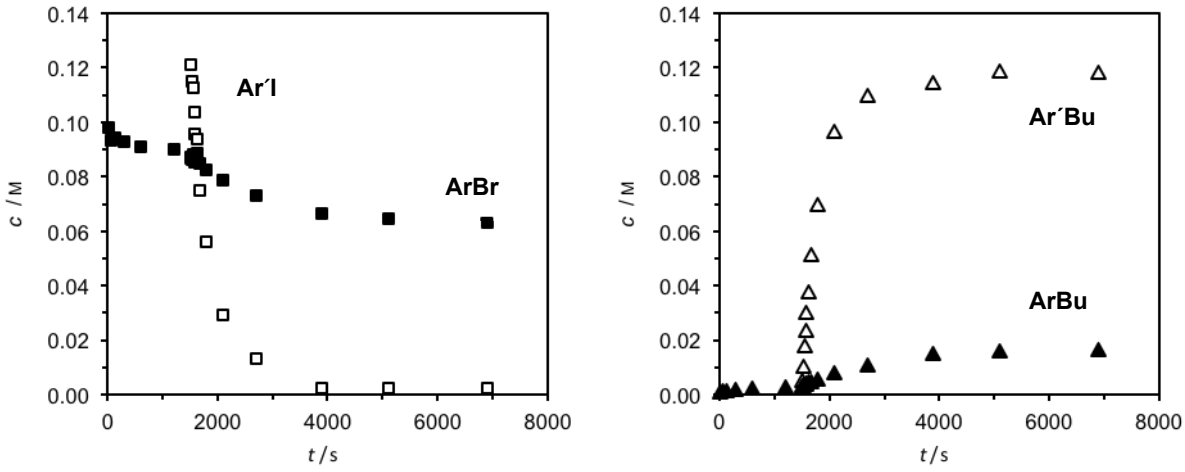

Figure 5.2 Left: Time profiles of the concentrations of the electrophiles ethyl 4-bromobenzoate ArBr (■, 0.1 M) and methyl 4-iodobenzoate Ar´I (□, 0.1 M) reacting with BuZnBr·LiBr (0.40 M) in THF at 298 K (precatalyst: $Pd(OAc)_2$/2S-PHOS, $5 \cdot 10^{-5}$ M) forming the products. Right: Time profiles of the concentrations of the products ethyl 4-butylbenzoate ArBu (▲) and methyl 4-butylbenzoate Ar´Bu (△).

To exclude transesterification as origin of the observed phenomenon, ArBr and Ar´I are mixed with the precatalyst, $Pd(OAc)_2$ and S-Phos and found that no mixed aryl halogen like ArI or Ar´Br is formed. Analogous experiments excluded the possibility that salt effects like LiBr and $ZnBr_2$ enable an exchange of the ester group. These experiments show no halogen exchange or transesterification in the absence of an organozinc compound (data not shown).

The phenomenon, that an iodo compound accelerates the reaction of a bromo compound, could open a new way. Maybe this observation is the first step to accelerate the cross-coupling reaction of less reactive aryl bromides by the addition of an iodine source. Therefore, it is investigated whether other sources of iodine have a similar effect.

Furthermore, phenyl iodide is chosen as representative electrophile for variable aryl iodide compounds. To the reaction of ethyl 4-bromobenzoate with BuZnBr·LiBr (0.40 M) catalyzed by $Pd(OAc)_2$/2S-PHOS ($5 \cdot 10^{-5}$ M), phenyl iodide (0.1 M) is added. This reaction gives ethyl 4-butylbenzoate in a yield of 10% and phenyl butane in 80%. Also, phenyl iodide is able to

accelerate the rate of the reaction of ethyl 4-iodobenzoate. The total consumption of phenyl iodide stops at 90% conversion.

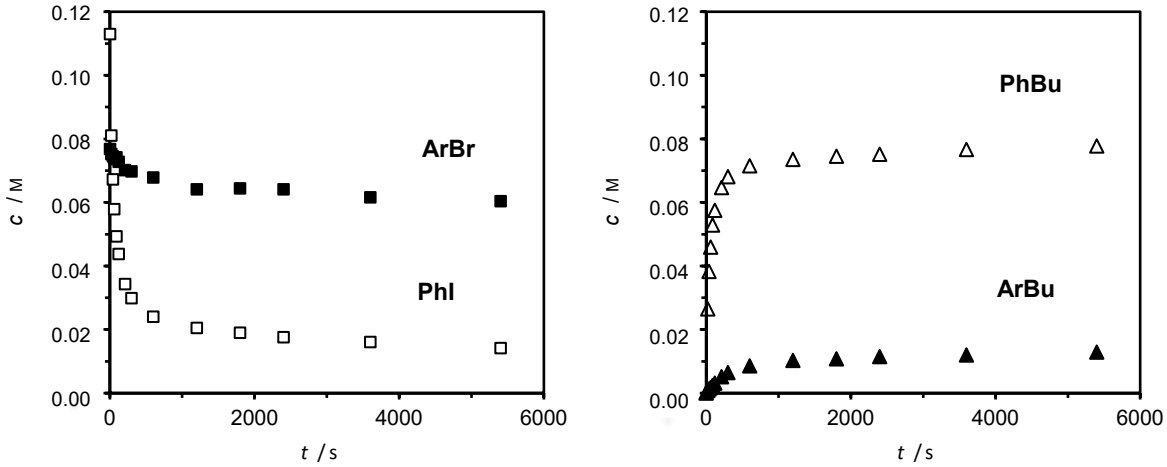

Figure 5.3 Left: Time profiles of the concentrations of ethyl 4-bromobenzoate ArBr (■, 0.1 M) and phenyl iodide PhI (□, 0.1 M) reacting with BuZnBr·LiBr (0.40 M) in THF at 298 K (precatalyst: $Pd(OAc)_2$/2 S-PHOS, $5 \cdot 10^{-5}$ M) formed the products. Right: Time profiles of the concentrations of the products ethyl 4-butylbenzoate ArBu (▲) and phenyl butane PhBu (△).

To investigate the effect on the rate of the reaction by aryl iodide compounds, other iodine sources like iodine and methyl iodide are also tested. Reaction conditions analogous to those employed in the reaction of the ethyl 4-bromobenzoate with BuZnBr·LiBr and precatalyst $Pd(OAc)_2$/2 S-PHOS are used. The added iodine and methyl iodide have not a significant effect on the rate of the cross-coupling reaction (data not shown).

On the basis of the observations discussed above, the mechanisms shown in Scheme 5.4 and Scheme 5.5 for the halogen exchange reaction with monomeric (Scheme 5.4) or dimeric (Scheme 5.5) palladium are suggested.

Path A in Scheme 5.4 shows one possible but limited appropriate way for the conversion of ethyl 4-bromobenzoate (ArBr) which is accelerated due to the addition of methyl 4-iodobenzoate (Ar´I). In the first step, the reactive monoligated palladium complex (PdL) reacts in oxidative addition with the bromide electrophile. The formed palladium(II) complex **I** reacts with the organozinc compound. The dehalogenated product and the homocoupling product are

formed by side reactions analogous to the reactions shown in chapter 3. Due to the addition of methyl 4-iodobenzoate, a halogen exchange could occur and simultaneously one equivalent of the replaced electrophile methyl 4-bromobenzoate Ar´Br is formed.

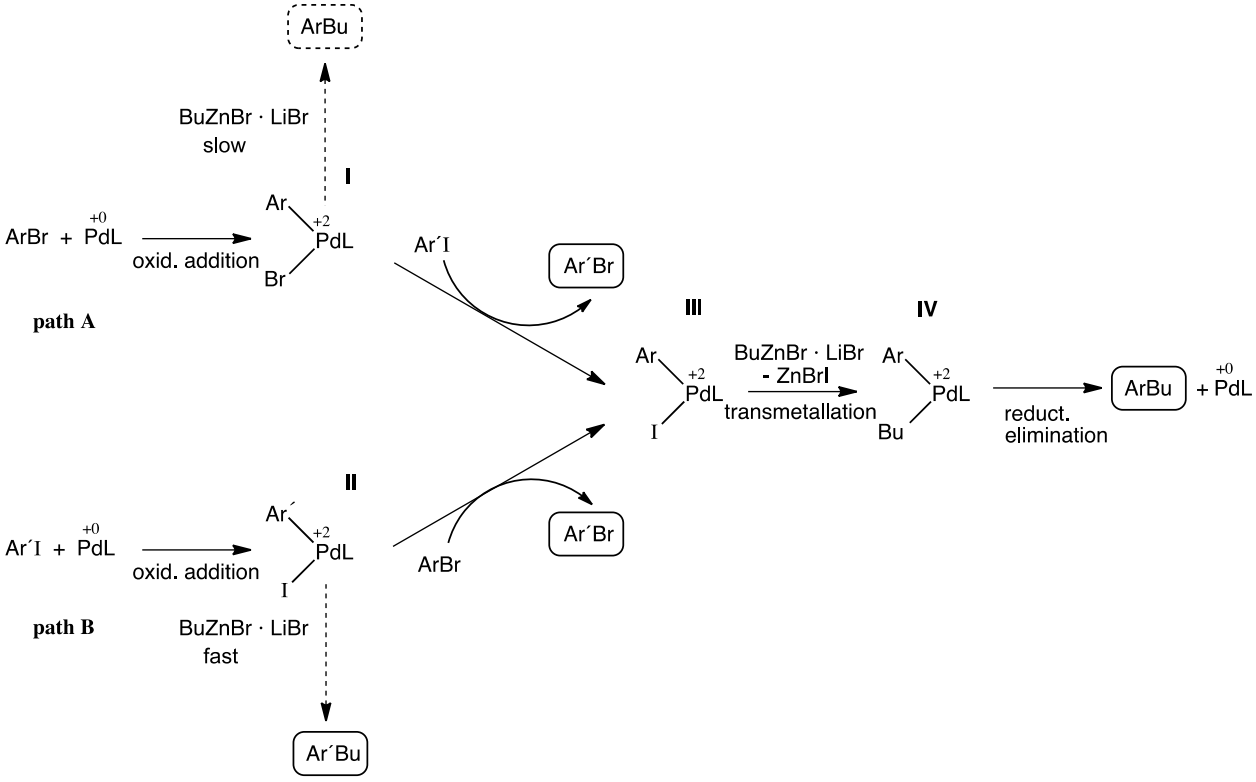

Scheme 5.4 Suggested mechanism of the halogen exchange with monomeric palladium.

The results in chapter 3 demonstrate that the oxidative addition, the rate limiting step in the Negishi cross-coupling reaction, is decelerated if ArBr (Figure 3.17 and 3.18) is used and accelerated if ArI is used. These findings are in contradiction to an oxidative addition of ArBr in the first step of the Negishi cross-coupling reaction to form the palladium(II) complex **I**. Consequently, it is more likely that methyl 4-iodobenzoate (Ar´I) is reacting in the first step with palladium catalyst as demonstrated in path B (Scheme 5.4) and forms palladium(II) complex **II**.

In both paths A and B Ar´ is exchanged with Ar. The formed palladium(II) complex **III** reacts with BuZnBr·LiBr in transmetalation and produces via palladium(II) complex **IV** the main product methyl 4-butylbenzoate (Ar´Bu). It is conceivable that a minor amount reacts with the ethyl 4-bromobenzoate and performs an exchange of the aryl group. The palladium(II) complex

III is formed, which contains the ethyl benzoate and the iodide group (ArPdLI). During transmetalation with BuZnBr·LiBr palladium(II) complex **IV** (ArPdLBu) is produced which forms in the reductive elimination ethyl 4-butylbenzate (ArBu). In both routes A and B, one equivalent of the replaced aryl halide (Ar´Br) should be formed, but this cannot be observed. This is not in accordance with the data of the experiment.

Likewise, the mechanism could also occur over a dimeric palladium complex as suggested by Schoenebeck at al.[99] (Scheme 5.5)

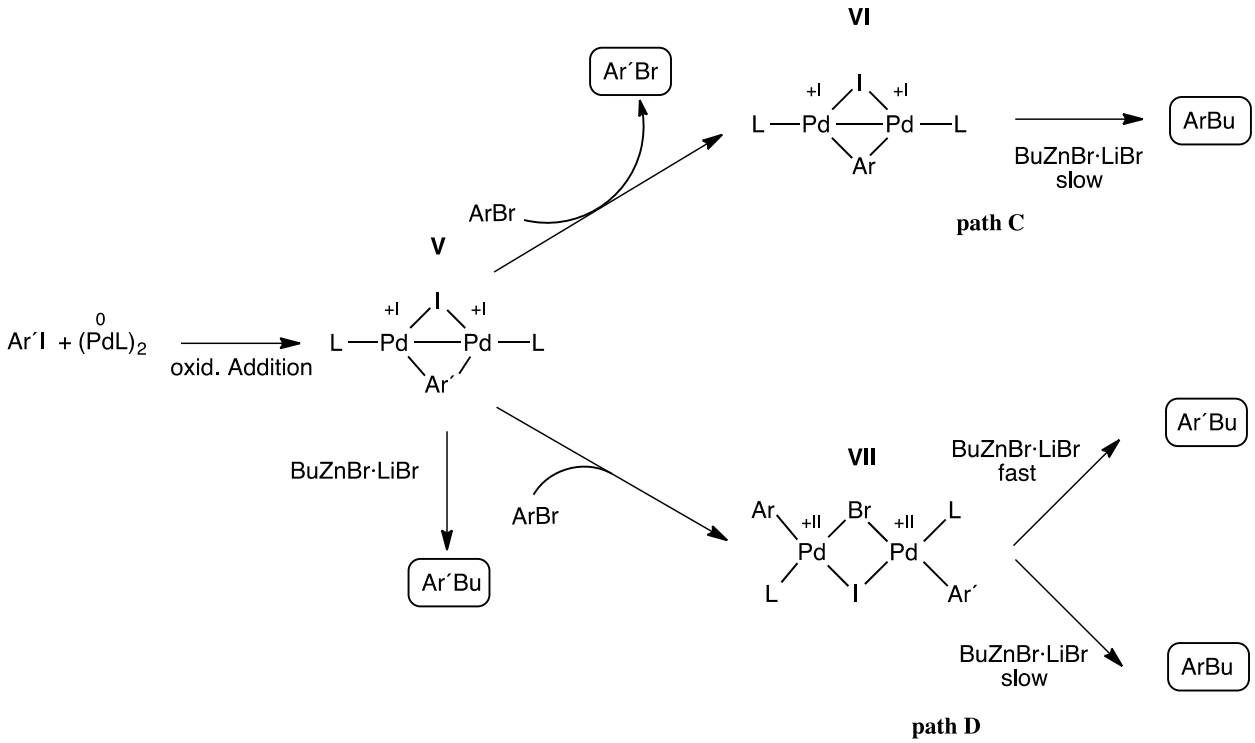

Scheme 5.5 Suggested mechanism of the halogen exchange with dimeric palladium

In the oxidative addition the more reactive Ar´I forms a palladium(I) dimer **V** with the dimeric palladium catalyst. It is believed that ArBr reacts faster with palladium(I) dimer **V** than with the other low-valent Pd species considered. The palladium(I) dimer **V** can react in two ways. Path C illustrates the exchange of the aryl group. Ethyl 4-bromobenzoate reacts with the complex and one equivalent of the replaced aryl halogen Ar´Br should be released, but the formation of the replaced aryl halogen is against the findings from the experimental data from this work.

In path D the palladium(I) complex **V** reacts with one additional equivalent of ethyl 4-bromobenzoate and forms a palladium(II) dimer **VII**. By transmetalation, ethyl 4-butylbenzoate (ArBu) and methyl 4-butylbenzoate (Ar´Bu) can be formed.

On the basis of observations discussed above, it can be concluded that the mechanisms A, B and C describe the reality insufficiently, as no formation of methyl 4-bromobenzoate (Ar´Br) is observed experimentally. Path D (Scheme 5.5) correctly describes that no transformed aryl halogen is produced in the reaction.

To improve the reactivity of relatively low-priced but less reactive aryl bromide compounds by adding an iodide, would be of great synthetic interest. Further experiments were designed to investigate whether adding small portions of the aryl iodide can enhance the yield of the cross-coupling product.

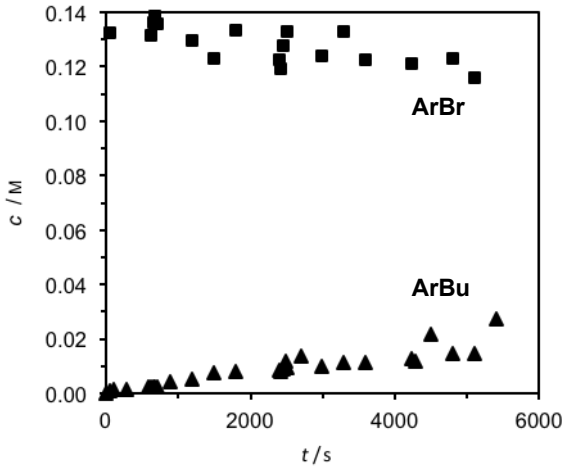

Figure 5.4 Time profile of the concentrations of electrophile ethyl 4-bromobenzoate ArBr (■, 0.1 M) reacting with BuZnBr·LiBr (0.40 M) in THF at 298 K (precatalyst: $Pd(OAc)_2$/2S-PHOS, $5 \cdot 10^{-5}$ M) and the concentration of the formed product ethyl 4-butylbenzoate ArBu (▲). 0.075 M methyl 4-iodobenzoate was added in three small portions of 0.025 M after 600 s, after 2400 s and after 4200 s over the measured period.

Possibly the conversions of bromide electrophiles do not depend on the quantity of the added iodide compound, but on the reaction time.

In the following, it is checked whether the time of the reaction of methyl 4-iodobenzoate has an influence on the amount of ethyl 4-bromobenzoate reacted. 0.075 M methyl 4-iodobenzoate is added in three small portions over the measured period. After 600s, after 2400s and after 4200, once each 0.025 M (data not shown) are added repeatedly to the reaction mixture of ethyl 4-bromobenzoate with BuZnBr·LiBr and precatalyst ($Pd(OAc)_2$/2S-Phos, $5 \cdot 10^{-5}$ M).

Unfortunately, the total yield of the ArBu is approximately the same, no matter if the iodide compound is added in small portions or at once. Figure 5.4 shows the concentrations of the reactant ethyl 4-iodobenzoate (ArBr) and the cross-coupling product ethyl 4-butylbenzoate (ArBu). For simplification the concentrations of methyl 4-iodobenzoate and the corresponding cross-coupling product methyl 4-butylbenzoate are not shown in Figure 5.4. Presumably, the conversion of the bromide electrophile directly depends on the conversion of the iodide electrophile and cannot be increased by longer reaction times of the aryl iodide.

6 Anionic Pd^0 and Pd^{II} ate complexes [e]

6.1 Introduction

A combination of electrospray ionization (ESI) mass spectrometry, electrical conductivity measurements, and multi-nuclear NMR spectroscopy are used to characterize anionic Pd^0 and Pd^{II} ate complexes. ^{31}P NMR spectroscopy is widely used for the analysis of Pd phosphine complexes.[29-30, 51a, 63b, 79a, 79c, 90a, 90c, 90d, 90k] The ESI mass spectrometry and the electrical conductivity measurements are capable to detect charged species. Therefore, they are particularly well-suited to address the present problem at hand. ESI mass spectrometry moreover has the advantage to afford stoichiometrically well-defined information and to permit coupling with gas-phase techniques.[27q, 89, 95c, 95f, 98b, 98f, 98h, 98i, 98l, 126, 149] Especially the existence of palladium ate species is an interesting point that has been discussed in the literature for years.[51a]

6.2 ESI mass spectrometry of Pd^0 ate complexes [f]

Initial experiments probe millimolar solutions of $[Pd(PPh_3)_4]$ and $Pd(OAc)_2$/2 S-PHOS respectively, with an excess of LiBr or LiBr/BuZnBr (5 eq.) in THF by ESI mass spectrometry, but do not find any Pd^0 ate complexes. If such complexes form in solution to a significant extent, they are apparently not sufficiently stable to survive the ESI process. It is concluded that the Pd^0 ate complexes can be stabilized by lowering their electron density. To this end, the ligand is exchanged for the electron-poor phosphine L_F. The resulting Pd complex $[Pd(L_F)_3]$ is already known as an active catalyst in cross-coupling reactions.[150, 151]

[e] Some of the schemes and text passages of this chapter have partially been published already in Lit [156]

[f] Prof. Koszinowski carried out the shown ESI mass spectrometry experiments.

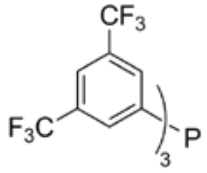

L_F

Solutions of $[Pd(L_F)_3]$ and LiBr (5 eq.) in THF give strong signals upon negative-ion mode ESI mass spectrometry (Figure 6.3).[152] The main peak observed correspond to the Pd^0 ate complex $[(L_F)_3PdBr]^-$; in addition, the ions $[(L_F)_2PdBr]^-$, $[(L_F)_3Pd_2Br_3]^-$, and $[(L_F)_4Pd_2Br]^-$ are detected. The latter closely resembles the dinuclear Pd^0 complex $[(PPh_3)_4Pd_2Br_2]^{2-}$ suggested by Jutand and Amatore.[51a] In all cases, the given assignments fully agree with the measured exact *m*/*z* ratios and the isotope patterns (Table 8.26, Figure 8.64, Figure 8.65, Figure 8.66 and Figure 8.67).

If LiBr is exchanged for NBu_4Br, the mononuclear complexes $[(L_F)_2PdBr]^-$ and $[(L_F)_3PdBr]^-$ can be observed. (Figure 6.1 and Table 8.27).

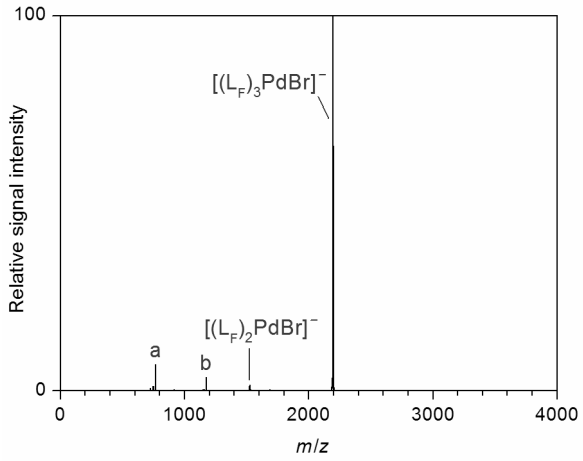

Figure 6.1 Negative-ion mode ESI mass spectrum of a solution of $[Pd(L_F)_3]$ (3 mM) and NBu_4Br (15 mM) in THF (a = $[(Ar_F)_3P(O)\cdot Br]^-$, b = $[(Ar_F)_5P_2O_3]^-$, L_F = tris[3,5-bis(trifluoromethyl)-phenyl]phosphine, Ar_F = 3,5-bis(trifluoromethyl)-phenyl).

In contrast, there is less of $[(L_F)Br]^-$, the Br^- adduct, detected when LiBr is added to the solutions of the phosphine (without Pd) (Figure 6.2 and Table 8.28).

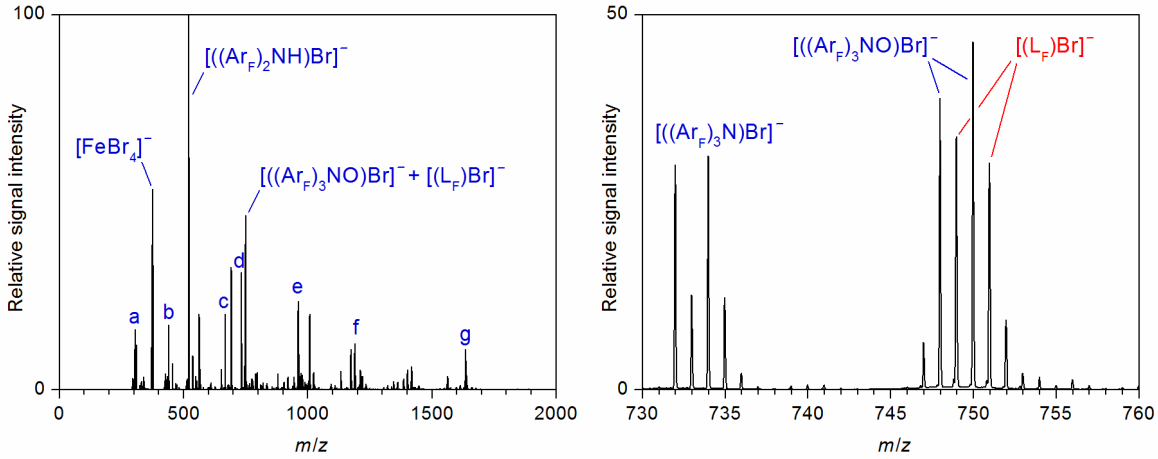

Figure 6.2 Negative-ion mode ESI mass spectrum of a solution of L_F (3 mM) and LiBr (15 mM) in THF (L_F = tris[3,5-bis(trifluoromethyl)-phenyl]phosphine, Ar_F = 3,5-bis(trifluoromethyl)-phenyl). Left: full spectrum (a = $[ZnBr_3]^-$, b = $[(Ar_F)_2N]^-$, c = $[(Ar_F)_2,(Ar_F–H),N,O]^-$, d = $[(Ar_F)_3NBr]^-$, e = $[((Ar_F)_2NH)_2Br]^-$, f = $[((Ar_F)_2NH)(Ar_F)_3NO)Br]^-$, g = $[(L_F)_2FeBr_3]^-$, right: section from the spectrum. $(Ar_F)_2NH$ and $(Ar_F)_3N$ presumably are byproducts from the synthesis of the phosphine L_F, which involves work-up with a concentrated aqueous solution of NH_4Cl.[151, 153] $[FeBr_4]^-$ and $[(L_F)_2FeBr_3)\ ]^-$ presumably result from the use of a steel capillary for the ESI process. $[ZnBr_3]^-$ presumably originates from a contamination of the ESI source.

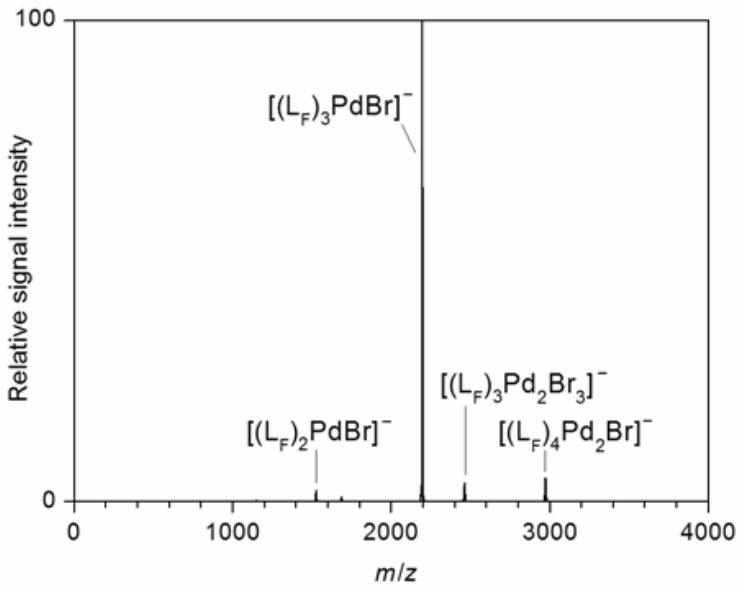

Figure 6.3 Negative-ion mode ESI mass spectrum of a solution of $[Pd(L_F)_3]$ (3 mM) and LiBr (15 mM) in THF.

This finding demonstrates that Br^- does not strongly bind to L_F. Therefore, it can be suggested that it coordinates directly to the metal center in the Pd-containing complexes. Solutions of $[Pd(L_F)_3]$ without any additive give only weak signal intensities as well (Figure 6.4 and Table 8.29).

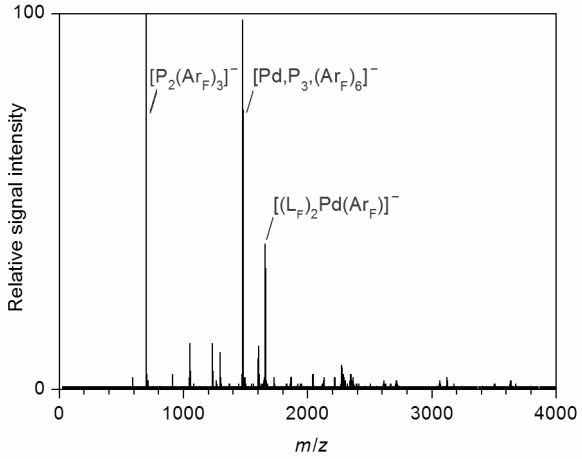

Figure 6.4 Negative-ion mode ESI mass spectrum of a solution of $[(L_F)_3Pd]$ (3 mM) in THF (L_F = tris[3,5-bis(trifluoromethyl)-phenyl]phosphine, Ar_F = 3,5-bis(trifluoromethyl)-phenyl).

Gas-phase fragmentation of mass-selected $[(L_F)_3PdBr]^-$ shows sequential losses of phosphine ligands, eq. (1) with n = 1 and 2 (Figure 6.5). Analogous reactions are also observed upon fragmentation of the other Pd ate complexes (Figure 8.68, Figure 8.69 and Figure 8.70).

$$[(L_F)_3PdBr]^- \rightarrow [(L_F)_{3-n}PdBr]^- + n\ L_F \quad (1)$$

It is found that the phosphine is split off more easily than the Br^- anion. This shows the strong interaction between the anion and the Pd center

Accordingly, it can be assumed that the complexes in solution presumably can also easily switch between different coordination states, eq. (2). However, the oxidative addition supposedly only takes place through the less coordinated complex.

$$[(L_F)_3PdBr]^- \rightarrow [(L_F)_2PdBr]^- + L_F \quad (2)$$

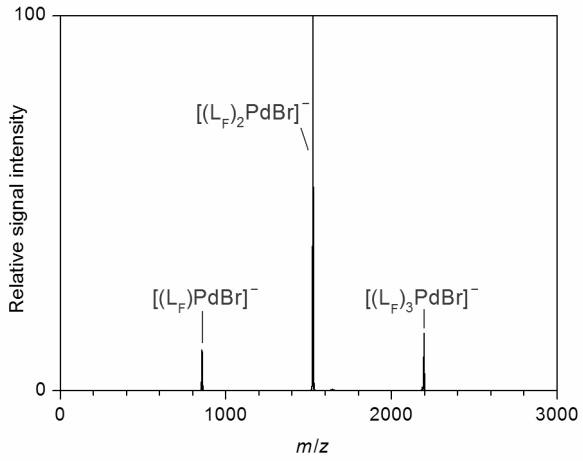

Figure 6.5 Mass spectrum of mass-selected $[(L_F)_3PdBr]^-$ and its daughter ions produced upon collision-induced dissociation (E_{LAB} = 12 eV, L_F = tris[3,5-bis(trifluoromethyl)-phenyl]phosphine).

6.3 Electrical conductivity measurements of Pd^0 ate complexes

Furthermore, electrical conductivity measurements are used for detection. A solution of $[Pd(L_F)_3]$ in THF shows a negligibly small conductivity, but it sharply increases when LiBr is added (Figure 6.6). As is already known from the literature the conductivity of LiBr in THF is very low.[27r, 154] An increase in conductivity is observed when the two components are mixed.

This reflects the formation of a new species that spontaneously yields free ions and must therefore correspond to the Pd^0 ate complex $Li^+[(L_F)_3PdBr]^-$ (and/or the related species $Li^+[(L_F)_2PdBr]^-$).

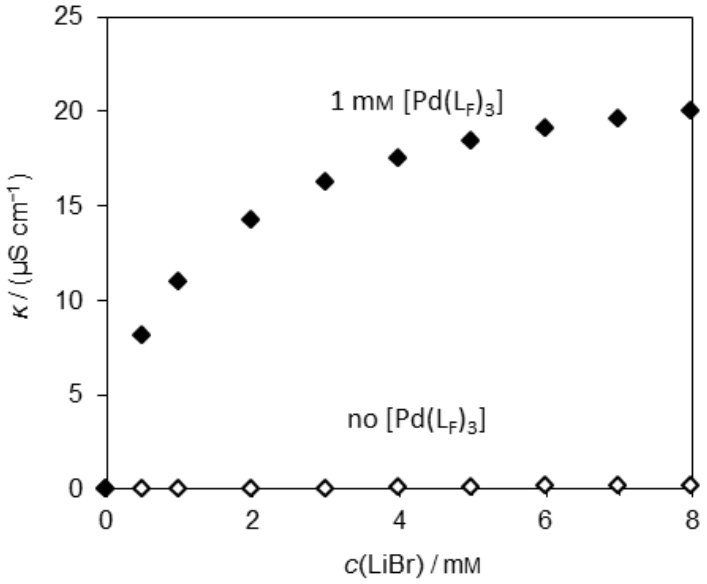

Figure 6.6 Specific electrical conductivities of a solution of $[Pd(L_F)_3]$ (c = 1 mM) with varying amounts of LiBr (filled symbols) and of solutions of LiBr in varying concentration (open symbols). Measurements taken in THF at 298 K.

The measured conductivity apparently approaches saturation at relatively low concentrations (Figure 6.6), which points to an appreciable tendency of $[Pd(L_F)_3]$ and LiBr to combine and form ate complexes.

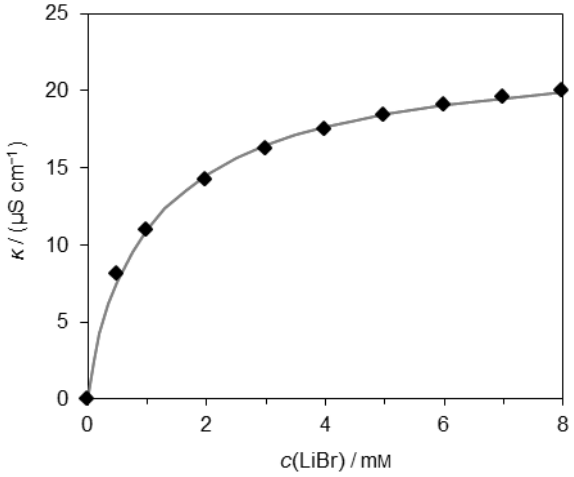

Figure 6.7 Measured specific electrical conductivities of a solution of $[Pd(L_F)_3]$ (c = 1 mM in THF, 298 K, L_F = tris[3,5-bis(trifluoromethyl)-phenyl]phosphine) with varying amounts of LiBr (filled symbols).

For the heterolytic dissociation of the resulting $Li^+[(L_F)_3PdBr]^-$ complexes, eq. (3), a relatively high tendency of the Pd(0) ate complex to form free ions is assumed.

$$Li^+[(L_F)_3PdBr]^- \rightarrow [(L_F)_3PdBr]^- + Li^+(solv) \qquad (3)$$

Analogous experiments with NBu_4Br as additive are not performed because this electrolyte, unlike LiBr, exhibits a substantial conductivity in THF. Instead, solutions of $[Pd(PPh_3)_4]$ and $Pd(OAc)_2$/2 S-PHOS are also analyzed in the absence and presence of LiBr. For both Pd complexes, the addition of LiBr results in an increase of the conductivity (Figure 6.8), but the effect is much smaller than in the case of $[Pd(L_F)_3]$.

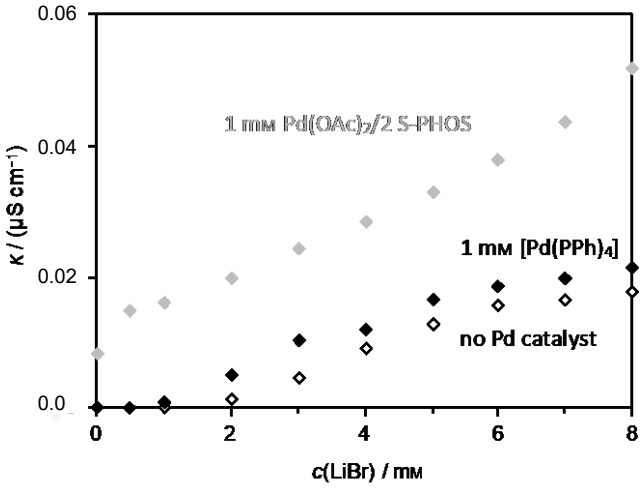

Figure 6.8 Specific electrical conductivities of solutions of $[Pd(Ph_3)_4]$ (c = 1 mM, black diamonds) and of $Pd(OAc)_2$/2 S-PHOS (c = 1 mM, grey diamonds), respectively, with varying amounts of LiBr and of solutions of LiBr in varying concentration (open diamonds). Measurements are taken in THF at 298 K.

This finding indicates that the more electron-rich Pd compounds have a lower tendency to add Br^- anions and form ate complexes, in line with the ESI-mass spectrometric results.

6.4 NMR spectroscopy of Pd^0 ate complexes[g]

Furthermore solutions of $[Pd(L_F)_3]$ in THF are investigated by NMR spectroscopy. $[Pd(L_F)_3]$ displays a sharp signal at 26.7 ppm in the ^{31}P NMR spectrum at 298 K (Figure 6.9). Upon addition of NBu_4Br, this signal is broadened considerably and shifted to 19.0 ppm. This behavior again demonstrates that the two components readily react with each other and that the formation of the Pd^0 ate complex involves a dynamic equilibrium. Upon lowering the temperature to 198 K, the dynamics stops and the signal of the free phosphine appears (Figure 6.10 and Figure 6.11).

[g] Prof. Karaghiosoff carried out the shown NMR experiments.

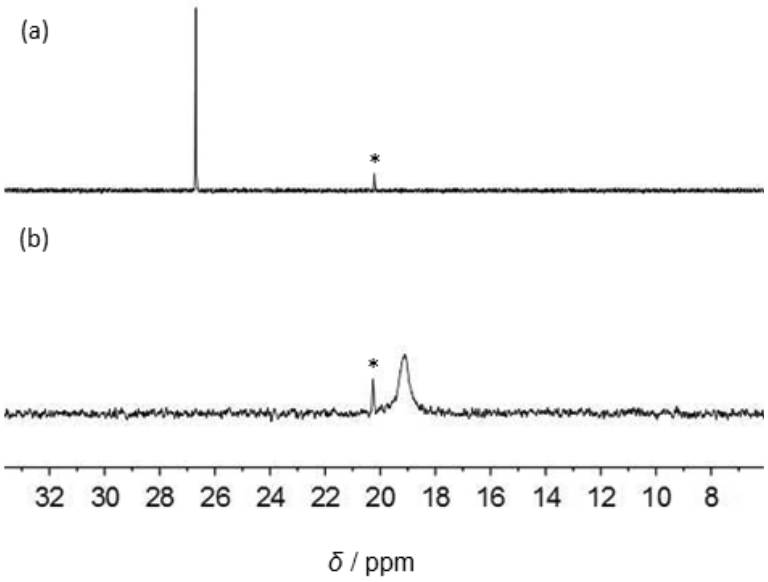

Figure 6.9 ^{31}P NMR spectra of a solution of [Pd(L_F)$_3$] (c = 1 mM) in THF at 298 K (a) in the absence and (b) in the presence of 1 eq. of NBu_4Br. The signal marked with an asterisk corresponds to the phosphine oxide derived of L_F.

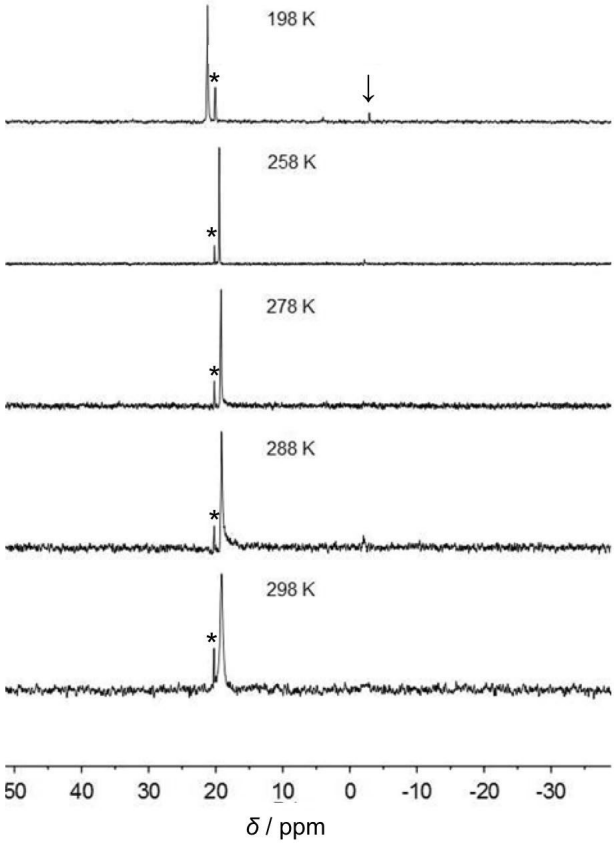

Figure 6.10 Temperature-dependent ^{31}P NMR spectra of a 1:1 solution of [Pd(L_F)$_3$] and NBu_4Br (c = 1 mM for each component) in THF. The signal marked with an arrow corresponds to free L_F, that marked with an asterisk to the phosphine oxide derived there of (L_F = tris[3,5-bis(trifluoromethyl)-phenyl]phosphine).

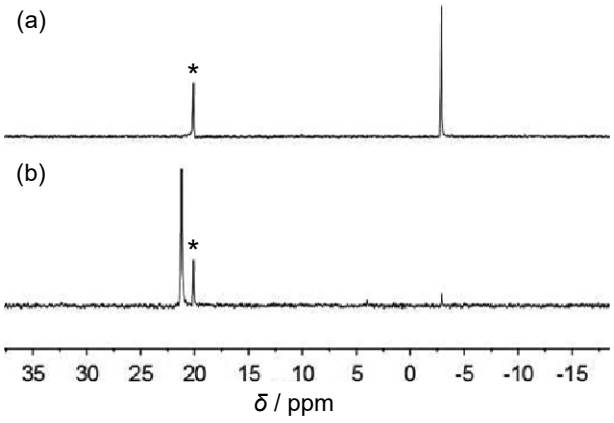

Figure 6.11 ^{31}P NMR spectra of (a) a solution of free L_F (298 K) and of (b) a 1:1 solution [Pd(L_F)$_3$] and NBu_4Br (c = 1 mM for each component, 198 K) in THF. The signal marked

with an asterisk corresponds to the phosphine oxide derived of L_F (L_F = tris[3,5-bis(trifluoromethyl)-phenyl]phosphine).

The small magnitude of the signal of free L_F indicates that the association/dissociation equilibrium between $[(L_F)_3PdBr]^-$ and $[(L_F)_2PdBr]^-$, eq. (2), lies largely on the side of the tetra-coordinated complex. Control experiments show no significant effect of NBu_4Br on the phosphine L_F itself and, thus, confirms that the latter does not add Br^- anions to any noticeable extent. Furthermore, ^{19}F NMR spectroscopy is used to analyze solutions of $[Pd(L_F)_3]$. Again, the addition of NBu_4Br leads to a broadening and shift of the ^{19}F signal, as one would expect for the formation of $[(L_F)_3PdBr]^-$ (Figure 6.12).

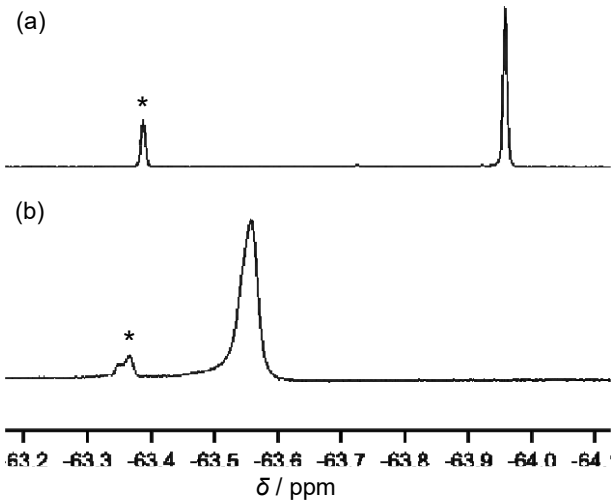

Figure 6.12 ^{19}F NMR spectra of a solution of $[Pd(L_F)_3]$ (c = 1 mM) in THF at 298 K (a) in the absence and (b) in the presence of 1 eq. of NBu_4Br. The signal marked with an asterisk corresponds to the phosphine oxide derived of L_F (L_F = tris[3,5-bis(trifluoromethyl)-phenyl]phosphine).

6.5 ESI mass spectrometry of Pd^{II} ate complexes[h]

Finally, ethyl 4-iodo-benzoate (ArI) is added to a solution of $[Pd(L_F)_3]$ and the resulting mixture is analyzed by ESI mass spectrometry. Besides the base peak $[(L_F)_2PdI_3]^-$ and a few minor species, two complexes with the stoichiometries $[(L_F),Pd,Ar,I_2]^-$ and $[(L_F)_2,Pd,Ar,I_2]^-$, respectively, are observed (Figure 6.13, Table 8.30, Figure 8.71, Figure 8.72, Figure 8.73, Figure 8.74, Figure 8.75 and Figure 8.76).

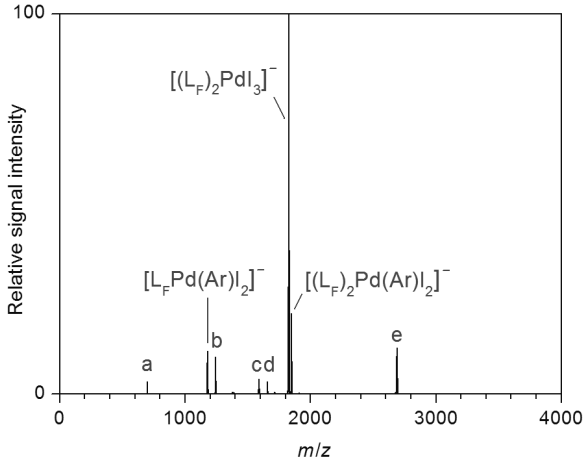

Figure 6.13 Negative-ion mode ESI mass spectrum of a solution of $[Pd(L_F)_3]$ (1.5 mM) and ArI (6 mM) in THF (a = $P_2(Ar_F)_3^-$, b = $[L_FPd(Ar_F)I_2]^-$, c = $[(L_F)_2,Pd,O,I]^-$, d = $[(L_F)_2CuI_2]^-$, e = $[(L_F)_3Pd_2(Ar_F)I_2]^-$, ArF = 3,5-bis(trifluoromethyl)-phenyl).

Fragmentation of the mass-selected complex results only in the loss of the phosphine ligands (Figure 6.14).

[h] Prof. Koszinowski carried out the shown ESI mass spectrometry experiments.

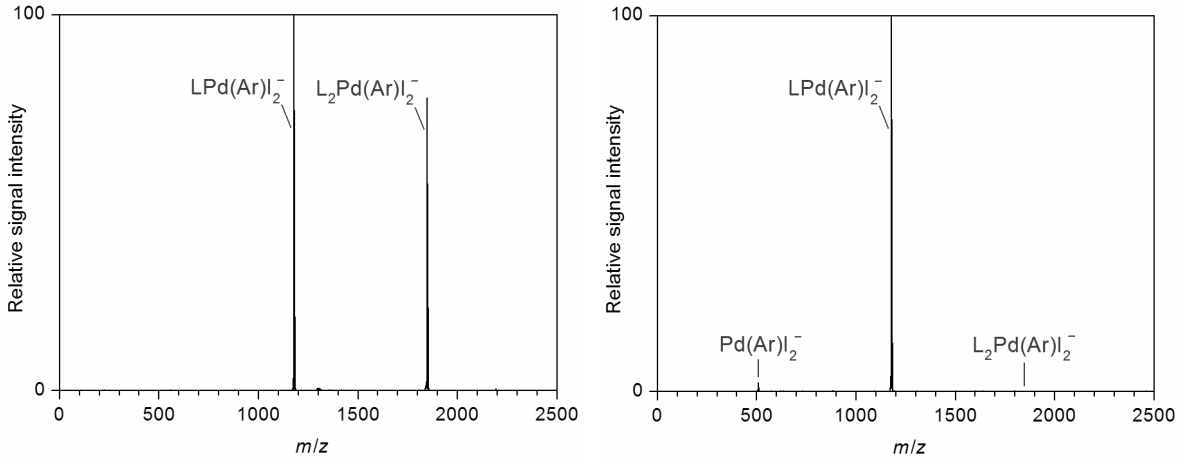

Figure 6.14 Mass spectra of mass-selected $[(L_F)_2Pd(Ar)I_2]^-$ and its daughter ions produced upon collision-induced dissociation at different collision energies (left: E_{LAB} = 5 eV, right: E_{LAB} = 15 eV, L_F = tris[3,5-bis(trifluoromethyl)-phenyl]phosphine).

This reactivity is consistent with a penta-coordinated structure of the parent ion (Scheme 6.1). However, it does not seem to be well compatible with the alternatively proposed square planar isomer, which should instead eliminate ArI.

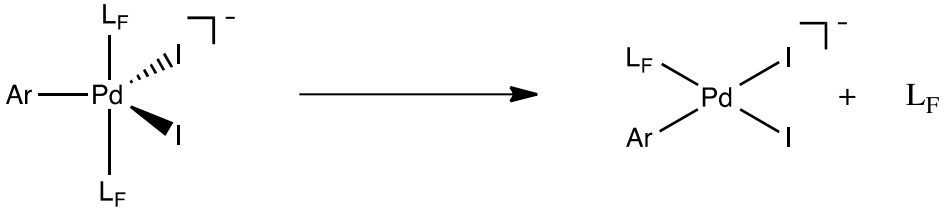

Scheme 6.1 Gas-phase fragmentation of $[(L_F)_2Pd(Ar)I_2^-]$.

A penta-coordinated structure for $[(L_F)_2PdI_3^-]$ is also assumed. Most likely, this species results from the hydrolysis of $[(L_F)_2Pd(Ar)I_2]^-$ and a consecutive OH^-/I^- exchange;[27i] such reactions easily occur during the ESI-mass spectrometric analysis of diluted solutions of organometallics because the exclusion of traces of moisture in these experiments is notoriously difficult.[27h, 98h,

[116] Upon fragmentation $[(L_F)_2PdI_3]^-$ looses the ligand L_F (Figure 6.15) and, thus, behaves analogously to $[(L_F)_2Pd(Ar)I_2]^-$.

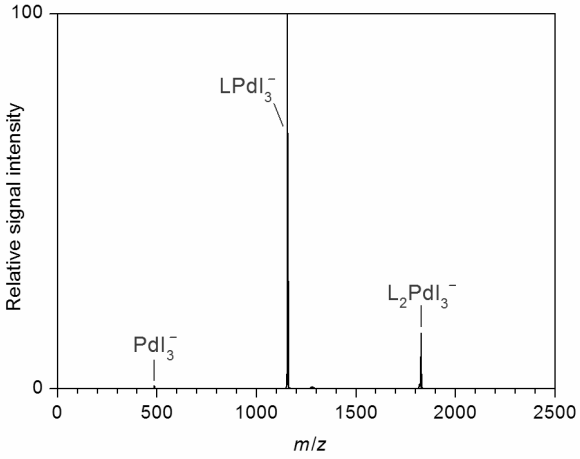

Figure 6.15 Mass spectrum of mass-selected $[(L_F)_2PdI_3]^-$ and its daughter ions produced upon collision-induced dissociation (E_{LAB} = 15 eV).

7 Summary

Palladium-catalyzed Heck and cross-coupling reactions have revolutionized organic synthesis. The researchers behind these reactions, Heck, Negishi, and Suzuki, were awarded the 2010 Nobel Prize in chemistry.[18] This field is extremely rich and productive and is likely to continue to grow with major synthetic applications and "green" implications in the future.[155] Organozinc halides, as used in Negishi cross-coupling reactions have a high reactivity in combination with an excellent tolerance towards functional groups and are easy accessible. Still, to the present day not all factors that affect the Negishi palladium catalyzed cross-coupling cycle are discovered. The canonical catalytic cycle is oversimplified and does not describe all the intermediate steps in detail. A more detailed understanding of the catalytic cycle would be important in helping to characterize and optimize the reaction. This understanding would allow a more efficient synthesis of the desired cross-coupling products. For this reason, the present thesis has sought to elucidate the details of the Negishi reaction and to find out how different additives and conditions influence the reaction.

The content of this thesis was based on four subprojects. First, the reaction kinetics of Negishi cross coupling was analyzed (chapter 3) before the in-situ formed intermediates were investigated spectrometrically and spectroscopically (chapter 4). In a minor part of this work, the accelerating effect of aryl iodo compounds on the reactivity of aryl bromides in Negishi cross-coupling reactions was examined (chapter 5). During these investigations, Pd ate complexes were observed and further studied (chapter 6).

7.1 Kinetic measurements on Negishi cross-coupling reactions

In the first subproject, kinetic measurements have been used to elucidate the mechanism of Pd-catalyzed Negishi cross-coupling reactions under realistic catalytic conditions. The kinetics of the palladium/S-Phos catalyzed Negishi cross-coupling reaction of ethyl 4-iodobenzoate with various butylzinc reagents in THF at room temperature (Scheme7.1) were investigated. Mainly gas chromatography was used for the studies. Even at low catalyst loading, the ArBu cross-coupling product is formed efficiently in approx. 90% yield.

Besides the desired cross-coupling product ArBu, the reaction (Scheme 7.1) also affords dehalogenation and homo-coupling products, i.e., ArH and Ar_2, though to only minor extents (approx. 10% in total). Analogous byproducts are well-known from the literature. [34a-d]

Dehalogenation products, such as ArH, actually correspond to ArZnBr or ArZnBr·LiBr, respectively, in their native state and furnish the detected ArH species only due to hydrolysis during the aqueous work-up before the gas-chromatographic analysis (see Experimental Section).

The formation of the ArZnBr species, which forms the dehalogenated product, may occur by two paths, which are shown in the kinetic investigations (Scheme 3.2).

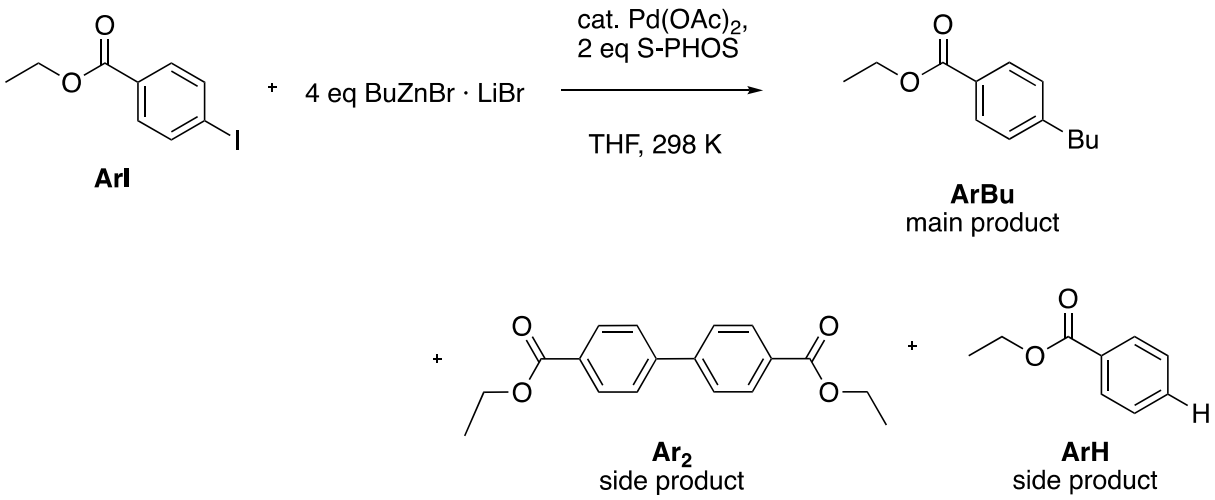

Scheme 7.1 Model reaction with side reaction products Ar_2 and ArH

The measured concentration profiles typically do not display a simple exponential decay, which would be expected for the oxidative addition as rate-limiting step under pseudo-first order conditions but show unexpected bimodal behavior. This indicated a higher complexity of the catalytic cycle and complicates the extraction of rate constants. Therefore, only the approximately linear areas of the time profiles were evaluated to determine the reaction order.

For efficient cross-coupling, the presence of 1 eq. of LiBr (relative to the organozinc reagent) is essential, whereas the addition of further LiBr has no significant effect. That excludes the involvement of so-called higher-order organozincates, such as $RZnBr_3^{2-}$ or the corresponding

Li^+ ion pairs. In all cases the LiBr additive had a strong effect and increased the reactivity whereas control experiments without LiBr showed drastically reduced reaction rates. In contrast, the addition of $ZnBr_2$ led to decreased reactivity.

Concentration-dependent experiments show that the reaction rate increases as function of *c*(Pd) and depends on the S-PHOS:Pd ratio. Besides S-PHOS, PPh_3 and the PEPPSI-IPr ligand catalyze the cross-coupling reaction, which also proceeds in the complete absence of an added ligand, however.

Further concentration-dependent experiments reveal that the reaction rate increases with *c*(ArI), although apparently not in a simple linear fashion. ArBr also undergoes cross-coupling under the given reaction conditions, but much more slowly than ArI, as revealed by competition experiments; in contrast, ArOTs does not react. The observed reactivity decreased in the series ArI > ArBr ≫ ArOTs.

Variation of *c*(BuZnBr·LiBr) does not significantly change the reaction rate, whereas substitution of BuZnBr·LiBr for PhZnBr·LiBr or BnZnBr·LiBr increases or decreases the cross-coupling efficiency, respectively (again probed in competition experiments). The overall reaction rate depended on the nature of the organozinc reagent (PhZnBr·LiBr ≫ BuZnBr·LiBr > BnZnBr·LiBr), which implied its involvement in the rate-limiting step/rate-determining states. In contrast, it is not clear how the nature of the organozinc reagent can also influence the overall rate although this reactant is not involved in the oxidative addition according to the conventional catalytic cycle. The organozinc reagents were also used without LiBr, the reactivity decreased as already described.

On the basis of the concentration-dependent experiments, the oxidative addition as rate-determining step of these reactions is identified. Taking into account that the pronounced effects of the LiX and $ZnBr_2$ additives imply a crucially important role in the oxidative addition, the situation becomes even more complex.

In general, the experiments provide good insights into the Negishi cross-coupling reaction, but they also show that in this complex reaction it is important to consider all reaction partners for every step of the catalytic cycle.

7.2 Identification of intermediates

To identify the intermediates formed in Pd-catalyzed Negishi cross-coupling reactions, electrospray ionization mass spectrometry, complemented by ^{31}P NMR and UV/Vis spectroscopy, was used in the second part.

^{31}P NMR spectroscopy gave first indications of a significant sample complexity. UV/Vis spectroscopy, in turn, pointed to Pd aggregation, eventually resulting in the formation of Pd black. More detailed insight was obtained from ESI mass spectrometry. For solutions of $Pd(OAc)_2$/2 S-PHOS in THF, cationic Pd(I) dimers are observed, which are analogous to complexes reported in the literature. These Pd(I) dimers could possibly be considered as onset of Pd aggregation, although, apart from a trinuclear anionic complex, no evidence for the formation of higher aggregates has been found. At the same time, degradation of the S-PHOS ligand due to C–P bond cleavage occurs, which also resembles processes described previously. In the presence of LiBr, the degradation of the phosphine is slowed down. Upon addition of BuZnBr or BuZnBr·LiBr, the Pd(I) dimers vanish and instead, among other ions, the complex L_2PdZnR^+ (L = S-PHOS, R = Bu) emerges. Gas-phase fragmentation experiments suggest that this species features a direct Pd−Zn bond. This shows that Pd(0) and Zn(II) spontaneously combine to afford a heterobimetallic dimer. Analogous species for L= PPh_3, R= Ph, Bn are detected. It was concluded that L_2PdZnR^+ and/or the corresponding neutral complex are relatively stable and readily form.

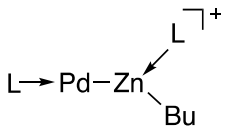

Scheme 7.2 Proposed structure for $L_2PdZnBu^+$.

Upon addition of the aryl iodide ArI to solutions of $Pd(OAc)_2$/2 S-PHOS, the detection of iodine-containing Pd(I) dimers reflects the C–I bond activation in the course of the oxidative addition. In the negative-ion mode, insertion products, such as $ArPdI_2^-$, are also directly visible. If both BuZnBr·LiBr and ArI are added to the catalyst, the heterobimetallic dimer L_2PdZnR^+ is formed again. Furthermore, the complex $Li(ArBu)_2^+$, which contains the cross-coupling

product, is observed. As expected, its signal intensity increases in time as the reaction proceeds, but the rather poor signal/noise ratio prohibits the extraction of meaningful rate constants.

The observation of Pd aggregation and ligand degradation processes explains why longer incubation times of the catalyst result in a moderate loss of activity. Both the kinetic measurements and the present spectroscopic experiments show that LiBr at least partially counteracts this deactivation.

Heterobimetallic dimers are observed in significant abundance although the present experiments employ only a modest excess of the RZnX reagent (fourfold relative to the catalyst). Under typical catalytic conditions, the much higher concentration of the organozinc reagent will drive the equilibrium further to the side of the heterobimetallic dimers. $L_2PdZnBu^+$ and related neutral complexes with a direct Pd–Zn interaction in solution explain how the organozinc reagent is able to modulate the reactivity of the Pd catalyst, thus rationalizing the results of the kinetic measurements. Theoretical calculations from Álvarez, Lera and Aurrecoechea[70] suggested that the complexation by the organozinc reagent lowers the activity of the Pd catalyst. These heterobimetallic dimers then may actually be the predominating Pd species present in solution. The involvement of these heterobimetallic complexes easily explains why the nature of the organozinc reagent can affect the oxidative addition. Also the kinetic measurements show these results. The Pd-Zn dimers are coordinatively more saturated and putatively less reactive compared to the free LPd catalyst. Presumably, a similar effect also causes the rate decrease observed upon addition of $ZnBr_2$.

Moreover, the bimodal behavior observed in kinetic measurements is also ascribed to the formation of Pd-Zn dimers. Upon addition of the catalyst, the initially present LPd is converted to the heterobimetallic dimer and, thereby, diminished in its catalytic activity. This change from high to lower catalytic activity supposedly gives rise to bimodal kinetics. Control experiments confirm that the order of addition of the reaction partners indeed has a notable effect on the (initial) rate. Finally, the rate-accelerating effect of LiBr and other lithium halides could also be related to the heterobimetallic Pd-Zn dimers and the extent to which they are produced. The organozincates $RZnX_2^-$ resulting from the lithium halides and the RZnX reagents are less Lewis acidic than the latter and do not easily combine with Pd(0) species. This supposedly protects the catalyst from complexation by the organozinc reagent thus avoids deactivation of the catalyst. Alternatively, the effect of lithium halides could possibly also arise from the formation

of anionic Pd(0) ate complexes. These Pd(0) ate complexes were not observed in the present experiments, however.

7.3 Reactivity enhancement of aryl bromides in the presence of aryl iodides

The experiments in chapter 5 confirmed that the aryl bromide reactant ethyl 4-bromobenzoate is less reactive in cross-coupling reactions than aryl iodide compound methyl 4-iodobenzoate. The presence of aryl iodide electrophiles like methyl 4-iodobenzoate and phenyl iodide accelerates the reaction of ethyl 4-bromobenzoate with BuZnBr·LiBr to form the cross-coupling product ethyl 4-butylbenzoate.

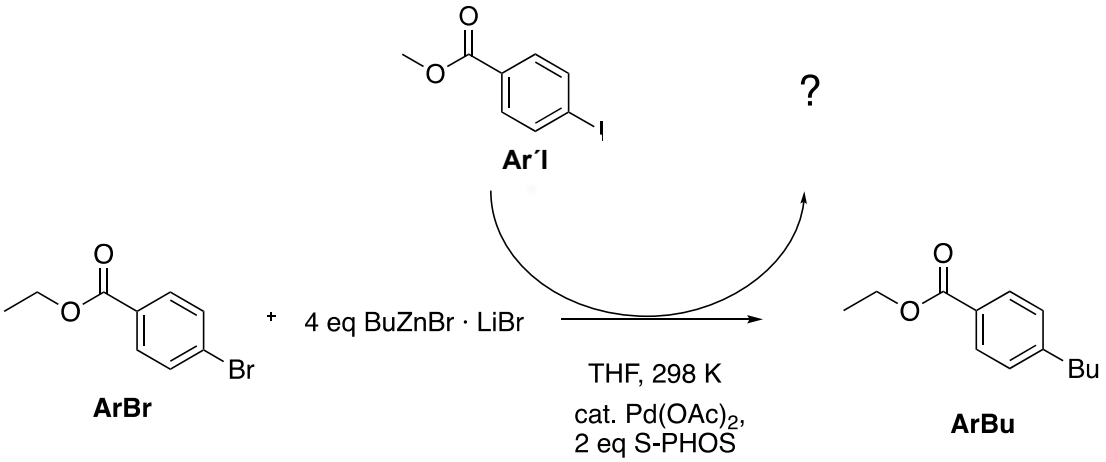

Scheme 7.3 Cross-coupling reaction of ArBr with BuZnBr·LiBr in presence of Ar´I

Hypothetically a reactive palladium(I) dimer V (Scheme 5.5) is formed as intermediate, which can react to the minor product ethyl 4-butylbenzoate. In the experiments the halogen-exchanged product Ar´Br could not be observed, however. In contrast to the activating effect of aryl iodide compounds, the presence of iodine and methyl iodide has no effect on the rate of reaction of ethyl 4-bromobenzoate.

On the basis of the experiments, one could suggest that the conversion of ethyl 4-bromobenzoate directly correlates with the conversion of methyl 4-iodobenzoate. According to that an extension of the reaction time of methyl 4-iodobenzoate could possibly affect the yield of the aryl bromide cross-coupling product. Based on these results, it could be concluded that

the otherwise sluggish conversion of ethyl 4-bromobenzoate to alkylarene is immediately accelerated upon addition of aryl iodide (phenyl iodide, methyl 4-iodobenzoate). In each case the ArI is consumed at a faster rate than the ethyl 4-bromobenzoate (see Figure 6.1). So far, the present results do not allow any conclusion about the mechanism of a presumed halogen exchange reaction.

However, the mechanism of the accelerating effect is not exactly understood. A halogen exchange, as proposed by Schoenebeck et al.,[99] can be easily excluded for the investigated reaction of Scheme 5.3; since there is no formation of the mixed electrophile Ar´Br detected. The replaced electrophile methyl 4-bromobenzoate should be formed simultaneously with the cross-coupling product. The transition metal catalyzed mechanism for halogen exchange proposed by Sheppard[138] shows a possibility but does not explain the demand of aryl halogen compounds, however. Nevertheless, by this suggested mechanism also charged compounds such as salts can promote halogen exchange, which is not observed for the lithium salts, present in the reaction mixtures. Consequently, the mechanism suggested by Sheppard cannot explain the experimental findings completely, either. The experiments show that no methyl 4-bromobenzoate (Ar´Br) was formed and only path D (Scheme 5.5) shows a possible mechanism for the halogen exchange.

It was not possible to increase the yield of ethyl 4-butylbenzoate by the addition of a small quantity of aryl iodide. However, this exchange would be a great chance for synthetic applications and more research should be done to explore the mechanism of acceleration of the aryl bromid compound in presence of the aryl iodide.

7.4 Palladium ate complexes

The fourth subproject focuses on palladium ate complexes. They are considered to be important intermediates in palladium catalyzed cross-coupling reactions, but complete characterization has not yet been achieved. Here, electrospray-ionization mass spectrometry, electrical conductivity measurements and ^{31}P NMR spectroscopy are used to investigate the tendency of Pd species to form ate complexes. It is shown that the electron-poor catalyst [Pd(L_F)$_3$] (L_F = tris[3,5-bis(trifluoromethyl)- phenyl]phosphine) readily reacted with Br^- ions to afford the anionic, zero-valent ate complex [(L_F)$_3$PdBr]$^-$. The resulting ate complex [(L_F)$_3$PdBr]$^-$ easily looses one L_F ligand. The resulting tri-coordinated Pd(0) ate complex is supposed to be the catalytically active intermediate in cross-coupling reactions. In contrast, more electron-rich Pd

pre-catalysts ($Pd(OAc)_2$/ 2 S-PHOS, $Pd(PPh_3)_4$, PEPPSI-IPr) display lower tendencies toward the formation of Pd(0) ate complexes. Combining $[Pd(L_F)_3]$ with an aryl iodide substrate ArI results in the observation of $[(L_F)Pd(Ar)I_2]^-$, $[(L_F)_2Pd(Ar)I_2]^-$ and $[(L_F)_2PdI_3]^-$.

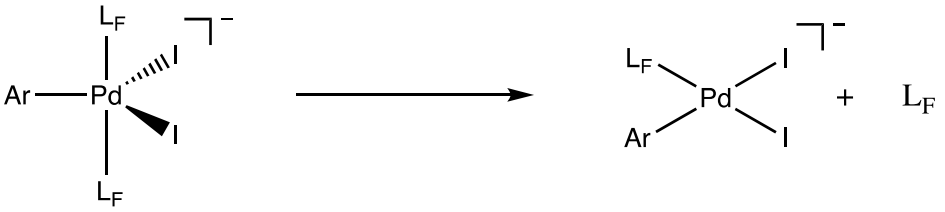

Scheme 7.4 Gas-phase fragmentation of $[(L_F)_2Pd(Ar)I_2^-]$.

Gas-phase fragmentation experiments suggests that the latter two complexes exhibit a penta-coordinated structure, thus demonstrating that such complexes are stable and can form as intermediates in palladium catalyzed cross-coupling reactions, in line with previous suggestions of Jutand, Amatore, and coworkers.[51b]

8 Appendix

8.1 Further data of Intermediates on Negishi cross-coupling reactions

8.1.1 ESI mass spectrometry − catalyst in the absence of substrate

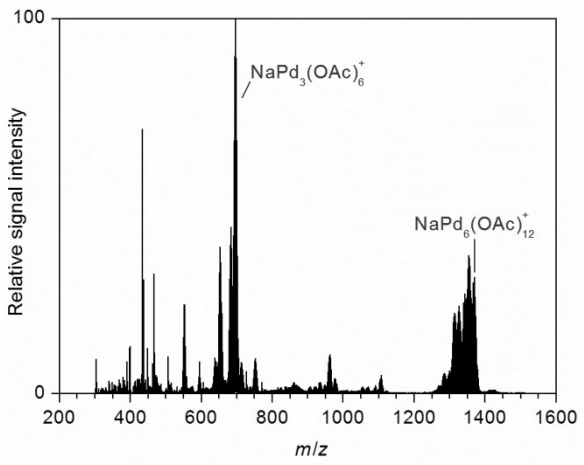

Figure 8.1 Positive-ion mode ESI mass spectrum of a solution of $Pd(OAc)_2$ (3 mM) in THF.

Table 8.1 Measured and theoretical *m*/*z* ratios of selected ions. For each ion, only the most abundant isotopologue is considered.

ion	sum formula	*m*/*z*(measured)	*m*/*z*(theoretical)
$NaPd_3(OAc)_6^+$	$C_{12}H_{18}NaO_{12}Pd_3^+$	696.79	696.78
$NaPd_6(OAc)_{12}^+$	$C_{24}H_{36}NaO_{24}Pd_6^+$	1369.58	1369.58

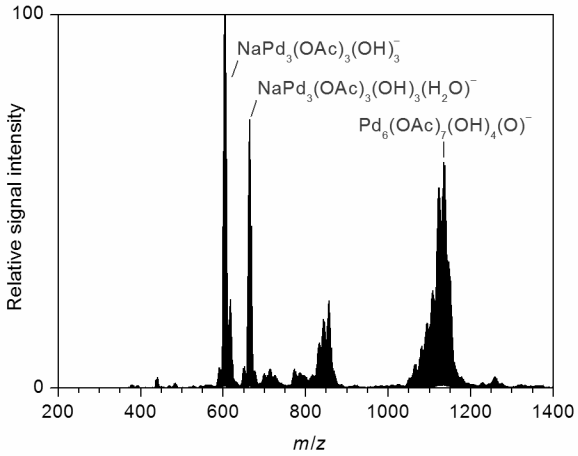

Figure 8.2 Negative-ion mode ESI mass spectrum of a solution of $Pd(OAc)_2$ (3 mM) in THF

Table 8.2 Measured and theoretical *m*/*z* ratios of selected ions. For each ion, only the most abundant isotopologue is considered.

ion	sum formula	*m*/*z*(measured)	*m*/*z*(theoretical)
$NaPd_3(OAc)_3(OH)_5^-$	$C_6H_{14}NaO_{11}Pd_3^-$	604.78	604.76
$NaPd_3(OAc)_3(OH)_5(HOAc)^-$	$C_8H_{18}NaO_{13}Pd_3^-$	664.80	664.78
$Pd_6(OAc)_7(OH)_4(O)^-$	$C_{12}H_{25}O_{19}Pd_6^-$	1134.51	1134.53

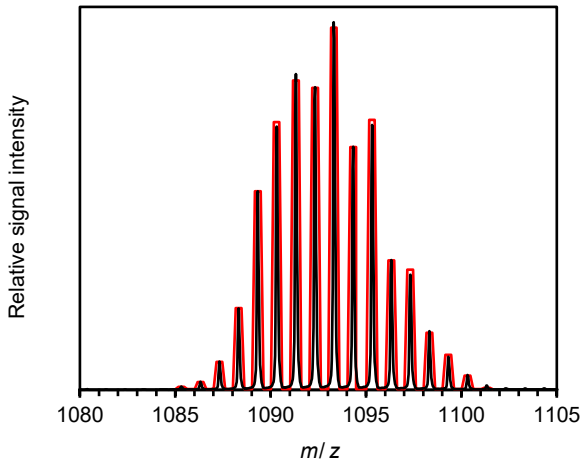

Figure 8.3 Measured (black) and simulated (red) isotope pattern of $L_2Pd_2(OAc)^+$ (L = S-PHOS).

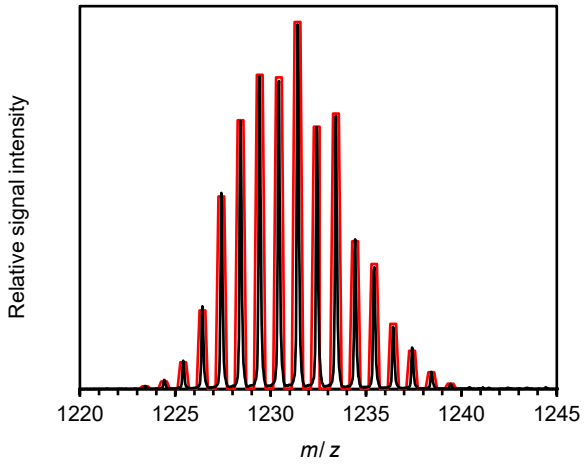

Figure 8.4 Measured (black) and simulated (red) isotope pattern of $L_2Pd_2(PCy_2)^+$ (L = S-PHOS).

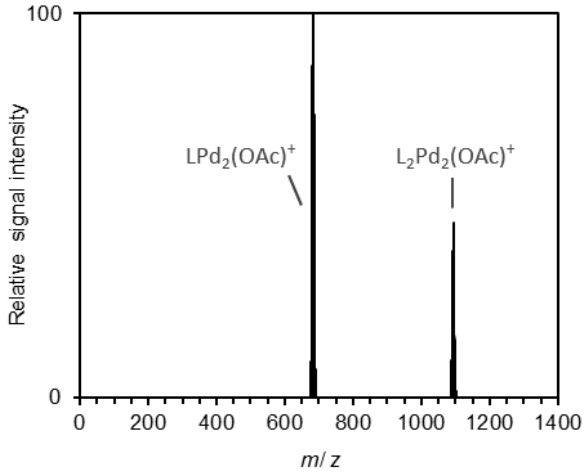

Figure 8.5 Mass spectrum of mass-selected $L_2Pd_2(OAc)^+$ and its daughter ion produced upon collision-induced dissociation (E_{LAB} = 20 eV).

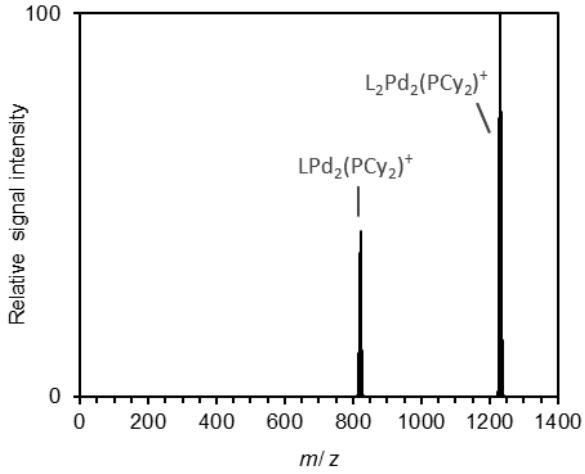

Figure 8.6 Mass spectrum of mass-selected $L_2Pd_2(PCy_2)^+$ and its daughter ion produced upon collision-induced dissociation (E_{LAB} = 30 eV).

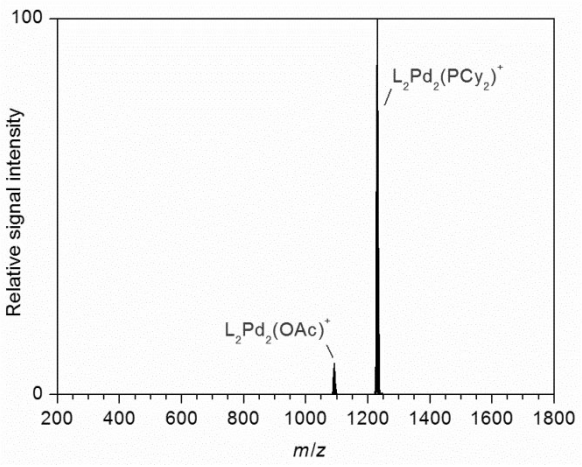

Figure 8.7 Positive-ion mode ESI mass spectrum of a solution of $Pd(OAc)_2$ (3 mM) and S-PHOS (L, 6 mM) in THF 90 min after mixing.

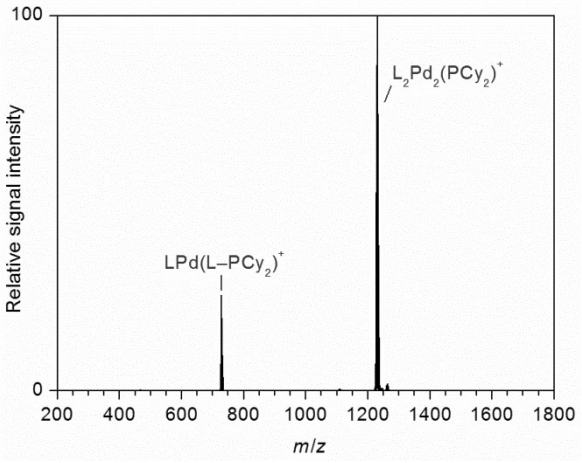

Figure 8.8 Positive-ion mode ESI mass spectrum of a solution of $Pd(OAc)_2$ (3 mM) and S-PHOS (L, 6 mM) in THF after exposure to air.

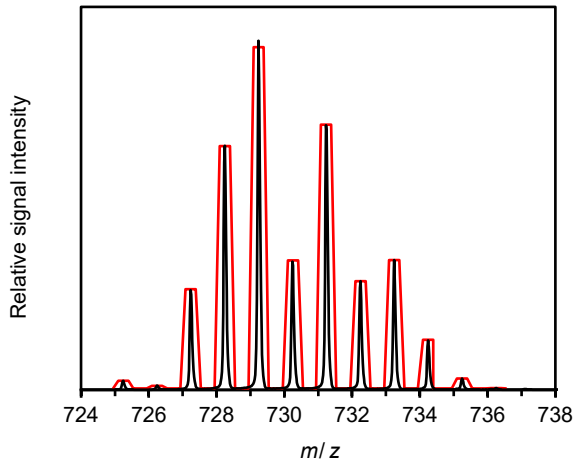

Figure 8.9 Measured (black) and simulated (red) isotope pattern of $LPd(L{-}PCy_2)^+$ (L = S-PHOS).

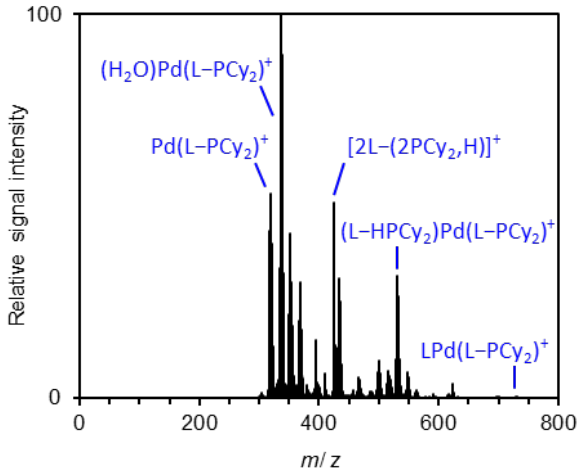

Figure 8.10 Mass spectrum of mass-selected $LPd(L{-}PCy_2)^+$ and its daughter ions produced upon collision-induced dissociation (E_{LAB} = 60 eV). The incorporated water originates from an ion-molecule reaction with H_2O present as a contamination in the vacuum system of the mass spectrometer.

Table 8.3 Measured and theoretical *m*/*z* ratios of selected ions. For each ion, only the most abundant isotopologue is considered.

ion	sum formula	*m*/*z*(measured)	*m*/*z*(theoretical)
$LPd(L{-}PCy_2)^+$	$C_{40}H_{48}O_4PPd^+$	729.25	729.23
$L_2Pd_2(OAc)^+$	$C_{54}H_{73}O_6P_2Pd_2^+$	1093.29	1093.30

$L_2Pd_2(PCy_2)^+$	$C_{64}H_{92}O_4P_3Pd_2^+$	1231.42	1231.43

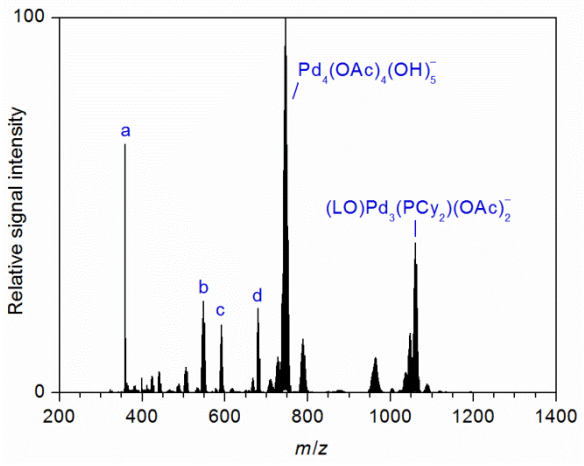

Figure 8.11 Negative-ion mode ESI mass spectrum of a solution of $Pd(OAc)_2$ (3 mM) and S-PHOS (L, 6 mM) in THF (a = $(LO{-}Cy)O^-$ [?], b = $NaPd_2(OAc)_5(OH)^-$, c = $(LO)Pd(OAc)^-$, d = $LPd(OAc)_2(NO_2)^-$ [?]). The tentative assignments given for a and d are consistent with the observed exact *m*/*z* ratios (Table S4), the isotope patterns (data not shown), and the gas-phase fragmentation behavior (data not shown), but the origin of these putative species is unclear.

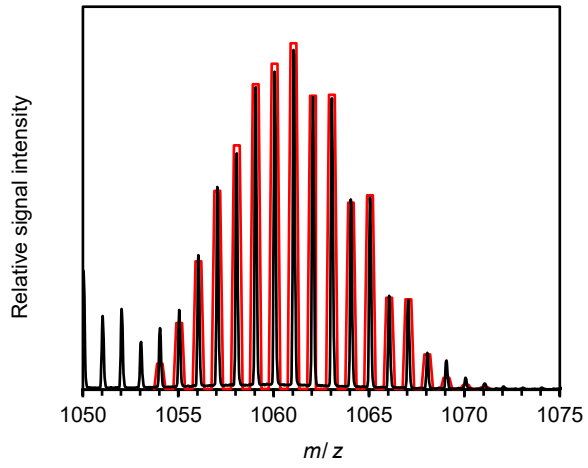

Figure 8.12 Measured (black) and simulated (red) isotope pattern of $(LO)Pd_3(PCy_2)(OAc)_2^-$ (L = S-PHOS).

Table 8.4 Measured and theoretical *m*/*z* ratios of selected ions. For each ion, only the most abundant isotopologue is considered.

ion	sum formula	*m*/*z*(measured)	*m*/*z*(theoretical)
$(LO{-}Cy)O^-$ [?][a]	$C_{20}H_{24}O_4P^-$	359.14	359.14
$NaPd_2(OAc)_5(OH)^-$	$C_{10}H_{16}NaO_{11}Pd_2^-$	548.86	548.87
$(LO)Pd(OAc)^-$	$C_{28}H_{38}O_5PPd^-$	591.15	591.15
$NaPd_3(OAc)_3(OH)_5^-$	$C_6H_{14}NaO_{11}Pd_3^-$	604.73	604.76
$NaPd_3(OAc)_3(OH)_5(HOAc)^-$	$C_8H_{18}NaO_{13}Pd_3^-$	664.75	664.78
$LPd(OAc)_2(NO_2)^-$ [?][a]	$C_{30}H_{41}NO_8PPd^-$	680.16	680.16
$Pd_4(OAc)_4(OH)_5^-$	$C_8H_{17}O_{13}Pd_4^-$	746.68	746.68
$(LO)Pd_3(PCy_2)(OAc)_2^-$	$C_{42}H_{63}O_7P_2Pd_3^-$	1061.15	1061.12

[a] Tentative assignment, see above.

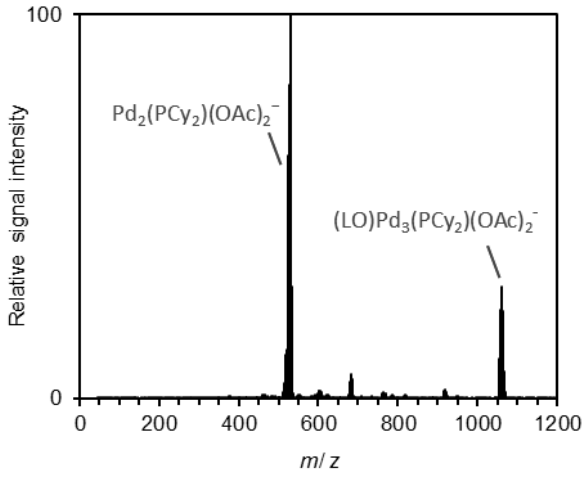

Figure 8.13 Mass spectrum of mass-selected $(LO)Pd_3(PCy_2)(OAc)_2^-$ and its daughter ions produced upon collision-induced dissociation (E_{LAB} = 30 eV).

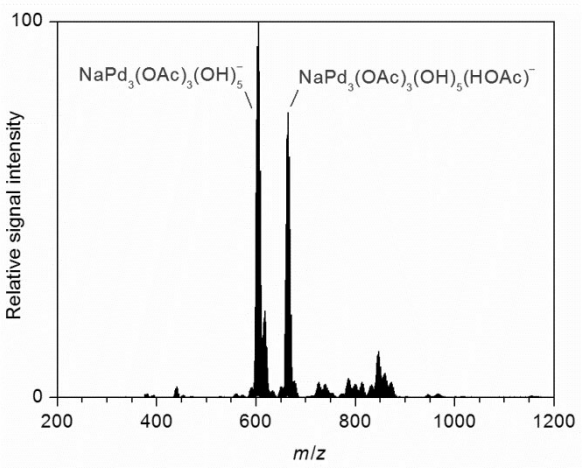

Figure 8.14 Negative-ion mode ESI mass spectrum of a solution of $Pd(OAc)_2$ (3 mM) and S-PHOS (L, 6 mM) in THF after exposure to air.

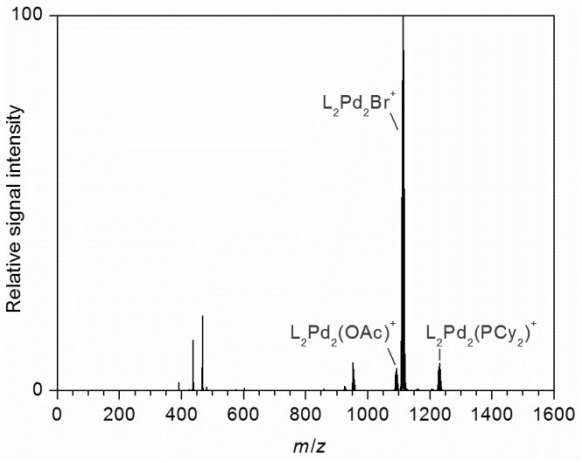

Figure 8.15 Positive-ion mode ESI mass spectrum of a solution of $Pd(OAc)_2$ (3 mM), S-PHOS (L, 6 mM), and LiBr (15 mM) in THF.

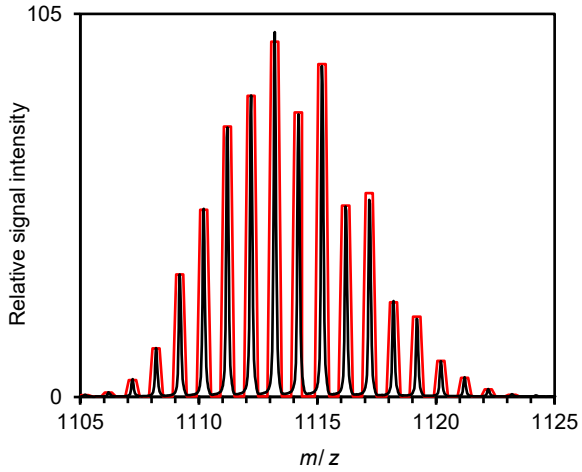

Figure 8.16 Measured (black) and simulated (red) isotope pattern of $L_2Pd_2Br^+$ (L = S-PHOS).

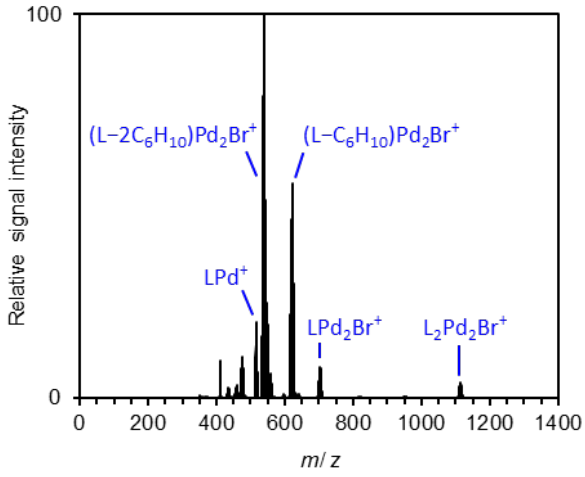

Figure 8.17 Mass spectrum of mass-selected $L_2Pd_2Br^+$ and its daughter ions produced upon collision-induced dissociation (E_{LAB} = 50 eV).

Table 8.5 Measured and theoretical *m*/*z* ratios of selected ions. For each ion, only the most abundant isotopologue is considered.

ion	sum formula	*m*/*z*(measured)	*m*/*z*(theoretical)
$L_2Pd_2(OAc)^+$	$C_{54}H_{73}O_6P_2Pd_2^+$	1093.30	1093.30
$L_2Pd_2Br^+$	$C_{52}H_{70}BrO_4P_2Pd_2^+$	1113.20	1113.20
$L_2Pd_2(PCy_2)^+$	$C_{64}H_{92}O_4P_3Pd_2^+$	1231.43	1231.43

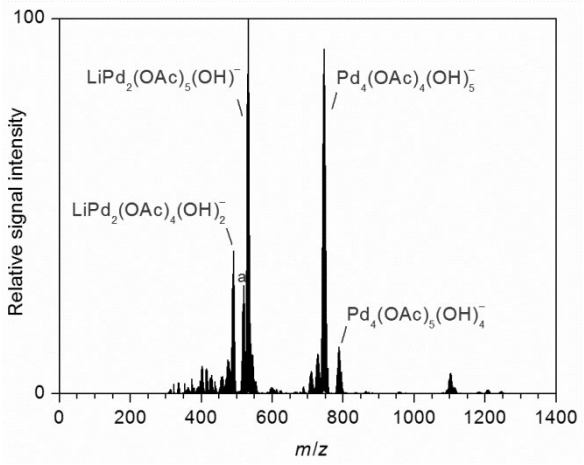

Figure 8.18 Negative-ion mode ESI mass spectrum of a solution of Pd(OAc)2 (3 mm), S-PHOS (L, 6 mm), and LiBr (15 mm) in THF (a = $LiPd_2(OAc)_4(OH)(NO_2)^-$?).

Table 8.6 Measured and theoretical *m*/*z* ratios of selected ions. For each ion, only the most abundant isotopologue is considered.

ion	sum formula	*m*/*z*(measured)	*m*/*z*(theoretical)
$LiPd_2(OAc)_4(OH)_2^-$	$C_8H_{14}LiO_{10}Pd_2^-$	490.88	490.88
$LiPd_2(OAc)_4(OH)(NO_2)^-$?[a]	$C_8H_{13}LiNO_{11}Pd_2^-$	519.86	519.87
$LiPd_2(OAc)_5(OH)^-$	$C_{10}H_{16}LiO_{11}Pd_2^-$	532.89	532.89
$Pd_4(OAc)_4(OH)_5^-$	$C_8H_{17}O_{13}Pd_4^-$	746.67	746.68
$Pd_4(OAc)_5(OH)_4^-$	$C_{10}H_{19}O_{14}Pd_4^-$	788.70	788.70

[a] Tentative assignment, see above.

8.1.2 ESI mass spectrometry – catalyst in the presence of organozinc reagents

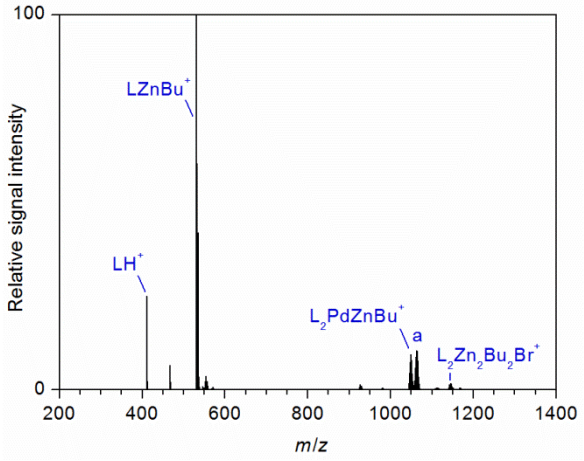

Figure 8.19 Positive-ion mode ESI mass spectrum of a solution of $Pd(OAc)_2$ (3 mM), S-PHOS (L, 6 mM), and BuZnBr (15 mM) in THF (a = $L_2Pd_2(NO_2)^+$?).

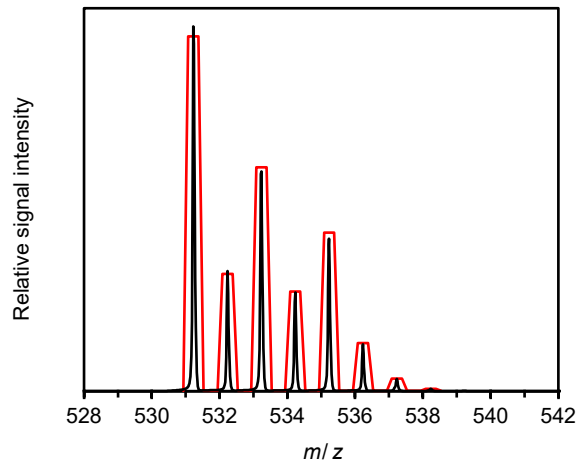

Figure 8.20 Measured (black) and simulated (red) isotope pattern of $LZnBu^+$ (L = S-PHOS).

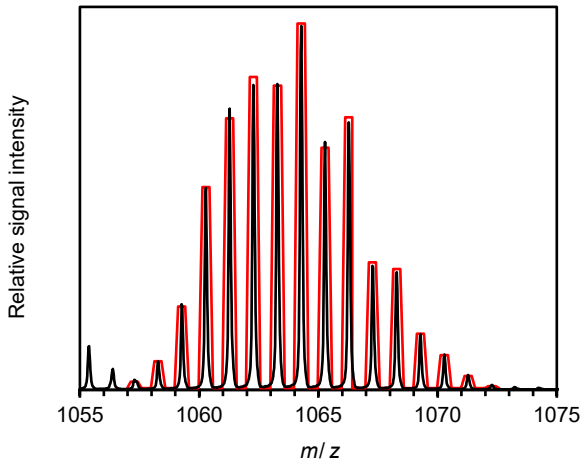

Figure 8.21 Measured isotope pattern of the ion centered at *m*/*z* 1064 (black) and simulated (dashed) isotope pattern of $L_2Pd_2(NO)^+$ (L = S-PHOS).

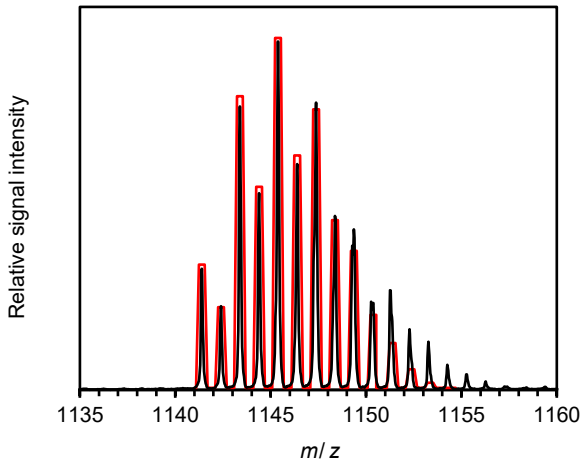

Figure 8.22 Measured (black) and simulated (dashed) isotope pattern of $L_2Zn_2Bu_2Br^+$ (L = S-PHOS).

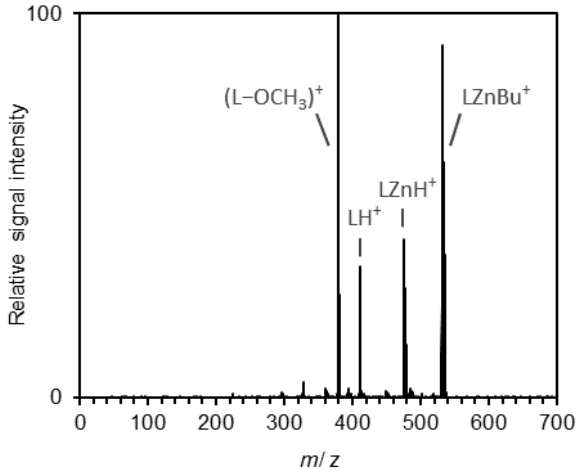

Figure 8.23 Mass spectrum of mass-selected $LZnBu^+$ and its daughter ions produced upon collision-induced dissociation (E_{LAB} = 40 eV).

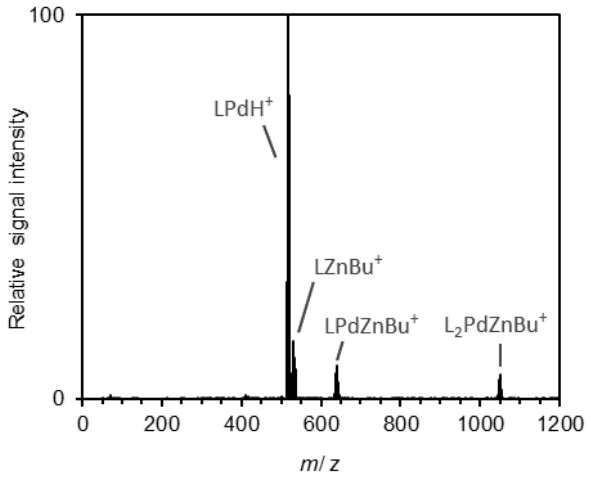

Figure 8.24 Mass spectrum of mass-selected $L_2PdZnBu^+$ and its daughter ions produced upon collision-induced dissociation (E_{LAB} = 35 eV).

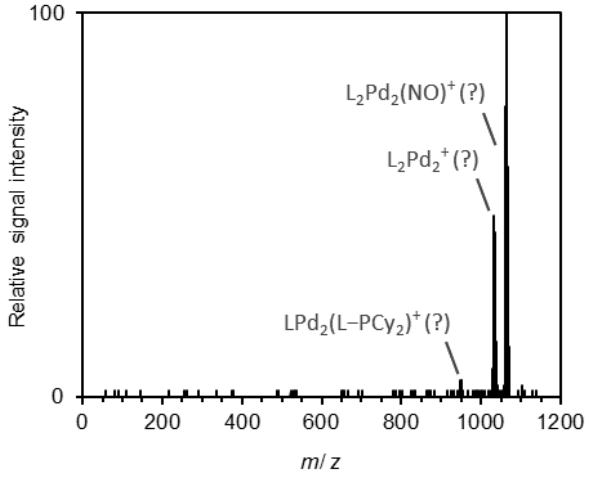

Figure 8.25 Mass spectrum of the mass-selected ion centered at *m*/*z* 1064 and its daughter ions produced upon collision-induced dissociation (E_{LAB} = 25 eV).

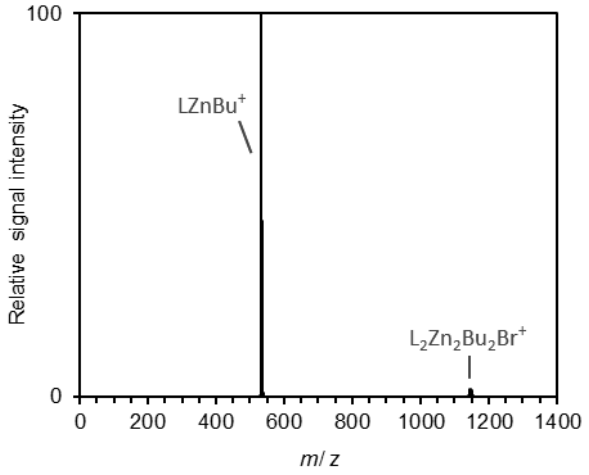

Figure 8.26 Mass spectrum of mass-selected $L_2Zn_2Bu_2Br^+$ and its daughter ions produced upon collision-induced dissociation (E_{LAB} = 10 eV).

Table 8.7 Measured and theoretical *m*/*z* ratios of selected ions. For each ion, only the most abundant isotopologue is considered.

ion	sum formula	*m*/*z*(measured)	*m*/*z*(theoretical)
LH^+	$C_{26}H_{36}O_2P^+$	411.24	411.25
$LZnBu^+$	$C_{30}H_{44}O_2PZn^+$	531.24	531.24
$L_2PdZnBu^+$	$C_{56}H_{79}O_4P_2PdZn^+$	1049.38	1049.38
$L_2Pd_2(NO)^+$?	$C_{52}H_{70}NO_5P_2Pd_2^+$	1064.28	1064.28
$L_2Zn_2Bu_2Br^+$	$C_{60}H_{88}BrO_4P_2Zn_2^+$	1145.39	1145.39

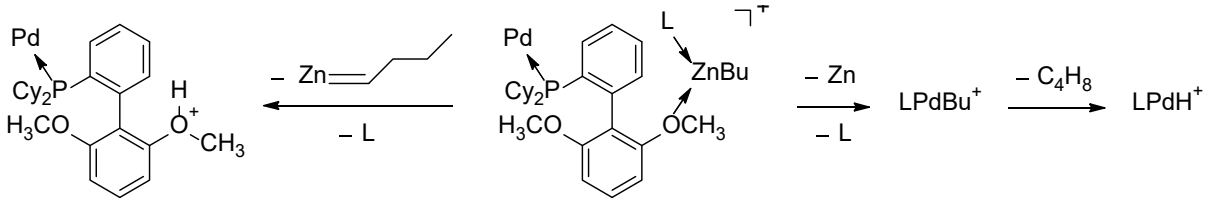

Scheme 8.1 Alternative mechanistic rationalizations of the fragmentation of $L_2PdZnBu^+$ resulting in the formation of $LPdH^+$.

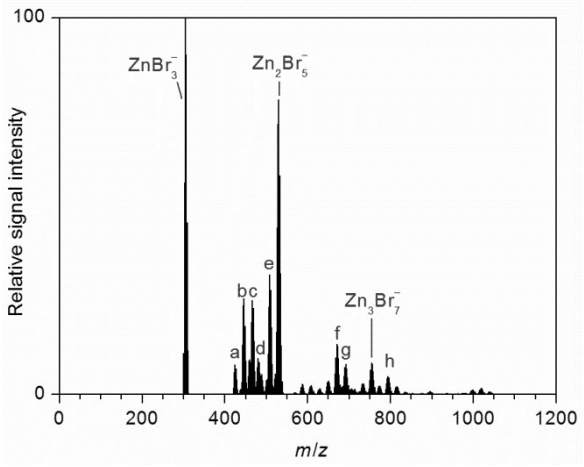

Figure 8.27 Negative-ion mode ESI mass spectrum of a solution of $Pd(OAc)_2$ (3 mM), S-PHOS (L, 6 mM), and BuZnBr (15 mM) in THF (a = $Zn_2Br_2(OAc)_2(OH)^-$, b = $Zn_2Br_3(OAc)(OH)^-$, c = $Zn_2Br_4(OH)^-$, d = $Zn_2Br_4(OCH_3)^-$, e = $Zn_2Br_4(OAc)^-$, f = $Zn_3Br_5(OAc)(OH)^-$, g = $Zn_3Br_6(OH)^-$, h = $Zn_3Br_6(OAc)(HOAc)^-$).

Table 8.8 Measured and theoretical *m*/*z* ratios of selected ions. For each ion, only the most abundant isotopologue is considered.

ion	sum formula	*m*/*z*(measured)	*m*/*z*(theoretical)
$ZnBr_3^-$	Br_3Zn^-	304.68	304.68
$Zn_2Br_2(OAc)_2(OH)^-$	$C_4H_7Br_2O_5Zn_2^-$	424.72	424.72
$Zn_2Br_3(OAc)(OH)^-$	$C_2H_4Br_3O_3Zn_2^-$	446.62	446.62
$Zn_2Br_4(OH)^-$	$HBr_4OZn_2^-$	466.53	466.53
$Zn_2Br_4(OCH_3)^-$	$CH_3Br_4OZn_2^-$	480.54	480.54
$Zn_2Br_4(OAc)^-$	$C_2H_3Br_4O_2Zn_2^-$	508.54	508.54
$Zn_2Br_5^-$	$Br_5Zn_2^-$	530.44	530.44
$Zn_3Br_5(OAc)(OH)^-$	$C_2H_4Br_5O_3Zn_3^-$	670.38	670.39
$Zn_3Br_6(OH)^-$	$HBr_6OZn_3^-$	692.28	692.29
$Zn_3Br_7^-$	$Br_7Zn_3^-$	754.20	754.21
$Zn_3Br_6(OAc)(HOAc)^-$	$C_4H_7Br_6O_4Zn_3^-$	794.31	794.32

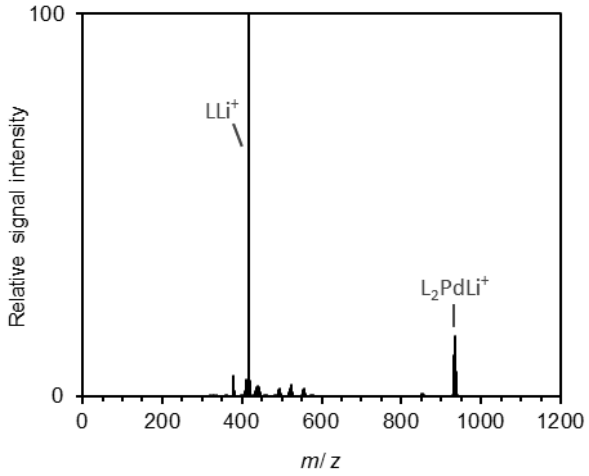

Figure 8.28 Mass spectrum of mass-selected L_2PdLi^+ and its daughter ions produced upon collision-induced dissociation (E_{LAB} = 35 eV).

Table 8.9 Measured and theoretical *m*/*z* ratios of selected ions. For each ion, only the most abundant isotopologue is considered.

ion	sum formula	*m*/*z*(measured)	*m*/*z*(theoretical)
$Li_3ZnBr(OAc)_3^+$	$C_6H_9BrLi_3O_6Zn^+$	342.93	342.93
LH^+	$C_{26}H_{36}O_2P^+$	411.24	411.24
LLi^+	$C_{26}H_{35}LiO_2P^+$	417.25	417.25
$(LO)Li^+$	$C_{26}H_{35}LiO_3P^+$	433.24	433.25
$LZnBu^+$	$C_{30}H_{44}O_2PZn^+$	531.23	531.24
L_2PdLi^+	$C_{52}H_{70}LiO_4P_2Pd^+$	933.39	933.40
$L_2PdZnBu^+$	$C_{56}H_{79}O_4P_2PdZn^+$	1049.37	1049.38

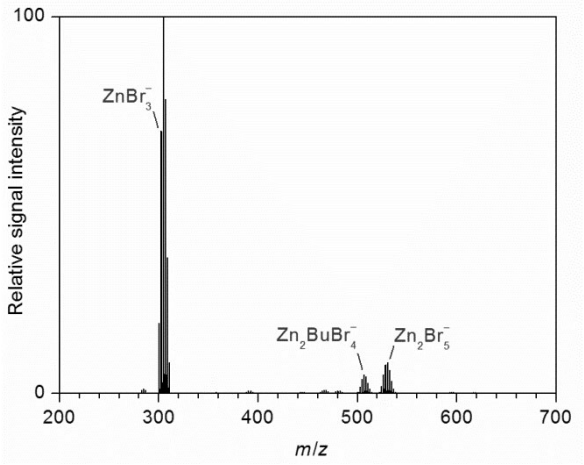

Figure 8.29 Negative-ion mode ESI mass spectrum of a solution of $Pd(OAc)_2$ (3 mM), S-PHOS (L, 6 mM), and BuZnBr·LiBr (15 mM) in THF.

Table 8.10 Measured and theoretical *m*/*z* ratios of selected ions. For each ion, only the most abundant isotopologue is considered.

ion	sum formula	*m*/*z*(measured)	*m*/*z*(theoretical)
$ZnBr_3^-$	Br_3Zn^-	304.68	304.68
$Zn_2BuBr_4^-$	$C_4H_9Br_4Zn_2^-$	506.59	506.60
$Zn_2Br_5^-$	$Br_5Zn_2^-$	530.44	530.44

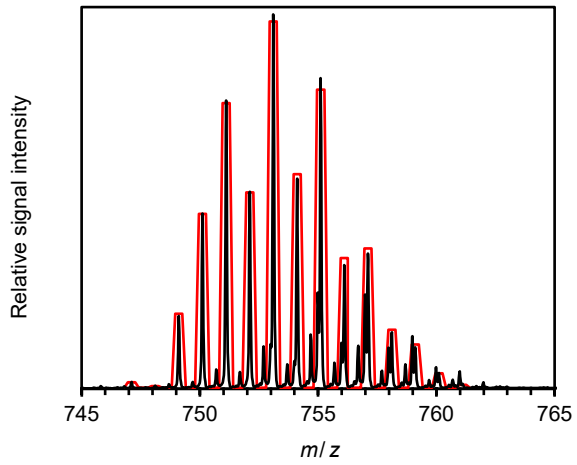

Figure 8.30 Measured (black) and simulated (red) isotope pattern of $L_2PdBuZn^+$ (L = PPh_3).

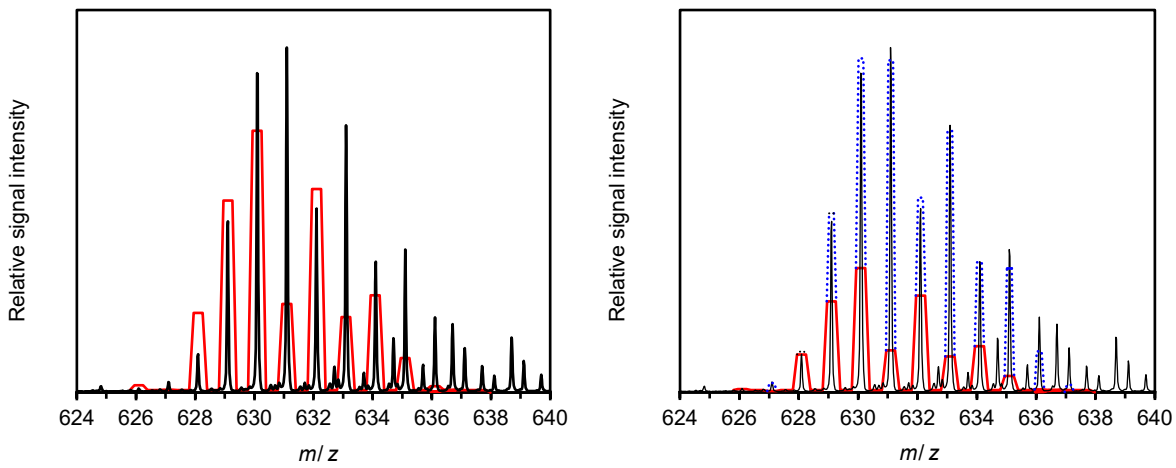

Figure 8.31 Left: Measured isotope pattern of the ion centered at *m*/*z* 631 (black) and simulated isotope pattern of L_2Pd^+ (red). Right: Measured isotope pattern of the ion centered at *m*/*z* 631 (black) together with simulated isotope patterns of L_2Pd^+ (red) L_2PdH^+(blue) in a ratio of 30:70 (L = PPh_3).)

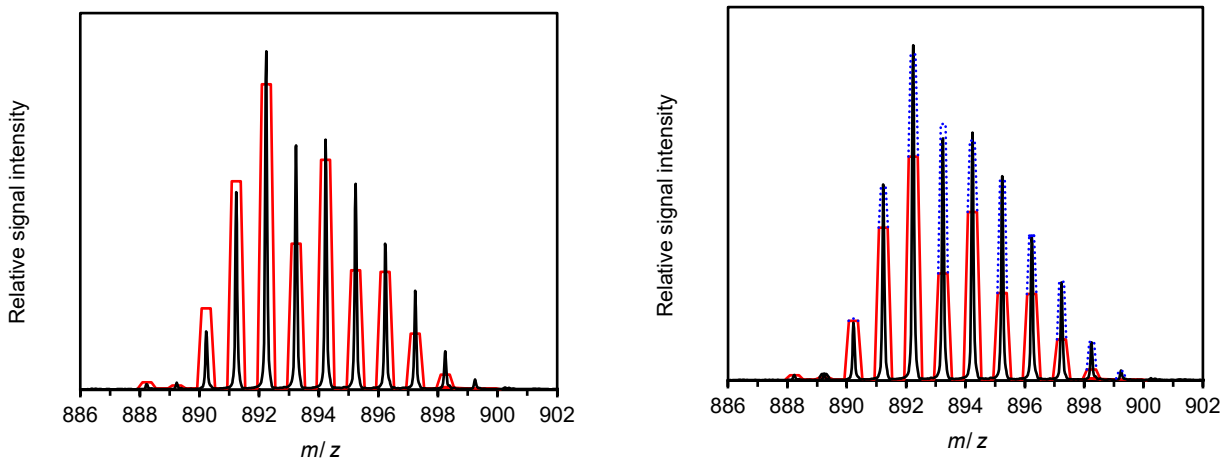

Figure 8.32 Left: Measured isotope pattern of the ion centered at *m/z* 893 (black) and simulated isotope pattern of L_3Pd^+ (red). Right: Measured isotope pattern of the ion centered at *m/z* 893 (black) together with simulated isotope patterns of L_3Pd^+ (red) and L_3PdH^+ (blue) in a ratio of 60:40 (L = PPh_3).

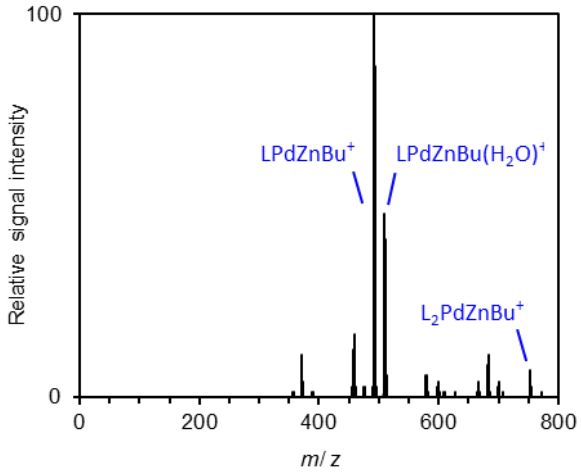

Figure 8.33 Mass spectrum of mass-selected $L_2PdZnBu^+$ and its daughter ions produced upon collision-induced dissociation (E_{LAB} = 10 eV, L = PPh_3). The incorporated water originates from an ion-molecule reaction with H_2O present as a contamination in the vacuum system of the mass spectrometer.

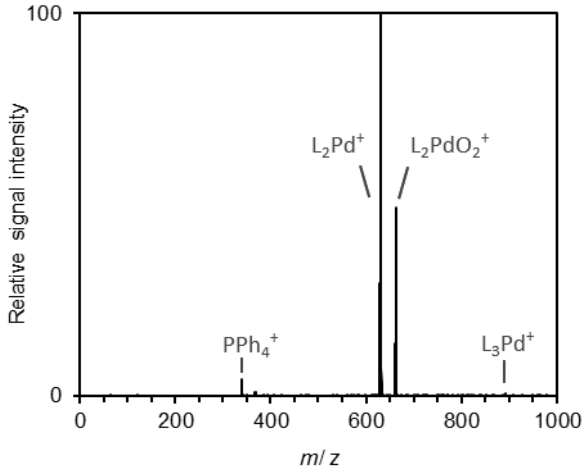

Figure 8.34 Mass spectrum of mass-selected $L_3{}^{106}Pd^+$ (*m*/*z* 892) and its daughter ions produced upon collision-induced dissociation (E_{LAB} = 20 eV). Note that the parent ion presumably is contaminated by isobaric $L_3{}^{105}PdH^+$. The ion $L_2PdO_2^+$ apparently results from an ion-molecule reaction with O2 present in the vacuum system of the mass spectrometer.

Table 8.11 Measured and theoretical *m*/*z* ratios of selected ions. For each ion, only the most abundant isotopologue is considered.

ion	sum formula	*m*/*z*(measured)	*m*/*z*(theoretical)
LLi_2Br^+	$C_{18}H_{15}BrLi_2P^+$	355.04	355.04
$Li_3ZnBr_4^+$	$Br_4Li_3Zn^+$	406.65	406.64
$Li_3ZnBr_4(THF)^+$	$C_{26}H_{36}O_2P^+$	478.70	478.70
$LLiZnBr_2^+$	$C_{18}H_{15}Br_2LiPZn^+$	492.86	492.87
$LLi_2ZnBr_3^+$	$C_{18}H_{15}Br_3Li_2PZn^+$	580.80	580.80
$LLi_2ZnBr_3(H_2O)^+$	$C_{18}H_{17}Br_3Li_2OPZn^+$	598.81	598.81
L_2Pd^+	$C_{36}H_{30}P_2Pd^+$	630.09	630.09
L_2PdH^+	$C_{36}H_{31}P_2Pd^+$	631.09	631.09
$LLi_3ZnBr_4^+$	$C_{18}H_{15}Br_4Li_3PZn^+$	668.73	668.73
$L_2PdZnBu^+$	$C_{40}H_{39}P_2PdZn^+$	753.08	753.08
L_3Pd^+	$C_{54}H_{45}P_3Pd^+$	892.18	892.18

L_3PdH^+	$C_{54}H_{46}P_3Pd^+$	893.18	893.19

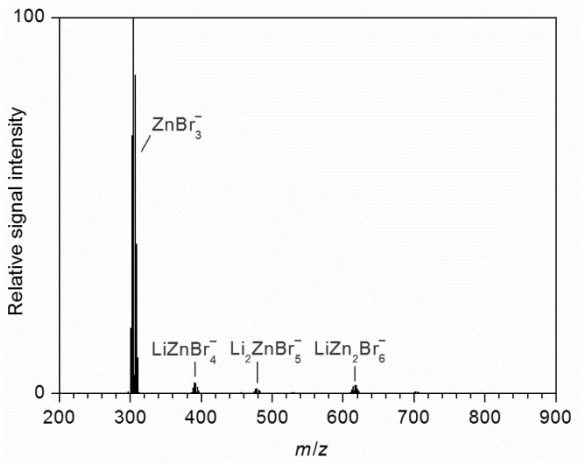

Figure 8.35 Negative-ion mode ESI mass spectrum of a solution of $Pd(PPh_3)_4$ (3 mM) and BuZnBr·LiBr (15 mM) in THF.

Table 8.12 Measured and theoretical *m*/*z* ratios of selected ions. For each ion, only the most abundant isotopologue is considered.

ion	sum formula	*m*/*z*(measured)	*m*/*z*(theoretical)
$ZnBr_3^-$	Br_3Zn^-	304.68	304.68
$LiZnBr_4^-$	Br_4LiZn^-	392.61	392.61
$Li_2ZnBr_5^-$	$Br_5Li_2Zn^-$	478.54	478.55
$LiZn_2Br_6^-$	$Br_6LiZn_2^-$	616.37	616.38

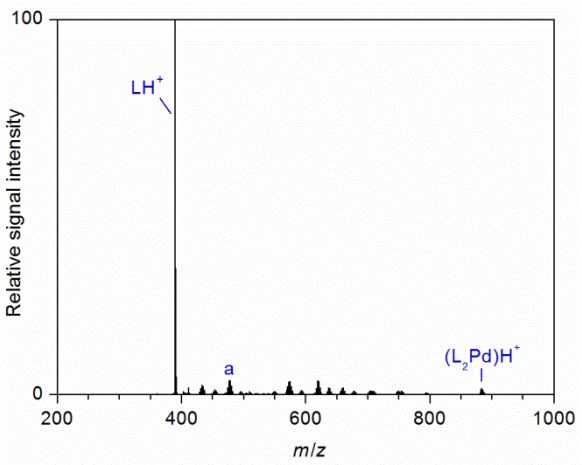

Figure 8.36 Positive-ion mode ESI mass spectrum of a solution of PEPPSI-IPr (3 mM) and BuZnBr·LiBr (15 mM) in THF (a = $Li_3ZnBr_4(THF)^+$, L = *N*-heterocyclic carbene).

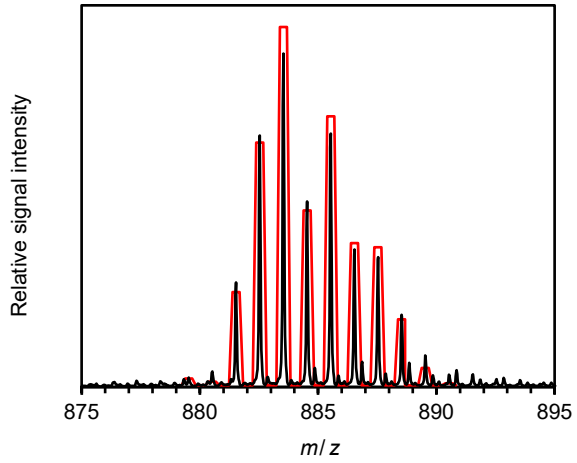

Figure 8.37 Measured (black) and simulated (red) isotope pattern of $(L_2Pd)H^+$ (L = *N*-heterocyclic carbene).

Table 8.13 Measured and theoretical *m*/*z* ratios of selected ions. For each ion, only the most abundant isotopologue is considered.

ion	sum formula	*m*/*z*(measured)	*m*/*z*(theoretical)
LH^+	$C_{27}H_{37}N_2^+$	389.29	389.30
$Li_3ZnBr_4(THF)^+$	$C_4H_8Br_4Li_3OZn^+$	478.69	478.70
$(L_2Pd)H^+$	$C_{54}H_{73}N_4Pd^+$	883.52	883.49

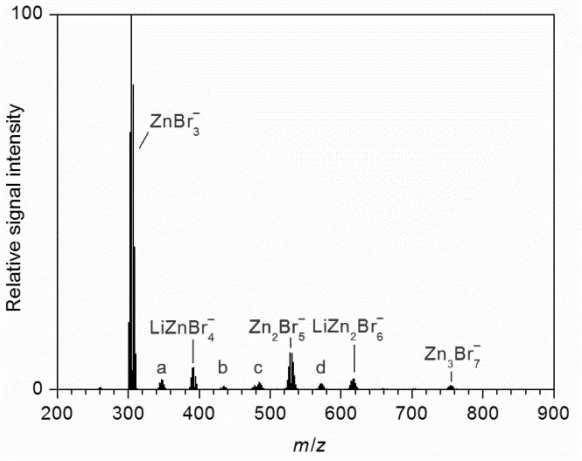

Figure 8.38 Negative-ion mode ESI mass spectrum of a solution of PEPPSI-IPr (3 mM) and BuZnBr·LiBr (15 mM) in THF (a = $LiZnClBr_3^-$, b = $Li_2ZnClBr_4^-$, c = $Zn_2ClBr_4^-$, d = $LiZn_2ClBr_5^-$).

Table 8.14 Measured and theoretical *m*/*z* ratios of selected ions. For each ion, only the most abundant isotopologue is considered.

ion	sum formula	*m*/*z*(measured)	*m*/*z*(theoretical)
$ZnBr_3^-$	Br_3Zn^-	304.68	304.68
$LiZnClBr_3^-$	$Br_3ClLiZn^-$	346.66	346.66
$LiZnBr_4^-$	Br_4LiZn^-	392.61	392.61
$Li_2ZnClBr_4^-$	$Br_4ClLi_2Zn^-$	434.58	434.60
$Zn_2ClBr_4^-$	$Br_4ClZn_2^-$	484.48	484.49
$Zn_2Br_5^-$	$Br_5Zn_2^-$	530.41	530.44
$LiZn_2ClBr_5^-$	$Br_5ClLiZn_2^-$	572.40	572.43
$LiZn_2Br_6^-$	$Br_6LiZn_2^-$	616.37	616.38
$Zn_3Br_7^-$	$Br_7Zn_3^-$	754.15	754.21

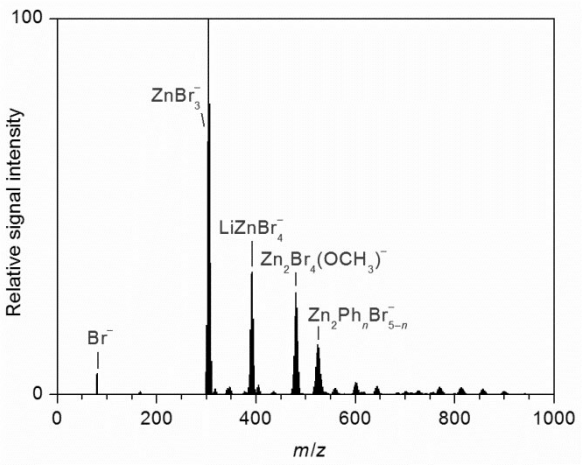

Figure 8.39 Negative-ion mode ESI mass spectrum of a solution of $Pd(OAc)_2$ (3 mM), S-PHOS (L, 6 mM), and PhZnBr·LiBr (15 mM) in THF.

Table 8.15 Measured and theoretical *m*/*z* ratios of selected ions. For each ion, only the most abundant isotopologue is considered.

ion	sum formula	*m*/*z*(measured)	*m*/*z*(theoretical)
Br^-	Br^-	78.93	78.92
$ZnBr_3^-$	Br_3Zn^-	304.68	304.68
$LiZnBr_4^-$	Br_4LiZn^-	392.61	392.61
$Zn_2Br_4(OCH_3)^-$	$CH_3Br_4OZn_2^-$	480.54	480.54
$Zn_2PhBr_4^-$	$C_6H_5Br_4Zn_2^-$	526.57	526.56
$Zn_2Br_5^-$	$Br_5Zn_2^-$	530.44	530.44

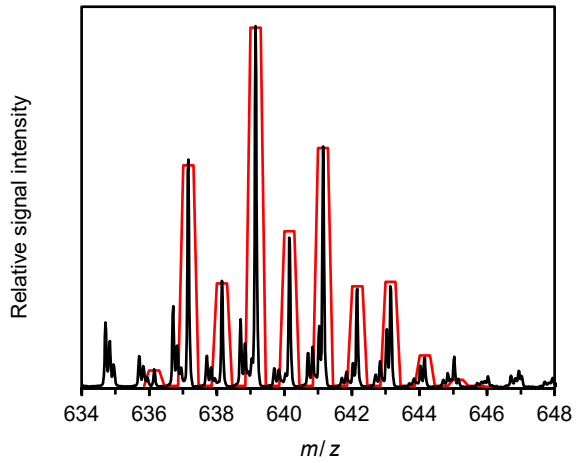

Figure 8.40 Measured (black) and simulated (red) isotope pattern of $LLiZnBnBr^+$ (L = S-PHOS).

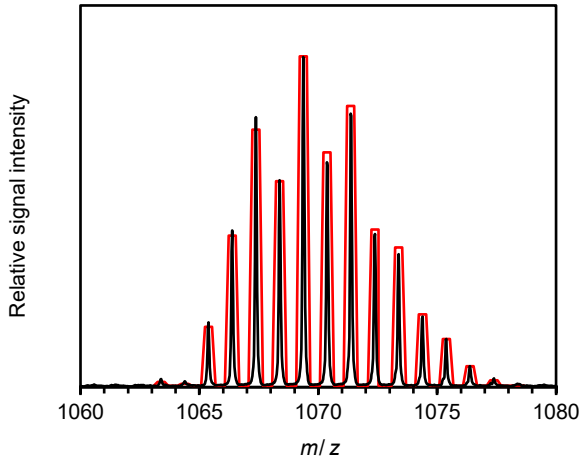

Figure 8.41 Measured (black) and simulated (red) isotope pattern of $L_2PdZnBn^+$ (L = S-PHOS).

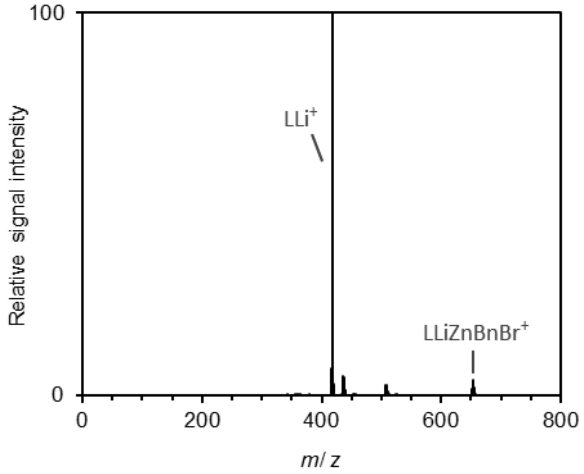

Figure 8.42 Mass spectrum of mass-selected $LLiZnBnBr^+$ and its daughter ions produced upon collision-induced dissociation (E_{LAB} = 10 eV).

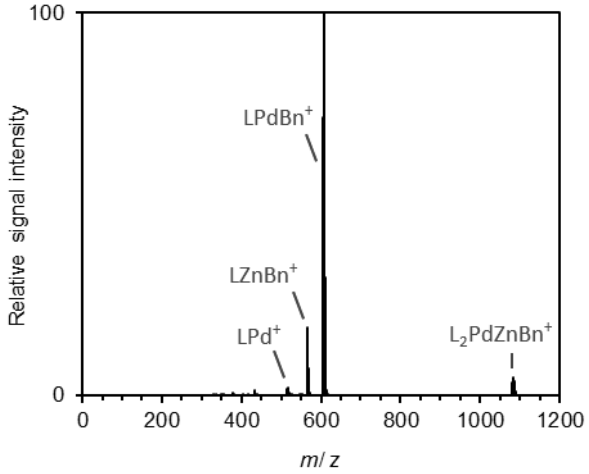

Figure 8.43 Mass spectrum of mass-selected $L_2PdZnBn^+$ and its daughter ions produced upon collision-induced dissociation (E_{LAB} = 30 eV).

Table 8.16 Measured and theoretical *m*/*z* ratios of selected ions. For each ion, only the most abundant isotopologue is considered.

ion	sum formula	*m*/*z*(measured)	*m*/*z*(theoretical)
$Li_3ZnBr(OAc)_3^+$	$C_6H_9BrLi_3O_6Zn^+$	342.93	342.93
$Li_2ZnBr_2(OAc)(THF)^+$	$C_6H_{11}Br_2Li_2O_3Zn^+$	368.86	368.87
LLi^+	$C_{26}H_{35}LiO_2P^+$	417.25	417.25

$(LO)Li^+$	$C_{26}H_{35}LiO_3P^+$	433.25	433.25
$Li_2ZnBr_3(THF)_2^+$	$C_8H_{16}Br_3Li_2O_2Zn^+$	462.83	462.83
$Li_3ZnBr_4(THF)^+$	$C_4H_8Br_4Li_3OZn^+$	478.70	478.70
$Li_4ZnBr_2(OAc)_3(THF)^+$	$C_{10}H_{17}Br_2Li_4O_7Zn^+$	500.92	500.92
$Li_2ZnBr_3(THF)_3^+$	$C_{12}H_{24}Br_3Li_2O_3Zn^+$	534.88	534.88
$Li_3ZnBr_4(THF)_2^+$	$C_8H_{16}Br_4Li_3O_2Zn^+$	550.76	550.76
$Li_3ZnBr_4(THF)_3^+$	$C_{12}H_{24}Br_4Li_3O_3Zn^+$	622.82	622.82
$LLiZnBnBr^+$	$C_{33}H_{42}BrLiO_2PZn^+$	653.15	653.15
L_2PdLi^+	$C_{52}H_{70}LiO_4P_2Pd^+$	933.40	933.40
$L_2PdZnBn^+$	$C_{59}H_{77}O_4P_2PdZn^+$	1083.37	1083.36

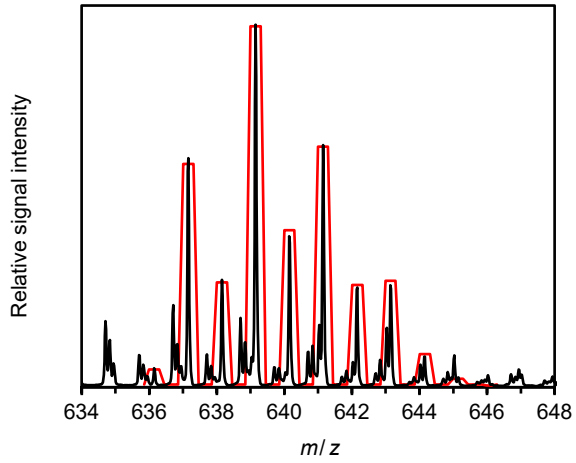

Figure 8.44 Measured (black) and simulated (red) isotope pattern of $LLiZnPhBr^+$ (L = S-PHOS).

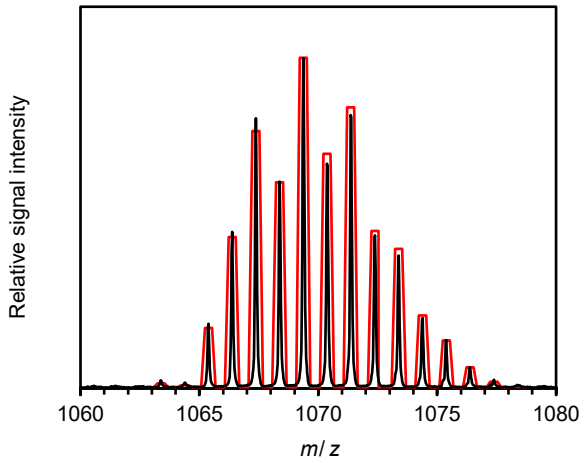

Figure 8.45 Measured (black) and simulated (red) isotope pattern of $L_2PdZnPh^+$ (L = S-PHOS).

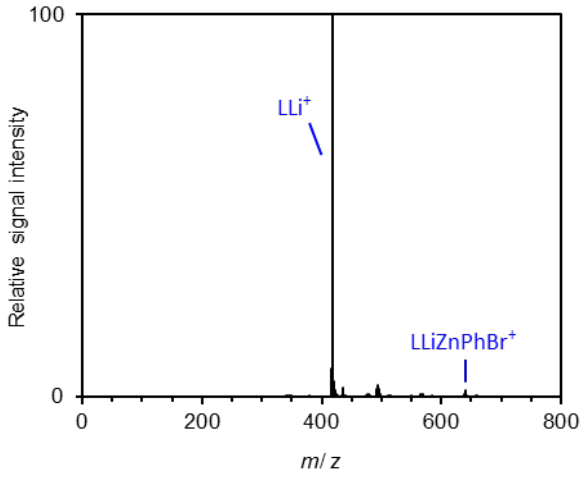

Figure 8.46 Mass spectrum of mass-selected $LLiZnPhBr^+$ and its daughter ions produced upon collision-induced dissociation (E_{LAB} = 10 eV).

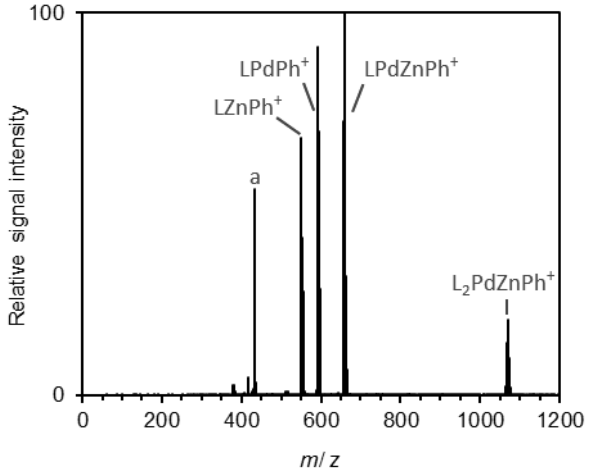

Figure 8.47 Mass spectrum of mass-selected $L_2PdZnPh^+$ and its daughter ions produced upon collision-induced dissociation (E_{LAB} = 30 eV). The peak labeled a corresponds to $(LO)Li^+$, which results from an isobaric contamination of the parent ion.

Table 8.17 Measured and theoretical *m*/*z* ratios of selected ions. For each ion, only the most abundant isotopologue is considered.

ion	sum formula	*m*/*z*(measured)	*m*/*z*(theoretical)
$Li_3ZnBr_3OH^+$	$Br_3HLi_3OZn^+$	342.74	342.73
$Li_3H_2Br_4(THF)^+$	$C_4H_{10}Br_4Li_3OZn^+$	414.80	414.79
LLi^+	$C_{26}H_{35}LiO_2P^+$	417.27	417.25
$(LO)Li^+$	$C_{26}H_{35}LiO_3P^+$	433.26	433.25
$Li_2ZnBr_3(THF)_2^+$	$C_8H_{16}Br_3Li_2O_2Zn^+$	462.84	462.83
$Li_3ZnBr_4(THF)^+$	$C_4H_8Br_4Li_3OZn^+$	478.72	478.70
$Li_3H_2Br_4(THF)_2^+$	$C_8H_{18}Br_4Li_3O_2^+$	486.86	486.85
$Li_2ZnBr_3(THF)_3^+$	$C_{12}H_{24}Br_3Li_2O_3Zn^+$	534.90	534.88
$Li_3ZnBr_4(THF)_2^+$	$C_8H_{16}Br_4Li_3O_2Zn^+$	550.78	550.76
$Li_3ZnBr_4(THF)_3^+$	$C_{12}H_{24}Br_4Li_3O_2Zn^+$	622.83	622.82
$LLiZnPhBr^+$	$C_{32}H_{40}BrLiO_2PZn^+$	639.16	639.14
$Li_3ZnBr_4(THF)_4^+$	$C_{16}H_{32}Br_4Li_3O_4Zn^+$	694.89	694.87

$LLiZnPhBr(THF)^+$	$C_{36}H_{48}BrLiO_3PZn^+$	711.21	711.20
L_2PdLi^+	$C_{52}H_{70}LiO_4P_2Pd^+$	933.42	933.40
$L_2PdZnPh^+$	$C_{58}H_{75}O_4P_2PdZn^+$	1069.38	1069.35
$L_2Zn_2Ph_2Br^+$	$C_{64}H_{80}BrO_4P_2Zn_2^+$	1185.36	1185.33

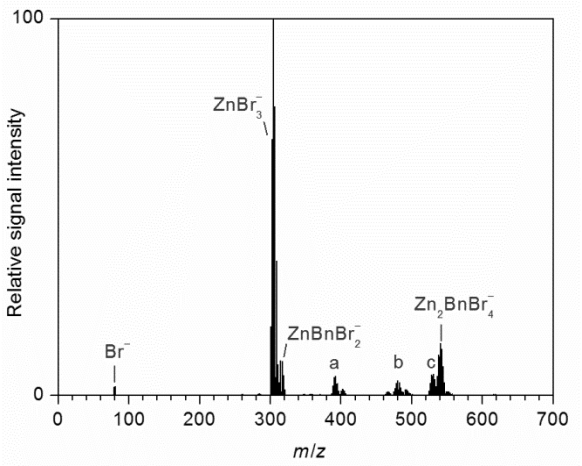

Figure 8.48 Negative-ion mode ESI mass spectrum of a solution of $Pd(OAc)_2$ (3 mM), S-PHOS (L, 6 mM), and BnZnBr·LiBr (15 mM) in THF (a = $LiZnBr_4^-$, b = $Zn_2Br_4(OCH_3)^-$, c = $Zn_2Br_5^-$).

Table 8.18 Measured and theoretical *m*/*z* ratios of selected ions. For each ion, only the most abundant isotopologue is considered.

ion	sum formula	*m*/*z*(measured)	*m*/*z*(theoretical)
Br^-	Br^-	78.93	78.92
$ZnBr_3^-$	Br_3Zn^-	304.68	304.68
$ZnBnBr_2^-$	$C_7H_7Br_2Zn^-$	314.81	314.82
$LiZnBr_4^-$	Br_4LiZn^-	392.60	392.61
$Zn_2Br_4(OCH_3)^-$	$CH_3Br_4OZn_2^-$	480.53	480.54
$Zn_2Br_5^-$	$Br_5Zn_2^-$	530.43	530.44
$Zn_2BnBr_4^-$	$C_7H_7Br_4Zn_2^-$	540.57	540.58

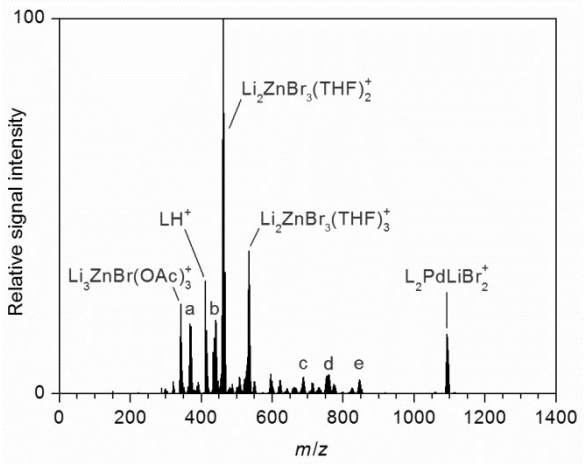

Figure 8.49 Positive-ion mode ESI mass spectrum of a solution of $Pd(OAc)_2$ (3 mM), S-PHOS (L, 6 mM), and $ZnBr_2$·LiBr (15 mM) in THF (a = $Li_2ZnBr_2(OAc)(THF)^+$, b = $Li_2ZnBr_2(OAc)(THF)_2^+$, c = $Li_2Zn_2Br_5(THF)_2^+$, d = $Li_3Zn_2Br_5(OAc)(THF)_2^+$/ $Li_2Zn_2Br_5(THF)_3^+$, e = $Li_3Zn_2Br_6(THF)_3^+$).

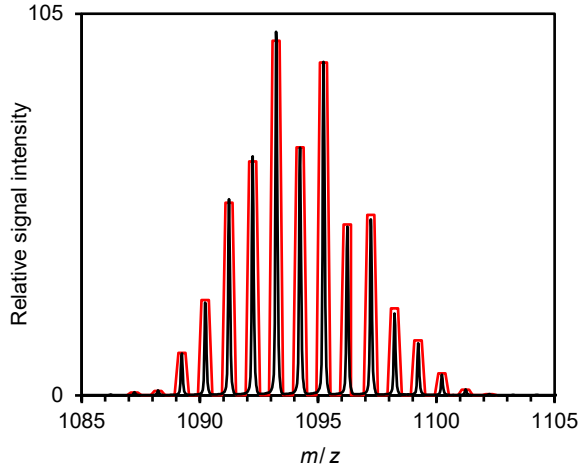

Figure 8.50 Measured (black) and simulated (red) isotope pattern of $L_2PdLiBr_2^+$ (L = S-PHOS).

Table 8.19 Measured and theoretical *m*/*z* ratios of selected ions. For each ion, only the most abundant isotopologue is considered.

ion	sum formula	*m*/*z*(measured)	*m*/*z*(theoretical)
$Li_3ZnBr(OAc)_3^+$	$C_6H_9BrLi_3O_6Zn^+$	342.94	342.93
$Li_2ZnBr_2(OAc)(THF)^+$	$C_6H_{11}Br_2Li_2O_3Zn^+$	368.87	368.87
LH^+	$C_{26}H_{36}O_2P^+$	411.25	411.24
$Li_2ZnBr_2(OAc)(THF)_2^+$	$C_{10}H_{19}Br_2Li_2O_3Zn^+$	440.92	440.92
$Li_2ZnBr_3(THF)_2^+$	$C_8H_{16}Br_3Li_2O_2Zn^+$	462.83	462.83
$Li_2ZnBr_3(THF)_3^+$	$C_{12}H_{24}Br_3Li_2O_3Zn^+$	534.89	534.88
$Li_2Zn_2Br_5(THF)_2^+$	$C_8H_{16}Br_5Li_2O_2Zn_2^+$	688.59	688.59
$Li_3Zn_2Br_5(OAc)(THF)_2^+$	$C_{10}H_{19}Br_5Li_3O_4Zn_2^+$	754.6	754.62
$Li_2Zn_2Br_5(THF)_3^+$	$C_{12}H_{24}Br_5Li_2O_3Zn_2^+$	760.65	760.65
$Li_3Zn_2Br_6(THF)_3^+$	$C_{12}H_{24}Br_6Li_3O_3Zn^+$	846.58	846.58
$L_2PdLiBr_2^+$	$C_{52}H_{70}Br_2LiO_4P_2Pd^+$	1093.24	1093.23

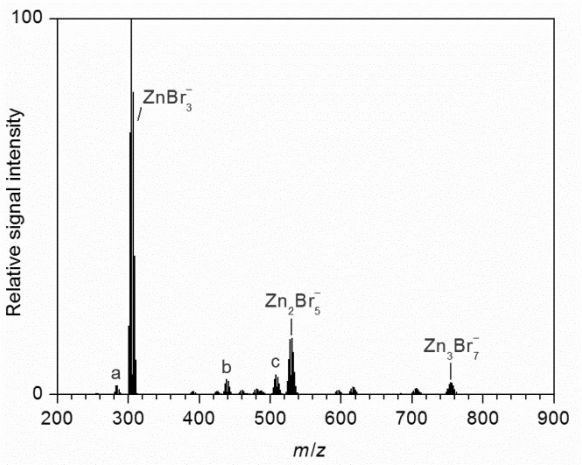

Figure 8.51 Negative-ion mode ESI mass spectrum of a solution of $Pd(OAc)_2$ (3 mM), S-PHOS (L, 6 mM), and $ZnBr_2$·LiBr (15 mM) in THF (a = $ZnBr_2(OAc)^-$, b = $Zn_2Br_2(OAc)_2(OCH_3)^-$, c = $Zn_2Br_4(OAc)^-$).

Table 8.20 Measured and theoretical *m*/*z* ratios of selected ions. For each ion, only the most abundant isotopologue is considered.

ion	sum formula	*m*/*z*(measured)	*m*/*z*(theoretical)
$ZnBr_2(OAc)^-$	$C_2H_3Br_2O_2Zn^-$	282.77	282.78
$ZnBr_3^-$	Br_3Zn^-	304.68	304.68
$Zn_2Br_2(OAc)_2(OCH_3)^-$	$C_5H_9Br_2O_5Zn^-$	438.73	438.74
$Zn_2Br_4(OAc)^-$	$C_2H_3Br_4O_2Zn_2^-$	508.53	508.54
$Zn_2Br_5^-$	$Br_5Zn_2^-$	530.44	530.44
$Zn_3Br_7^-$	$Br_7Zn_3^-$	754.20	754.21

8.1.3 ESI mass spectrometry – catalyst in the presence of aryl iodide substrate

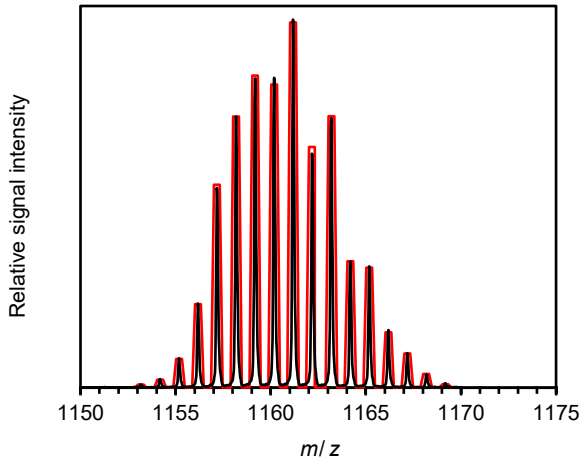

Figure 8.52 Measured (black) and simulated (red) isotope pattern of $L_2Pd_2I^+$ (L = S-PHOS).

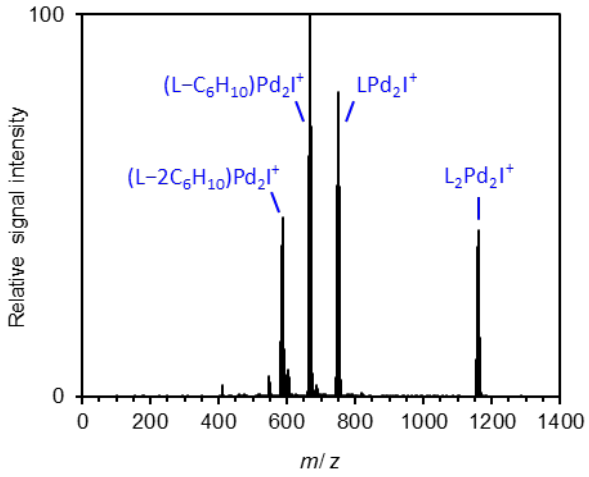

Figure 8.53 Mass spectrum of mass-selected $L_2Pd_2I^+$ and its daughter ions produced upon collision-induced dissociation (E_{LAB} = 40 eV).

Table 8.21 Measured and theoretical *m*/*z* ratios of selected ions. For each ion, only the most abundant isotopologue is considered.

ion	sum formula	*m*/*z*(measured)	*m*/*z*(theoretical)
$L_2Pd_2I^+$	$C_{52}H_{70}IO_4P_2Pd_2^+$	1161.18	1161.19
$L_2Pd_2(PCy_2)^+$	$C_{64}H_{92}O_4P_3Pd_2^+$	1231.42	1231.43

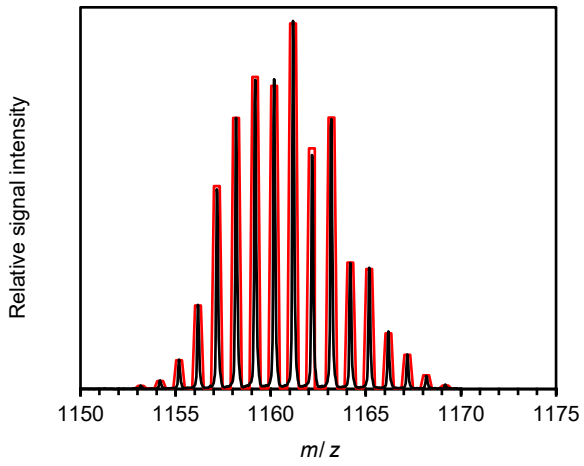

Figure 8.54 Measured (black) and simulated (red) isotope pattern of $L_2Pd_2I^+$ (L = S-PHOS).

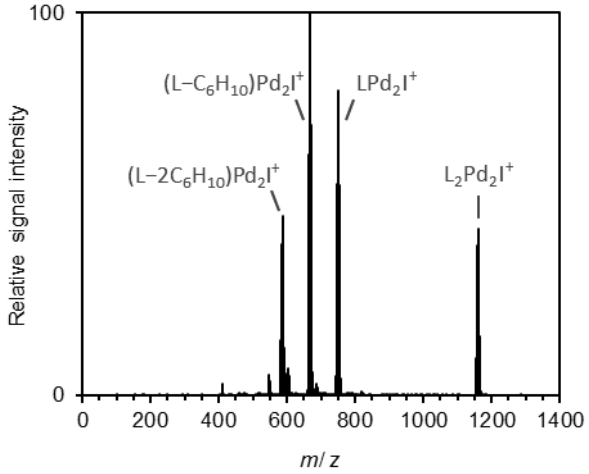

Figure 8.55 Mass spectrum of mass-selected $L_2Pd_2I^+$ and its daughter ions produced upon collision-induced dissociation (E_{LAB} = 40 eV).

Table 8.22 Measured and theoretical *m*/*z* ratios of selected ions. For each ion, only the most abundant isotopologue is considered.

ion	sum formula	*m*/*z*(measured)	*m*/*z*(theoretical)
$L_2Pd_2I^+$	$C_{52}H_{70}IO_4P_2Pd_2^+$	1161.18	1161.19
$L_2Pd_2(PCy_2)^+$	$C_{64}H_{92}O_4P_3Pd_2^+$	1231.42	1231.43

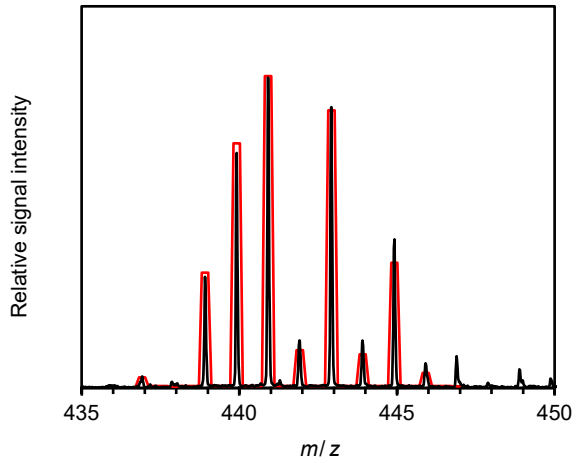

Figure 8.56 Measured (black) and simulated (red) isotope pattern of $ArPdI(OAc)^-$ (Ar = 4-EtOOC-C_6H_4).

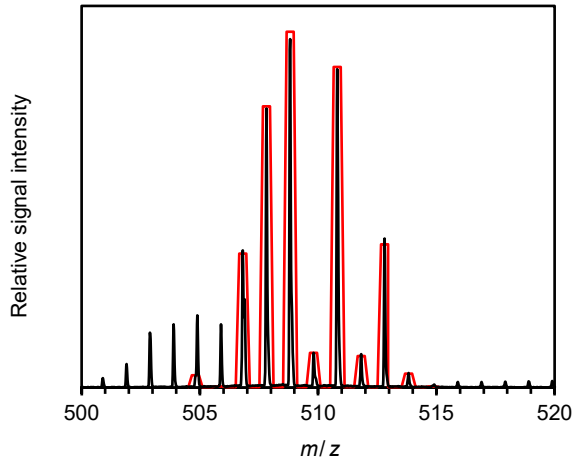

Figure 8.57 Measured (black) and simulated (red) isotope pattern of $ArPdI_2^-$ (Ar = 4-EtOOC-C_6H_4).

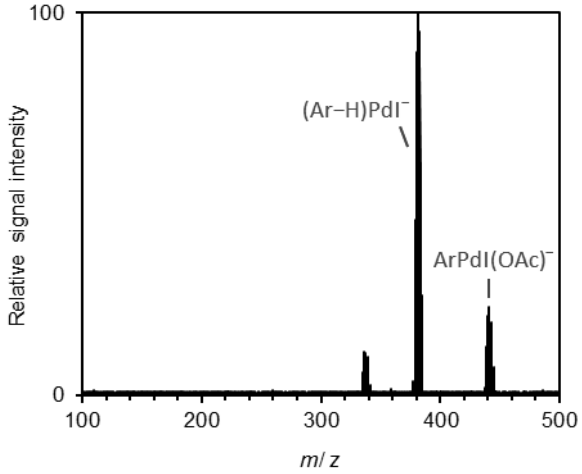

Figure 8.58 Mass spectrum of mass-selected $ArPdI(OAc)^-$ and its daughter ions produced upon collision-induced dissociation (E_{LAB} = 15 eV).

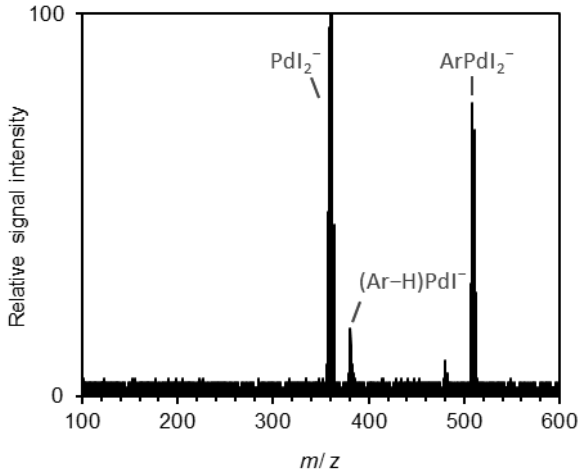

Figure 8.59 Mass spectrum of mass-selected $ArPdI_2^-$ and its daughter ions produced upon collision-induced dissociation (E_{LAB} = 30 eV).

Table 8.23 Measured and theoretical *m*/*z* ratios of selected ions. For each ion, only the most abundant isotopologue is considered.

ion	sum formula	*m*/*z*(measured)	*m*/*z*(theoretical)
$ArPdI(OAc)^-$	$C_{11}H_{12}IO_4Pd^-$	440.92	440.88
$ArPdI_2^-$	$C_9H_9I_2O_2Pd^-$	508.81	508.77
$NaPd_2(OAc)_5(OH)^-$	$C_{10}H_{16}NaO_{11}Pd_2^-$	548.91	548.87

$Pd_4(OAc)_4(OH)_5^-$	$C_8H_{17}O_{13}Pd_4^-$	746.74	746.68

8.1.4 ESI mass spectrometry – catalyst in the simultaneous presence of organozinc reagent and aryl iodide substrate

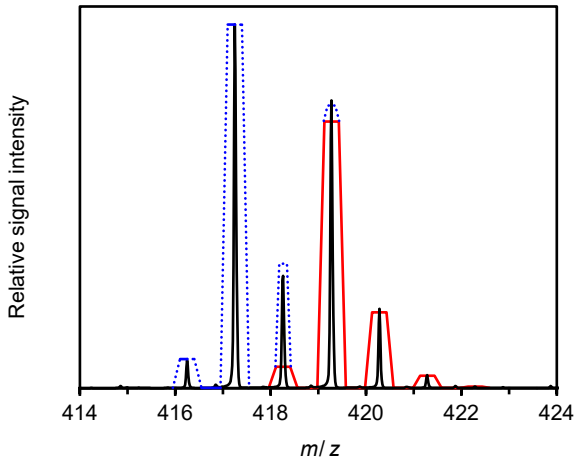

Figure 8.60 Section from the positive-ion mode ESI mass spectrum of a solution of $Pd(OAc)_2$ (3 mM), S-PHOS (L, 6 mM), BuZnBr·LiBr (15 mM), and ArI (Ar = 4-EtOOC-C_6H_4, 3 mM) in THF together with simulated isotope patterns of LLi^+ (blue) and $(ArBu)_2Li^+$ (red) in a ratio of 57:43.

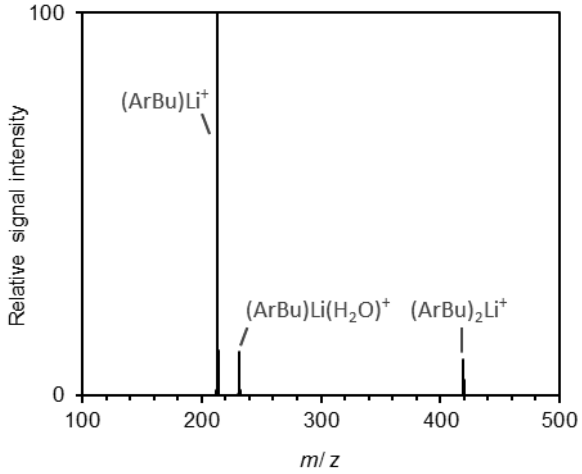

Figure 8.61 Mass spectrum of mass-selected $(ArBu)_2Li^+$ and its daughter ions produced upon collision-induced dissociation (E_{LAB} = 10 eV). The incorporated water originates from an ion-molecule reaction with H_2O present as a contamination in the vacuum system of the mass spectrometer.

Table 8.24 Measured and theoretical *m*/*z* ratios of selected ions. For each ion, only the most abundant isotopologue is considered.

ion	sum formula	*m*/*z*(measured)	*m*/*z*(theoretical)
$Li_3ZnBr(OAc)_3^+$	$C_6H_9BrLi_3O_6Zn^+$	342.93	342.93
$Li_2ZnBr_2(OAc)(THF)^+$	$C_6H_{11}Br_2Li_2O_3Zn^+$	368.86	368.87
LLi^+	$C_{26}H_{35}LiO_2P^+$	417.25	417.25
$(ArBu)_2Li^+$	$C_{26}H_{36}LiO_4^+$	419.28	419.28
$(LO)Li^+$	$C_{26}H_{35}LiO_3P^+$	433.25	433.25
$Li_3ZnBr_3(OAc)(THF)^+$	$C_6H_{11}Br_3Li_3O_3Zn^+$	456.80	456.80
$Li_3ZnBr_4(THF)^+$	$C_4H_8Br_4Li_3OZn^+$	478.70	478.70
$LZnBu^+$	$C_{30}H_{44}O_2PZn^+$	531.24	531.24
$LLiZnBr_2^+$	$C_{26}H_{35}Br_2LiO_2PZn^+$	643.02	643.01
L_2PdLi^+	$C_{52}H_{70}LiO_4P_2Pd^+$	933.40	933.40
$L_2PdZnBu^+$	$C_{56}H_{79}O_4P_2PdZn^+$	1049.38	1049.38

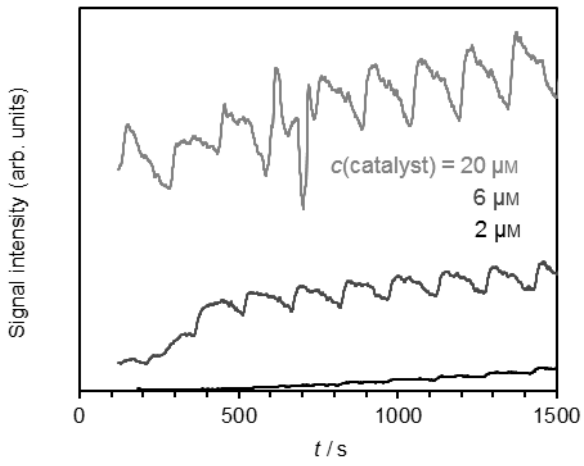

Figure 8.62. Time dependence of the signal intensity of $(ArBu)_2Li^+$ (*m*/*z* 420.3) formed in the cross-coupling reaction between ArI (6 mM) and BuZnBr·LiBr (15 mM) in THF at room temperature with different catalyst loadings (precatalyst: $Pd(OAc)_2$/2 S-PHOS). The reactions are monitored with positive-ion mode ESI mass spectrometry after combination of all reaction partners at t = 0 and stirring. The observed oscillations presumably do not reflect periodic changes of the concentration of ArBu, but rather the uneven motion of the step motor of the syringe pump used to inject the sample solution.

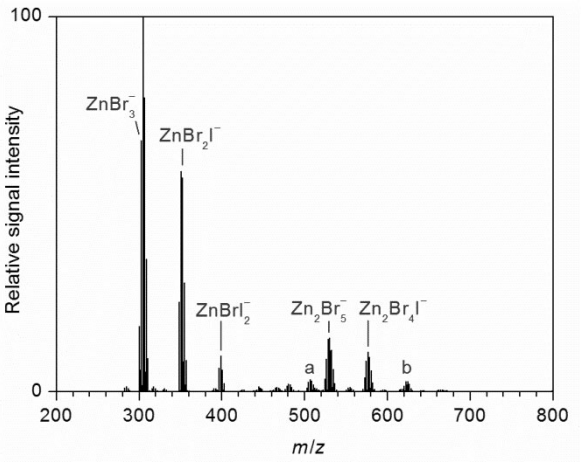

Figure 8.63 Negative-ion mode ESI mass spectrum of a solution of $Pd(OAc)_2$ (3 mM), S-PHOS (L, 6 mM), BuZnBr·LiBr (15 mM), and ArI (Ar = 4-EtOOC-C_6H_4, 3 mM) in THF (a = $Zn_2BuBr_4^-$, b = $Zn_2Br_3I_2^-$).

Table 8.25 Measured and theoretical *m*/*z* ratios of selected ions. For each ion, only the most abundant isotopologue is considered.

ion	sum formula	*m*/*z*(measured)	*m*/*z*(theoretical)
$ZnBr_3^-$	Br_3Zn^-	304.68	304.68
$ZnBr_2I^-$	Br_2IZn^-	350.67	350.67
$ZnBrI_2^-$	BrI_2Zn^-	398.65	398.65
$Zn_2BuBr_4^-$	$C_4H_9Br_4Zn_2^-$	506.59	506.60
$Zn_2Br_5^-$	$Br_5Zn_2^-$	530.44	530.44
$Zn_2Br_4I^-$	$Br_4IZn_2^-$	576.43	576.43
$Zn_2Br_3I_2^-$	$Br_3I_2Zn_2^-$	624.41	624.42

8.2 Further data of Intermediates on Anionic Pd^0 and Pd^{II} Ate Complexes

Table 8.26 Measured and theoretical *m*/*z* ratios of selected ions. For each ion, only the most abundant isotopologue is considered.

ion	sum formula	*m*/*z*(measured)	*m*/*z*(theoretical)
$[(L_F)_2PdBr]^-$	$C_{48}H_{18}BrF_{36}P_2Pd^-$	1526.88	1526.85
$[(L_F)_3PdBr]^-$	$C_{72}H_{27}BrF_{54}P_3Pd^-$	2196.91	2196.87
$[(L_F)_3Pd_2Br_3]^-$	$C_{72}H_{27}Br_3F_{54}P_3Pd_2^-$	2462.65	2462.61
$[(L_F)_4Pd_2Br]^-$	$C_{96}H_{36}BrF_{72}P_4Pd_2^-$	2972.86	2972.79

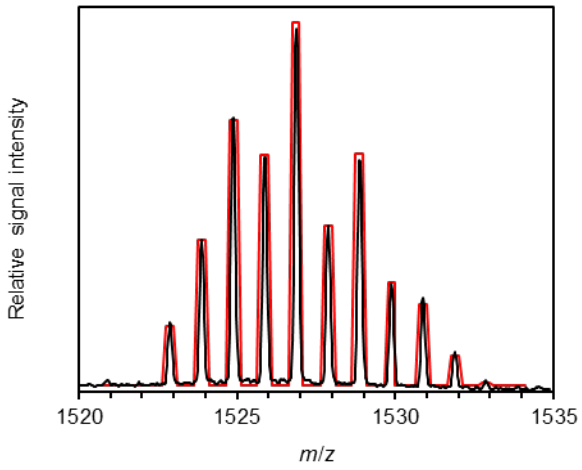

Figure 8.64 Measured (black) and simulated (red) isotope pattern of $[(L_F)_2PdBr]^-$ (L_F = tris[3,5-bis(trifluoromethyl)-phenyl]phosphine).

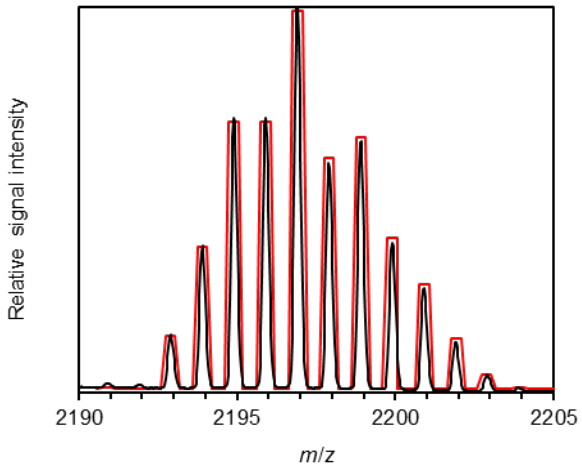

Figure 8.65 Measured (black) and simulated (red) isotope pattern of $[(L_F)_3PdBr]^-$ (L_F = tris[3,5-bis(trifluoromethyl)-phenyl]phosphine).

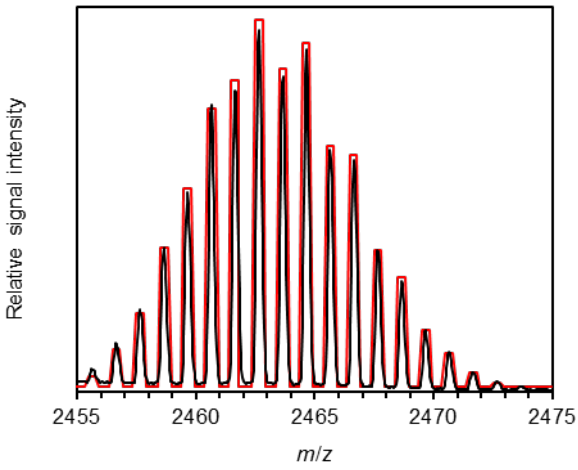

Figure 8.66 Measured (black) and simulated (red) isotope pattern of $[(L_F)_3Pd_2Br_3]^-$ (L_F = tris[3,5-bis(trifluoromethyl)-phenyl]phosphine).

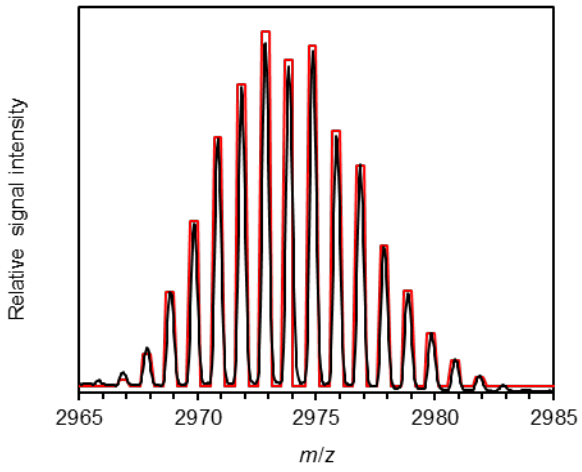

Figure 8.67 Measured (black) and simulated (red) isotope pattern of $[(L_F)_4Pd_2Br]^-$ (L_F = tris[3,5-bis(trifluoromethyl)-phenyl]phosphine).

Table 8.27 Measured and theoretical *m*/*z* ratios of selected ions. For each ion, only the most abundant isotopologue is considered.

ion	sum formula	*m*/*z*(measured)	*m*/*z*(theoretical)
$[(Ar_F)_3P(O)\cdot Br]^-$	$C_{24}H_9BrF_{18}OP^-$	766.94	766.93
$[(Ar_F)_5P_2O_3]^-$	$C_{40}H_{15}F_{30}O_3P_2^-$	1175.02	1175.00

Table 8.28 Measured and theoretical *m*/*z* ratios of selected ions. For each ion, only the most abundant isotopologue is considered.

ion	sum formula	*m*/*z*(measured)	*m*/*z*(theoretical)
$[ZnBr_3]^-$	Br_3Zn^-	304.69	304.68
$[FeBr_4]^-$	Br_4Fe^-	375.61	375.60
$[(Ar_F)_2N]^-$	$C_{16}H_6F_{12}N^-$	440.04	440.03
$[((Ar_F)_2NH)Br]^-$	$C_{16}H_7BrF_{12}N^-$	519.97	519.96
$[(Ar_F)_2,(Ar_F{-}H),N,O]^-$	$C_{24}H_8F_{18}NO^-$	668.04	668.03
$[((Ar_F)_3N)Br]^-$	$C_{24}H_9BrF_{18}N^-$	733.97	733.96
$[((Ar_F)_3NO)Br]^-$	$C_{24}H_9BrF_{18}NO^-$	749.97	749.96
$[(L_F)Br]^-$	$C_{24}H_9BrF_{18}P^-$	750.96	750.93
$[((Ar_F)_2NH)_2Br]^-$	$C_{32}H_{14}BrF_{24}N_2^-$	963.01	962.99
$[((Ar_F)_2NH)(Ar_F)_3NO)Br]^-$	$C_{40}H_{16}BrF_{30}N_2O^-$	1191.03	1191.00
$[(L_F)_2FeBr_3]^-$	$C_{48}H_{18}Br_3F_{36}FeP_2^-$	1636.78	1636.72

Table 8.29 Measured and theoretical *m*/*z* ratios of selected ions. For each ion, only the most abundant isotopologue is considered.

ion	sum formula	*m*/*z*(measured)	*m*/*z*(theoretical)
$[P_2(Ar_F)_3]^-$	$C_{24}H_9F_{18}P_2^-$	701.01	700.99
$[Pd,P_3,(Ar_F)_6]^-$	$C_{48}H_{18}F_{36}P_3Pd^-$	1476.97	1476.91
$[(L_F)_2PdAr_F]^-$	$C_{56}H_{21}F_{42}P_2Pd^-$	1658.99	1658.95

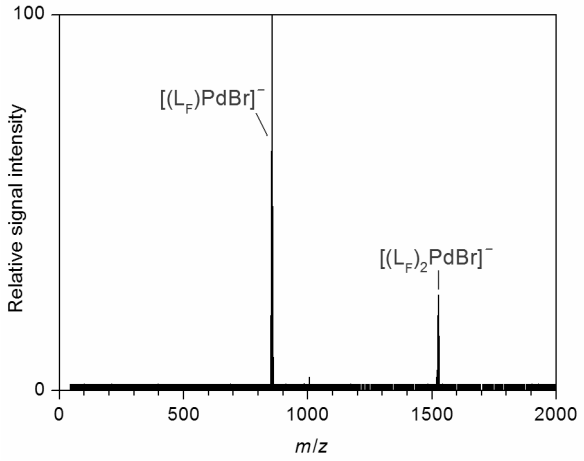

Figure 8.68 Mass spectrum of mass-selected $[(L_F)_2PdBr]^-$ and its daughter ions produced upon collision-induced dissociation (E_{LAB} = 15 eV, L_F = tris[3,5-bis(trifluoromethyl)-phenyl]phosphine).

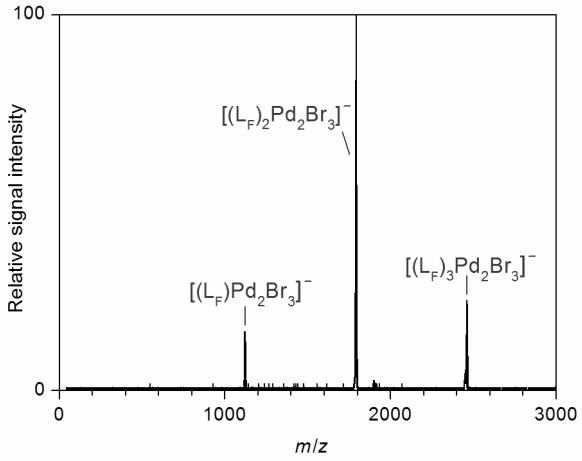

Figure 8.69 Mass spectrum of mass-selected $[(L_F)_3Pd_2Br_3]^-$ and its daughter ions produced upon collision-induced dissociation (E_{LAB} = 15 eV, L_F = tris[3,5-bis(trifluoromethyl)-phenyl]phosphine).

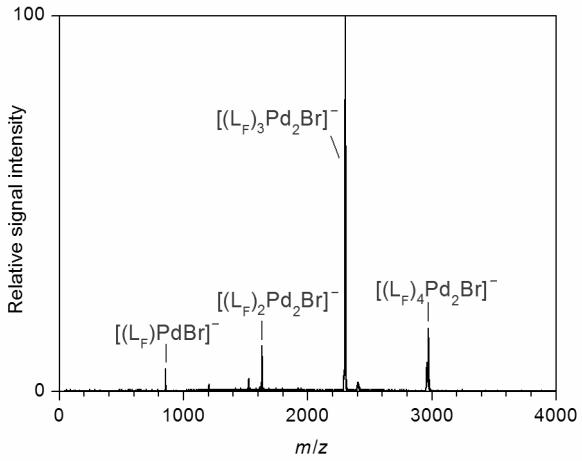

Figure 8.70 Mass spectrum of mass-selected $[(L_F)_4Pd_2Br]^-$ and its daughter ions produced upon collision-induced dissociation (E_{LAB} = 15 eV, L_F = tris[3,5-bis(trifluoromethyl)-phenyl]phosphine).

Table 8.30 Measured and theoretical *m*/*z* ratios of selected ions. For each ion, only the most abundant isotopologue is considered.

ion	sum formula	*m*/*z*(measured)	*m*/*z*(theoretical)
$[P_2(Ar_F)_3]^-$	$C_{24}H_9F_{18}P_2^-$	701.02	700.99
$[(L_F)Pd(Ar)I_2]^-$	$C_{33}H_{18}F_{18}I_2O_2PPd^-$	1178.83	1178.79
$[(L_F)Pd(Ar_F)I_2]^-$	$C_{32}H_{12}F_{24}I_2PPd^-$	1242.78	1242.74
$[(L_F)_2,Pd,O,I]^-$	$C_{48}H_{18}F_{36}IOP_2Pd^-$	1588.89	1588.84
$[(L_F)_2CuI_2]^-$	$C_{48}H_{18}CuF_{36}I_2P_2^-$	1656.82	1656.77
$[(L_F)_2PdI_3]^-$	$C_{48}H_8F_{36}I_3P_2Pd^-$	1826.71	1826.65
$[(L_F)_2Pd(Ar)I_2]^-$	$C_{57}H_{27}F_{36}I_2O_2P_2Pd^-$	1848.87	1848.81
$[(L_F)_3Pd_2(Ar_F)I_2]^-$	$C_{80}H_{30}F_{60}I_2P_3Pd_2^-$	2690.78	2690.68

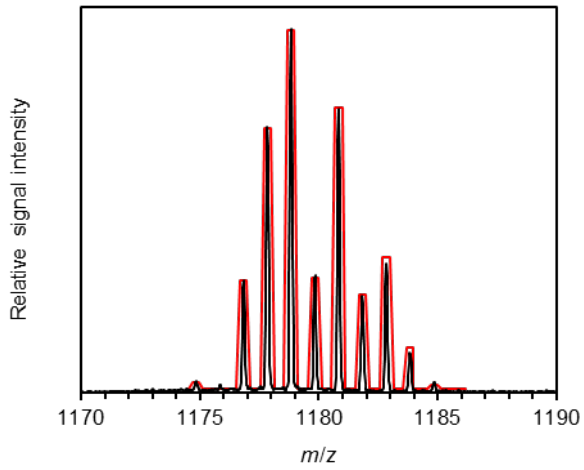

Figure 8.71 Measured (black) and simulated (red) isotope pattern of $[(L_F)Pd(Ar)I_2]^-$ (L_F = tris[3,5-bis(trifluoromethyl)-phenyl]phosphine).

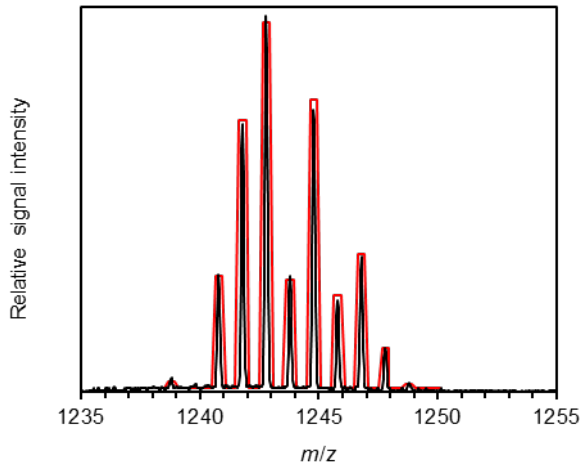

Figure 8.72 Measured (black) and simulated (red) isotope pattern of $[(L_F)Pd(Ar_F)I_2]^-$ (L_F = tris[3,5-bis(trifluoromethyl)-phenyl]phosphine, Ar_F = 3,5-bis(trifluoromethyl)-phenyl).

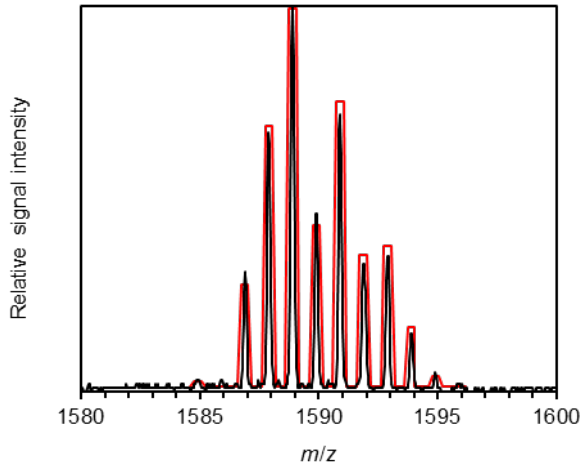

Figure 8.73 Measured (black) and simulated (red) isotope pattern of $[(L_F)_2,Pd,O,I]^-$ (L_F = tris[3,5-bis(trifluoromethyl)-phenyl]phosphine).

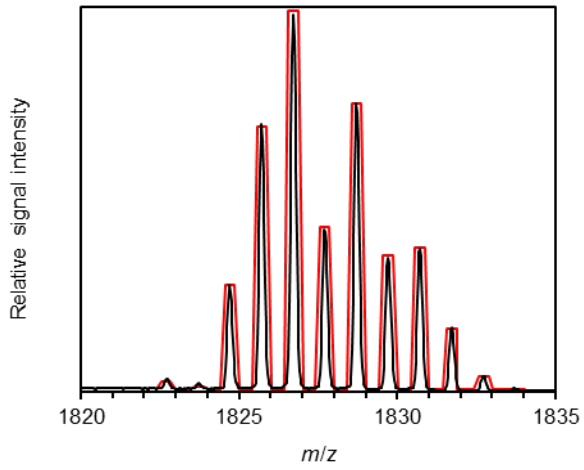

Figure 8.74 Measured (black) and simulated (red) isotope pattern of $[(L_F)_2PdI_3]^-$ (L_F = tris[3,5-bis(trifluoromethyl)-phenyl]phosphine).

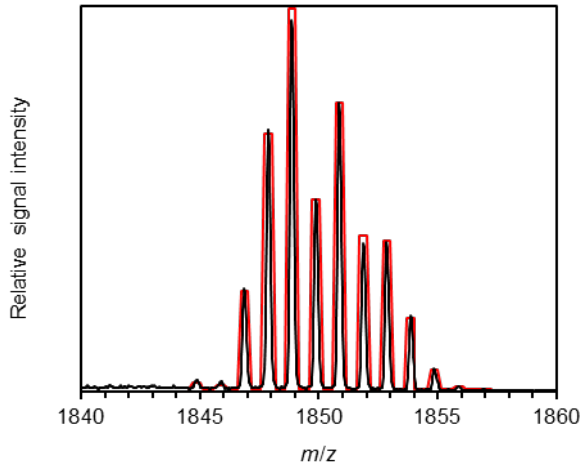

Figure 8.75 Measured (black) and simulated (red) isotope pattern of $[(L_F)_2Pd(Ar)I_2]^-$ (L_F = tris[3,5-bis(trifluoromethyl)-phenyl]phosphine).

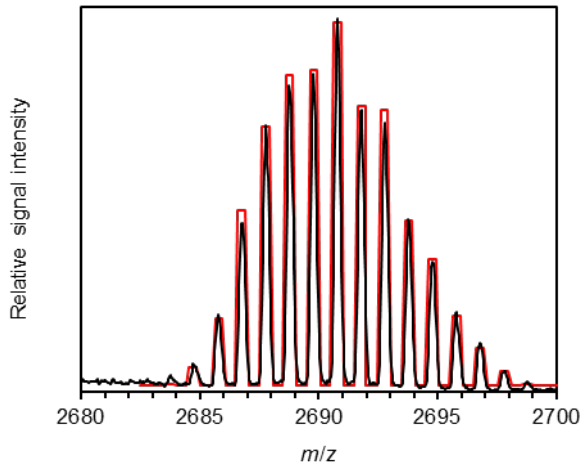

Figure 8.76. Measured (black) and simulated (red) isotope pattern of $[(L_F)_3Pd_2(Ar_F)I_2]^-$ (L_F = tris[3,5-bis(trifluoromethyl)-phenyl]phosphine, Ar_F = 3,5-bis(trifluoromethyl)-phenyl).

9 Literature

[1] K. C. Nicolaou, D. Vourloumis, N. Winssinger, P. S. Baran, *Angew. Chem. Int. Ed.* **2000**, *39*, 44–122.

[2] B. M. Trost, *Angew. Chem. Int. Ed.* **1995**, *34*, 259–281.

[3] P. Knochel (Eds.), *Handbook of Functionalized Organometallics*, Wiley-VCH Verlag GmbH & Co. KGaA, **2005**.

[4] a) F. Diederich, P. Stang (Eds.), *Metal-catalyzed Cross-Coupling Reactions*, Wiley-VCH, Weinheim, Germany, **1998**; b) A. de Meijere, F. Diederich (Eds.), *Metal-Catalyzed Cross-Coupling Reactions, Second Completely Revised and Enlarged Edition. Vol. 2*, Wiley-VC Ch Verlag GmbH & Co, KGaA, **2004**; c) A. de Meijere, F. Diederich (Eds.), *Metal-Catalyzed Cross-Coupling Reactions, Second Completely Revised and Enlarged Edition. Vol. 1*, Wiley-VC Ch Verlag GmbH & Co, KGaA, **2004**.

[5] E. Negishi, A. O. King, N. Okukado, *J. Org. Chem.* **1977**, *42*, 1821–1823.

[6] a) R. F. Heck, *J. Am. Chem. Soc.* **1968**, *90*, 5535–5538; b) R. F. Heck, *J. Am. Chem. Soc.* **1968**, *90*, 5518–5526; c) R. F. Heck, J. P. Nolley, *J. Org. Chem.* **1972**, *37*, 2320–2322.

[7] a) E.-i. Negishi, L. Valente, F., M. Kobayashi, *J. Am. Chem. Soc.* **1980**, *102*, 3298–3299; b) E.-i. Negishi, *Angew. Chem.* **2011**, *123*, 6870–6897; *Angew. Chem. Int. Ed*. **2011**, *50*, 6738–6764.

[8] a) D. Milstein, J. K. Stille, *J. Am. Chem. Soc.* **1978**, *100*, 3636–3638; b) D. Milstein, J. K. Stille, *J. Am. Chem. Soc.* **1979**, *101*, 4992–4998.

[9] a) N. Miyaura, K. Yamada, A. Suzuki, *Tetrahedron Lett.* **1979**, *20*, 3437–3440; b) N. Miyaura, T. Yanagi, A. Suzuki, *Synth. Commun.* **1981**, *7*, 513–519; c) A. Suzuki, *Angew. Chem.* **2011**, *123*, 6854–6869; *Angew. Chem. Int. Ed.* **2011**, *50*, 6722–6737.

[10] M. Kumada, *Pure Appl. Chem.* **1980**, *52*, 669–679.

[11] A. de Meijere, S. Bräse, M. Oestreich (Eds.), *Metal-Catalyzed Cross-Coupling Reactions and More*, Wiley-VCH, Weinheim, **2014**.

[12] a) M. R. Netherton, G. C. Fu, *Adv. Synth. Catal.* **2004**, *346*, 1525–1532; b) A. C. Frisch, M. Beller, *Angew. Chem.* **2005**, *117*, 680–695; *Chem. Int. Ed.* **2005**, *44*, 674–688; c) E. Negishi, Q. Hu, Z. Huang, G. Wang, N. Yin, (Eds.: Z. Rappoport, I. Marek), Wiley, Chichester, **2006**, pp. 457-553.

[13] a) E.-i. Negishi, Z. Huang, G. Wang, S. Mohan, C. Wang, H. Hattori, *Acc. Chem. Res.* **2008**, *41*, 1474–1485; b) G. C. Fu, *Acc. Chem. Res.* **2008**, *41*, 1555–1564; c) G. Manolikakes, M. A. Schade, C. Muñoz Hernandez, H. Mayr, P. Knochel, *Org. Lett.* **2008**, *10*, 2765–2768; d) T. Thaler, B. Haag, A. Gavryushin, K. Schober, E. Hartmann, R. M. Gschwind, H. Zipse, P. Mayer, P. Knochel, *Nature Chem* **2010**, *2*, 125–130; e) S. Çalimsiz, M. Sayah, D. Mallik, M. G. Organ, *Angew. Chem.* **2010**, *122*, 2058–2061; *Angew. Chem. Int. Ed*. **2010**, *49*, 2014–2017; f) A. Krasovskiy, C. Duplais, B. H. Lipshutz, *Org. Lett.* **2010**, *12*, 4742–4744; g) N. Hadei, G. T. Achonduh, C. Valente, C. J. O'Brien, M. G. Organ, *Angew. Chem.* **2011**, *123*, 3982–3985; *Angew. Chem. Int. Ed*. **2011**, *50*, 3896–3899; h) A. Krasovskiy, B. H. Lipshutz, *Org. Lett.* **2011**, *13*, 3818–3821; i) A. Krasovskiy, B. H. Lipshutz, *Org. Lett.* **2011**, *13*, 3822–3825; j) P. Ribagnac, M. Blug, J. Villa-Uribe, X.-F. Le Goff, C. Gosmini, N.

Mézailles, *Chem. Eur. J.* **2011**, *17*, 14389–14393; k) C. I. Stathakis, S. Bernhardt, V. Quint, P. Knochel, *Angew. Chem.* **2012**, *124*, 9563–9567; *Angew. Chem. Int. Ed*. **2012**, *51*, 9428–9432; l) Y. Yang, N. J. Oldenhuis, S. L. Buchwald, *Angew. Chem.* **2013**, *125*, 643–647; *Angew. Chem. Int. Ed*. **2013**, *52*, 615–619; m) Y. Yang, T. J. L. Mustard, P. H.-Y. Cheong, S. L. Buchwald, *Angew. Chem.* **2013**, *125*, 14348–14352; *Angew. Chem. Int. Ed*. **2013**, *52*, 14098–14102; n) J. R. Colombe, S. Bernhardt, C. Stathakis, S. L. Buchwald, P. Knochel, *Org. Lett.* **2013**, *15*, 5754–5757.

[14] a) P. Knochel, H. Leuser, L.-Z. Gong, F. F. Kneisel, in *Handbook of Functionalized of Organometallics, Vol. 1* (Ed.: P. Knochel), Wiley-VCH, Weinheim, **2005**, pp. 251-346; b) A. Krasovskiy, V. Malakhov, A. Gavryushin, P. Knochel, *Angew. Chem.* **2006**, *118*, 6186–6190; *Angew. Chem. Int. Ed.* **2006**, *45*, 6040–6044; c) H. Ren, G. Dunet, P. Mayer, P. Knochel, *J. Am. Chem. Soc.* **2007**, *129*, 5376–5377; d) N. Boudet, S. Sase, P. Sinha, C.-Y. Liu, A. Krasovskiy, P. Knochel, *J. Am. Chem. Soc.* **2007**, *129*, 12358–12359.

[15] a) W. Clegg, S. H. Dale, A. M. Drummond, E. Hevia, G. W. Honeyman, R. E. Mulvey, *J. Am. Chem. Soc.* **2006**, *128*, 7434–7435; b) W. Clegg, B. Conway, E. Hevia, M. D. McCall, L. Russo, R. E. Mulvey, *J. Am. Chem. Soc.* **2009**, *131*, 2375–2384; c) J. A. Garden, A. R. Kennedy, R. E. Mulvey, S. D. Robertson, *Chem. Commun.* **2012**, *48*, 5265–5267.

[16] a) S. H. Wunderlich, P. Knochel, *Angew. Chem.* **2007**, *119*, 7829–7832; *Angew. Chem. Int. Ed*. **2007**, *46*, 7685–7688; b) M. Mosrin, P. Knochel, *Chem. Eur. J.* **2009**, *15*, 1468–1477; c) T. Bresser, M. Mosrin, G. Monzon, P. Knochel, *J. Org. Chem.* **2010**, *75*, 4686–4695; d) C. I. Stathakis, S. M. Manolikakes, P. Knochel, *Org. Lett.* **2013**, *15*, 1302–1305.

[17] C. Elschenbroich, in *Organometallics*, 3rd ed., Wiley-VCH, Weinheim, **2006**.

[18] R. F. Heck, Nobel Lect., http://www.nobelprize.org/nobel_prizes/chemistry/laureates/2010/heck-lecture.html 2010.

[19] J. K. Stille, *Angew Chem. Int. Ed. Engl.* **1956**, *25*, 508–524.

[20] Y. Hatanaka, T. Hiyama, *J. Org. Chem.* **1988**, *53*, 918–920.

[21] A. R. Muci, S. L. Buchwald, *Top. Curr. Chem.* **2002**, *219*, 131–209.

[22] J. F. Hartwig, *Acc. Chem. Res.* **1998**, *31*, 852–860.

[23] a) T. Jeffery, *J. Chem. Soc. Chem.* **1984**, 1287–1289; b) T. Jeffery, *Tetrahedron Lett.* **1985**, *26*, 2667–2670; c) W. Cabri, I. Candiani, S. DeBernardinis, F. Francalanci, S. Penco, R. Santi, *J. Org. Chem.* **1991**, *56*, 5796–5800; d) T. Jeffery, *Tetrahedron* **1996**, *52*, 10113–10130; e) J. P. Robert, W. B. David, *J. Org. Chem.* **1996**, *61*, 7482–7485; f) T. Jeffery, *Tetrahedron Lett.* **1999**, *40*, 1673-1676; g) Z. Wang, Z. Zhang, X. Lu, *Organometallics* **2000**, *19*, 775–780; h) Z. Zhang, X. Lu, Z. Xu, Q. Zhang, X. Han, *Organometallics* **2001**, *20*, 3724–3728; i) K. Fagnou, M. Lautens, *Angew. Chem.* **2002**, *114*, 26–49; *Angew. Chem. Int. Ed*. **2002**, *41*, 26–47; j) S. T. Handy, M. Okello, *Tetrahedron Lett.* **2003**, *44*, 8395-8397; k) A. H. Roy, J. F. Hartwig, *Organometallics* **2004**, *23*, 194–202; l) P. M. Maitlis, A. Haynes, B. R. James, M. Catellani, G. P. Chiusoli, *Dalton Trans.* **2004**, 3409-3419; m) S. P. H. Mee, V. Lee, J. E. Baldwin, *Chem. Eur. J.* **2005**, *11*, 3294-3308; n) I. J. S. Fairlamb, R. J. K. Taylor, J. L. Serrano, G. Sanchez, *New J. Chem.* **2006**, *30*, 1695–1704; o) S. Shekhar, J. F. Hartwig, *Organometallics* **2007**, *26*, 340-351; p) B. P. Carrow, J. F. Hartwig, *J. Am. Chem. Soc.*

2010, *132*, 79-81; q) F. Proutiere, F. Schoenebeck, *Angew. Chem.* **2011**, *123*, 8342–8345; *Angew. Chem. Int. Ed*. **2011**, *50*, 8192–8195.

[24] Z. Huang, M. Qian, D. J. Babinski, E. Negishi, *Organometallics* **2005**, *24*, 475–478.

[25] Z. Rappoport, I. Marek (Eds.), *The chemistry of organozinc compounds*, John Wiley, Chichester, England; Hoboken, NJ, **2006**.

[26] a) P. K. Byers, A. J. Canty, M. Crespo, R. J. Puddephatt, J. D. Scott, *Organometallics* **1988**, *7*, 1363-1367; b) P. K. Byers, A. J. Canty, B. W. Skelton, P. R. Traill, A. A. Watson, A. H. White, *Organometallics* **1992**, *11*, 3085-3088; c) M. Portnoy, M. D., *Organometallics* **1993**, *12*, 1665–1673; d) P. Cianfriglia, V. Narducci, C. Lo Sterzo, E. Viola, G. Bocelli, T. A. Kodenkandath, *Organometallics* **1996**, *15*, 5220-5230; e) J. Manna, C. J. Kuehl, J. A. Whiteford, P. J. Stang, *Organometallics* **1997**, *16*, 1897–1905; f) A. L. Casado, P. Espinet, *Organometallics* **1998**, *17*, 954-959; g) R. Oilunkaniemi, R. S. Laitinen, M. Ahlgrén, *J. Organomet. Chem.* **1999**, *587*, 200–206; h) L. M. Alcazar-Roman, J. F. Hartwig, A. L. Rheingold, L. M. Liable-Sands, I. A. Guzei, *J. Am. Chem. Soc.* **2000**, *122*, 4618–4630; i) L. M. Alcazar-Roman, J. F. Hartwig, *J. Am. Chem. Soc.* **2001**, *123*, 12905–12906; j) A. H. Roy, J. F. Hartwig, *J. Am. Chem. Soc.* **2003**, *125*, 8704–8705; k) F. Barrios-Landeros, J. F. Hartwig, *J. Am. Chem. Soc.* **2005**, *127*, 6944–6945; l) T. E. Barder, M. R. Biscoe, S. L. Buchwald, *Organometallics* **2007**, *26*, 2183–2192; m) F. Barrios-Landeros, B. P. Carrow, J. F. Hartwig, *J. Am. Chem. Soc.* **2009**, *131*, 8141–8154.

[27] a) Y.-Q. Fang, M. I. J. Polson, G. S. Hanan, *Inorganic Chemistry* **2003**, *42*, 5-7; b) T. J. Anderson, D. A. Vicic, *Organometallics* **2004**, *23*, 623–625; c) R. Álvarez, A. R. de Lera, J. M. Aurrecoechea, A. Durana, *Organometallics* **2007**, *26*, 2799–2802; d) J. A. Cesares, P. Espinet, B. Fuentes, G. Salas, *J. Am. Chem. Soc.* **2007**, *129*, 3508–3509; e) X. Lin, D. L. Phillips, *J. Org. Chem.* **2008**, *73*, 3680-3688; f) Q. Liu, H. Duan, X. Luo, Y. Tang, G. Li, R. Huang, A. Lei, *Adv. Synth. Catal.* **2008**, *350*, 1349-1354; g) L. Jin, H. Zhang, P. Li, J. R. Sowa, A. Lei, *J. Am. Chem. Soc.* **2009**, *131*, 9892-9893; h) K. Koszinowski, P. Böhrer, *Organometallics* **2009**, *28*, 100–110; i) K. Koszinowski, P. Böhrer, *Organometallics* **2009**, *28*, 771–779; j) J. Liu, H. Wang, H. Zhang, X. Wu, H. Zhang, Y. Deng, Z. Yang, A. Lei, *Chem. Eur. J.* **2009**, *15*, 4437–4445; k) Q. Liu, Y. Lan, J. Liu, G. Li, Y.-D. Wu, A. Lei, *J. Am. Chem. Soc.* **2009**, *131*, 10201–10210; l) G. Manolikakes, M. S. Z. Dong, H. Mayr, J. Li, P. Knochel, *Chem. Eur. J.* **2009**, *15*, 1324–1328; m) V. B. Phapale, D. J. Cárdenas, *Chem. Soc. Rev.* **2009**, *38*, 1598; n) E. Hevia, J. Z. Chua, P. Garcia-Alvarez, A. R. Kennedy, M. D. McCall, *Proc. Natl. Acad. Sci. USA* **2010**, *107*, 5294–5299; o) L. Jin, J. Xin, Z. Huang, J. He, A. Lei, *J. Am. Chem. Soc.* **2010**, *132*, 9607-9609; p) G. T. Achonduh, N. Hadei, C. Valente, S. Avola, C. J. O'Brien, M. G. Organ, *Chem. Commun.* **2010**, *46*, 4109–4111; q) M. A. Schade, J. E. Fleckenstein, P. Knochel, K. Koszinowski, *J. Org. Chem.* **2010**, *75*, 6848–6857; r) J. E. Fleckenstein, K. Koszinowski, *Organometallics* **2011**, *30*, 5018–5026; s) H. N. Hunter, N. Hadei, V. Blagojevic, P. Patschinski, G. T. Achonduh, S. Avola, D. K. Bohme, M. G. Organ, *Chem. Eur. J.* **2011**, *17*, 7845–7851; t) L. Jin, A. Lei, *Org. Biomol. Chem.* **2012**, *10*, 6817–6825.

[28] E. Negishi, *Acc. Chem. Res.* **1982**, *15*, 340–348.

[29] B. E. Mann, A. Musco, *J. Chem. Soc., Dalton Trans.* **1975**, 1673–1677.

[30] E. Negishi, T. Takahashi, K. Akiyoshi, *J. Chem. Soc., Chem. Commun.* **1986**, 1338–1339.

[31] (a) Y. Takahashi, T. Ito, S. Sakai, Y. Ishii, *Chem. Commun*. **1970**, 1065. (b) T. Ukai, H. Kawazura, Y. Ishii, J. J. Bonnet, J. A. Ibers, *J. Organomet. Chem*. **1974**, *65*, 253. (c) T. Ito, S. Hasegawa, Y. Takahashi, Y. Ishii, *J. Organomet. Chem*. **1974**, *73*, 401. (d) Y. Ishii, S. Hasegawa, S. Kimura, K. Itoh, *J. Organomet. Chem*. **1974**, *73*, 411. (e) M. F. Rettig, P. N. M. Maitlis, *Inorg. Synth*. **1990**, *28*, 110.

[32] C. Amatore, A. Jutand, F. Khalil, M. A. M'Barki, L. Mottier, *Organometallics* **1993**, 3168–3178.

[33] E.-i. Negishi (Eds.), *Handbook of Organopalladium Chemistry for Organic Synthesis, Vol. 1*, **2002**.

[34] a) N. A. Bumagin, A. B. Ponomaryov, I. P. Beletskaya, *J. Organomet. Chem.* **1985**, *291*, 129–132; b) E. Negishi, T. Takahashi, K. Akiyoshi, *J. Organomet. Chem.* **1987**, *334*, 181–194; c) Y. Okamoto, K. Yoshioka, T. Yamana, H. Mori, *J. Organomet. Chem.* **1989**, *369*, 285–290; d) R. van Asselt, C. Elsevier, J., *Organometallics* **1994**, *13*, 1972–1980; e) M. G. Organ, H. Ghasemi, C. Valente, *Tetrahedron* **2004**, *60*, 9453–9461; f) E. G. Dennis, D. W. Jeffery, M. V. Perkins, P. A. Smith, *Tetrahedron* **2011**, *67*, 2125–2131.

[35] K. J. Bonney, F. Schoenebeck, *Chem. Soc. Rev.* **2014**, *43*, 6609–6638.

[36] J. C. B. Ziegler, R. F. Heck, *J. Org. Chem.* **1978**, *43*, 2941–2946.

[37] F. Paul, J. Patt, J. F. Hartwig, *Organometallics* **1995**, *14*, 3030-3039.

[38] a) A.F. Littke, G.C. Fu, *Angew. Chem.* **2002**, *114*, 4350–

4386; b) A.F. Littke, G.C. Fu, *Angew. Chem. Int. Ed.* **2002**, *41*, 4176–4211.

[39] a) J. F. Hartwig, *Synlett* **1997**, 329–340; b) A. Aranyos, D. W. Old, A. Kiyomori, J. P. Wolfe, J. P. Sadighi, S. L. Buchwald, *J. Am. Chem. Soc.* **1999**, *121*, 4369-4378; c) J. P. Stambuli, M. Bühl, J. F. Hartwig, *J. Am. Chem. Soc.* **2002**, *124*, 9346-9347; d) J. P. Stambuli, C. D. Incarvito, M. Bühl, J. F. Hartwig, *J. Am. Chem. Soc.* **2004**, *126*, 1184-1194.

[40] a) X. Wu, B. P. Fors, S. L. Buchwald, *Angew. Chem.* **2011**, *123*, 10117–10121; b) X. Wu, B. P. Fors, S. L. Buchwald, *Angew. Chem. Int. Ed.* **2011**, *50*, 9943–9947.

[41] a) D. S. Surry, S. L. Buchwald, *Chem. Sci.* **2011**, *2*, 27–50; b) D. S. Surry, S. L. Buchwald, *Angew. Chem.* **2008**, *120*, 6438–6461; *Angew. Chem. Int. Ed.* **2008**, *47*, 6338–6361; c) R. Martin, S. L. Buchwald, *Acc. Chem. Res.* **2008**, *41*, 1461–1473.

[42] a) D. A. Culkin, J. F. Hartwig, *Acc. Chem. Res.* **2003**, *36*, 234–245; b) J. F. Hartwig, *Accounts Chem. Res.* **2008**, *41*, 1534–1544.

[43] F. Bellina, A. Carpita, R. Rossi, *Synthesis* **2004**, 2419–2440

[44] The active Pd(0) catalyst forms by reduction in situ:, C. Amatore, A. Jutand, M. A. M'Barki, *Organometallics* **1992**, *11*, 3009–3013.

[45] C. Amatore, E. Carré, A. Jutand, M. A. M'Barki, *Organometallics* **1995**, 1818–1826.

[46] M. R. Biscoe, B. P. Fors, S. L. Buchwald, *J. Am. Chem. Soc.* **2008**, *130*, 6686–6687.

[47] U. Christmann, R. Vilar, *Angew. Chem.* **2005**, *117*, 370–378; *Angew. Chem. Int. Ed*. **2005**, *44*, 366–374.

[48] H. Zhang, X. Luo, K. Wongkhan, H. Duan, Q. Li, L. Zhu, J. Wang, A. S. Batsanov, J. A. Howard, T. B. Marder, A. Lei, *Chemistry* **2009**, *15*, 3823-3829.

[49] M. Piber, A. E. Jensen, M. Rottländer, P. Knochel, *Org. Lett.* **1999**, *1*, 1323-1326.

[50] A. E. Jensen, P. Knochel, *J. Org. Chem.* **2002**, *67*, 79-85.

[51] a) C. Amatore, M. Azzabi, A. Jutand, *J. Am. Chem. Soc.* **1991**, *113*, 8375–8384; b) C. Amatore, A. Jutand, *Acc. Chem. Res.* **2000**, *33*, 314–321.

[52] L. Zhu, R. M. Wehmeyer, R. D. Rieke, *J. Org. Chem.* **1991**, *56*, 1445-1453.

[53] a) D. R. Armstrong, W. Clegg, P. García-Álvarez, A. R. Kennedy, M. D. McCall, L. Russo, E. Hevia, *Chem. Eur. J.* **2011**, *17*, 8333–8341; b) E. Hevia, R. E. Mulvey, *Angew. Chem.* **2011**, *123*, 6576–6578; *Angew. Chem. Int. Ed.* **2011**, *50*, 6448–6450.

[54] L. C. McCann, H. N. Hunter, J. A. C. Clyburne, M. G. Organ, *Angew. Chem.* **2012**, *124*, 7130–7133; *Angew. Chem. Int. Ed*. **2012**, *51*, 7024–7027.

[55] a) J. E. Fleckenstein, K. Koszinowski, *Chem. Eur. J.* **2009**, *15*, 12745–12753; b) A. Hernán-Gómez, E. Herd, E. Hevia, A. R. Kennedy, P. Knochel, K. Koszinowski, S. M. Manolikakes, R. E. Mulvey, C. Schnegelsberg, *Angew. Chem.* **2014**, *126*, 2744–2748; *Angew. Chem. Int. Ed*. **2014**, *53*, 2706–2710.

[56] I. S. MacIntosh, C. N. Sherren, K. N. Robertson, J. D. Masuda, C. C. Pye, J. A. C. Clyburne, *Organometallics* **2010**, *29*, 2063–2068.

[57] C.-Y. Liu, X. Wang, T. Furuyama, S. Yasuike, A. Muranaka, K. Morokuma, M. Uchiyama, *Chem. Eur. J.* **2010**, *16*, 1780–1784.

[58] L. Jin, C. Liu, J. Liu, F. Hu, Y. Lan, A. S. Batsanov, J. A. K. Howard, T. B. Marder, A. Lei, *J. Am. Chem. Soc.* **2009**, *131*, 16656–16657.

[59] H. Ochiai, M. Jang, K. Hirano, H. Yorimitsu, K. Oshima, *Org. Lett.* **2008**, *10*, 2681–2683.

[60] Y. Asada, S. Yasuda, H. Yorimitsu, K. Oshima, *Organometallics* **2008**, *27*, 6050–6052.

[61] K. B. Urkalan, M. S. Sigman, *J. Am. Chem. Soc.* **2009**, *131*, 18042–18043.

[62] M. G. Organ, S. Avola, I. Dubovyk, N. Hadei, E. A. B. Kantchev, C. J. O'Brien, C. Valente, *Chem. Eur. J.* **2006**, *12*, 4749–4755.

[63] a) C. Amatore, A. Jutand, A. Suarez, *J. Am. Chem. Soc.* **1993**, *115*, 9531–9541; b) C. Amatore, E. Carré, A. Jutand, M. A. M'Barki, G. Meyer, *Organometallics* **1995**, *14*, 5605–5614; c) C. Amatore, A. Jutand, *J. Organomet. Chem.* **1999**, *576*, 254–278.

[64] A. Joshi-Pangu, M. Ganesh, M. R. Biscoe, *Org. Lett.* **2011**, *13*, 1218–1221.

[65] C. Valente, M. E. Belowich, N. Hadei, M. G. Organ, *Eur. J. Org. Chem.* **2010**, 4343–4354.

[66] L. C. McCann, M. G. Organ, *Angew. Chem.* **2014**, *126*, 4475–4478; *Angew. Chem. Int. Ed*. **2014**, *53*, 4386–4389.

[67] M. García-Melchor, B. Fuentes, A. Lledós, J. A. Casares, G. Ujaque, P. Espinet, *J. Am. Chem. Soc.* **2011**, *133*, 13519–13526.

[68] a) G. A. Chass, C. J. O'Brien, N. Hadei, E. A. B. Kantchev, W.-H. Mu, D.-C. Fang, A. C. Hopkinson, I. G. Csizmadia, M. G. Organ, *Chem. Eur. J.* **2009**, *15*, 4281–4288; b) B. Fuentes, M. García-Melchor, A. Lledós, F. Maseras, J. A. Casares, G. Ujaque, P. Espinet, *Chem. Eur. J.* **2010**, *16*, 8596–8599.

[69] a) C. M. Fafard, C.-H. Chen, B. M. Foxman, O. V. Ozerov, *Chem. Commun.* **2007**, 4465–4467; b) T. Bollermann, K. Freitag, C. Gemel, R. W. Seidel, R. A. Fischer, *Organometallics* **2011**, *30*, 4123–4127; c) T. Bollermann, K. Freitag, C. Gemel, M.

Molon, R. W. Seidel, M. Hopffgarten, P. Jerabek, G. Frenking, R. A. Fischer, *Inorg. Chem.* **2011**, *50*, 10486–10492; d) T. Bollermann, C. Gemel, R. A. Fischer, *Coord. Chem. Rev.* **2012**, *256*, 537–555.

[70] A. B. González-Pérez, R. Álvarez, O. N. Faza, Á. R. d. Lera, J. M. Aurrecoechea, *Organometallics* **2012**, *31*, 2053–2058.

[71] P. Espinet, A. M. Echavarren, *Angew. Chem.* **2004**, *116*, 4808–4839; *Angew. Chem. Int. Ed*. **2004**, *43*, 4704-4734.

[72] J. G. de Vries, *Dalton Trans.* **2006**, 421–429.

[73] A. H. M. d. Vries, F. J. Parlevliet, L. S.-v. d. Vondervoort, J. H. M. Mommers, H. J. W. Henderickx, M. A. M. Walet, J. G. d. Vriesa, *Adv. Synth. Catal.* **2002**, *344*, 996–1002.

[74] M. Kalek, J. Stawinski, *Organometallics* **2007**, *26*, 5840–5847.

[75] C. Amatore, A. Jutand, F. Lemaítre, J. L. Ricard, S. Kozuch, S. Shaik, *J. Organomet. Chem.* **2004**, *689*, 3728-3734.

[76] L. J. Goossen, D. Koley, H. L. Hermann, W. Thiel, *Organometallics* **2005**, *24*, 2398-2410.

[77] a) L. J. Gooßen, D. Koley, H. Hermann, W. Thiel, *Chem. Commun.* **2004**, 2141–2143; b) L. J. Goossen, D. Koley, H. L. Hermann, W. Thiel, *J. Am. Chem. Soc.* **2005**, *127*, 11102-11114.

[78] a) C. Amatore, E. Carré, A. Jutand, H. Tanaka, Q. Ren, S. Torii, *Chem. Eur. J.* **1996**, *2*, 957-966; b) C. Amatore, A. Jutand, *Chem. Eur. J.* **1999**, *5*, 466–473.

[79] a) S. Kozuch, S. Shaik, A. Jutand, C. Amatore, *Chem. Eur. J.* **2004**, *10*, 3072–3080; b) S. Verbeeck, C. Meyers, P. Franck, A. Jutand, B. U. W. Maes, *Chem. Eur. J.* **2010**, *16*, 12831–12837; c) C. Amatore, A. Jutand, G. Le Duc, *Angew. Chem.* **2012**, *124*, 1408-1411; *Angew. Chem. Int. Ed.* **2012**, *51*, 1379-1382.

[80] A. Echavarren, M., J. K. Stille, *J. Am. Chem. Soc.* **1987**, *109*, 5478–5486.

[81] For selected previous kinetic studies of Pd-catalyzed Negishi cross-coupling reactions, see: a) E.-i. Negishi, T. Takahashi, D. Van Horn, E., S. Baba, N. Okukado, *J. Am. Chem. Soc*. **1987**, *109*, 2393–2401; b) J. A. Cesares, P. Espinet, B. Fuentes, G. Salas, *J. Am. Chem. Soc*. **2007**, *129*, 3508–3509; c) H. Wang, J. Liu, Y. Deng, T. Min, G. Yu, X. Wu, Z. Yang, A. Lei, *Chem. Eur. J*. **2009**, *15*, 1499–1507; d) Q. Liu, Y. Lan, J. Liu, G. Li, Y.-D. Wu, A. Lei, *J. Am. Chem. Soc*. **2009**, *131*, 10201–10210; e) H. Zhang, X. Luo, K. Wongkhan, H. Duan, Q. Li, L. Zhu, J. Wang, A. S. Batsanov, J. A. K. Howard, T. B. Marder, A. Lei, *Chem. Eur. J*. **2009**, *15*, 3823–3829.

[82] C. Amatore, A. Fuxa, A. Jutand, *Chem. Eur. J.* **2000**, *6*, 1474–1482.

[83] I. Ghosh, P. A. Jacobi, *J. Org. Chem.* **2002**, *67*, 9304–9309.

[84] H. Zhang, X. Luo, K. Wongkhan, H. Duan, Q. Li, L. Zhu, J. Wang, A. S. Batsanov, J. A. K. Howard, T. B. Marder, A. Lei, *Chem. Eur. J.* **2009**, *15*, 3823–3829.

[85] J. Li, L. Jin, C. Liu, A. Lei, *Org. Chem. Front.* **2014**, *1*, 50-53.

[86] A. Gillie, J. K. Stille, *J. Am. Chem. Soc.* **1980**, *102*, 4933–4941.

[87] X. Luo, H. Zhang, H. Duan, Q. Liu, L. Zhu, T. Zhang, A. Lei, *Org. Lett.* **2007**, *9*, 4571–4574.

[88] S. Kozuch, J. M. L. Martin, *ChemPhysChem* **2011**, *12*, 1413–1418.

[89] K. L. Vikse, M. A. Henderson, A. G. Oliver, J. S. McIndoe, *Chem. Commun.* **2010**, *46*, 7412–1714.

[90] a) C. Amatore, A. Jutand, M. A. M'Barki, *Organometallics* **1992**, *11*, 3009–3013; b) Z. Csákai, R. Skoda-Földes, L. Kollár, *Inorg. Chim. Acta* **1999**, *286*, 93–97; c) J.-C. Hierso, A. Fihri, R. Amardeil, P. Meunier, H. Doucet, M. Santelli, B. Donnadieu, *Organometallics* **2003**, *22*, 4490–4499; d) S. Erhardt, V. V. Grushin, A. H. Kilpatrick, S. A. Macgregor, W. J. Marshall, D. C. Roe, *J. Am. Chem. Soc.* **2008**, *130*, 4828–4845; e) D. Evrard, D. Lucas, Y. Mugnier, P. Meunier, J.-C. Hierso, *Organometallics* **2008**, *27*, 2643–2653; f) R. Šebesta, F. Bilčík, B. Horváth, *Eur. J. Org. Chem.* **2008**, *2008*, 5157–5161; g) R. Pratap, D. Parrish, P. Gunda, D. Venkataraman, M. K. Lakshman, *J. Am. Chem. Soc.* **2009**, *131*, 12240–12249; h) D. J. M. Snelders, C. van der Burg, M. Lutz, A. L. Spek, G. van Koten, R. J. M. Klein Gebbink, *Chem. Cat. Chem.* **2010**, *2*, 1425–1437; i) M. A. Fredricks, M. Drees, K. Köhler, *Chem. Cat. Chem.* **2010**, *2*, 1467–1476; j) B. Lü, P. Li, C. Fu, L. Xue, Z. Lin, S. Ma, *Adv. Synth. Catal.* **2011**, *353*, 100–112; k) A. Kurbangalieva, D. Carmichael, K. K. M. Hii, A. Jutand, J. M. Brown, *Chem. Eur. J.* **2014**, *20*, 1116–1125.

[91] O. V. Tyukalova, G. V. Raovskii, F. K. Shmidt, *Zh. Obshch. Khim.* **2001**, *71*, 946–951.

[92] M. Tromp, J. R. A. Sietsma, J. A. v. Bokhoven, G. P. F. v. Strijdonck, R. J. v. Haaren, A. M. J. v. d. Eerden, P. W. N. M. v. Leeuwen, D. C. Koningsberger, *Chem. Commun.* **2003**, 128–129.

[93] J. Wang, H. F. M. Boelens, M. B. Thathagar, G. Rothenberg, *Chem. Phys. Chem.* **2004**, *5*, 93–98.

[94] A. Roglans, A. Pla-Quintana, in *Reactive Intermediates*, (L. S. Santos, Ed.), Wiley-VCH, Weinheim, **2010**, pp. 229–275.

[95] a) A. O. Aliprantis, J. W. Canary, *J. Am. Chem. Soc.* **1994**, *116*, 6985–6986; b) J. M. Brown, K. K. Hii, *Angew. Chem.* **1996**, *108*, 679–682; *Angew. Chem. Int. Ed.* **1996**, *35*, 657–659; c) M. A. Aramendía, F. Lafont, M. Moreno-Mañas, R. Pleixats, A. Roglans, *J. Org. Chem.* **1999**, *64*, 3592–3594; d) A. A. Sabino, A. H. L. Machado, C. R. D. Correia, M. N. Eberlin, *Angew. Chem.* **2004**, *116*, 2568–2572; *Angew. Chem. Int. Ed*. **2004**, *43*, 2514–2518; e) H. Guo, R. Qian, Y. Liao, S. Ma, Y. Guo, *J. Am. Chem. Soc.* **2005**, *127*, 13060–13064; f) P.-A. Enquist, P. Nilsson, P. Sjöberg, M. Larhed, *J. Org. Chem.* **2006**, *71*, 8779–8786; g) C. Markert, M. Neuburger, K. Kulicke, M. Meuwly, A. Pfaltz, *Angew. Chem.* **2007**, *119*, 5996–5999; *Angew. Chem. Int. Ed.* **2007**, *46*, 5892–5895; h) J. Masllorens, I. González, A. Roglans, *Eur. J. Org. Chem.* **2007**, 158–166; i) L. S. Santos, G. B. Rosso, R. A. Pilli, M. N. Eberlin, *J. Org. Chem.* **2007**, *72*, 5809–5812; j) A. Svennebring, P. J. R. Sjöberg, M. Larhed, P. Nilsson, *Tetrahedron* **2008**, *64*, 1808–1812.

[96] C. Chevrin, J. Le Bras, F. Hénin, J. Muzart, A. Pla-Quintana, A. Roglans, R. Pleixats, *Organometallics* **2004**, *23*, 4796-4799.

[97] C. Raminelli, M. H. G. Prechtl, L. S. Santos, M. N. Eberlin, J. V. Comasseto, *Organometallics* **2004**, *23*, 3990-3996.

[98] a) A. Jutand, S. Négri, *Organometallics* **2003**, *22*, 4229–4237; b) C. Markert, A. Pfaltz, *Angew. Chem.* **2004**, *116*, 2552–2554; *Angew. Chem. Int. Ed*. **2004**, *43*, 2498–2500; c) A. Pla-Quintana, A. Roglans, *Arkivoc* **2005**, 51–62; d) L. K. Hwang, Y. Na, J. Lee, Y. Do, S. Chang, *Angew. Chem.* **2005**, *117*, 6322–6325; *Angew. Chem. Int. Ed.* **2005**, *44*, 6166–6169; e) N. Taccardi, R. Paolillo, V. Gallo, P. Mastrorilli, C. F.

Nobile, M. Räisänen, T. Repo, *Eur. J. Inorg. Chem.* **2007**, 4645–4652; f) C. A. Müller, C. Markert, A. M. Teichert, A. Pfaltz, *Chem. Commun.* **2009**, 1607–1618; g) D. Agrawal, E.-L. Zins, D. Schröder, *Chemistry - An Asian Journal* **2010**, *5*, 1667–1676; h) D. Agrawal, D. Schröder, C. M. Frech, *Organometallics* **2011**, *30*, 3579–3587; i) K. L. Vikse, Z. Ahmadi, C. C. Manning, D. A. Harrington, J. S. McIndoe, *Angew. Chem.* **2011**, *123*, 8454–8456; *Angew. Chem. Int. Ed.* **2011**, *50*, 8304–8306; j) F. F. D. Oliveira, M. R. dos Santos, P. M. Lalli, E. M. Schmidt, P. Bakuzis, A. A. M. Lapis, A. L. Monteiro, M. N. Eberlin, B. A. D. Neto, *J. Org. Chem.* **2011**, *76*, 10140–10147; k) A. Vasseur, D. Harakat, J. Muzart, J. Le Bras, *J. Org. Chem.* **2012**, *77*, 5751–5758; l) J. Hývl, J. Roithová, *Org. Lett.* **2014**, *16*, 200–203.

[99] K. J. Bonney, F. Proutiere, F. Schoenebeck, *Chem. Sci.* **2013**, *4*, 4434–4439.

[100] a) R. Qian, H. Guo, Y. Liao, H. Wang, X. Zhang, Y. Guo, *Rapid Commun. Mass Spectrom.* **2006**, *20*, 589–594; b) R. Qian, Y.-X. Liao, Y.-L. Guo, H. Guo, *J. Am. Soc. Mass Spectrom.* **2006**, *17*, 1582–1589; c) J. Lindh, J. Sävmarker, P. Nilsson, P. J. R. Sjöberg, M. Larhed, *Chem. Eur. J.* **2009**, *15*, 4630–4636; d) K. Vikse, T. Naka, J. S. McIndoe, M. Besora, F. Maseras, *Chem. Cat. Chem* **2013**, *5*, 3604–3609.

[101] a) J. Evans, L. O'Neill, V. L. Kambhampati, G. Rayner, S. Turin, A. Genge, A. J. Dent, T. Neisius, *J. Chem. Soc., Dalton Trans.* **2002**, 2207–2212; b) C. J. Jones, J. A. McCleverty, A. S. Rothin, H. Adams, N. A. Bailey, *J. Chem. Soc., Dalton Trans.* **1986**, 2055–2061; c) J. H. Kirchhoff, M. R. Netherton, I. D. Hills, G. C. Fu, *J. Am. Chem. Soc.* **2002**, *124*, 13662–13663; d) T. E. Barder, S. D. Walker, J. R. Martinelli, S. L. Buchwald, *J. Am. Chem. Soc.* **2005**, *127*, 4685–4696; e) C.-Y. Liao, K.-T. Chan, C.-Y. Tu, Y.-W. Chang, C.-H. Hu, H. M. Lee, *Chem. Eur. J.* **2009**, *15*, 405–417; f) K. R. Chaudhari, A. P. Wadawale, V. K. Jain, *J. Organomet. Chem.* **2012**, *698*, 15–21; g) C.-H. Ke, B.-C. Kuo, D. Nandi, H. M. Lee, *Organometallics* **2013**, *32*, 4775–4784.

[102] a) H. M. Senn, T. Ziegler, *Organometallics* **2004**, *23*, 2980–2988; b) S. Kozuch, C. Amatore, A. Jutand, S. Shaik, *Organometallics* **2005**, *24*, 2319–2330; c) L. J. Gossen, D. Koley, H. L. Hermann, W. Thiel, *Organiometallics* **2006**, *25*, 54–67; d) S. Moncho, G. Ujaque, A. Lledós, P. Espinet, *Chem. Eur. J.* **2008**, *14*, 8986–8994; e) F. Schoenebeck, K. N. Houk, *J. Am. Chem. Soc.* **2010**, *132*, 2496–2497; f) S. Kozuch, J. M. L. Martin, *ACS Catal.* **2011**, *1*, 246–253; g) B. Pudasaini, B. G. Janesko, *Organometallics* **2011**, *30*, 4564–4571; h) M. García-Melchor, A. A. C. Braga, A. Lledós, G. Ujaque, F. Maseras, *Acc. Chem. Res.* **2013**, *46*, 2626–2634.

[103] C. J. O'Brien, E. A. B. Kantchev, C. Valente, N. Hadei, G. A. Chass, A. Lough, A. C. Hopkinson, M. G. Organ, *Chem. Eur. J.* **2006**, *12*, 4743–4748.

[104] R. Gerber, O. Blacque, C. M. Frech, *Dalton Trans.* **2011**, *40*, 8996.

[105] S. D. Walker, T. E. Barder, J. R. Martinelli, S. L. Buchwald, *Angew. Chem.* **2004**, *116*, 1907–1912; *Angew. Chem. Int. Ed.* **2004**, *43*, 1871–1876.

[106] a) S. Sase, M. Jaric, A. Metzger, V. Malakhov, P. Knochel, *J. Org. Chem.* **2008**, *73*, 7380–7382; b) T. Zhang, X. Gao, H. B. Wood, *Tetrahedron Lett.* **2011**, *52*, 311–313.

[107] a) C.-L. Sun, H. Li, D.-G. Yu, M. Yu, X. Zhou, X.-Y. Lu, K. Huang, S.-F. Zheng, B.-J. Li, Z.-J. Shi, *Nature Chemistry* **2010**, *2*, 1044–1049; b) M. Opanasenko, A. Dhakshinamoorthy, M. Shamzhy, P. Nachtigall, M. Horáček, H. Garcia, J. Čejka, *Catalysis Science & Technology* **2013**, *3*, 500; c) F. A. Westerhaus, R. V. Jagadeesh, G. Wienhöfer, M.-M. Pohl, J. Radnik, A.-E. Surkus, J. Rabeah, K. Junge, H. Junge, M. Nielsen, A. Brückner, M. Beller, *Nature Chemistry* **2013**, *5*, 537–543; d) A.

Kamimura, T. Kotake, Y. Ishihara, M. So, T. Hayashi, *J. Org. Chem. (The Journal of Organic Chemistry)* **2013**, *78*, 3961–3971.

[108] J. H. Gross (Eds.), *Mass spectrometry: A textbook*, 2nd ed ed., Springer, Heidelberg; New York, **2011**.

[109] a) J. B. Fenn, M. Mann, C. K. Meng, S. F. Wong, C. M. Whitehouse, *Science* **1989**, *246*, 64–71; b) J. B. Fenn, *J. Am. Soc. Mass Spektrom.* **1993**, *4*, 524–535.

[110] M. Dole, L. L. Mark, R. L. Hines, R. C. Mobley, L. D. Ferguson, M. B. Alice, *The Journal of Chemical Physics* **1968**, *49*, 2240–2249.

[111] N. B. Cech, C. G. Enke, *Mass Spectrometry Reviews* **2001**, *20*, 362–387.

[112] D. F. Hunt, J. R. Yates, J. Shabanowitz, S. Winstone, C. L. Hauer, *Proc. Natl. Acad. Sci. USA* **1989**, *83*, 6233–6237.

[113] a) K. Koszinowski, *J. Am. Chem. Soc.* **2010**, *132*, 6032–6040; b) W. Henderson, J. S. McIndoe (Eds.), *Mass Spectrometry of Inorganic, Coordination and Organometallic Compounds: Tools-Techniques-Tips*, John Wiley & Sons, Cichester, **2005**.

[114] R. B. Cole, *J. Mass Spektrom.* **2000**, *35*, 763–772.

[115] K. Koszinowski, F. Lissy, *Int. J. of Mass Spectrom.* **2013**, *354/355*, 219–228.

[116] A. Putau, K. Koszinowski, *Organometallics* **2011**, *30*, 4771–4778.

[117] H. M. McNair, J. M. Miller (Eds.), *Basic gas chromatography*, 2nd ed., John Wiley & Sons, Hoboken, New Jersey, **2009**.

[118] S. Cacchi, F. L. Torre, *Synthesis* **1977**, *5*, 301–305.

[119] F.F. Kneisel, Dissertation, LMU München, 2003

[120] H. K. Hofstee, J. Boersma, J. D. v. d. Meulen, G. J. M. v. d. Kerk, *J. Organomet. Chem.* **1978**, *153*, 245.

[121] P. Kochel, K. Arkady, *Synthesis* **2006**, 890–891.

[122] K. Mitsudo, T. Shiraga, D. Kagen, D. Shi, J. Y. Becker, H. Tanaka, *Tetrahedron* **2009**, *65*, 8384-8388.

[123] In the solid state, such bis-ligated complexes have been detected: T. E. Barder, S. D. Walker, J. R. Martinelli, S. L. Buchwald, *J. Am. Chem. Soc*. **2005**, *127*, 4685–4696.

[124] For the calculation of the relative reactivities, the small background amount of ArBu observed at $t = 0$ is corrected for.

[125] a) A. L. Casado, P. Espinet, *J. Am. Chem. Soc.* **1998**, *120*, 8978–8985; b) A. Ariafard, Z. Lin, I. J. S. Fairlamb, *Organometallics* **2006**, *25*, 5788–5794.

[126] K. Böck, J. E. Feil, K. Karaghiosoff, K. Koszinowski, *Chem. Eur. J.* **2015**, *21*, 5548-5560.

[127] M. J. L. Tschan, E. J. García-Suárez, Z. Freixa, H. l. n. Launay, H. Hagen, J. Benet-Buchholz, P. W. N. M. van Leeuwen, *J. Am. Chem. Soc.* **2010**, *132*, 6463-6473.

[128] T. E. Barder, *J. Am. Chem. Soc.* **2006**, *128*, 898–904.

[129] A. Serra-Muns, A. Jutand, M. Moreno-Mañas, R. Pleixats, *Organometallics* **2008**, *27*, 2421–2427.

[130] a) J. A. Creighton, D. G. Eadon, *J. Chem. Soc. Faraday Trans.* **1991**, *87*, 3881–3891; b) Ö. Metin, S. Duman, M. Dinç, S. Özkar, *J. Phys. Chem. C* **2011**, *115*, 10736–10743.

[131] a) G. Allegra, A. Immirzi, L. Porri, *J. Am. Chem. Soc.* **1965**, *87*, 1394–1395; b) T. Murahashi, H. Kurosawa, *Coord. Chem. Rev.* **2002**, *231*, 207–228.

[132] a) M. Driess, K. Merz, R. Schoenen, *Organometallics* **2007**, *26*, 2133–2136; b) L. Caggiano, R. F. W. Jackson, A. J. H. M. Meijer, B. T. Pickup, K. A. Wilkinson, *Chem. Eur. J.* **2008**, *14*, 8798–8802; c) F. Dreiocker, J. Oomens, A. J. H. M. Meijer, B. T. Pickup, R. F. W. Jackson, M. Schäfer, *J. Org. Chem.* **2010**, *75*, 1203–1213; d) A. J. Ross, F. Dreiocker, M. Schäfer, J. Oomens, A. J. H. M. Meijer, B. T. Pickup, R. F. W. Jackson, *J. Org. Chem.* **2011**, *76*, 1727–1734; e) A. R. Massah, F. Dreiocker, R. F. W. Jackson, B. T. Pickup, J. Oomens, A. J. H. M. Meijer, M. Schäfer, *Physical Chemistry Chemical Physics* **2011**, *13*, 13255–13267; f) K. Koszinowski, C. Müller, H. Brand, J. E. Fleckenstein, *Organometallics* **2012**, *31*, 7165–7170; g) X. Yan, E. Sokol, X. Li, G. Li, S. Xu, R. G. Cooks, *Angew. Chem.* **2014**, *126*, 6041-6045; *Angew. Chem. Int. Ed.* **2014**, *53*, 5931-5935.

[133] B. Nohra, E. Rodriguez-Sanz, C. Lescop, R. Réau, *Chem. Eur. J.* **2008**, *14*, 3391–3403.

[134] R. Kretschmer, M. Schlangen, H. Schwarz, *Angew. Chem.* **2011**, *123*, 5499–5503; *Angew. Chem. Int. Ed*. **2011**, *50*, 5387–5391.

[135] G. J. Van Berkel, *J. Mass Spectrom.* **2000**, *35*, 773–783.

[136] a) D. A. Dixon, A. J. Arduengo III, *J. Phys. Chem.* **1991**, *95*, 4180–4182; b) H. Chen, D. R. Justes, R. G. Cooks, *Org. Lett.* **2005**, *7*, 3949–3952; c) J. C. Bernhammer, G. Frison, H. V. Huynh, *Chem. Eur. J.* **2013**, *19*, 12892–12905.

[137] Small amounts of water are inevitably present in the vacuum system of the mass spectrometer, as revealed by the occurrence of ion-molecule reactions with H2O in a few cases, see Supporting Information.

[138] T. D. Sheppard, *Org. Biomol. Chem.* **2009**, *7*, 1043–1052.

[139] K. L. Vikse, M. P. Woods, J. S. McIndoe, *Organometallics* **2010**, *29*, 6615–6618.

[140] a) U. Christmann, D. A. Pantazis, J. Benet-Buchholz, J. E. McGrady, F. Maseras, R. Vilar, *J. Am. Chem. Soc.* **2006**, *128*, 6376–6390; b) X. Han, Z. Weng, T. S. A. Hor, *J. Organomet. Chem.* **2007**, *692*, 5690–5696; c) F. Proutiere, M. Aufiero, F. Schoenebeck, *J. Am. Chem. Soc.* **2012**, *134*, 606–612.

[141] a) W. A. Herrmann, C. Broβmer, K. Öfele, M. Beller, H. Fischer, *J. Organomet. Chem.* **1995**, *491*, C1-C4; b) W. A. Herrmann, C. Broßmer, K. Öfele, M. Beller, H. Fischer, *Journal of Molecular Catalysis A: Chemical* **1995**, *103*, 133–146; c) V. V. Grushin, *Organometallics* **2000**, *19*, 1888–1900; d) S. A. Macgregor, *Chem. Soc. Rev.* **2007**, *36*, 67–76.

[142] R. G. Parr, R. G. Pearson, *J. Am. Chem. Soc.* **1983**, *105*, 7512–7516.

[143] The kinetic measurements found that the rate constants apparently do not strongly depend on the concentration of the organozinc reagent, though. This observation could indicate that even at the lowest concentration probed, most of the Pd(0) is tied up in the heterobimetallic dimers. Alternatively, the situation may be complicated by the effect of the LiBr additive, whose concentration was varied together with that of the organozinc reagent.

[144] To facilitate a direct comparison and exclude the interference of other effects, we repeated the experiment with adding the reaction partners in a different order, but using the same stock solutions.

[145] J. Terao, N. Kambe, *Acc. Chem. Res.* **2008**, *41*, 1545–1554.

[146] A. Klapars, S. L. Buchwald, *J. Am. Chem. Soc.* **2002**, *124*, 14844–14845.

[147] a) A. A. Cant, R. Bhalla, S. L. Pimlott, A. Sutherland, *Chem. Commun.* **2012**, *48*, 3993–3995; b) X. Feng, Y. Qu, Y. Han, X. Yu, M. Bao, Y. Yamamoto, *Chem. Commun.* **2012**, *48*, 9468–9470.

[148] V. V. Grushin, H. Alper, *Chem. Rev.* **1994**, *94*, 1047–1062.

[149] a) K. L. Vikse, G. N. Khairallah, R. A. J. O'Hair, *Organometallics* **2012**, *31*, 7467–7475; b) M. J. Woolley, G. N. Khairallah, G. da Silva, P. S. Donnelly, B. F. Yates, R. A. J. O'Hair, *Organometallics* **2013**, *32*, 6931–6944.

[150] A. Faulkner, J. F. Bower, *Angew. Chem.* **2012**, *124*, 1707-1711; *Angew. Chem. Int. Ed.* **2012**, *51*, 1675-1679.

[151] Z. Daliczek, T. Soós, Z. Finta, G. Timári, G. Vlád, US20130281700 A1, **2013**.

[152] E. Psillakis, J. Cheng, M. R. Hoffmann, A. J. Colussi, *J. Phys.Chem. A* **2009**, *113*, 8826–8829; correction: ibid., 9050.

[153] H. G. Alt, R. Baumgärtner, H. A. Brune, *Chem. Ber.* **1986**, *119*, 1694-1703.

[154] Z. Chen, M. Hojo, *J. Phys. Chem. B* **1997**, *101*, 10896-10902.

[155] D. Astruc, *Anal Bioanal Chem* **2010**, *399*, 1811-1814.

[156] M. Kolter, K. Böck, K. Karaghiosoff, K. Koszinowski, *Angew. Chem.* **2017**, *129*, 13427-13431; *Angew. Chem. Int. Ed*. **2017**, *56*, 13244-13248.